University of Nevada, Reno

Buffalo Canyon: An Oligocene Greisen-Like Intrusion-Related Gold Deposit in the Union Mining District, Nye County, Nevada

A thesis submitted in partial fulfillment of the requirements
for the degree of Master of Science in Geology

by

Patrick D. Quillen

Dr. John L. Muntean/Thesis Advisor

May, 2017

THE GRADUATE SCHOOL

We recommend that the thesis
prepared under our supervision by

PATRICK D. QUILLEN

Entitled

Buffalo Canyon: An Oligocene Greisen-Like Intrusion-Related Gold Deposit in the Union Mining District, Nye County, Nevada

be accepted in partial fulfillment of the
requirements for the degree of

MASTER OF SCIENCE

Dr. John L. Muntean, Advisor

Dr. Michael W. Ressel , Committee Member

Dr. Douglas P. Boyle , Graduate School Representative

David W. Zeh, Ph.D., Dean, Graduate School

May, 2017

Abstract

Reduced intrusion-related gold (RIRG) deposits have been documented around the globe, and have been best studied in Alaska and Yukon, but few examples have been documented in Nevada. One occurrence in Nevada is the Jurassic Bald Mountain deposit in eastern Nevada; however, for most Nevada occurrences there has been insufficient work that establishes a genetic connection to intrusions or determines their age.

Buffalo Canyon is a gold prospect located near the historic Berlin mining area in northern Nye County, Nevada, where gold, silver, copper, lead and zinc were mined in the past from mesothermal quartz veins. Buffalo Canyon contains the more recently discovered Everson prospect, a poorly defined gold deposit, which has characteristics of RIRG deposits. The district includes a series of intrusions emplaced into Triassic metasedimentary and metavolcanic rocks. These previously undated intrusions vary in composition from diorite to granodiorite and granite. U-Pb dating of zircons by LA-ICPMS has revealed distinct intrusive events in the Jurassic, Cretaceous, and Oligocene. Metaluminous, biotite-pyroxene diorite stocks to porphyritic granodiorite dikes have been dated at 162.03 $\pm$ 0.91 Ma and 158.72 $\pm$ 0.94 Ma, respectively. Peraluminous, ilmenite-bearing leucogranite plugs and dikes have been dated at 81.96 $\pm$ 0.43 Ma and 82.9 $\pm$ 0.30 Ma, respectively. A variety of Oligocene dikes and small plugs that include quartz-monzodiorite, quartz monzonite, dacite and granite are metaluminous to peraluminous and locally ilmenite-bearing. Four dates of Oligocene intrusions fall within error of each other. They yielded dates of 25.13 $\pm$ 0.29, 24.9 $\pm$ 0.30, 24.8 $\pm$ 0.40 Ma and 24.6 $\pm$ 0.30 Ma.

Country rocks at Buffalo Canyon, particularly those near Jurassic intrusions, are metamorphosed to biotite hornfels. Biotite hornfels is overprinted by sodic-calcic alteration that is likely related to Jurassic intrusive activity, and consists primarily of actinolite + albite in veins and disseminated patchworks. Mesothermal quartz veins have a Au-Ag-(Sb-Pb-As-Cu) geochemical signature, are composed predominantly of moderately deformed, recrystallized quartz and contain liquid CO_2-bearing fluid inclusions. Mesothermal quartz veins are hosted within Jurassic intrusions and are post-Luning-Fencemaker thrust (mid-Jurassic) deformation. Small volumes of Oligocene intrusive rocks are variably altered to muscovite-tourmaline or propylitic assemblages. Base-metal sulfide mineralization occurs as veins and replacements, both of which are associated with tourmaline as a dominant gangue mineral. Base-metal sulfide mineralization has a Ag-Pb-Zn-Sb-As-(Au-Bi-Cu-Mo) signature.

Free gold within low sulfide, 1-10cm thick, sheeted, crack-seal quartz veins with locally developed sericite-tourmaline envelopes define the bulk of the Everson gold mineralization. Other gangue minerals in these veins include muscovite, tourmaline and fluorite. The veins have a Au-Te-(Mo-Bi-Sn) signature and high Au:Ag ratios (>1:1). The quartz in these gold-bearing veins contain common hypersaline brine and coexisting vapor-rich fluid inclusions, indicative of trapping within the two-phase brine + vapor field. Combined with estimated thicknesses of older and coeval Oligocene volcanic rocks, the fluid inclusions suggest the deposit formed at <~3 km paleodepth. The Everson-related quartz veins also cross-cut mapped Jurassic intrusive rocks, sodic-calcic veins, base-metal sulfide mineralization, and Oligocene granitic intrusions. Muscovite and tourmaline $\pm$ fluorite associated with alteration and mineralization suggest a greisen-

like style of alteration and mineralization. The preponderance of evidence suggests that most gold mineralization at Buffalo Canyon is Oligocene in age, related to a felsic intrusion that only crops outs locally, but is likely extensive in the subsurface. Buffalo Canyon bears strong similarities to typical RIRG systems, and there are likely additional unknown examples within Nevada. A significant outcome of this study is that Buffalo Canyon formed in the Oligocene, related to volcanism during slab rollback that led to the ignimbrite flare-up in the central Nevada. Though most RIRG systems in Nevada could indeed be Mesozoic, the research on Buffalo Canyon opens the possibility that similar deposits may also be related to much younger intrusions that may be largely covered by coeval Tertiary volcanic rocks.

Acknowledgements

Foremost I would like to thank my advisor, Dr. John Muntean, for his knowledge, guidance, support and patience along the way. His enthusiasm, dedication, work ethic and passion for geology are unparalleled and truly inspirational. I would also like to thank Dr. Mike Ressel for reviewing the manuscript and for his helpful comments. Thanks are also owed to Dr. Doug Boyle for serving on my committee. Thank you to all the great geologists and people with whom I've had a chance to work with at Renaissance Gold. Their expertise, financial and time contributions are greatly appreciated, which includes footing the bill for my "rescue." I want to single out Dan Pace, who was always willing to lend time and energy to help when I had questions or needed assistance. In addition, Richard Bedell, Marilyn Miller, Mark Coolbaugh, Seth Saunders, Lindsay Craig and Eric Struhsacker were very helpful and supportive throughout. Thank you to Dr. Joel DesOrmeau (UNR) and Carolina Zamora (UNR) for lending their help and expertise with Geochronology. Thank you to Dr. Jeff Vervoort (WSU) for allowing me to use his LA-ICPMS lab. I would also like to thank the Mackay School of Earth Sciences and Engineering, the Ralph J. Roberts Center for Research in Economic Geology (CREG) and the Society of Economic Geologists (SEG) for their financial support that made this project possible.

Thank you to all my fellow CREG cohorts and other graduate students for providing insightful discussions of geology, in addition to all the fun and relaxing times. Special thanks to Carol for her unwavering confidence and for putting up with me. I would be remiss if I didn't thank the people who were responsible for me making it to graduate school in the first place. To all my friends from the University of Minnesota,

Duluth who made studying geology so enjoyable and rewarding, thank you. Also thank you to Dr. Jim Miller, who first motivated me to pursue the field of economic geology, and provided an excellent role model for how to be a great person and geologist. Thank you to Mr. Todd Bergstedt, who first turned my attention to geology, and whose unique teaching style and attitude provided me with my favorite high school class. Without his class, which I took only because of the "space" part of "Earth and Space Science", I'm not sure I would have ever given the field of geology a chance.

Last but certainly not least, I would like to say thank you to my parents Bob and Patti and my brother Kevin for their love and continued support as I've made my way out west away from home, which will always be northern Minnesota.

Table of Contents

List of Tables

List of Figures

1. INTRODUCTION

Numerous gold ± silver deposits associated with quartz veins occur in many parts of Nevada. Many, but not all, are spatially associated with Mesozoic intrusions. Most have only minor historic production, but some have produced significant gold or silver. Examples include Bald Mountain, with over 3.6 million ounces of gold in past production and current resources (Nutt and Hofstra, 2007; Davis and Muntean, 2017) and Rochester with over 186 million ounces of silver in past production and current resources (Vikre, 1981, 2014; Davis and Muntean, 2016). These deposits are sources of gold for some of the most productive placer deposits in Nevada, such as those of the Spring Valley, Sierra, and Rochester districts (Johnson, 1973). Characteristics of these deposits resemble both intrusion-related systems, related to magmatic-hydrothermal fluids (Thompson et al., 1999; Thompson and Newberry, 2000; Lang et al., 2000; Hart, 2007) and orogenic gold deposits related to regional metamorphism (Goldfarb et al., 1991; Goldfarb et al., 2005; Dube and Gosselin, 2007). Bald Mountain (Nutt and Hofstra, 2007), Rochester (Vikre 1981; 2014) and Spring Valley (Crosby, 2012) have been interpreted as intrusion-related deposits occurring within Nevada. Orogenic deposits occur within California, in the Motherlode belt (Weir and Kerrick, 1987), and have been suggested for several deposits in Nevada (e.g. Spring Valley, Rochester, Candelaria), (Cheong, 2000; Crosby, 2012; Johnston et al., 2015). Controversy remains for many gold deposits associated with quartz veins throughout the world, centering on whether they are intrusion-related or orogenic in nature.

The focus of this Master's thesis is the Buffalo Canyon prospect, which is located in Union district and NW Nye County, 27 km east of Gabbs (Fig. 1). The district contains

the historic mining areas of Ione, Berlin and Grantsville and has historically produced significant amounts of Au, Ag, Pb, Cu, Zn and Hg. Much of the mineralization, especially gold, silver, and copper, is related to mesothermal quartz veining. Like most mining districts in Nevada with gold-silver mesothermal quartz vein deposits, the Union district is poorly studied with insufficient mapping, petrography, and geochronology to constrain the temporal relationship between vein mineralization and intrusions. Consequently, both intrusion related and orogenic models have been proposed to explain gold mineralization found throughout the district (Abrams, 1979; Nash, 1994).

The Buffalo Canyon prospect is defined by a small area of exposed quartz veins (~0.25 km^2) along the range front 1 km south of Buffalo Canyon proper. This area of quartz veining was not explored or exploited during historic mining in the district, and is currently being explored by Renaissance Gold Inc. as a reduced intrusion-related gold system (RIRGS), which are common in Yukon and Alaska but seemingly scarce within Nevada (Thompson and Newberry, 2000; Hart, 2007). Exploration in the 1990's focused on this area of quartz veining, and outlined a body of mineralization known as the Everson deposit, which has a mineral inventory of approximately 300,000 ounces of gold averaging 0.37–0.40 g/t. Mineralization is associated with quartz veining developed within a contact aureole surrounding an intrusive center. In addition, historically produced Au-Ag mesothermal quartz veins that are distinct from Everson related quartz veins occur throughout the district and are also found proximal to the Everson deposit.

The Buffalo Canyon prospect, including the Everson deposit, has characteristics of both intrusion-related and orogenic type gold deposits. Both styles are commonly spatially and locally temporally related to intrusive rocks, have similar alteration and

Fig. 1. Location map showing the Union district, which is made up of Ione, Berlin and Grantsville, located within the southern Shoshone Mountains. Location of the Berlin-Ichthyosaur State Park is marked in black, south of the Buffalo Canyon project.

elemental associations, and are hosted in metamorphic rocks (Hart and Goldfarb, 2005). There are few published studies discussing these deposit styles in Nevada, making it difficult to assess their economic potential and whether they constitute a legitimate exploration target. More work is needed to document temporal relationships between vein mineralization and intrusions, along with characterizing in detail, vein characteristics, fluid inclusions and structural relationships. Buffalo Canyon is an ideal project to investigate these occurrences. Knowing whether they are orogenic or intrusion-related would greatly influence how they are explored in the future within Nevada.

This study aimed at testing intrusion related and metamorphic hypotheses by: 1) determining the ages and histories of intrusive rocks within the Union district and whether they represent one evolving magmatic system or discrete periods of magmatism, 2) characterizing alteration and mineralization styles within the Buffalo Canyon property, 3) determining how mineralization and alteration relate temporally and spatially to intrusive activity, and 4) determining whether mineralization within the district represents

one evolving hydrothermal system or overprinting events. To answer these questions, a variety of field, petrographic, geochemical and geochronologic methods were employed.

2. GEOLOGIC FRAMEWORK

Tertiary volcanic rocks dominate exposures in the southern Shoshone Mountains where Buffalo Canyon is located, and in the surrounding region. These rocks unconformably overlie Mesozoic sedimentary, volcanic and intrusive rocks, which are variably deformed by crustal shortening events and intruded by a variety of Mesozoic intrusions. The Union District and the Buffalo Canyon project are primarily hosted by weakly deformed, metamorphosed Mesozoic sedimentary units and lesser amounts of intrusive rocks.

2.1. Regional Geology

Cordilleran subduction initiated along the western edge of North America in the early Triassic, resulting in the formation of a backarc basin in what is now central Nevada (Dickinson, 2006). From late Triassic through early Jurassic time, marine sedimentation and volcanism deposited material in the shelf to basin environment in western and central Nevada, as a result of backarc extension and arc volcanism (Oldow and Bartel, 1987; Wyld, 2001). These rocks were later deformed as part of the Luning-Fencemaker thrust system during the mid-Jurassic, where basinal units were thrust over shelf facies (Oldow, 1984; Wyld, 2002). This compressional event has been attributed to an island-arc collision at the continental margin (Dickinson, 2006).

A variety of intrusive rocks are found throughout northern Nevada that range in composition mostly from granodiorite to granite with lesser mafic varieties, and in age from Jurassic through Cretaceous and Tertiary (du Bray, 2007). Middle to late Jurassic backarc plutonism is attributed to slab breakoff of the Mezcalera plate, resulting from arc

accretion and a transition to Farallon plate subduction (Dickinson, 2006). This Jurassic intrusive episode has a stronger mantle isotopic signature than later Cretaceous magmatism (Wright and Wooden, 1991). Jurassic intrusive activity in Nevada is linked to a variety of ore deposit types, most notably porphyry Cu (e.g., Yerington district in western Nevada), intrusion related Au (e.g., Bald Mountain in eastern Nevada), and iron-oxide types (Humboldt mafic complex) (Barton et al., 2011; Johnson and Barton, 2000). Cretaceous magmatism is also common in Nevada, related to shallowing of Laramide subduction in the Cretaceous and eastward migration of magmatism, late Cretaceous magmatism (< ~90 Ma) is also associated with more peraluminous phases resulting from crustal thickening and heating (Barton, 1990; Dickinson, 2006; du Bray, 2007). A diverse suite of lithophile element (Be, F, W, Mo, Sn, and Zn) mineralization styles have been linked to late Cretaceous two-mica granitic magmatism within the Great Basin; however, significant ore deposits related to Cretaceous magmatism in western and central Nevada are lacking (Barton, 1987). Polymetallic occurrences are commonly associated with mid-to-late Cretaceous intrusions throughout the state, and in eastern Nevada, Cretaceous magmatism is linked to porphyry Cu (Mo,Au) mineralization in the Robinson District (Barton 1990; McDowell and Kulp, 1967). In the Humboldt Range, Au and Ag mineralization in the Rochester District has been suggested to be linked to Cretaceous magmatism, although much of the mineralization is substantially younger (~10-15 Ma.) than exposed Cretaceous stocks (Vikre, 1981; 2014).

Continued shallowing of subduction led to cessation of magmatism within Nevada from ca. 65–45 Ma. Subsequent slab rollback in the Eocene led to a southwestern sweep of magmatism across Nevada, which resulted in extensive volcanism; and related

Oligocene calderas have been documented near the Union district (Humphreys, 1995, Henry and John, 2013). Miocene and younger extension, starting at 17 Ma throughout the Great Basin, resulted in the current basin and range topography (Dickinson, 2006; John et al., 2008; Colgan et al., 2014).

2.2. Union District Geology

Historically the Union District produced appreciable amounts of Au, Ag, Hg, Pb, Cu and Zn. The district was active primarily between 1863 and 1909. It includes the producing areas of Ione in the north, Berlin in the central part of the district, which is now home to the Berlin-Ichthyosaur State Park, and Grantsville in the south. Total estimated production was 36,000 troy oz of Au, 2,300,000 troy oz of Ag, 805,000 lbs. Pb, 38,000 lbs. Cu, 16,000 lbs. Zn, and >11,000 flasks of Hg were produced (Garside and Muntean, unpublished compilation).

The Union district has had very little research, and no studies have examined the mineralization at Buffalo Canyon. Kral (1951) described the individual mining properties and histories. The first geologic study was conducted by Silberling (1959), which focused on pre-Tertiary rocks. Vitaliano and Vitaliano (1972), described the Tertiary geology. A thesis by Abrams (1979) built upon Silberling's stratigraphic framework and added more descriptions of the igneous rocks and styles of hydrothermal mineralization. Nash (1994) carried out a reconnaissance study of the mineralization from a few areas within the district, including fluid inclusion studies.

2.2.1. Stratigraphy

The pre-Tertiary rocks of the Union district mapped and described by Silberling (1959) and Abrams (1979), including their map and stratigraphic column respectively, along with locations of known mineralization within the district are shown in Figure 2. The sequence is dominated by moderately southeast-dipping Mesozoic sedimentary rocks that have mineral assemblages dominated by chlorite, attributed to regional metamorphism by Silberling (1959). The base of the section is characterized by fine-grained sediments overlain by volcanic and volcanic debris units, separated by a thin limestone member. Originally interpreted by Silberling to be the Permian Pablo Canyon Formation, this package of rocks is now informally known as the Triassic Knickerbocker formation (Abrams, 1979).

The Knickerbocker is the most extensive unit found at Buffalo Canyon, and was divided into three members by Abrams (1979). The basal member is a lower 400-meter-thick clastic member composed of alternating siltstone, greywacke, volcaniclastic, conglomerate and andesitic flows. Overlying the clastic member is a 60-meter-thick limestone member, which in turn is overlain by a 400-meter-thick greenstone member that is composed of volcanic agglomerates (andesitic 1–10 cm sub-angular to sub-rounded volcanic fragments in a volcanic matrix) and local andesitic flows. Silberling's mapping clearly shows the majority of mesothermal quartz veins in the district are hosted by this upper Knickerbocker volcanic unit (Abrams, 1979; Silberling 1959).

Summarized from Silberling (1959), units overlying the Knickerbocker (in stratigraphic order from low to high) include the 220-meter-thick Grantsville Formation (Middle Triassic), which is composed of chert pebble conglomerate, argillaceous sandstone and limestone. The Luning Formation (Upper Triassic), which hosts famous

Ichthyosaur fossils at the Berlin State Park, is also composed of chert pebble conglomerate, argillaceous sandstone and limestone, but totals over 800 meters of thickness. Relatively minor units include the grouped Triassic to Jurassic Gabbs and Sunrise Formations (total thickness of 818 m), which are composed of calcareous siltstone, shale and limestone, and the Middle Jurassic Dunlap Formation (280 m), composed of sandstone and dolomite (Middle Jurassic). The Gabbs, Sunrise and Dunlap Formations are only found south of Grantsville, and are omitted from Figure 2.

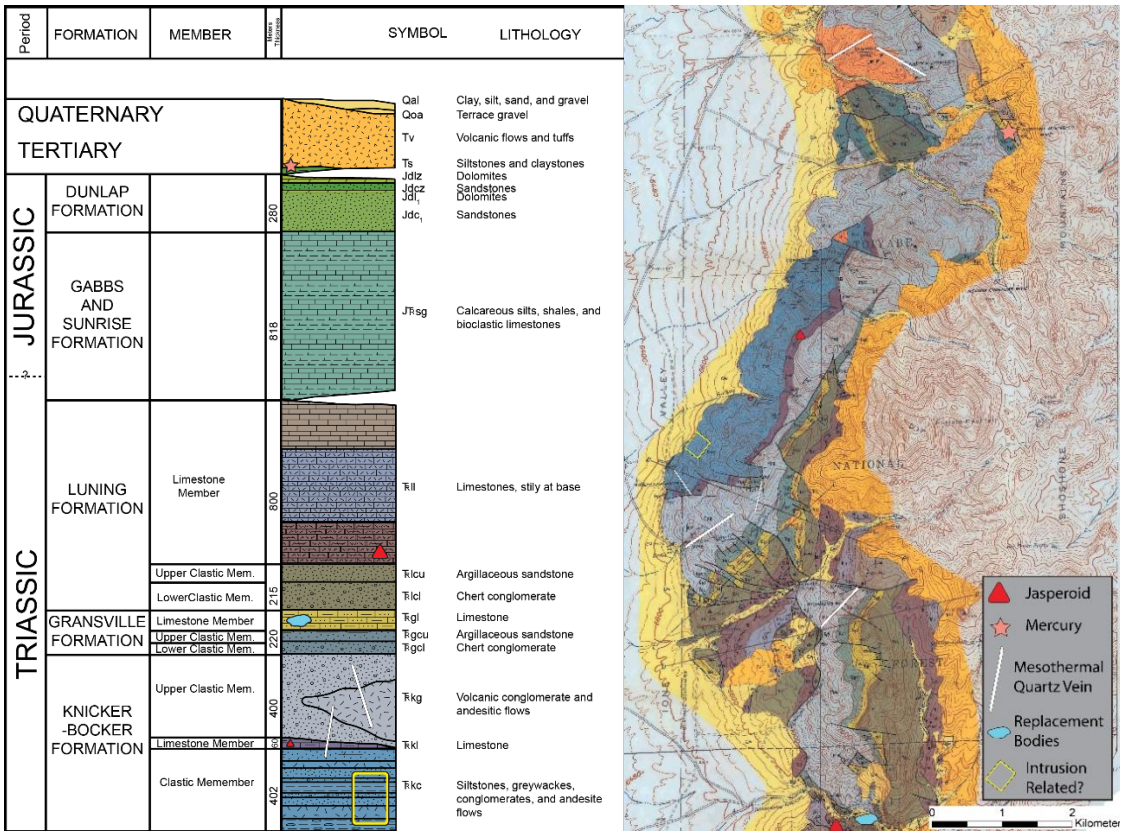

Fig. 2. Stratigraphic column and geologic map of the Union district, with mineralized locations noted. The most southern portion of the district is omitted from Silberling's map. Yellow box corresponds to the location of the Everson deposit. Modified from Abrams (1970) and Silberling (1959) respectively.

2.2.2 Intrusive Rocks

Intrusive rocks have been poorly documented within the Union district. The largest extent of intrusive rock mapped, named the Shamrock diorite by Silberling

(1959), occurs near Ione (Fig. 2). The ~1 km^2 Shamrock stock hosts mesothermal quartz veins at the Shamrock mine and other nearby workings. Abrams (1979) mapped and described additional intrusive units, including diorite dikes scattered throughout the district, a quartz monzonite stock near Ione and granodiorite dikes between Berlin and Ione. An unpublished Union Carbide Corporation K-Ar date on hornblende of 91.8 Ma was reported in Abrams (1979) from an altered, poorly exposed diorite body near Grantsville (Abrams, 1979). This is the only known radiometric date on intrusions within the district prior to this study.

2.2.3. Volcanic Rocks

The oldest dated Tertiary volcanic rocks in the district include 30.0 $\pm$ 0.9 Ma (K-Ar) welded tuffs, whose source is unknown (McKee and John, 1987). Whitebread et al., (1988) and Vitaliano and Vitaliano, (1972) describe several units stratigraphically below the dated unit, including those that directly overlie the Buffalo Canyon area. These include minor amounts the Mission Spring Formation composed of rhyolite to dacite tuffs and flows and the Third Canyon Formation of dacite and andesite flows and tuffs, which have a combined thickness of 780 m elsewhere in the district. The most voluminous units directly overlying the Buffalo Canyon area are stratigraphically above the ca. 30 Ma welded tuff, and include the 1,150 meter thick tuff breccia of Grantsville Canyon, which is overlain by the 330-meter-thick rhyolite of Union Canyon/tuff of Gabbs Valley composed of various tuffaceous rocks and rhyolite flows and breccias (Vitaliano and Vitaliano, 1972; Whitebread et al., 1988). The last major unit, that caps most of the range including Buffalo Mountain, is the 600-meter-thick tuff of Arc Dome, which is a rhyolite to high-silica rhyolite ash flow tuff. The tuff of Arc Dome is sourced from the 25.2 (K-

Ar) Ma Arc Dome caldera that is interpreted to be located on the east side of the Shoshone Mountains in the southern Reese River Valley (Henry and John, 2013). The tuff of Ione Canyon/Sheep Canyon is a rhyolite, dacite and trachyandesite tuff located to the west in the Paradise Range and to the north in the central Shoshone Mountains where it is several hundreds of meters thick. Its source is unknown (Henry and John, 2013). This unit, is also identified and mapped extensively near Ione by Whitebread (1988), but does not occur near Buffalo Canyon. Two K-Ar dates on biotite from this unit give ages of 24.4 and 24.9 Ma (Armstrong, 1970; John, 1992). The youngest volcanic rocks in the range (22.9-21.4 Ma; K-Ar) are included in the tuff of Toiyabe, which is up to 1 km thick (John, 1992). This unit is a quartz latite that was sourced from the Toiyabe caldera in the southern Toiyabe Range. The total stratigraphic thickness of Tertiary volcanic rocks in the southern Shoshone Mountains is determined to be >3,000 meters (Vitaliano and Vitaliano, 1972).

2.2.4. Structural Geology

The structural geology of the district was described in detail by Silberling (1959), who documented a variety of fault systems, including the northwest-trending Union Canyon fault zone that truncates the north-south-trending Richmond Hill fault zone. These north-trending, west-dipping faults with both normal and reverse motion and northwest transverse faults are the dominant structures throughout the district, likely the result of contractional deformation and range-front faulting (Silberling, 1959). Basin and Range faulting is clearly observed in the northern part of the district near mercury operations, and elsewhere within the district where Tertiary ignimbrites are at lower elevations than Mesozoic sediments due to normal faulting (Silberling, 1959). In

addition, pre-Tertiary rocks within the district are moderately dipping to the southeast whereas overlying Tertiary rocks are generally flat lying, creating an angular unconformity between the two (Silberling, 1959; Vitaliano, 1963).

Overall, Silberling (1959) interpreted the district as a series of folds that were dissected by likely coeval thrust faulting and subsequent Basin and Range normal faulting. A southeast plunging, faulted, asymmetric anticline is present in the Grantsville area, whose upright northeast limb is represented by 45º east-dipping units of the Knickerbocker. The Shoshone thrust, which puts the Luning Formation over the Gabbs and Sunrise Formations is exposed south of Grantsville. However, while large structures have been mapped in the area, more detailed work over the entire district is necessary to better understand the structural history of the district, which was beyond the scope of this study.

2.2.5. Mineralization

As previously mentioned, most known mineralization in the district is related to mesothermal quartz veins. Figure 2 shows the location of known mineralization occurrences within the district. Historical production records indicate silver:gold ratios of ~7 to 12 within the Berlin ores (Daggett, 1907). This is significantly higher than most orogenic gold systems around the world (Goldfarb, 2005). Mesothermal quartz veins, hosted in the Shamrock diorite and upper Knickerbocker volcanic units, were also mined near Ione. The Berlin vein is 2–3 feet thick, trends northeast and dips 45° to the southeast, is described as fissure fill and is generally truncated on all sides by faults (Daggett, 1907). The nearby Richmond vein has similar structural characteristics. Other than mesothermal quartz veins, mineralization also occurred in sulfide replacement bodies in

limestone of the Grantsville Formation around the Grantsville area. Grantsville ore contains silver, lead and zinc, and operations in 1947 report three months of data which average: 5.15 oz Ag, 3% Pb, and 1.87% Zn (Kral, 1951). Kral also notes that 0.2% WO_3 was found in dump samples. In addition, scheelite and granitic rocks were noted in underground workings (Kleinhampl and Ziony, 1984). Grantsville has seen various revival attempts since the 1920's, with Fury Explorations of Nevada, Ltd. targeting epithermal Ag-bearing veins during the late 1980's being the latest attempt (Kral, 1951; Meeuwig, 1988). In addition, fluorite was briefly mined from silicified shear zones south of Grantsville. Fluorite veins containing 10–20 ppm Mo and jasperoid bodies have also been documented on Grantsville Ridge (Kral, 1951; Nash, 1994). Mercury production also came from the area near Ione, at the head of Sheep Canyon along a north trending fault, where Tertiary rocks are down dropped relative to the Knickerbocker. Mercury is hosted in both Tertiary and pre-Tertiary rocks.

2.3. Geology of the Buffalo Canyon Project

Geology of the Buffalo Canyon project has been investigated by Renaissance Gold geologists, including mapping by Saunders (unpublished), magnetic surveys, drilling of four core holes and several reverse-circulation holes, and surface sampling. Work by Renaissance geologists and during this study identified additional intrusive rocks than what were previously mapped. These included outcrops, subcrop, and float of diorite, granite and mafic dikes. Additional diorite and granite were intercepted in a 2011 core drilling campaign conducted by Eldorado Gold Corp. and Renaissance Gold. A geologic map and cross sections of the Buffalo Canyon project, which includes mapping

completed during this study, was integrated with the mapping done by Saunders (unpublished), (Figs. 3 and 4). The map shows locations of intrusive rocks within the project area, along with the location of the Everson deposit, drill holes and samples with geochronologic analyses. The project area is dominated by the Knickerbocker Formation, with only minor rocks of the Grantsville Formation occurring near the eastern boundary of the map. The Everson deposit (Fig. 3) is characterized by sheeted and stockwork quartz ± tourmaline veins and actinolite-albite stockwork veins. This area of veining occurs within a biotite ± pyrrhotite hornfels aureole within the lower clastic member of the Knickerbocker Formation. Bordering the north end of the Everson is a small intrusive complex ranging from diorite to granite, which has an exposure of roughly 0.12 km^2.

The mapping in this study was mostly limited to the lower clastic member of the Knickerbocker, which was divided into three distinct lithologies. The lowest part of the Knickerbocker is characterized by an interbedded siltstone, greywacke and tuffaceous argillite. Overlying this unit is a 0 to 15-meter-thick conglomerate consisting predominantly of rounded to sub-rounded andesitic volcanic clasts and coarser, quartz monzonite clasts hosted in a volcanic matrix (Silberling, 1959). This distinctive conglomerate serves as a useful marker bed. Overlying the conglomerate are volcaniclastic beds, andesitic volcanic flows, and rare felsic units, which are difficult to distinguish due to metamorphism. The upper andesitic volcanic unit of the lower Knickerbocker contains sparse plagioclase phenocrysts and indigenous limonite grains. The matrix, as determined using a scanning electron microscope (SEM), consists of microcrystalline potassium feldspar and albite, with minor fine grained titanite and apatite. Mafic minerals are altered to variable amounts of chlorite, illite, and smectite.

The sequence of metamorphosed clastic-conglomerate-andesitic rocks that define the lower Knickerbocker is repeated within certain parts of the project area (Fig. 3). Both Silberling (1959) and Abrams (1979) described the lower Knickerbocker as having multiple horizons of conglomerate and andesitic flows, but field observations and relationships show normal faulting resulted in repetition of units within the project area (Fig. 4). North of Buffalo Canyon a section of the Knickerbocker limestone and greenstone are down-dropped below the lower Knickerbocker units, and a break in slope across the range combined with 90° bends in drainages also suggest displacement along normal faults that cut through parts of the project area.

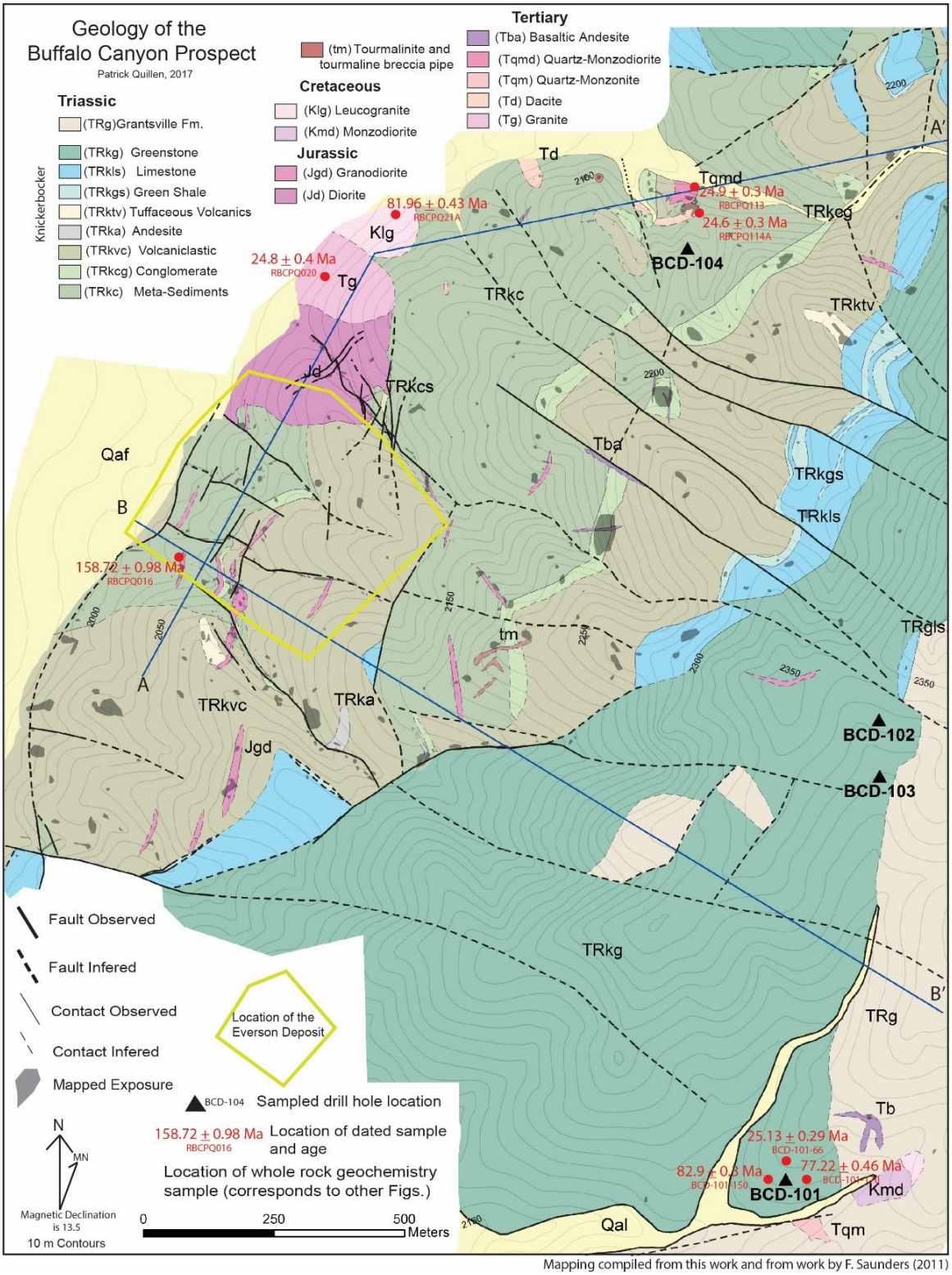

Fig. 3. Reference Map of the Buffalo Canyon project including mapped lithology and structure. Compiled from mapping for this project and mapping done by Fred Saunders. The only dated sample not located here is the Shamrock diorite (162.03 ± 0.91 Ma) near Ione. Descriptions for units can be found in the text. Cross section lines correspond to sections in Figure 4.

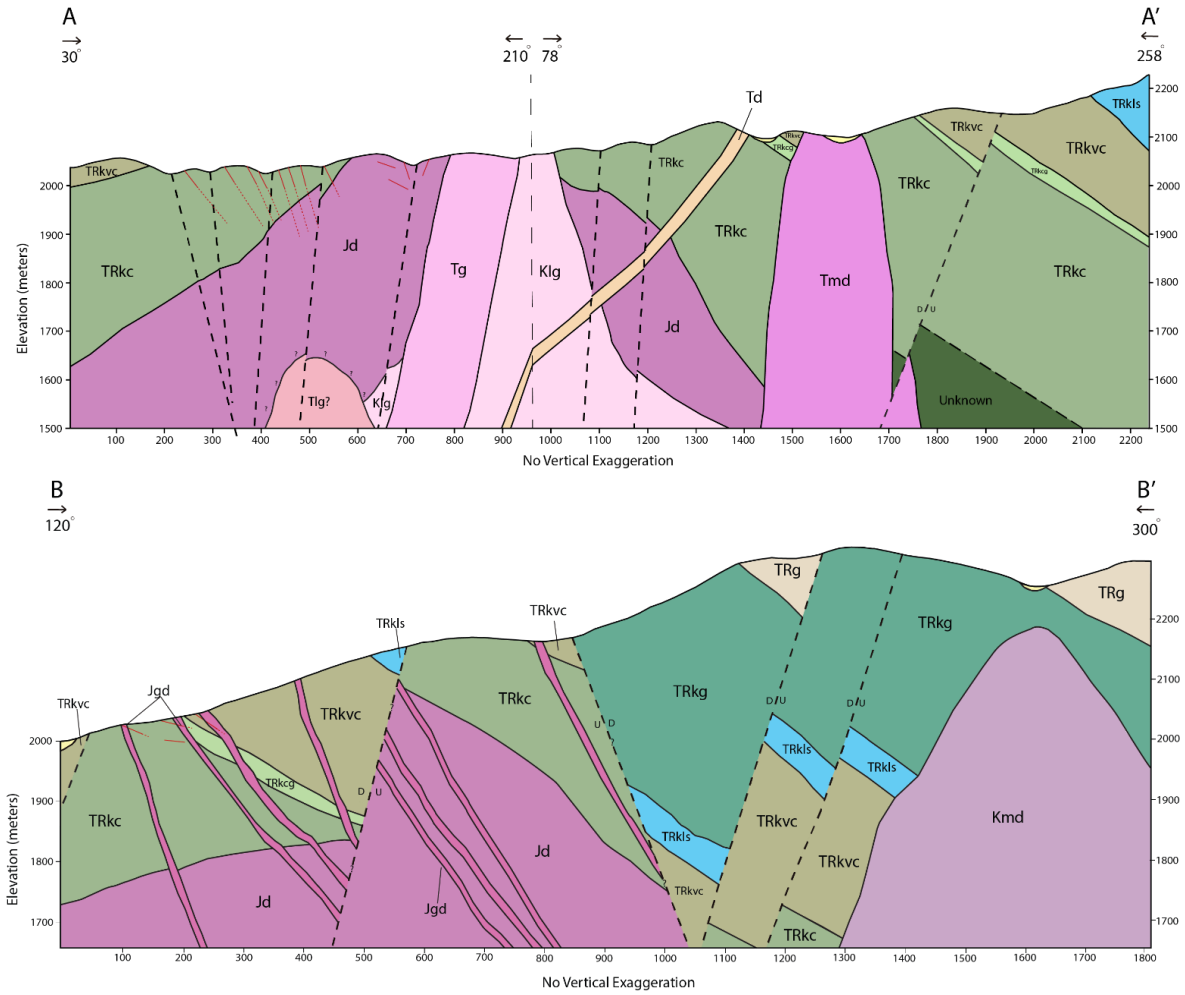

Fig. 4. Interpretive cross sections from A-A' and B-B' from Fig. 3, illustrating interpreted geology. Red lines indicate approximate dips of Everson veins. Intrusions shown in subsurface are interpreted from work discussed in the text.

3. METHODOLOGY

A variety of observational and analytical methods have been utilized in an attempt to achieve the proposed objectives. Observational methods included field work, core logging, sampling, petrography and optical microscopy. Analytical work was comprised of imaging and energy dispersive spectroscopy (EDS) microanalyses with a scanning electron microscope (SEM), along with U-Pb geochronology and whole rock geochemical analyses.

3.1. Field Work and Sampling

For this project, detailed mapping focused on spatial and temporal relationships between intrusive rocks, alteration and veining. Most mapping was performed in and around the Everson deposit in order to focus on the controls of gold mineralization. Approximately 50 days were spent mapping during the summer and fall of 2015 and 2016.

Mapping was conducted using a modified Anaconda method suited for a tablet computer and GPS. GIS Pro by Garafa was used on an Apple iPad tablet computer, utilizing detailed station points to note lithology, structures, alteration styles, mineralization, vein orientations, sample locations, field photos, and field notes. This style of field-work allowed for a comprehensive suite of samples to be taken, and relevant geologic data to be digitally recorded, including a minimum of lithology, alteration and mineralization for 1,697 stations. Mapping was compiled and final maps produced in ArcMap. In total, 123 surface samples were collected, and described using a binocular microscope. Supplementary geochemical samples were taken during

Renaissance Gold exploration activity that contributed additional data to this project. Four core holes were logged to understand the unweathered characteristics of units. Locations of holes are noted in Figure 3. Core logging focused on basic lithology, alteration and mineralization breaks. In total, 178 individual samples were collected from all four core holes, with hole BCD-101-104 being the most sampled. In total 2,324 feet of core was logged and sampled. All samples collected were sawed into slabs and described using a binocular microscope.

3.2. Petrography

A total of 83, 30-micron polished thin sections were described and analyzed using transmitted and reflected light. Descriptions focused on lithologic character, primary mineralogy, alteration mineralogy and vein textures. A subset of thin sections, particularly ones with complicated textures and mineralogies, were analyzed using the JEOL-JSM 6010LA scanning electron microscope (SEM) at the University of Nevada, Reno (UNR). Back-scattered electron (BSE) mode was used for imaging, and energy dispersive spectroscopy (EDS) was used for semi-quantitative mineral compositions. Settings commonly used included a voltage of 15.0 kV, a spot size of 64 and a working distance of 10 mm.

An additional 19 thin sections of a variety of quartz vein types were prepared with a 90 μm thickness. Of those, 11 were doubly polished and 8 were unpolished. Petrographic descriptions of fluid inclusion characteristics were made using a transmitted light microscope equipped with a 100x objective and 10x ocular. No heating or freezing experiments were performed.

3.3. Geochemistry

Whole rock geochemical analyses were done for 29 of the least-altered igneous rocks to characterize the compositional variety found within the project area. Samples were analyzed at ALS Minerals using analytical package CCP-PKG03, which utilized a lithium borate fusion for whole-rock analysis by wave-dispersive x-ray fluorescence spectrometry (ME-XRF26), in combination with total sulfur and carbon measured with a Leco infrared analyzer (S-IR08 and C-IR07). Samples for rare earth analysis (REE's) were prepared using a lithium borate fusion and analyzed by inductively coupled plasma mass spectrometer (ME-MS81), while base-metal analysis used a four-acid digestion and inductively coupled plasma atomic emission spectroscopy finish (ME-4ACD81). Volatile elements were analyzed using an aqua regia digestion and ICP-MS finish (ME-MS42).

Samples of vein material and mineralized rock were analyzed by ALS minerals using package ME-MS61, which included a four-acid digestion and ICP-MS for 48 elements. Au was determined by Au-ICP21, using fire assay and an ICP-AES finish. In total, 157 mineralization samples were taken during the course of this study, both during field work and during recent sampling by Renaissance Gold. These data were combined with data previously collected by Renaissance Gold. When samples taken during this project were combined with existing data, 669 rock chip analyses were available for evaluation of geologic characteristics related to gold mineralization, spatial patterns, and zoning patterns. The total included historical samples that were only used for plotting the spatial distribution of Au:Ag ratios. Of the total sample database, 256 samples were used for multi-element correlations because they included all relevant elements, which were

analyzed at a sufficiently low detection limit for Spearman correlation matrixes. A database of soil samples was also utilized for geochemical interpretation.

Geochemical results were plotted and evaluated using ioGAS software. Igneous whole rock data were plotted using a variety of igneous classification diagrams. These included REE spider diagrams, total alkali vs silica plots (TAS), alumina saturation indices, various element ratio plots, and Streckeisen QAPF plots (Middlemost, 1994; McDonough and Sun, 1995; Barton and Young, 2002). Spearman rank correlation matrices were used to correlate elements for various vein types to recognize geochemical patterns and to determine if field groupings matched statistical classifications. Geochemical maps were produced using ArcGIS and ioGAS using the ArcGIS add-on.

3.4. Geochronology

Zircon from 10 intrusive rocks were separated using standard mineral separation techniques at GeoSeps, Inc., in Moscow, Idaho and at the University of Nevada, Reno for U-Pb dating. Five initial samples (RBCPQ014, RBCPQ020, RBCPQ021A, RBCPQ088, BCD-101-11-66) were separated by GeoSeps and six subsequent samples were separated at UNR (RBCPQ020, RBCPQ113, RBCPQ114A, RBCPQ114B, BCD-101-11-150, BCD-101-11-170). Samples were crushed and sieved to a size <425 μm, washed and dried to remove low-density particles. Magnetic separation via the Frantz was performed at two stages, 0.35 A/20º and 0.60 A/20º to remove magnetic minerals. The non-magnetic 0.60 A/20º fraction was then separated further with methylene iodide (MeI; specific gravity of 3.33). Zircons were handpicked from the denser fraction and mounted in epoxy before being polished. Lastly, mounted zircons were imaged using a JEOL JSM-7100F

using the cathodoluminescence (CL) detector at 10.0kV and a 10.7 mm working distance. CL imaging helped determine where laser spots should be located for ICPMS analysis based on the continuity and thickness of growth zones and lack of irregularities.

All samples were dated at Washington State University (WSU) using a laser ablation inductively coupled plasma mass spectrometer (LA-ICPMS). The Peter Hooper GeoAnalytical laboratory houses a Finnigan Element2 ICP-MS with New Wave UP-213 laser ablation system. For all analyses, the laser settings included a 10 Hz repetition rate, and a 30 μm diameter laser spot, producing a typical ablation depth of 2-7 μm. Standards were typically run at the beginning, end, and after analysis of 10 unknowns, in order to correct for instrument drift. Spots were placed on cores and rims when applicable. For the zircon analyses, the standards included: Plešovice and FC-1, with a secondary standard of 91500 (Sláma et al., 2008; Paces and Miller, 1993; Wiedenbeck et al., 2004). Once reduced, U–Pb data with corresponding 2σ errors were plotted using conventional $^{207}Pb/^{235}U$ versus $^{206}Pb/^{238}U$ rations in concordia diagrams constructed using Et_Redux software (Bowring et al., 2011).

4. IGNEOUS ROCKS

Several different varieties of intrusive rocks were documented in and around the Buffalo Canyon property. Mapped intrusions comprise a small percentage of surface exposure (Fig. 3). Intrusions were grouped and classified using field relationships, hand sample, thin section petrography, and whole-rock geochemistry. Rock names are based mainly on modal percentages using petrography, but total alkali versus silica plots (TAS), alumina saturation index plots (ASI), normalized rare-earth element spider diagrams, and Harker variation plots were also used to characterize and group igneous rocks (Figs. 5, 6 and 7). Lithologies include diorite to quartz-diorite, basaltic andesite, monzodiorite, quartz-monzonite, granodiorite, dacite, granite, and leucogranite; hand samples of each are shown in Figure 8. Although least-altered examples of each rock type were analyzed, caution is needed when interpreting certain geochemical patterns to verify alteration did not affect geochemical plots. Ages of intrusive rocks are Jurassic, Cretaceous and Oligocene.

All intrusive rocks show typical calc-alkaline fractionation trends and are dominantly sub-alkaline, but vary from metaluminous to peraluminous, (Fig. 5). REE spider diagrams were particularly useful in distinguishing intrusive suites in that certain groups show distinct trends compared to others. All major intrusive rock types are summarized in Table 1.

4.1. Diorite to Quartz Diorite (Jd)

4.1.1 Petrographic Descriptions and Field Relationships

The most voluminous intrusive rock type exposed within the district is a suite of rocks that range from diorite through quartz diorite. This includes the ~1 km^2 Shamrock diorite stock near Ione and a small intrusive plug mapped on the north side of the Everson

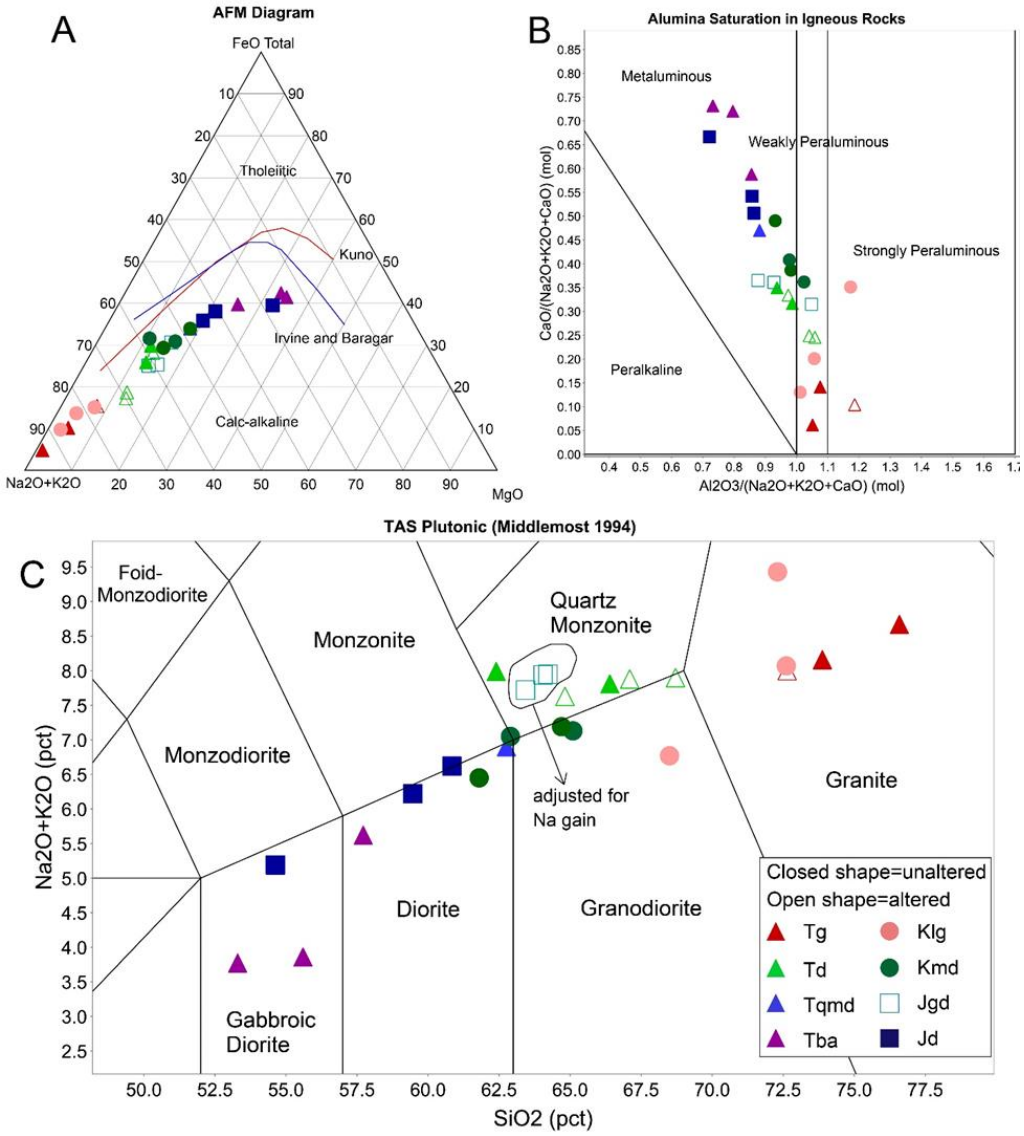

Fig. 5. Summary of whole rock geochemistry for igneous rocks. Colors of symbols correspond to groupings, shapes correspond to age, and open symbols are altered compared to closed symbols. **A)** Typical Alkali-MgO-FeO diagram. All Buffalo Canyon intrusive rocks follow a typical calc-alkaline trend. **B)** Alumina saturation index for Buffalo Canyon intrusive rocks. (From Barton and Young, 2002). **C)** Total alkalis ($Na_2O + K_2O$) vs. SiO_2 diagram, showing the range of compositions for Buffalo Canyon igneous rocks. Note when adjusted for hydrothermal Na metasomatism, samples of Jgd plot closer to the granodiorite field (From Middlemost, 1994).

deposit (Fig. 3). Diorite to quartz diorite rocks are fine to medium-grained, equigranular and dark grey in color. Samples typically contain 76-87% subhedral to euhedral plagioclase of andesine composition (<1-3 mm, determined from EDS) forming a hypidomorphic matrix with slightly coarser-grained, subhedral to euhedral pyroxene (2–10%, ≤ 1mm). Pyroxene is predominantly augite and most abundant in the Shamrock diorite. Pyroxene locally forms glomerophenocrysts (Fig. 9). Orthoclase (0–8%) is fine-grained, anhedral and interstitial, often rimming plagioclase. Quartz (0–7%) is anhedral, interstitial and fine-grained. Fine-grained biotite (2–5%, ≤2mm) is subhedral to anhedral and most often mantles pyroxene grains. Minor hornblende (0–7%, <1 mm), occurs locally and is anhedral. Hornblende commonly replaces pyroxene (uralitization), and completely replaced grains occur as hornblende pseudomorphs after pyroxene. Other minor magmatic phases include ≤ 1% fine-grained magnetite, apatite, and zircon. Previous work reported abundant hornblende within the Shamrock diorite with lesser pyroxene and biotite (Abrams, 1979).

Compared to the Shamrock diorite, exposures of this intrusive suite in and around Buffalo Canyon are much smaller. Bordering the Everson deposit to the north is a ~0.08 km^2 plug of quartz diorite that occurs as float with local, small outcroppings, exposed best within a scoured drainage that trends NW-SE on the north end of the Everson (Fig 3). This plug is only partially unroofed, with narrow (~10 cm wide) dioritic dikes intruding hornfels that lie directly above the exposed plug.

4.1.2. Geochemistry and Geochronology

Based on geochemical and petrographic data for three samples, Jd is the most mafic, major intrusive suite. Based on TAS plots, the diorite samples plot mostly in the

diorite field with RBCPQ088 (Shamrock diorite) plotting in the gabbroic diorite field, with all samples falling below the sub-alkaline line (Fig. 5). Total SiO_2 ranges from 55–61%, with quartz diorite samples from near the Everson falling on the higher end. Alumina saturation ratios indicate that this unit is metaluminous (Fig. 5). Harker variation diagrams illustrate Jd samples as early stage fractionation products, with sample RBCPQ088 plotting as the most primitive (Fig. 6). REE spider diagrams reveal that diorite samples cluster tightly together, with similar slopes and weak Eu anomalies, except for RBCPQ088 which has no Eu anomaly. This indicates that plagioclase was not previously fractionated, further suggesting the Shamrock diorite to be the most primitive phase in the suite.

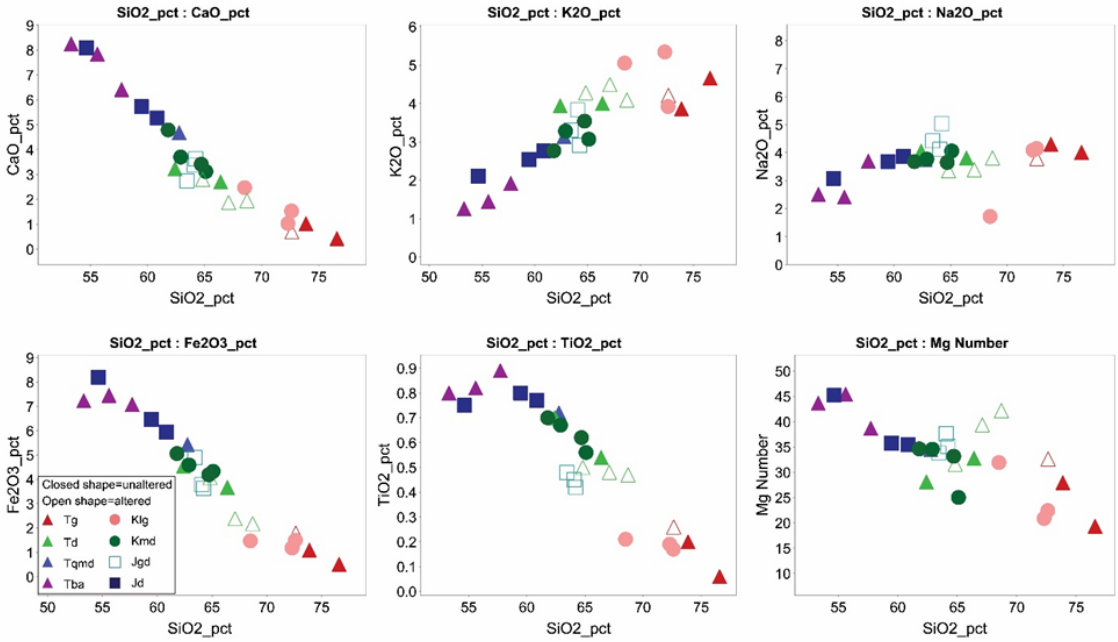

Fig. 6. Harker variation diagrams for select elements and SiO_2. Samples follow typical fractionation trends where unaltered. Note the Shamrock diorite (darkest blue square) is among the most primitive. Samples from different groupings correlate well together. Magnesium number=100*(MgO/(MgO + FeO)).

Zircons from a sample of fine grained Shamrock diorite (RBCPQ088) were dated at 162.03 ± 0.91 Ma (Fig. 10). Zircons show broad oscillatory zoning and no inheritance (Fig. 11). No zircons were recovered from the Buffalo Canyon quartz diorite.

4.2. Granodiorite Dikes (Jgd)

4.2.1. Petrographic Descriptions and Field Relationships

A series of granodiorite dikes are mapped throughout the Everson deposit area (Fig. 3). This unit was named using a TAS plot (Fig.5). Jgd is significantly affected by alteration wherever it has been observed, which masks textures and affects chemical data. These altered samples are illustrated as open shapes in chemical plots. The most obvious feature of this unit is the abundance of fine-grained feldspar phenocrysts hosted in a light tan to light grey aphanitic groundmass, which includes a larger percentage of quartz than Jd. Plagioclase phenocrysts are predominantly subhedral, altered to albite, and weakly resorbed (8–20%, ≤2 mm).

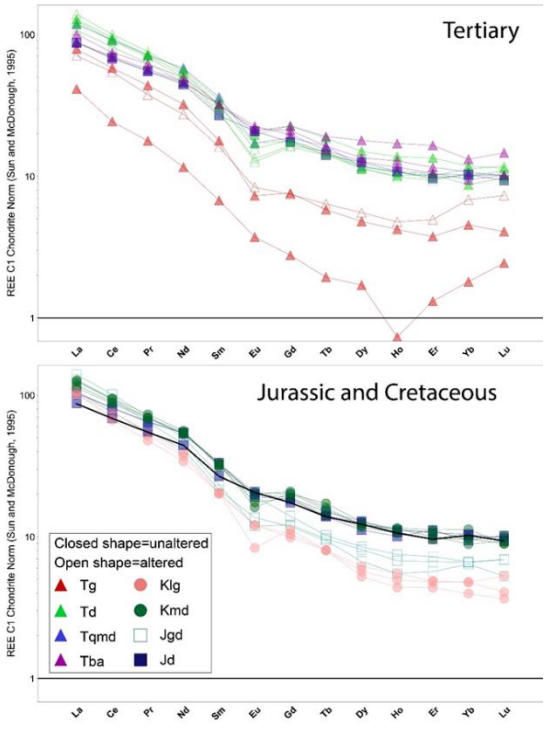

Fig. 7. Chondrite-normalized rare-earth element spider diagrams for Mesozoic and Oligocene intrusions. The dark line on the Mesozoic plots highlights the Shamrock diorite, which has no Eu anomaly. Note that several Oligocene intrusive phases have a positive heavy REE slope in Yb and Lu. Granitic phases in both the Cretaceous and Oligocene show no Eu anomaly (From McDonough and Sun, 1995).

Other phenocrysts include relict grains of both subhedral amphibole (1–3%, 1–3 mm) and subhedral biotite (0–2%, 1–3 mm). Groundmass feldspars are generally

anhedral and altered to albite with indistinct grain boundaries.

Rocks of this type have only been observed as dikes that crop out, mainly in the Everson area. Thicknesses of the dikes range from 2–8 m. Dikes strike predominantly NE, with 66–89° SE dips. Some dikes strike NNW to NW and dip to the NE at similar angles. Float of Jgd dikes have been traced to the contact with the Jd plug north of the Everson, but no definitive cross-cutting relationships were observed.

4.2.2. Geochemistry and Geochronology

No unaltered Jgd dikes were observed. For this reason, samples, which plot as quartz monzodiorites in Figure 5, are adjusted to the granodiorite field due to addition of Na during sodic-calcic alteration. Three geochemical analyses of Jgd show a tight range of 63–65% SiO_2 (Fig. 5). Within AFM and Harker fractionation diagrams, Jgd samples are more evolved than Jd (Figs. 5 and 6). Jgd samples have a significantly different REE pattern than Jd that is defined by a steeper negative slope.

One sample of a Jgd dike (RBCPQ016) from the Everson deposit yielded a date of 158.72 $\pm$ 0.98 Ma, and all analyses cluster together and are generally concordant, showing no inheritance (Fig. 10). Zircons had no obvious cores and showed obvious oscillatory zoning (Fig. 11).

Table 1. Summary of Igneous Rocks

Unit	Rock type	Texture	Mineralogy†	Age	Inheritance	Distinguishing Features	Occurrence
Diorite (Jd)	Diorite, quartz diorite	Phaneritic, fine to medium-grained equigranular to weakly porphyritic	Pl: 76-87% Px: 2-10% Ksp: 0-8% Bt: 2-5% Hbl: 0-4% Qtz: 0-7%	Jurassic (162.03 ± 0.91 Ma)	N/A	Equigranular; fine to medium-grained; pyroxene, biotite, magnetite bearing	~1 km^2 stock (Shamrock diorite) and smaller plugs near Buffalo Canyon
Porphyritic Dikes (Jgd)	Granodiorite	Finely porphyritic with an aphanitic groundmass, holocrystalline	Pl: 8-20%, ≤3 mm Bt*: 0-2%, 1-3 mm Hbl*: 1-3%, 1-3 mm	Jurassic (158.72 ± 0.98 Ma)	N/A	Abundant (8-20%) 1-3 mm subhedral plagioclase phenocrysts with 3-8% relict mafic minerals in an aphanitic matrix	2-4 m wide, sub vertical dikes, most readily exposed within the Everson area
Porphyritic quartz monzodiorite (Kmd)	Monzodiorite to granodiorite	Holocrystalline, porphyritic, aphanitic to fine-grained groundmass	Pl: 5-15%, 1-4 mm Bt*: 0-3%, <4 mm Kfs: <1%, 1-4mm	Cretaceous (77.22 ± 0.46 Ma)	approx. 260.3 ± 3.2 Ma	Compared to Jgd, contains slightly less plagioclase phenocrysts, which are coarser and often contains more, coarser biotite. More evolved versions have kfs phenocrysts. Coarser groundmass than Jgd.	Primarily observed in drill core (BCD-101-11), and float in and around Berlin Canyon
Leucogranite (Klg)	Granite	Allotriomorphic, phaneritic, medium to coarse-grained	Ksp: 60-70%, 3-10 mm Qtz: 15-23%, 2-6 mm Pl: 8-12%, <3 mm Ms+Bt: <2%, <2mm	Cretaceous (81.96 ± 0.43 Ma and 82.9 ± 0.3 Ma)	approx. 100 Ma and 160 Ma	Quartz grains (eyes) surrounded by feldspar, often allotriomorphic, trace mafic minerals. Ilmenite and muscovite bearing.	Occurs as a plug of float south of Buffalo Canyon and dikes intersected in drill hole BCD-101-11 and minor float on surface in Berlin Canyon
Quartz monzonite dike (Tqm)	Quartz monzonite	Equigranular to weakly porphyritic, phaneritic, medium-grained, seriate	Pl: 40-45% Ksp: 40-45% Qtz: 10-12% Bt*: 3-5%	Tertiary (25.13 ± 0.29 Ma)	N/A	Matrix is more potassium feldspar rich than similar Mesozoic rocks. Seriate texture with largest grains being relict mafic minerals.	Occurs as a dike intercepted in drill hole BCD-101-11
Granite (Tg)	Granite	Equigranular to weakly porphyritic, fine-grained	Ksp: 60-65% Qtz: 25-30% Bt*: 5-10% Pl: 3-8%	Oligocene (24.8 ± 0.4 Ma)	79.6 ± 0.7 Ma	Sparsely porphyritic in a fine-grained equigranular matrix with up to 15% fine grained mafic minerals (bt?).	Occurs as a small plug (or dike?) of float on the range front south of Buffalo Canyon in between Jd and Klg
Dacite Dikes (Td)	Dacite	Holocrystalline, moderately porphyritic, aphanitic groundmass	Pl: 3-8%, 1-3 mm Ksp: 1-3%, 1-3 mm Bt: 2-5%, <1-2 mm Hbl: <1-2%, <1 mm	Oligocene (24.6 ± 0.3 Ma)	79.9 ± 0.5 Ma	More quartz rich than Kqm, with finer-grained phenocrysts	Occurs as a dike and sparse outcrops on the south edge of Buffalo Canyon
Quartz monzodiorite (Tqmd)	Quartz monzodiorite	Equigranular, medium grained	Pl: 65-70% Kfs:10-12% Qtz: 6-10% Pyx: 5% Bt: 3% <3% total Amph and Ilm	Oligocene (24.9 ± 0.3 Ma)	approx. 81 Ma and 255 Ma	Equigranular, more evolved than Jd, ilmenite + pyrrhotite bearing.	Occurs as a small plug exposed on the south wall of Buffalo Canyon
Basaltic Andesite Dikes (Tba)	Basaltic Andesite	Porphyritic, aphanitic groundmass	Pl: 0-10%, 1-4 mm Px:* 3-12%, <3 mm	Undated, inferred to Tertiary	N/A	Dark aphanitic groundmass with resorbed phenocrysts of plagioclase and relict pyroxene	Occurs as ≤2 m wide dikes in the Everson area, primarily in the conglomerate member of the Knickerbocker Fm.

* Almost entirely or entirely relict; Abbreviations: Pl=plagioclase, Ksp=potassium feldspar, Qtz=quartz, Px=pyroxene, Bt=biotite, Hbl=hornblende, Mgt=magnetite, Ms=muscovite

†For porphyritic rocks phenocryst mineralogy is described, matrix mineralogy is described for equigranular rocks

4.3. Porphyritic Quartz Monzodiorite (Kmd)

4.3.1. Petrographic Descriptions and Field Relationships

This suite is similar to Jd and is differentiated by its more evolved geochemical character, porphyritic nature, aphanitic groundmass, and lack of pyroxene. Biotite is also the most abundant ferromagnesian phase. Lithologies are predominantly monzodiorite, but quartz-monzodiorite phases are locally present. Fresh hand samples are a lighter grey color than phases of the Jd suite. The unit contains subhedral to euhedral plagioclase phenocrysts (5–15%, 1-4 mm) that are often glomerophyric; long mostly relict subhedral to anhedral biotite phenocrysts (0–3%, ≤4 mm); and anhedral hornblende (1–3%, ≤1 mm; Fig. 9). Plagioclase phenocrysts are weakly resorbed and have a jagged, fractured morphology. The groundmass is holocrystalline, fine-grained to aphanitic (≤0.3 mm), contains abundant subhedral plagioclase with interstitial orthoclase (10–22%) and quartz (3–8%). Minor euhedral pyroxene (<1 mm) is locally encased by plagioclase phenocrysts. Other magmatic minerals in trace amounts (<1%) include apatite and titanite. Samples have also been observed containing miarolitic cavities.

Outcrops of Kmd are not documented on surface within the project area, but occurrences of this unit are found as float within Berlin Canyon. Hole BCD-101-11 contains a large volume of Kmd.

4.3.2. Geochemistry and Geochronology

Four samples were analyzed by whole-rock geochemistry and can be differentiated from equigranular diorite phases (Jd) by their higher SiO_2 content, which ranges from 63–67%. Harker correlation diagrams show that Kmd samples plot along a predicted fractionation trend away from Jd samples, toward more evolved compositions

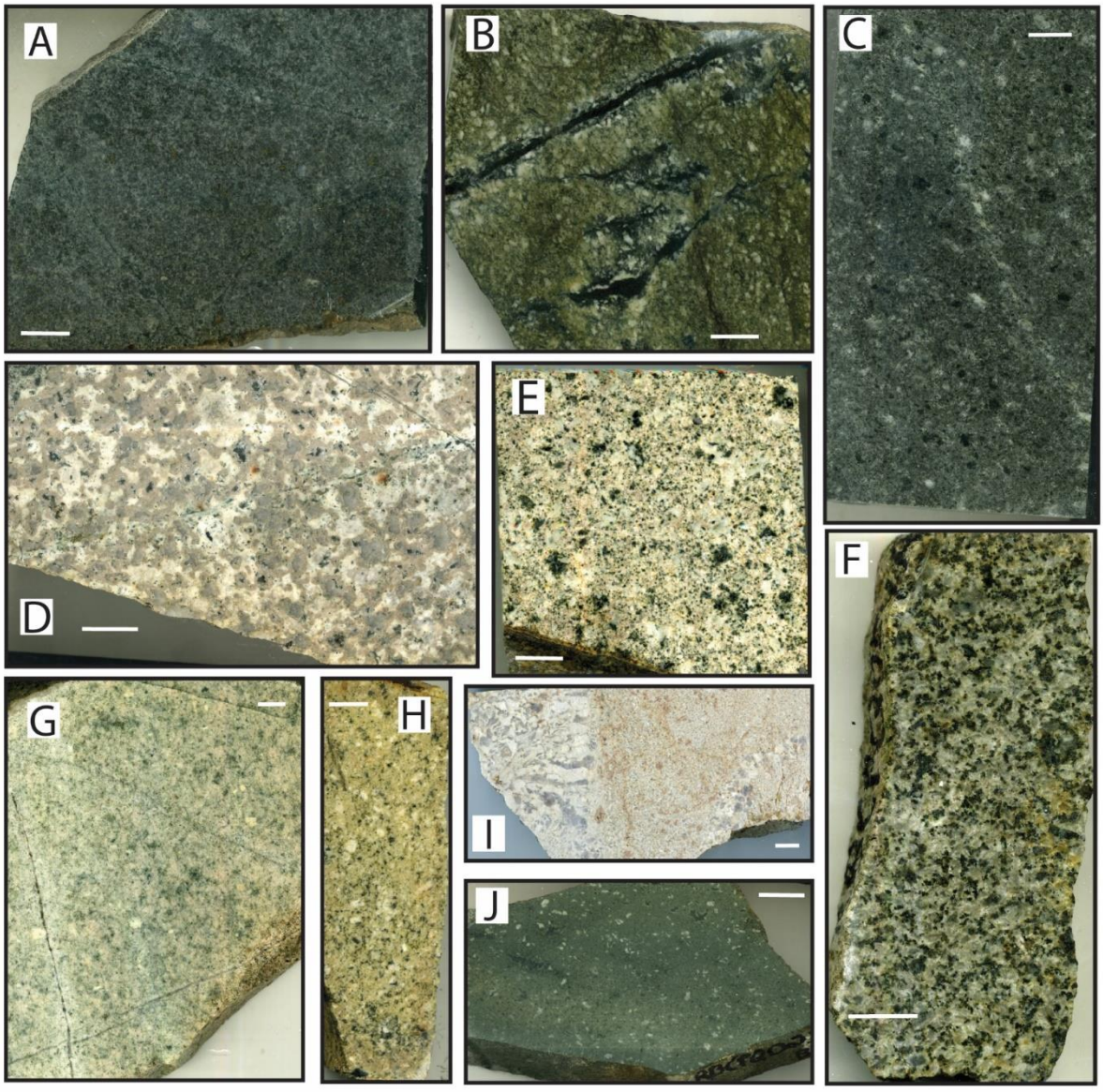

Fig. 8. Photographs of representative hand samples of intrusive rocks. All scale bars equal 1 cm. A) Jurassic diorite (Jd) from a plug just north of the Everson. B) Jurassic granodiorite dike (Jgd) from the Everson area, dated at 159 Ma. Note the actinolite-albite alteration, which occurs in all samples of Jgd. C) Cretaceous monzodiorite (Kmd) from drill hole BCD-101-11, dated at 77 Ma. D) Cretaceous leucogranite (Klg) from the range front north of the Everson, dated at 81 Ma. Note the allotriomorphic texture. E) Oligocene quartz monzodiorite (Tqm) from drill hole BCD-101-11. Dated at 25.1 Ma. F) Oligocene quartz monzodiorite (Tqmd) from the south wall of Buffalo Canyon, dated at 24.9 Ma. G) Oligocene granite (Tg), dated at 24.8 Ma, from the range front north of the Everson deposit. H) Dacite dike (Td) from the south wall of Buffalo Canyon, dated at 24.6 Ma. I) Granitic rock with aplitic (right) and UST textures (left). Similar granitic dikes from the same outcrop cut a dike of Td, so these granitic phases are inferred to the Tertiary. J) Undated basaltic andesite dike (Tba) interpreted to the Tertiary. It is the most mafic unit at Buffalo Canyon, but is a minor phase.

(Fig. 6). Kmd was classified as a quartz monzodiorite using QAPF modal abundances. On a TAS diagram, samples plot as granodiorite, near the border with quartz monzonite (Fig. 5). Kmd samples are predominantly metaluminous but are locally weakly peraluminous. Kmd differs most from Jgd in its REE patterns. Compared to Jd and Kmd, which have very similar REE patterns and differ mostly in their Eu anomaly, Jgd is slightly more elevated in light rare-earth elements (LREE) and depleted in heavy rare-earth elements (HREE), resulting in steeper negative slopes for the Jgd samples. In addition, Jgd analyses show no Eu anomaly, which contrasts with the Kmd analyses.

One sample (BCD-101-11-170) was dated from hole BCD-101-11 in Berlin Canyon. The analysis had a spread of ages, with no tight cluster (Fig. 10). A best fit yielded a date of 77.2 $\pm$ 0.5 Ma, although analyses ranged as young as 69 Ma and as old as 83 Ma. The sample also included an inherited grain of approximately 260 Ma. Zircons in Kmd show rare inherited cores, but most often show broad oscillatory zoning (Fig. 11).

4.4. Coarse-Grained Leucogranite (Klg)

4.4.1. Petrographic Descriptions and Field Relationships

Klg is a texturally and compositionally distinct compared to the other intrusive phases. It contains very few ferromagnesian minerals, and is much coarser than other significant felsic intrusive phases. Klg is holocrystalline, mostly allotriomorphic, equigranular, and medium to coarse-grained. The most distinguishing characteristic of Klg is quartz eyes (25-35%, 2–6 mm) that are surrounded by graphically intergrown potassium feldspar and quartz. Potassium feldspar is the predominant phase (60–70% 3-10 mm), and is typically anhedral, with rare megacrysts up to 2 cm long. Albite is

magmatic and minor (≤10%, <1mm), and forms anhedral, fine grained intergrowths with both quartz and potassium feldspar. Granophyric textures are abundant in the interstices of quartz and orthoclase. Anhedral to subhedral biotite is the most common ferromagnesian mineral (≤2 %, ≤ 2 mm), and commonly altered. Fine-grained accessory phases include trace muscovite and ilmenite (Figs. 9). Ilmenite, locally rimmed by titanite, also occurs. A 10-cm-wide, pegmatitic potassium feldspar crystal with tourmaline was found in one sample.

The main body of Klg occurs as a small area of float on the range front north of the Everson (Fig. 3). Klg is also documented within drill hole BCD-101-11, where it occurs as two dikes with apparent thickness of 3 and 5 meters, cutting Kmd, which is the only cross cutting relationship observed between Klg and other igneous rocks. Dates suggest Klg is older than Kmd, but cross-cutting relationships indicate the reverse relationship, which suggests that the age of Klg dikes in BCD-101-11 does not represent an emplacement age.

4.4.2. Geochemistry and Geochronology

All but one sample of Klg plots firmly within the granite field on a TAS diagram; while the one sample plots in the granodiorite field. Total SiO_2 ranges from 68–73%, and samples lie on the evolved end of fractionation trends. All samples are weakly to strongly peraluminous (Fig. 5). Compared to more mafic units (Jd, Jgd, Kmd), Klg samples are more depleted in REE's, and have steeper negative slopes. Apart from one sample, analyses have no Eu anomaly compared to analyses of Jd and Kmd.

Cretaceous zircons, unlike others in the Jurassic and Tertiary are more complex, which is manifested by multiple ages of inherited cores (Fig. 11). Two samples of Klg

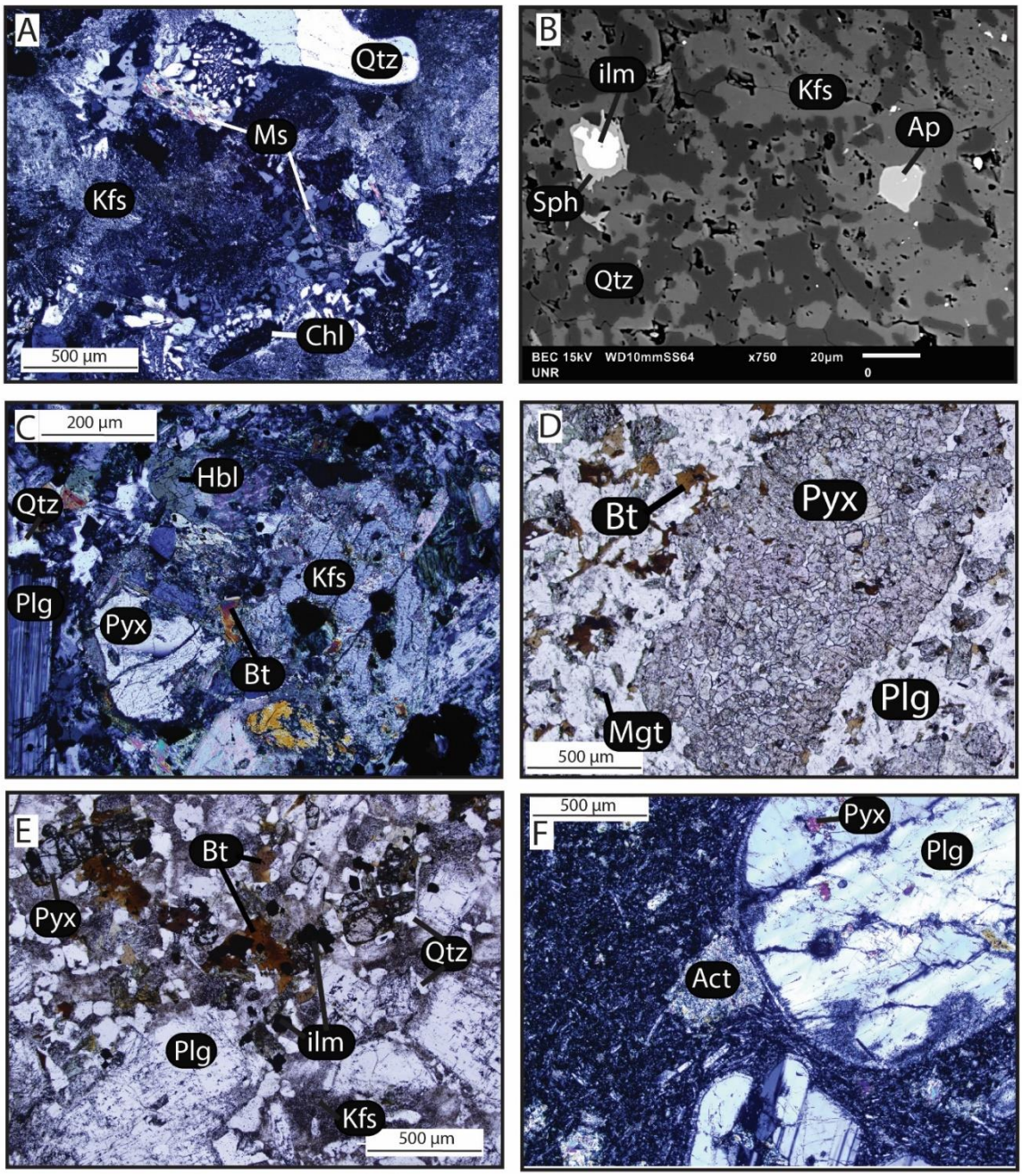

Fig. 9. Select representative photomicrographs of important features of intrusive rocks. A) XPL image of magmatic muscovite and biotite (chl) from a sample of Klg (BCD-101-150) that was dated at 83 Ma. B) SEM image of leucogranite (Klg) showing primary ilmenite, rimmed by titanite interpreted to be the result of sub-solidus oxidation. Dated at 81Ma. C) XPL image of pyroxene, biotite, hornblende bearing monzodiorite (Kmd). D) PPL image of pyroxene glomerophyric diorite from the Shamrock plug, dated at 162 Ma. Note that it is magnetite-bearing and the abundant pyroxene and glomerophyric nature also support it being an early fractionation product. E) PPL image of pyroxene (pigeonite)-biotite-ilmenite-bearing quartz monzodiorite (Tqmd) from the south wall of Buffalo Canyon. F) XPL image of Tba that contains strongly resorbed, coarse plagioclase phenocrysts in an aphanitic groundmass, which also includes relict pyroxene clots altered to actinolite and calcite. Act=Actinolite, Ap=Apatite, Bt=Biotite, Chl=Chlorite, Hbl=Hornblende, ilm=Ilmenite, Kfs=Potassium Feldspar, Mgt=Magnetite, Ms=Muscovite, Pyx=Pyroxene, Plg=Plagioclase, Qtz=Quartz, Sph=Titanite

(RBCPQ021A and BCD-101-150) yielded dates of 81.96 ± 0.43 Ma and 82.9 ± 0.3 Ma respectively (Figs 10). Both samples have inherited cores that range from Cretaceous (ca. 100 Ma) to Jurassic (ca. 140-160 Ma). In one zircon, a 250 Ma sector-zoned core is rimmed by finely oscillatory zoned Jurassic zircon (144 Ma), which is resorbed and rimmed by late Cretaceous zircon (73 Ma; Fig. 11).

4.5. Fine-Grained Granite (Tg)

4.5.1. Petrographic Descriptions and Field Relationships

Float of fine-grained granitic rock (Tg) occurs north of the Everson between Jd and Klg. One outcrop is exposed in an old prospect pit, from which samples were collected. Float covers a larger area (~0.05 km^2; Fig. 3). Tg is similar to Klg, but is distinguished primarily by texture. Exposures are hydrothermally altered, primarily to sericite, making it difficult to classify. Tg is holocrystalline, fine-grained, and equigranular to weakly porphyritic, which distinguishes it from other granitic phases. The rock is typically light tan to pink. Phenocrysts are mostly subhedral potassium feldspar (≤1 %, ≤2 mm), along with relict biotite phenocrysts (1-3%, ≤3 mm). The fine-grained matrix of the rock is mostly composed of anhedral potassium feldspar (60-65%) and quartz (25-30%), which are graphically intergrown. Fine grained (<0.3 mm) biotite also occurs as part of the groundmass (5-10%), and plagioclase is a minor, anhedral, interstitial phase (3-8%). No other definitive magmatic minerals were observed. Cross-cutting relationships indicate Tg intrudes Jd.

4.5.2. Geochemistry and Geochronology

One analysis of Tg contained 73% SiO_2, is sub-alkaline, and plots in the peraluminous field. Due to alteration and lack of magmatic muscovite, it is difficult to evaluate whether the peraluminous nature is truly magmatic or related to hydrothermal alteration. The Tg sample has a similar REE trend to Klg, but has a positive slope in Yb an Lu (Fig. 7).

One sample of Kg (RBCPQ020), with two splits (separated by different labs at different times) yielded ages of 25.74 $\pm$ 0.43 Ma and 24.8 $\pm$ 0.4 Ma (Fig. 10). A population of xenocrysts yielded ages of 78.75 $\pm$ 0.66 Ma and 79.6 $\pm$ 0.7 Ma respectively. Oligocene and Cretaceous zircons represent two distinct populations. Oligocene zircons have planar zoning and no cores, whereas Cretaceous zircons display oscillatory zoning, occasionally have older cores (ca. 90 Ma), and lack Oligocene rims that are recognizable or large enough to date (Fig. 11).

4.5.3. Tertiary Leucogranite Phases

A small area of sub-cropping leucogranite with distinct textures locally occur on the south wall of Buffalo Canyon, where they cross-cut a Td dike. Lack of exposure prevents more detailed characterization. Textures include megacrystic potassium feldspar, quartz phenocrysts, aplitic textures and unidirectional solidification textures (UST; Fig. 8-I). In thin section, granophyric and clots of resorbed potassium feldspar and quartz are common. This phase includes subhedral, megacrystic, and resorbed potassium feldspar, which differentiates it from Klg. Subhedral to euhedral potassium feldspar (65-70%, $\leq$6 mm), anhedral quartz (25-30%, $\leq$3 mm) and minor interstitial albite (5-10%, <0.5 mm) comprise most of the groundmass. Other fine-grained minerals include titanite, apatite, chlorite after biotite, and allanite occur in trace amounts (<1%).

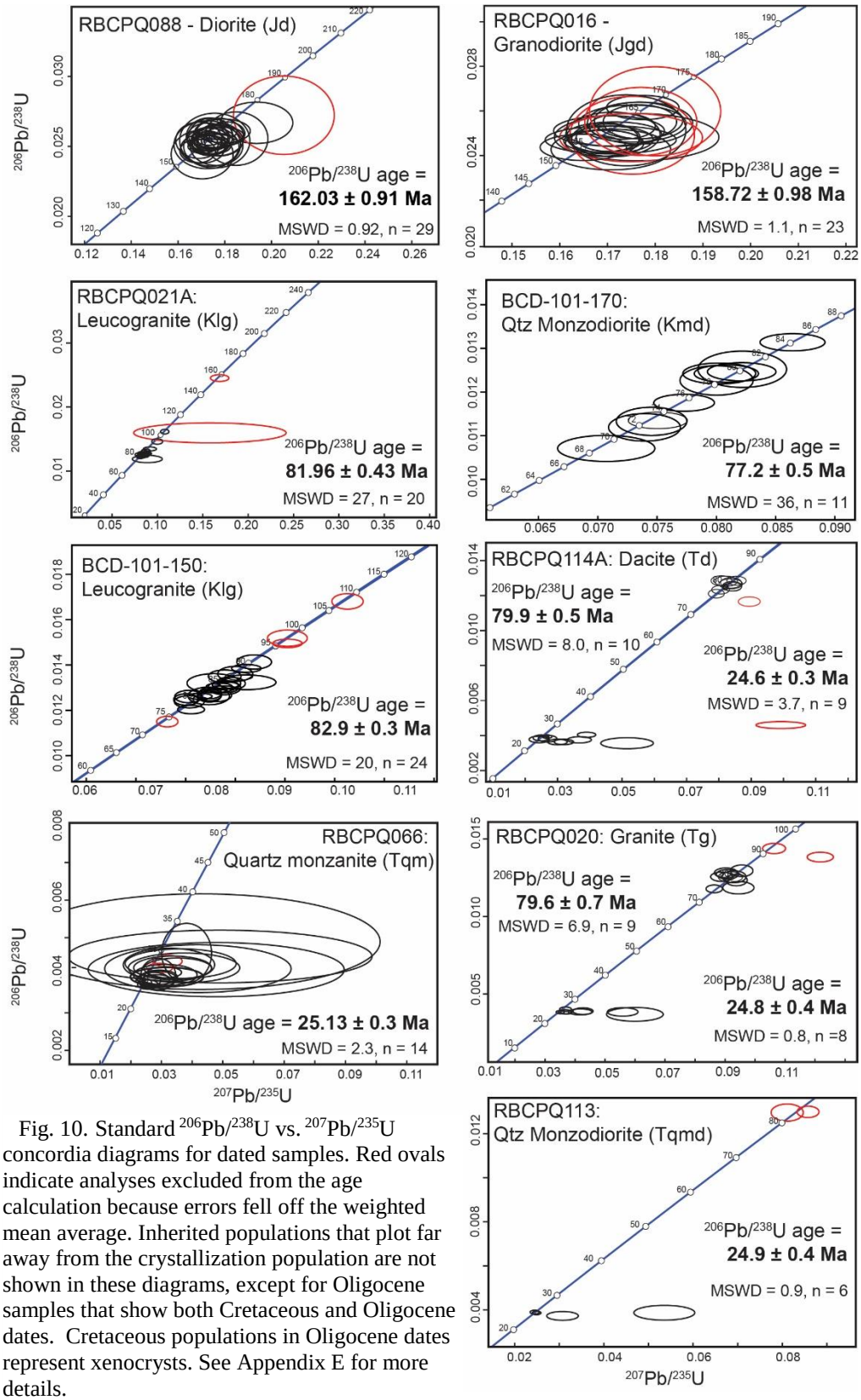

Fig. 10. Standard $^{206}Pb/^{238}U$ vs. $^{207}Pb/^{235}U$ concordia diagrams for dated samples. Red ovals indicate analyses excluded from the age calculation because errors fell off the weighted mean average. Inherited populations that plot far away from the crystallization population are not shown in these diagrams, except for Oligocene samples that show both Cretaceous and Oligocene dates. Cretaceous populations in Oligocene dates represent xenocrysts. See Appendix E for more details.

Geochemically, these younger leucogranite phases have similar signatures to Klg, but have distinctive, positive REE slopes in Yb and Lu. One sample with a UST has a strong negative Ho anomaly. These phases contain 75-77% SiO_2, making them the most silica-rich samples observed. One sample was dated, but all zircons were strongly metamict, and no concordant age could be determined.

4.6. Tertiary Dacite Dikes (Td)

4.6.1 Petrographic Descriptions and Field Relationships

Dikes of dacitic composition are found on the south wall of Buffalo Canyon and within drill hole BCD-101-11 (Fig. 3). Apparent thicknesses range from 3 meters on surface to 12 meters in core. In hand sample, Td can resemble Jgd, and it has a similar geochemistry to Kmd. Td is distinguished from Jgd by having less plagioclase phenocrysts, but more potassium feldspar and biotite phenocrysts. Td also has more quartz than Jgd. Td is distinguished from Kmd by having significantly more SiO_2 and a greater abundance of phenocrysts (Kfs, Bt, Hbl) that are finer grained, but lesser plagioclase phenocrysts which are also finer grained in Td. Td is holocrystalline, and phenocrysts are composed of weakly resorbed to angular, fragmented plagioclase (3-8%, 1-3mm) and potassium feldspar (1-3%, 1-3mm). Minor phenocrysts include subhedral biotite (2-5%, $\leq$1-2mm) and subhedral hornblende ($\leq$1-2%, $\leq$1 mm). The aphanitic matrix contains subhedral to interstitial quartz (15-20%), subhedral plagioclase (30-40%) and subhedral to anhedral potassium feldspar (30-32%).

4.6.2. Geochemistry and Geochronology

Four analyzed samples plot similarly on geochemical diagrams with SiO_2 values between 64 and 70%, slightly more evolved than Kqm (Figs. 5 and 6). Unaltered samples are metaluminous, with weakly sericitized samples plotting as weakly peraluminous. Samples show REE patterns similar with other phases, such as Jd and Kqm. Three of four samples show a weak positive slope in Yb and Lu.

A dike sample from the south wall of Buffalo Canyon (RBCPQ114A) was dated at 24.6 $\pm$ 0.3 Ma, with a separate, significant zircon xenocryst population at 79.9 $\pm$ 0.5 Ma (Fig. 10). Like other Oligocene intrusive rocks, no rims formed on the typically prismatic, oscillatory zoned Cretaceous xenocrysts. As in Tg, the Oligocene zircons show elongate, planar zoning with no cores (Fig. 11).

4.7. Tertiary Quartz Monzonite (Tqm)

4.7.1. Petrographic Descriptions and Field Relationships

Occurring as a very minor phase, only one sample of a quartz monzonite has been documented. A dike with an apparent thickness of 5.5 meters cutting upper Knickerbocker volcanic rocks was intercepted in drill hole BCD-101-11. Tqm is holocrystalline, light pink, and medium-grained to seriate. Samples contain subhedral to anhedral relict biotite (3–5%, $\leq$5 mm) and subhedral to anhedral plagioclase (40–45%, $\leq$4 mm). The remainder of the sample is anhedral, medium to fine-grained potassium feldspar (40–45%). Quartz is fine-grained, anhedral and interstitial (10–12%, <0.5mm). Primary accessory minerals include titanite and zircon (<1%, <1 mm).

4.7.2. Geochemistry and Geochronology

One analysis of Tqm showed 67% SiO_2, but had more Na_2O+K_2O than all other intrusive rocks. The sample follows a typical calc-alkaline trend and is metaluminous (Fig. 5). The REE pattern for this analysis has a slope and minor Eu anomaly very similar to Jd, Jgd, Kmd and Td. One sample of Tqm (RBCPQ066) was dated and yielded a concordant age of 25.13 $\pm$ 0.29 Ma (Fig. 10). There were no identified inherited grains, and zircons show poorly defined zoning (Fig. 11).

4.8. Tertiary Quartz Monzodiorite (Tqmd)

4.8.1. Petrographic Descriptions and Field Relationships

A small quartz monzodiorite plug outcrops on the south wall of Buffalo Canyon, and is <10 m^2 in size. Based on mineralogy, this phase is similar to Jd, but is distinguished by its equigranular, medium-grained texture and by abundant ilmenite. Tqmd is lighter grey in color, and is composed of euhedral to subhedral plagioclase (65-70%, andesine based on EDS), subhedral to anhedral potassium feldspar (10-12%), anhedral, often interstitial quartz (6-10%), subhedral to euhedral clinopyroxene (5%, pigeonite based on EDS), subhedral biotite (3%) and hornblende after pyroxene (<3%, uralitization). Significantly, Tqmd also contains primary ilmenite and magmatic pyrrhotite (Fig. 9). Apatite is a trace magmatic mineral. Tqmd crops out within 3 meters of a Td dike, but no definitive cross-cutting relationship was observed.

4.8.2 Geochemistry and Geochronology

Tqmd contains 62.5% SiO_2 and is metaluminous, showing a typical fractionation trend, in line with all other intrusive samples (Fig 6). REE spider plots show a similar pattern to other metaluminous phases, including a weak Eu anomaly.

One sample (RBCPQ113) of Tqmd was dated at 24.9 ± 0.3 Ma (Fig. 10). Zircons are generally small (<30µm), and in contrast to other dated samples, a 20 µm spot size was used. Grains have weak, broad oscillatory zoning, and due to their fine-grained nature, no core to rim relationships could be distinguished. In addition, no obvious cores or rims were observed in CL. Multiple xenocrysts were also dated. Two inherited grains with no rims had distinct, oscillatory zoning, and were dated at approximately 80 Ma (Fig. 11). Another inherited grain with no rims was dated at approximately 255 Ma, and has much broader oscillatory and sector zoning.

4.9. Basaltic Andesite Porphyritic Dikes (Tba)

4.9.1. Petrographic Descriptions and Field Relationships

Minor amounts of basaltic andesite dikes primarily occur within the lower Knickerbocker conglomerate. Basaltic andesite is the most mafic unit in the study area and is distinguished by its porphyritic nature, and abundant pyroxene and plagioclase phenocrysts set in an aphanitic groundmass.

These dikes are differentiated from other porphyritic phases based on their phenocrysts. Mafic phenocrysts are significantly more abundant than other suites and the phenocrysts are more clearly resorbed. Plagioclase phenocrysts (0-10%, 1-4 mm) are embayed and hydrothermally albitized. Where not altered to actinolite and calcite, relict pyroxene (3-12%, ≤3 mm) is also strongly resorbed (Fig. 9). The groundmass is aphanitic and hypocrystalline, and is composed almost entirely of felty, very fine-grained plagioclase. Minor, fine grained ilmenite was observed in the groundmass.

4.9.2. Geochemistry and Geochronology

Geochemically, Tba samples are generally the most mafic, with SiO_2 content ranging from 53–58%. In addition to this lithology, only sample RBCPQ088 from the Shamrock diorite plots on the primitive end of fractional crystallization diagrams. All Tba analyses are metaluminous and sub-alkaline (Fig. 5). REE patterns are similar to Jd samples, particularly RBCPQ088, where there is little to no Eu anomaly and overall negative slope. Tba dikes are slightly more depleted in LREE's and enriched in HREE's.

No datable material was separated, but the age of Tba is speculated to be Tertiary. The composition of Tba most resembles Tqmd. Tba, like Tqmd, contains ilmenite, pyroxene and has relatively fresher plagioclase. Tertiary intrusive rocks also show the largest range of compositions, while examples of Jurassic and Cretaceous rocks are uniform. It cannot be ruled out that Tba is of a different age.

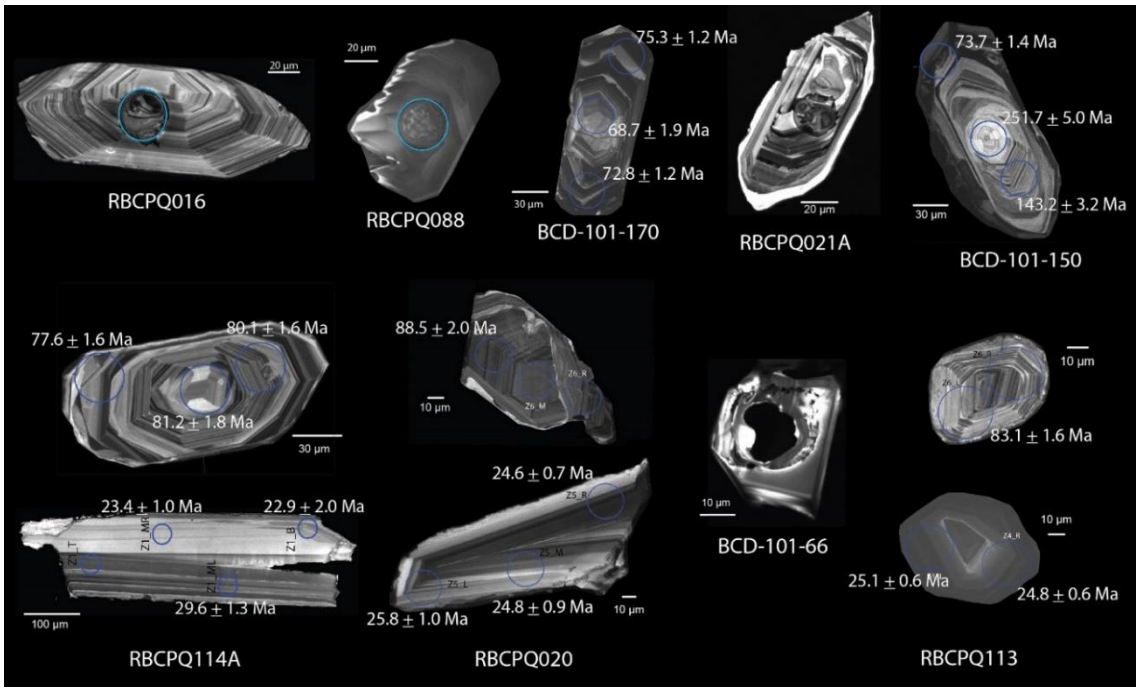

Fig. 11. Representative CL images from zircons from all dated samples. Note the samples (RBCPQ114A, RBCPQ020, RBCPQ113) that contain a bimodal distribution of both inherited Cretaceous xenocrysts with no significant rims that have more oscillatory zoned, prismatic grains and Oligocene grains that contain no cores, are elongate, non-prismatic and more planar zoned. The one exception is RBCPQ113, which does not contain planar zoned zircons. Jurassic grains display oscillatory zoning and no inherited cores, while Cretaceous grains commonly contain Permo-Triassic and Jurassic cores (BCD-101-150).

5. HYDROTHERMAL ALTERATION AND MINERALIZATION

A variety of alteration and mineralization styles have been observed in and around the Buffalo Canyon project area. Styles of alteration and mineralization were characterized and grouped based on field mapping, hydrothermal mineral assemblages, vein textures, elemental associations, and relative timing determined from cross cutting relationships. The styles are described below, in interpreted geochronological order, and are summarized in Table 2. In many cases, there is insufficient evidence to definitively determine the relative timing between some of the alteration and mineralization styles. The mapped spatial distribution of hydrothermal alteration and vein types is shown in Figure 12.

In addition to hydrothermal metasomatic alteration, contact metamorphism is included in this section as well. Hydrothermal alteration is limited in extent and is typically confined to susceptible lithologies, particularly intrusive rocks. Mineralization in the Buffalo Canyon area is predominantly vein-controlled. Veins are divided into three broad categories that include: 1) mesothermal “bull quartz” veins; 2) tourmaline-base metal sulfide veins; and 3) Au-bearing, crack-seal quartz veins that are the main control on the Everson gold deposit. The spatial distribution and orientations of the three vein types are illustrated in Figures 13 and 14 respectively.

5.1. Contact Metamorphism (Hfls)

Host rocks in and around the Buffalo Canyon area are weakly to moderately affected by thermal metamorphism, related to underlying intrusions. Clastic units (TRkc) are metamorphosed to hornfels consisting of very fine grained quartz + biotite $\pm$

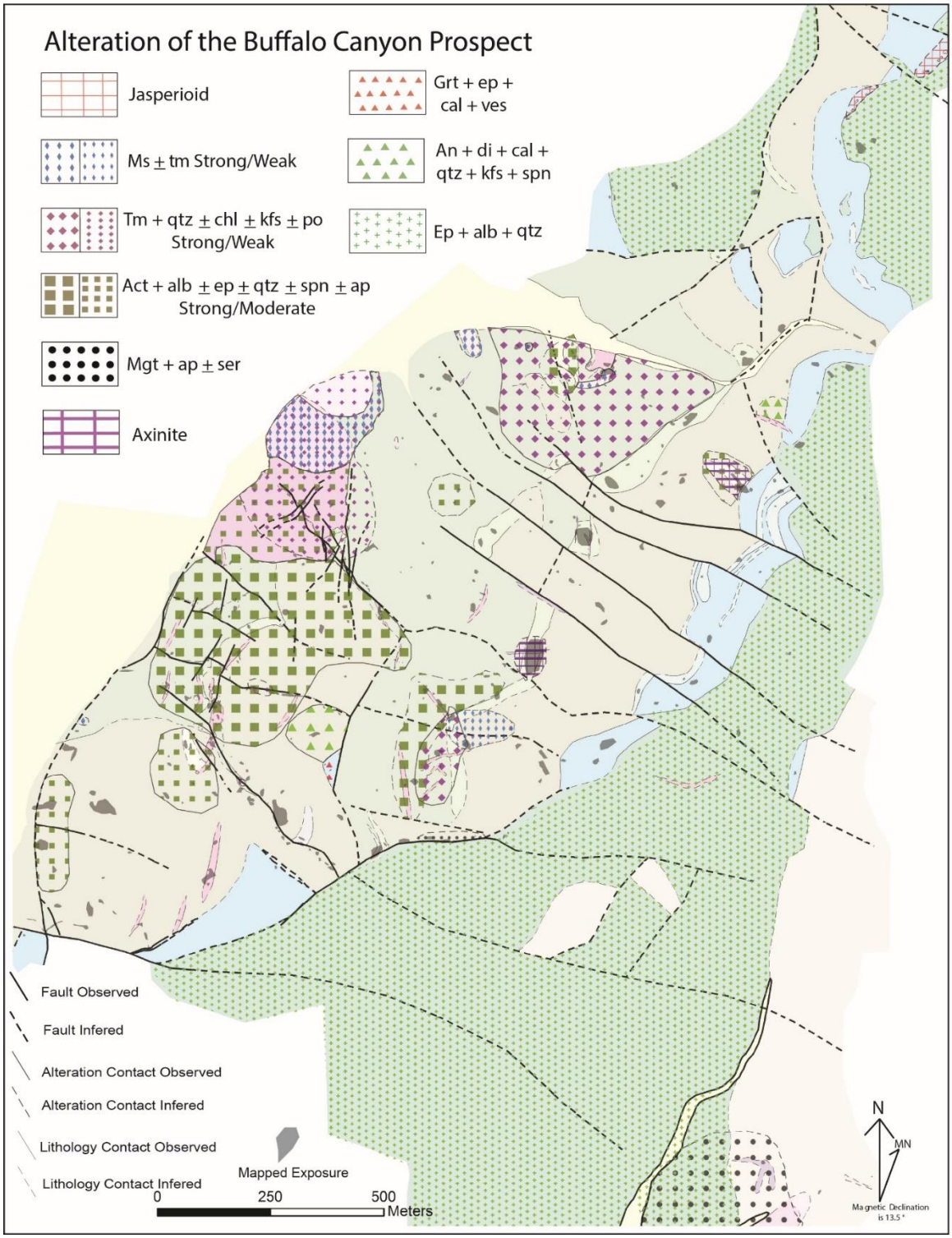

Fig. 12. Mapped distribution of alteration assemblages at Buffalo Canyon. Weak actinolite + albite is not shown here for simplification, but occurs weakly throughout the lower Knickerbocker.

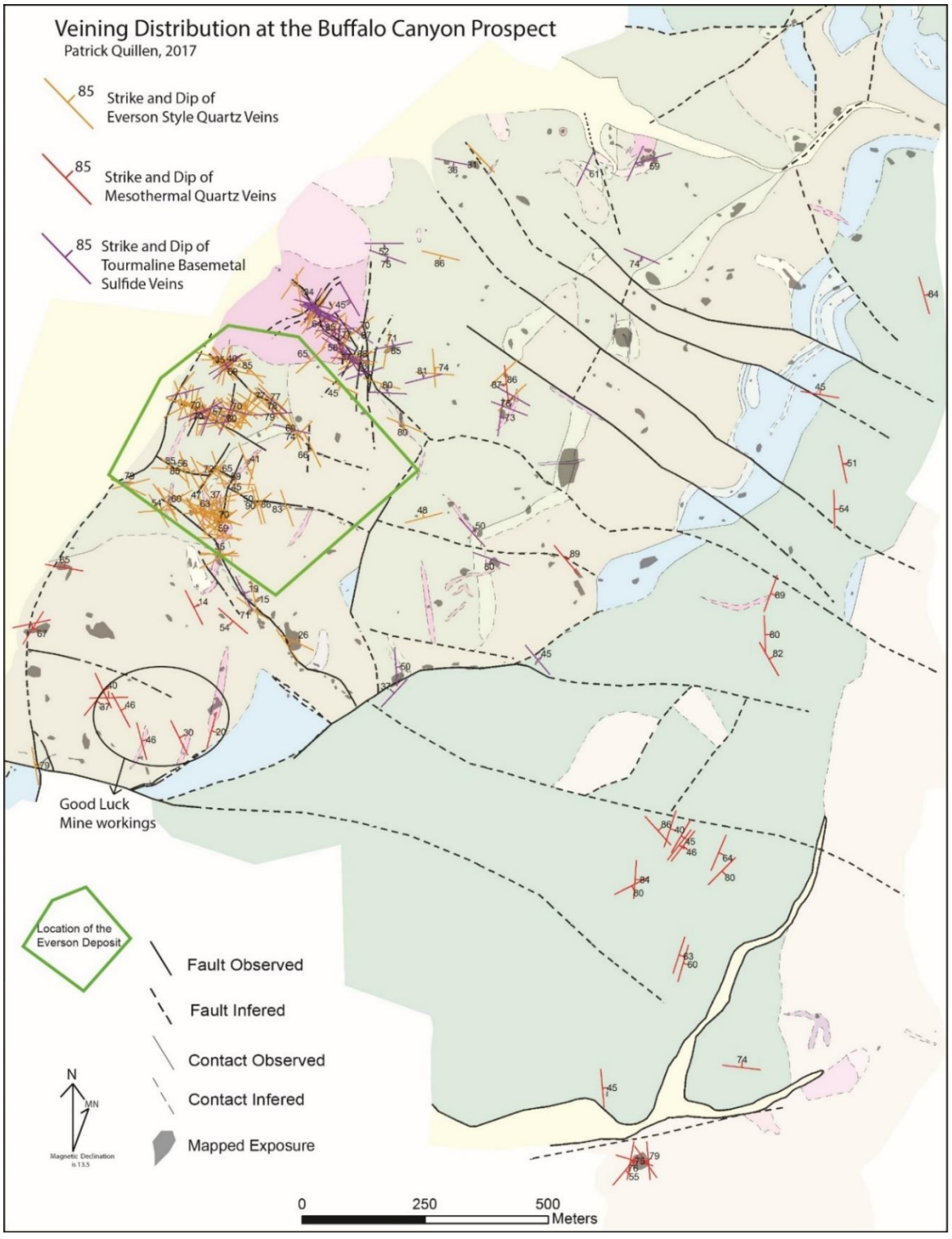

Fig. 13. Mapped distribution of the three mineralizing veins discussed. Notice that Everson quartz veins in yellow are restricted to the Everson area, and tourmaline base metal sulfide veins occur mostly on the NE side of the deposit area and up to Buffalo Canyon. Mesothermal quartz veins occur outboard of the other vein types.

pyrrhotite. Pyrrhotite is not observed in surface exposures, but is observed within core hole BCD-104-11. Volcanic rocks (TRkvc) are metamorphosed to hornfels consisting of albite + potassium feldspar + biotite + quartz with accessory titanite, apatite and pyrrhotite. Local occurrences of pyrrhotite on surface have been observed in hornfels of TRkvc. The limestone member of the Knickerbocker (TRkls) is weakly recrystallized in hand sample. The upper Knickerbocker volcanic unit (TRkg) is pervasively altered to albite + epidote + quartz. Here this assemblage is attributed to contact metamorphism, whereas Silberling (1959) attributed the assemblage to regional metamorphism.

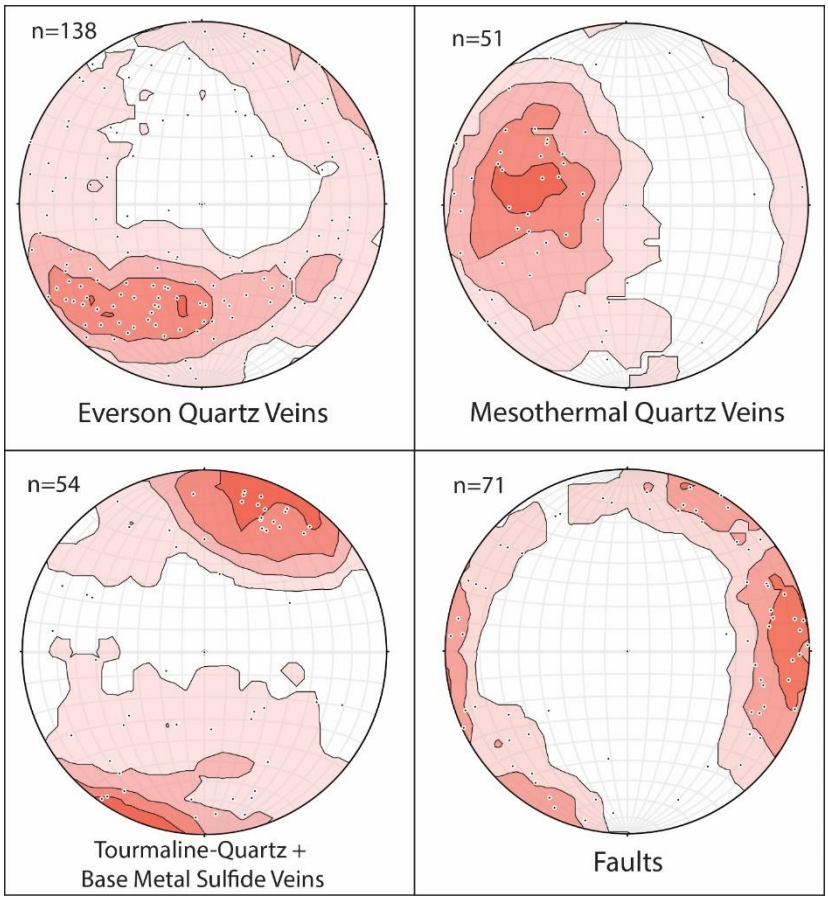

Fig. 14. Lower hemisphere stereographic projections of Kamb contoured poles to planes for all structural measurements. Notice that there is a common, general WNW-ESE strike for Eq veins, Tbm veins and faults. Faults have two dominant, steeply dipping strikes that match the district trend noted by Silberling (1959) and Abrams (1979). Mesothermal veins have a distinctly attitude compared to the other vein types.

Lower Knickerbocker rocks are most strongly metamorphosed, while upper Knickerbocker volcanics are less so. Formations above the Knickerbocker do not show significant signs of metamorphism or hydrothermal alteration. Metamorphism is most intense near contacts of Jgd dikes, where hornfels takes on a darker purple color (Fig. 15). No intrusive rocks show effects of thermal metamorphism, suggesting the contract metamorphism is associated with the Jurassic intrusions, which are oldest known intrusions in the district.

5.2. Sodic-Calcic Alteration (Sc)

Sodic-calcic alteration is characterized by variably pervasive alteration and veins of mainly actinolite and albite (with lesser oligoclase). Wall rock alteration overprints hornfels and is expressed as bleached zones within lower Knickerbocker units (Fig. 15). The hydrothermal alteration assemblage consists of actinolite + albite $\pm$ quartz $\pm$ epidote $\pm$ titanite $\pm$ rutile $\pm$ apatite, both in veins and wall rock. Alteration is strongly associated with Jgd dikes, occurring within dikes, along their margins and in clastic host rocks proximal to dikes (Fig. 15). Alteration of clastic rocks in the Knickerbocker predominantly occurs as veins or broad zones of albitic bleaching. Veins are discontinuous, typically around a mm thick, but can be up to 2 cm thick. Envelopes of albite are readily apparent in hand sample, forming halos around both veins and patches, making this alteration style easily identifiable. Actinolite-albite veins have no strong preferred orientation and do not appear to be spatially or temporally related to gold mineralization. Veins are mainly restricted to the lower Knickerbocker. Actinolite-albite alteration also weakly affects Jd intrusions just north of the Everson area, which includes

thin (<1 mm) veinlets of actinolite with albite envelopes and partial replacement of mafic minerals with actinolite.

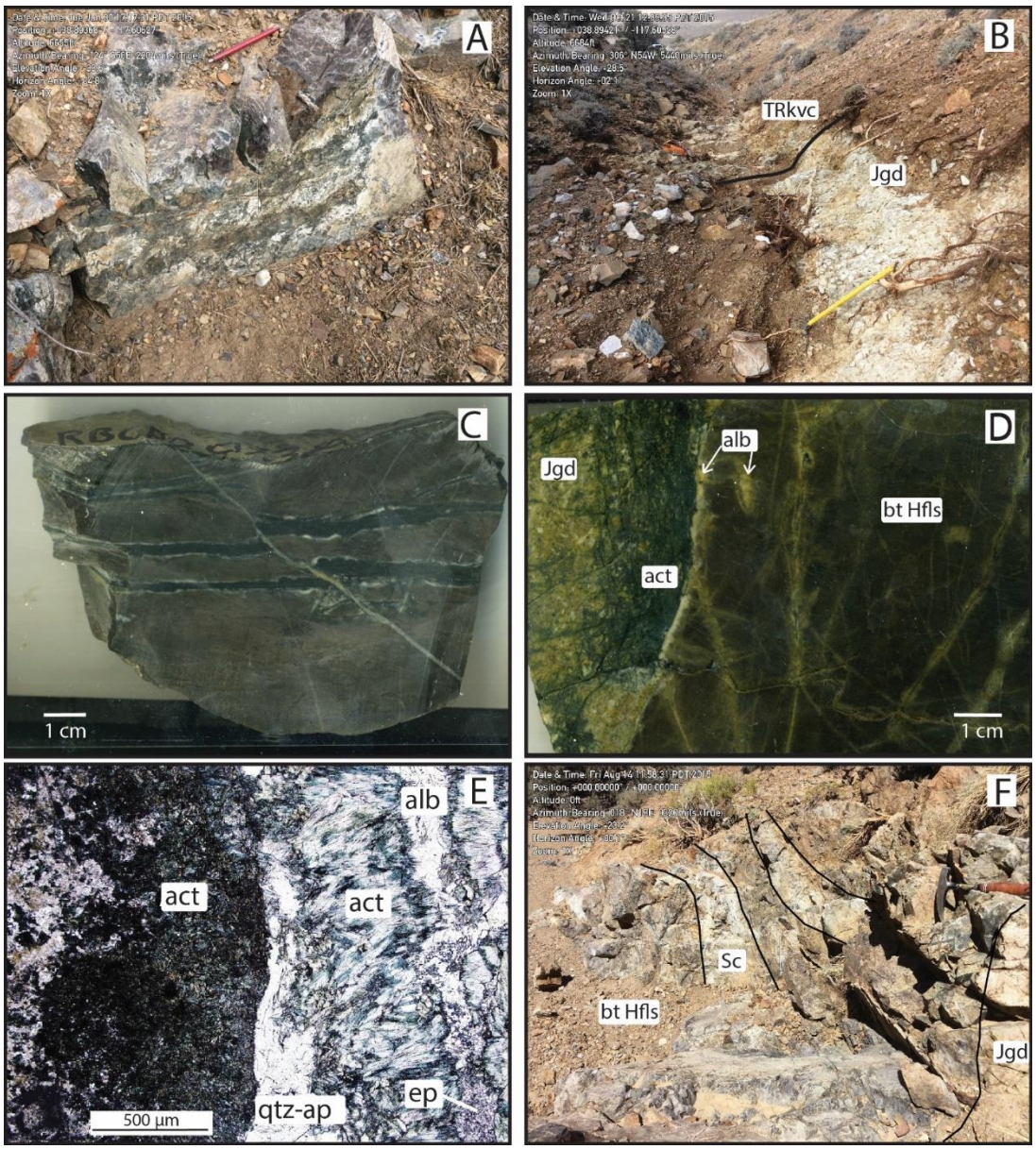

Fig. 15. Representative photos of actinolite-albite alteration (Sc). A) |Field photo showing strong patchy Sc alteration (actinolite-albite) that is overprinting purple biotite hornfels. B) Field photo of a Jgd dike exposed in a drainage that is strongly bleached white (albite) by Sc alteration. C) Hand sample of typical actinolite-albite veins, which are cut and offset by a later quartz vein. D) Hand sample showing actinolite patches occurring at the contact of Jgd and biotite hornfels, with albite bleaching along veinlets. E) PPL photomicrograph of a thicker Sc vein, with coarser actinolite-albite-epidote and minor qtz-apatite contained in the vein along with a strong actinolite selvage. F) Field photo showing areas of albite bleaching and actinolite-albite patches and veins (Sc) cutting biotite hornfels (Bt Hfls) hosted in TRkc, near a Jgd dike.

Table 2. Summary of Hydrothermal Alteration and Mineralization (listed from interpreted oldest to youngest)

Style	Location and Extent	Mineralogy	Vein Quartz Textures and Fluid Inclusions	Morphology	Relationship to Intrusive Rocks	Relationship to Other Alteration & Mineralization	Additional Comments
Contact metamorphism/metasomatism (Hfls)	Forms aureole within Knickerbocker.	**TRkc:** qtz + bt ± po **TRkvc:** alb + kfs + qtz + tit + po + ap **TRkg:** alb + ep + qtz	N/A	Massive, fine grained alteration.	All Knickerbocker host rocks affected, no intrusive rocks show affects.	Overprinted by Sc veins, skarn, Tm-qtz, Ser and Eq veins.	Massive contact metamorphism to metasomatism of Knickerbocker host rocks. Assemblages vary depending on lithology.
Sodic-calcic (Sc)	Lower Knickerbocker primarily.	Act + alb ± qtz ± ep ± tit ± rt ± ap	N/A	Discontinuous veins (0.2-1 cm wide, `10-30 cm long), patches (~2-10 cm diameter) within and around Jgd dikes, or zones of massive alb bleaching within dikes and in surround country rocks.	Hosted in and strongly, spatially associated with Jgd dikes, weakly hosted in Jd as veinlets. Does not affect other intrusive rocks.	Overprints Hfls alteration in lower Knickerbocker. Cut by Eq veins, overprinted by ill-smec-chl in TRkvc.	Alteration assemblage dominated by act-alb that mostly forms veins and patches but also replaces mafic minerals in TRkvc.
Iron-oxide apatite (Ioa)	Drill hole BCD-101-11, hosted in TRkg and weakly in TRkvc near the Everson.	Mgt + ap ± ser	N/A	Massive replacement of matrix in TRkg and partial replacement in TRkvc.	Cut by dike of Tqm.	Cut by skarn veins.	Massive mgt + ap formed dominantly within the fine-grained matrix of the volcanic agglomerate unit of TRkg where is makes up, up to 15% of the rock.
Mesothermal quartz veins (Mq)	Occur mainly in the Upper Knickerbocker. Account for historic production at the Berlin, Richmond and Shamrock mines.	**Gangue:** qtz ± tm **Opaque:** py + cpy + sph + ten-tet **Element Assoc.:** Au-Ag-(Sb-Pb-As) **Alt. selvage:** lacking to ill + cal + chl + py	**Qtz Texture:** Recrystallized mosaic. Undulatory extinction and moderate grain boundary migration textures. **FLINCS:** dominantly 2 phase with lesser 3 phase liquid CO2-bearing inclusions.	Occur as both fault fill and extensional veins, 0.5-2 m wide, continuous for meters, parallel walls that are straight, locally boudinaged.	Cuts Jd (Shamrock diorite).	Un-mineralized Mq vein cut by Eq vein in one sample.	Milky, bull white quartz easily distinguishable on surface. Berlin and Richmond veins strike NE and dip moderately SE. Mq veins near Buffalo Canyon strike N and dip moderately to steeply to the E.
Skarn	Exoskarn locally formed in TRkls and TRkvc. Retrograde skarn veins weakly found throughout the project area.	**Exoskarn (TRkls):** and + ves **Retrograde:** cal + ep **Exoskarn (TRkvc):** an + di + qtz + tit **Vein Gangue:** cal + qtz + and + tm + ep + act + ap + all **Alt. Selvage:** qtz + tm or ax	N/A	**Exoskarn (TRkls):** Cm-scale pods of euhedral and and ves surrounded by cal in a matrix of massive ep + qtz. **Endoskarn (TRkvc)**: massive and buff white. **Vein:** Forms 0.1-2 cm thick veins that have parallel walls. Continuous for 10s of cms.	Does not occur in intrusive rocks.	Both skarn and veins postdate hornfels.	Small, locally developed bodies in TRkls and TRkvc. Found along a NNW trending fault. No recognizable metallic minerals, but is strongly anomalous in Bi. Retrograde calcite-rich veins occur throughout the project area.
Tourmaline-Quartz-Chlorite (Tm-qtz)	Occurs in BCD-104-11 and weakly on surface near Buffalo Canyon. Affects meta-sediments, particularly coarser, more permeable units.	**Alteration Patches: t**m + qtz + chl ± po ± kfs ± ser **Veinlets:** tm + chl + qtz + po + py + all, Selvage of bt or ser **Orbicular Features:** qtz + chl + cal + po + py + sph + gn, contain bleached sericitic halos	N/A	Alteration patches replace permeable beds in clastic rocks, and form veins in in finer grained, less permeable units. Orbicular features are oblong spheroids 2-8 cm in diameter.	Tourmaline flooding follows bedding planes and cuts Td.	Overprints biotite Hfls.	Replacement features found primarily with TRkc. Tm + po is also disseminated in clastic rocks in hole BCD-104. Occurs most commonly near Buffalo Canyon an along the lower contact between TRkc and TRkcg.

Table 2. Continued. Summary of Hydrothermal Alteration and Mineralization (listed from interpreted oldest to youngest)

Style	Location and Extent	Mineralogy	Vein Quartz Textures and Fluid Inclusions	Morphology	Relationship to Intrusive Rocks	Relationship to Other Alteration & Mineralization	Additional Comments
Tourmaline Base Metal Veins (Tbm)	Occurs in in surface exposure just north of the Everson and weakly in drill core near Buffalo Canyon.	**Gangue:** Tm ± qtz **Opaque:** Early py + apy + gn + sph + cpy **Element Assoc.:** Ag-Pb-Zn-Sb-As-(Au-Bi-Cu-Mo) **Alt. selvage:** weak tm + qtz	**Qtz Texture:** Quartz is minor but is subhedral and equant. **Tm Texture:** Euhedral and equant to prismatic.	0.5-1 cm thick, straight walled, meters long. Strike NW and dip steeply NE.	Cuts Jd.	Overprints biotite hornfels. Cut by Eq veins with dominant sinistral offset.	Tourmaline-rich veins that contain lesser quartz and have centers filled with sulfide, which is generally oxidized due to surface exposure.
Propylitic (Prop)	Hosted in all igneous rocks.	Chl + cal + alb + tit ± mgt ± ep ± ap	N/A	Moderate to pervasive throughout most intrusive rocks.	Clearly affects Klg, Kmd, Tg, Td, Tqm and weakly Tqmd.	Overprinted by Ser in Td.	Mafic minerals, including hbl and bt are altered to chl + cal + tit + mgt + ep and pl is altered to alb and cal.
Sericitization (Ser)	Hosted primarily in intrusive rocks throughout the area, strongest in Td on south wall of Buffalo Canyon and Tg on the rangefront north of the Everson. Occurs in BCD-101-11 with significant pyrite.	Ms + ill + qtz ± tm ± py ± chl **Associated Veining:** qtz + py + aspy	N/A	Pervasive alteration that bleaches intrusive rocks. Ms is fine- to medium- grained and primarily replaces feldspars. Locally masks igneous textures.	Strongly affects Td and Kg, weakly affects Tqm, Tqmd and Klg. Kmd and Td show stronger qtz + ser + py alteration in BCD-101-11.	Overprints Prop alteration in Td. Similar to selvages of EQ veins. Breccia pipe near Buffalo Canyon also has tm+ser along with a cal matrix. Weakly to moderately overprints biotite hornfels near Buffalo Canyon in core. Associated with qtz+cal+aspy that contain up to 0.9 ppm Au in BCD-101-11.	Most intense alteration occurs on the south wall of Buffalo Canyon in Td, near the contact with Tqmd, which is only weakly affected.
Everson Quartz Veins (Eq)	Defines the Everson area, locally found outside of the Everson.	**Gangue:** qtz ± tm ± ms ± fl ± bis ± mnz **Opaque:** Trace Au and py **Element Assoc.:** Au-Te-(Mo-Bi-Sn) **Alt. Selvage:** Often absent, but can include tm + ser or kfs (when hosted in TRkvc)	**Qtz Texture:** Dominantly blocky to elongate-blocky syntaxial crack seal veins with occasional comb quartz. **FLINCS:** Common hypersaline inclusions with multiple daughter minerals, lesser vapor-rich inclusions. Abundant two phase liquid-inclusions.	<1-12 cm thick, sheeted, continuous for meters, parallel, wavy to straight walled. Vary from single stage to laminated veins with many crack sealing events. Strike WNW and dip steeply NE.	Hosted in Jd and cuts Jgd. Single stage, blocky veins <0.1-0.5 cm thick that contain gold are hosted in Tg.	Cuts Sc, Tbm and other Eq veins. Later Eq veins tend to have thicker stages, are more elongate-blocky to comb textured and re-open earlier Eq veins. Later stages contain more fl, tm and ms. Has alteration selvages similar to sericitization alteration.	Eq veins define the Everson area. Commonly show sinistral motion where they offset other veins. Represent multiple generations of crack seal events and the latest stage of hydrothermal alteration/ mineralization.

Alteration and mineralization styles listed in interpreted chronologic order from oldest to youngest.

Act=actinolite, alb=albite, all= allanite, and=andradite ap=apatite, aspy=arsenopyrite ax=axinite, bis=bismite, bt=biotite, cal=calcite, chl=chlorite, cpy=chalcopyrite, ep=epidote, fl=fluorite, gn=galena, kfs=potassium feldspar, mgt=magnetite, mnz=monazite, po=pyrrhotite, py=pyrite, qtz=quartz, rt=rutile, ser=sericite, smec=smectite, sph=sphalerite, ten-tet=tennantite-tetrahedrite, tit=titanite, tm=tourmaline, ves=vesuvianite

As mentioned, actinolite-albite alteration is best developed proximal to Jgd dikes. Locally dikes are intensely altered to albite and bleached white (Fig. 15). Veins and patches are discontinuous within Jgd dikes, commonly occurring along dike contacts. Plagioclase phenocrysts in Jgd are strongly altered to albite, in comparison to most other intrusive phases. No Cretaceous or Oligocene intrusions show evidence of sodic-calcic alteration. The mineralogy, styles and timing of actinolite-albite alteration are somewhat similar to sodic-calcic alteration of Jurassic age that has been documented elsewhere in Nevada (Yerington District, Carten, 1986; Stillwater Range and Buena Vista Hills, Johnson and Barton, 2000). Based on these observations and analogies, the sodic-calcic alteration in the Buffalo Canyon area is interpreted to be related to Jurassic intrusive activity.

5.3. Iron Oxide-Apatite (Ioa)

An assemblage of magnetite + apatite $\pm$ sericite is observed locally around the project area. In hole BCD-101-11, upper Knickerbocker volcanic agglomerates (TRkg) have a matrix that is strongly altered to magnetite + apatite $\pm$ sericite (Fig. 16). Another locality occurs east-southeast of the Everson deposit in a drainage, where exposures of 2 cm wide dark bands of magnetite-apatite-sericite occur in lower Knickerbocker volcanic rocks and form ovoid rings 1 meter in diameter (TRkvc). This alteration style in BCD-101-11 is cut by a dike of Tqm, thus, is constrained between Triassic and Oligocene. However, based on similar assemblages described in Jurassic sodic-calcic alteration zones by Johnson and Barton (2000), iron oxide-apatite alteration here is interpreted to be

temporally related to the sodic-calcic alteration and the Jurassic intrusions in the Buffalo Canyon area.

5.4. Mesothermal Quartz Veins (Mq)

Mesothermal quartz veins (Mq), which accounted for the most of the gold and silver production in the Union District, occur at Richmond and Berlin within upper Knickerbocker volcanic rocks (TRkg). They are also hosted within the Shamrock diorite (Jd), but no other relationships to intrusive rocks have been observed. Within the project area, Mq veins occur within ~700 meters from the Everson deposit in TRkg, and within a few hundred meters in TRkvc (Fig. 13). Minor workings occur on veins throughout the project area, including the Good Luck mine in the southwestern portion of Figure 13, 300 meters south of the Everson.

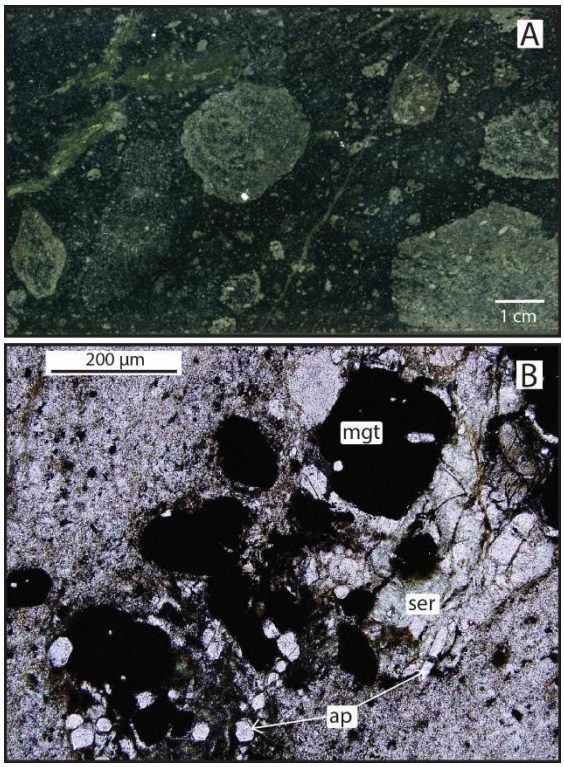

Fig. 16. Representative images of Ioa alteration. A) Sample of drill core from BCD-101-11 showing strongly altered TRkg. Much of the dark matrix material is magnetite, which floods the groundmass of the rock. B) PPL photomicrograph of Ioa alteration hosted in TRkvc southeast of the Everson area. Magnetite (mgt) and apatite (ap) are intergrown, and surrounded by sericite (ser).

Mq veins are milky white, with recrystallized quartz textures. Veins are typically much wider (0.5-1 m) than other vein types, have a variety of orientations, but most commonly strike north-south, dipping moderately to the east (Fig. 14). Veins are extensional or to a lesser extent occupy fault zones. Veins can also locally form boudins.

Quartz in Mq veins is medium to fine grained and consists of a mosaic of jigsaw quartz with occasion elongate quartz grains, using the; terminology of Dong (1995). Quartz grains show moderate to strong undulatory extinction and sutured grains with significant grain boundary migration, whereas other samples show cataclastic textures (Fig. 17). In both Richmond and Berlin vein samples, mineralization is associated with a later, finer-grained stage of quartz that is also recrystallized (Fig. 17).

Due to the level of recrystallization in Mq veins, many inclusions are likely secondary, which is what gives the veins their milky white appearance. The dominant type of fluid inclusion observed in several Mq samples were micron-scale, liquid-rich two-phase inclusions. In addition, Mq samples contain rare, three-phase, liquid CO_2-bearing inclusions (Fig 17).

Mesothermal veins contain Ag>Au. Ag:Au ratios of ore from the Berlin mine averaged 7-12:1, (Dagget, 1907). Mesothermal veins have a Au-Ag-(Sb-Pb-As-Cu) elemental association (Fig. 18). Many Mq veins are barren, with the primary recognizable difference between mineralized samples being the presence of sulfides, which are generally < 1%. Ore mineralogy is variable and includes pyrite, chalcopyrite, galena, sphalerite, arsenopyrite and tennantite-tetrahedrite. Besides quartz, the only other observed gangue mineral is local, minor tourmaline. Visible gold was observed in a sample from the Berlin mill. This coarse gold was not associated with sulfides. Alteration envelopes are typically absent, but locally consist of sericite + calcite + chlorite + pyrite along the Richmond vein, and calcite-siderite? + sericite and chlorite along the Shamrock veins.

5.5. Skarn

Local alteration of limestone units occurs in the Buffalo Canyon area. Most significantly, a skarn assemblage occurs in the middle Knickerbocker limestone member (TRkls) contained in the hanging wall of a north-northeast-trending fault (Fig. 12). Previous surface sampling indicates that gossanous parts of skarn are strongly anomalous in Bi, Cu, Pb and Zn, but not significantly anomalous in Au. The skarn occurs as 2-3 cm wide pods of garnet surrounded by calcite and further out into a quartz-epidote matrix. Garnet compositions grade outward from 100% andradite (no Al detected using SEM EDS analyses) to more grossularite rich (60% andradite) compositions, which are rimmed

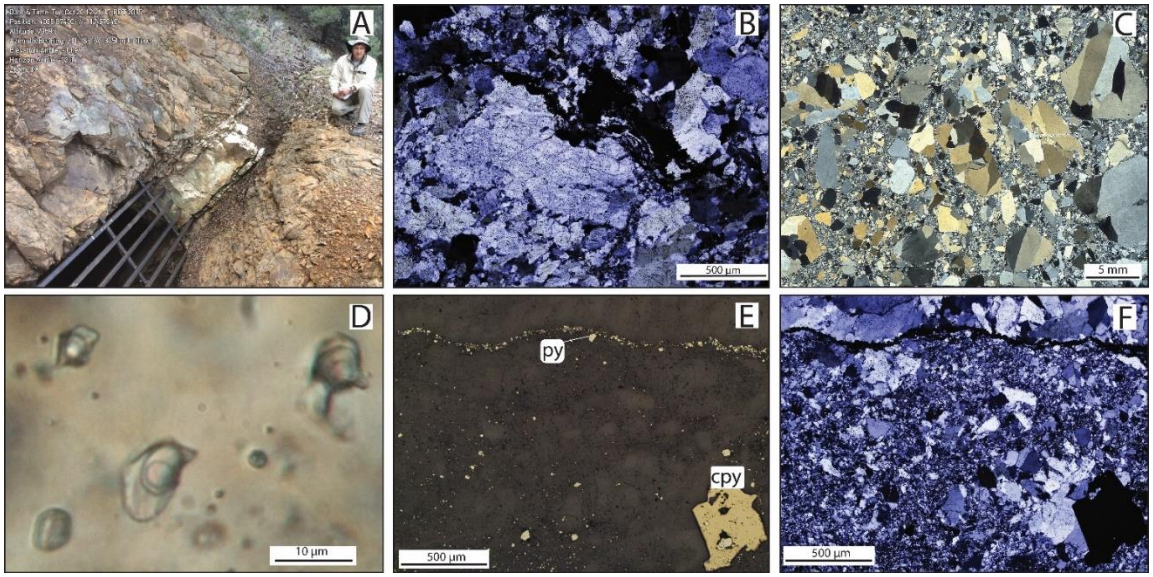

Fig. 17. Representative photos for Mq veins. A) Field photo of the Richmond vein which strikes to NNE and dips 45°SE. Mq veins are typically thicker than other vein types, up to a meter, and milky white. Not easily visible in the photo are green secondary copper minerals along the vein surface. B) XPL photomicrograph of a representative texture for most Mq veins. Grains are weakly to moderately recrystallized and show evidence of grain boundary migration and undulatory extinction. Most samples of Mq veins show recrystallization of quartz., C) XPL scan of a thin section showing cataclastic deformation in an Mq vein, which is common. D) PPl photomicrograph of 3 phase, liquid CO_2 bearing inclusions which are found in several Mq vein samples. This image is from a sample of Berlin dump material, which includes the best examples of such inclusions. E) Reflected light photomicrograph showing a later stage of pyrite and chalcopyrite. Lesser fine-grained tennantite-tetrahedrite and sphalerite also occur with chalcopyrite. F) XPL image of the same view from E, which shows quartz textures associated with the mineralizing event. Later finer-grained quartz contains all sulfide mineralization compared to the coarser, earlier variety. Both show evidence of recrystallization.

Mesothermal Quartz Veins N=42

Spearman	Au_ppm	Ag_ppm	As_ppm	Bi_ppm	Cu_ppm	Mo_ppm	Pb_ppm	Sb_ppm	Sn_ppm	Te_ppm	W_ppm	Zn_ppm
Au_ppm	1											
Ag_ppm	0.7	1										
As_ppm	0.31	0.44	1									
Bi_ppm	0.012	0.23	0.4	1								
Cu_ppm	0.24	0.7	0.27	0.49	1							
Mo_ppm	0.23	0.47	0.57	0.39	0.46	1						
Pb_ppm	0.33	0.36	0.51	0.13	0.098	0.36	1					
Sb_ppm	0.41	0.72	0.4	0.043	0.43	0.35	0.21	1				
Sn_ppm	0.067	0.12	0.14	-0.15	0.077	0.1	0.11	0.31	1			
Te_ppm	-0.0069	0.0084	0.23	0.17	0.036	0.081	0.11	0.11	0.76	1		
W_ppm	0.11	0.13	0.14	-0.22	-0.093	0.0034	0.22	0.27	0.09	0.028	1	
Zn_ppm	0.18	0.47	0.4	0.11	0.45	0.14	0.22	0.57	0.24	0.17	0.076	1

Tourmaline Base Metal Sulfide Veins N=27

Spearman	Au_ppm	Ag_ppm	As_ppm	Bi_ppm	Cu_ppm	Mo_ppm	Pb_ppm	Sb_ppm	Sn_ppm	Te_ppm	W_ppm	Zn_ppm
Au_ppm	1											
Ag_ppm	0.48	1										
As_ppm	0.44	0.74	1									
Bi_ppm	0.46	0.41	0.13	1								
Cu_ppm	0.63	0.37	0.46	0.28	1							
Mo_ppm	0.37	0.5	0.59	0.29	0.38	1						
Pb_ppm	0.49	0.89	0.84	0.28	0.47	0.49	1					
Sb_ppm	0.45	0.75	0.9	0.26	0.42	0.59	0.72	1				
Sn_ppm	0.08	0.31	0.21	-0.23	0.041	0.012	0.27	0.23	1			
Te_ppm	0.3	0.11	0.049	0.35	-0.055	0.11	0.0081	0.26	0.25	1		
W_ppm	0.15	0.39	0.38	-0.16	0.14	0.16	0.48	0.27	0.65	-0.064	1	
Zn_ppm	0.48	0.77	0.8	0.016	0.49	0.39	0.85	0.75	0.43	0.063	0.57	1

Everson Quartz Veins N=44

Spearman	Au_ppm	Ag_ppm	As_ppm	Bi_ppm	Cu_ppm	Mo_ppm	Pb_ppm	Sb_ppm	Sn_ppm	Te_ppm	W_ppm	Zn_ppm
Au_ppm	1											
Ag_ppm	0.18	1										
As_ppm	-0.17	0.26	1									
Bi_ppm	0.38	0.26	-0.29	1								
Cu_ppm	0.18	-0.1	0.095	0.15	1							
Mo_ppm	0.44	-0.0069	-0.12	0.25	0.54	1						
Pb_ppm	-0.19	0.57	0.43	-0.003	-0.048	-0.093	1					
Sb_ppm	0.17	0.37	0.41	0.32	0.16	-0.073	0.23	1				
Sn_ppm	0.35	-0.26	-0.11	0.28	0.47	0.41	-0.091	0.34	1			
Te_ppm	0.56	-0.011	-0.31	0.74	0.17	0.41	-0.38	0.25	0.27	1		
W_ppm	0.27	0.3	0.44	0.17	0.16	-0.019	0.45	0.75	0.45	0.022	1	
Zn_ppm	-0.37	0.21	0.44	-0.35	0.1	-0.076	0.71	-0.038	0.022	-0.59	0.29	1

Fig. 18. Correlation matrices for each vein type with selected elements of interest, for full assay date for each sample see appendix D. A) In Mq veins Au correlates strongly with Ag, and lesser with As, Pb and Sb. Ag is correlated strongly with Cu, Sb and lesser with As, Mo, Pb and Zn. B) Tbm veins contain Au correlates moderately with Ag, As, Bi, Cu, Pb, Sb and Zn. Ag correlates strongly with As, Pb, Sb, Zn and lesser so with Mo. C) In Eq veins Au correlates with Te and lesser so with Bi, Mo and Sn. Ag correlates strongly with Pb and lesser so with Sb and W. Zn and Pb are negatively correlated with Au, Bi and Te.

by Fe-vesuvianite (Fig. 19). The calcite and epidote likely represent a retrograde assemblage. There is no clear temporal relationship between intrusive phases and skarn alteration.

Stratigraphically below, and in contact with the exoskarn in TRkls, is a body of exoskarn hosted within TRkvc. This skarn is easily recognized in the field due to its white color and massive nature (Fig. 19). It is composed entirely of anorthite (based on EDS), diopside and quartz, with lesser potassium feldspar and titanite (Appendix B). Neither style of exoskarn appear to be related to mineralization.

A series of calcite-dominant veins contain a similar mineralogy to the skarn, and are therefore included in the same alteration style, but are the result of retrograde alteration. These veins are defined by an abundance of Ca-bearing minerals, and are not associated with any mineralization. These vein types are relatively minor in abundance, but have been observed in all four core holes and multiple locations on the surface proximal to or within the Everson area.

Calcite is the primary vein constituent in all occurrences of this vein type, forming medium grained elongate crystals (Fig. 19). The veins also contain early euhedral garnet or tourmaline, along with subhedral to euhedral quartz. Garnet is pure andradite with very minor grossularite component that are no more than a few mole percent (based on EDS analyses). Pods of calcite with euhedral andradite also occur in wall rocks near garnet-bearing veins. Accessory vein minerals include later epidote, actinolite, chlorite, apatite and allanite. Axinite, a calcium-aluminum-borosilicate, locally forms vein envelopes and massive pods in volcanic host rocks (TRkvc, TRktv) and conglomerate units (TRkcg). Axinite is mapped as a separate alteration assemblage in Figure 12. In each case these

veins are later features, overprinting or cutting hornfels and iron oxide-apatite alteration. Axinite is known to form instead of tourmaline where Ca is in excess and carbonatization is limited (Dubé and Guha, 1993). Skarn assemblages in both limestone and veins likely represent fluid interaction with Knickerbocker limestone.

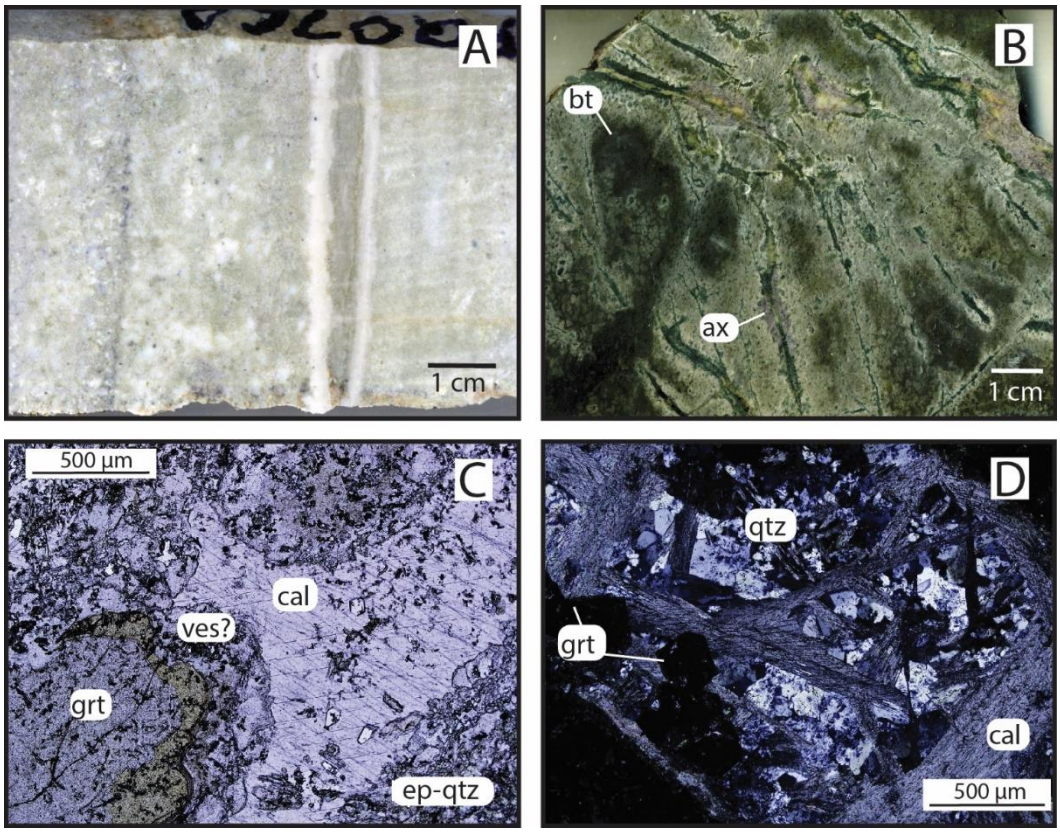

Fig. 19. Images of skarn mineralization. A) Hand sample of skarn in TRkvc, composed of mainly anorthite with diopside-quartz-potassium feldspar and titanite (see Appendix B for more detail). B) Hand sample of retrograde skarn veins of calcite-epidote-actinolite-chlorite with an axintite (ax, purple) selvage overprinting biotite (bt) hornfels hosted in TRkvc. C) PPl photomicrograph of exoskarn containing pods of andradite (gt), likely vesuvianite (ves?) and calcite (cal) hosted in a matrix of epidote and quartz (ep-qtz). D) XPL photomicrograph of a vein of quartz (qtz) and andradite (grt) with later (retrograde) calcite (cal) hosted in TRkg.

5.6. Tourmaline-Quartz-Chlorite-Potassium Feldspar (Tm-qtz)

Tourmaline is common throughout the Buffalo Canyon area, occurring in a variety of assemblages. One such alteration style is composed of tourmaline + quartz + chlorite + potassium feldspar + pyrrhotite that affects clastic host rocks. This alteration

style is primarily observed in drill hole BCD-104-11, and on surface within lower Knickerbocker clastic rocks on the south wall of Buffalo Canyon (Fig. 12). This assemblage is present in core as podiform replacement features that preferentially form within coarser sedimentary beds, < 1 mm wide wavy veinlets that cut bedding at oblique angles, and orbicular features that vary from 2-8 cm in diameter (Fig. 20). This alteration style overprints biotite hornfels in clastic rocks and associated veinlets have been observed cutting a dike of Td (Fig 20). No temporal relationship between Tm-qtz and intrusive rocks was observed, but the densest area of alteration occurs near Buffalo Canyon in the area of outcropping Oligocene intrusions.

In podiform patches, medium grained skeletal tourmaline (50-50 mix of dravite and schorl; based on EDS analyses) and quartz are intergrown, occasionally with interstitial pyrrhotite, which grades out into very fine grained chlorite, which in turn grades out to very fine grained potassium feldspar or sericite (Fig. 20). Tourmaline and quartz replace individual beds and form along fractures, bedding planes, and can comprise >25% of the rock. Outside of patches, tourmaline, sericite and pyrrhotite are disseminated throughout host rocks. The most intense tourmaline + quartz alteration occurs at the contact between the lower Knickerbocker clastic (TRkc) and conglomerate (TRkcg) units (Fig. 12).

Veinlets commonly have similar mineralogy, grading out from tourmaline + pyrrhotite-pyrite + quartz + allanite to chlorite and potassium feldspar with envelope of sericite, or local biotite (Fig. 20). The presence of biotite indicates a portion of the biotite hornfels may be hydrothermal in origin, although examples of clearly metasomatic biotite are rare. Veinlets are < 1mm wide and wavy with matching vein walls. Veinlets and patches appear to be synchronous in age, with morphology controlled by the host bedding (Fig. 20).

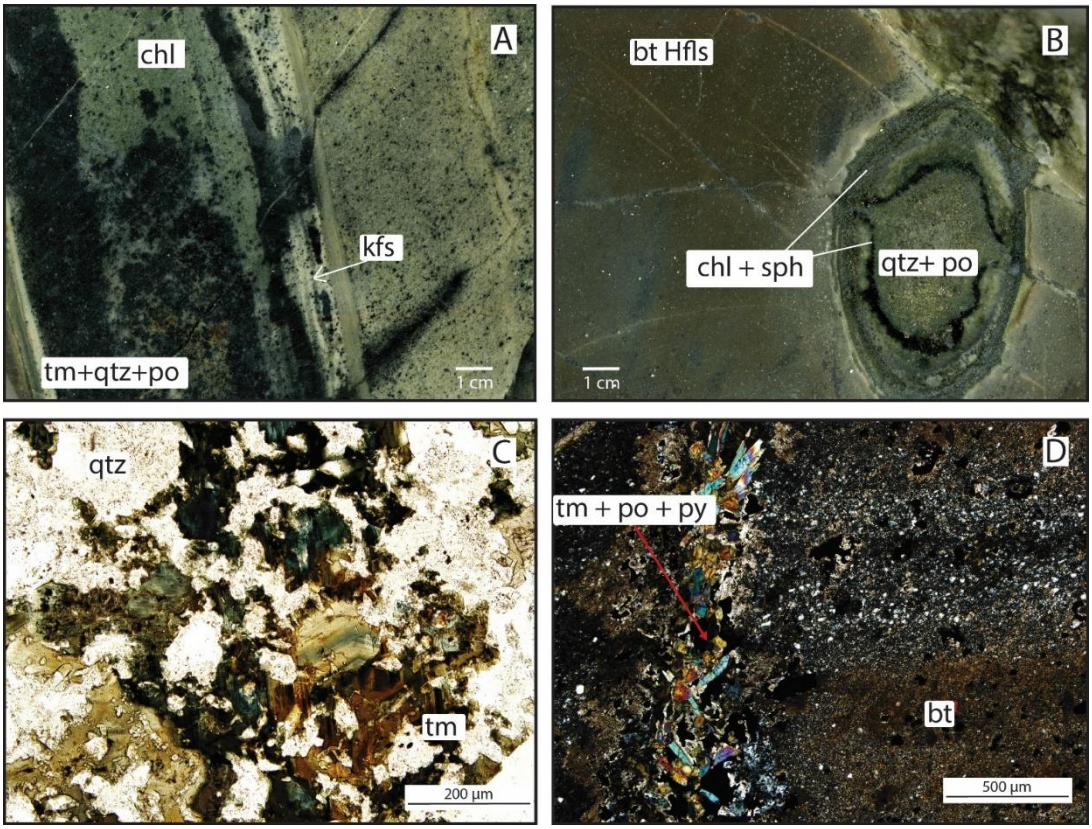

Fig. 20. Photos of tourmaline-quartz-chlorite alteration from core hole BCD-104-11. A) Hand sample of typical patchy Tm-qtz with a center of tourmaline-quartz-pyrrhotite (tm+qtz+po) grading out into chlorite (chl, dull green) and potassium feldspar (kfs, buff white). Notice how tourmaline in fractures bleeds out in coarser beds. B) Hand sample of orbicular features in biotite hornfels (bt Hfls) that commonly contain quartz-chlorite-calcite-pyrrhotite and sphalerite (chl+sph, qtz+po). C) PPL photomicrograph of a Tm-qtz patchy zone, where tourmaline displays a skeletal texture where the tourmaline grain is optically continuous. D) XPL photomicrograph of a tourmaline-pyrrhotite/pyrite-chlorite-allanite veinlet with a weak biotite envelope.

Orbicular (orbs) features are distinct ovoid shapes formed within clastic host rocks that range in diameter from 2-8 cm. Orbs have a similar mineralogy to veins and patches, apart from a lack of tourmaline and abundance of sphalerite with lesser galena. Whereas patches are oblong and tend to follow individual beds of the host rock, orbs have round to slightly oblong shapes. Orbs contain a core of quartz + pyrrhotite that grades out into rings of chlorite intergrown with calcite, sphalerite (with significant chalcopyrite disease) and pyrrhotite with lesser pyrite, which are interspersed with albite, sericite, titanite and lesser galena. Sericite also forms a bleached halo surrounding orbs.

5.7. Tourmaline ± Quartz ± Sulfide Veins (Tbm)

Base metal sulfide mineralization associated with veining occurs mainly north of the Everson deposit and south of Buffalo Canyon. However, the paucity of occurrences makes them difficult to characterize. This style of mineralization is distinguished by its higher base metal signature and ubiquitous presence of tourmaline as a primary vein mineral (Fig. 21).

Veins contain tourmaline + quartz with centerlines of sulfides that are completely oxidized on surface. Most often veins are 0.2-0.5 cm thick with minor alteration envelopes of tourmaline + quartz. Thicker, 1-2 cm veins with lesser tourmaline and more sulfides also occur. Tbm veins are continuous for meters with wavy, matching vein walls. They strike WNW and dip steeply to the NNE and SSE (Fig. 14). Mapped vein densities are greatest in the drainage which cuts the diorite plug of Jd, located north of the Everson (Fig. 13). Here veins are clearly hosted in Jd. Veins are only weakly found in TRkc. Most tourmaline hosted in Jd is associated with veining, but near the contact with TRkc

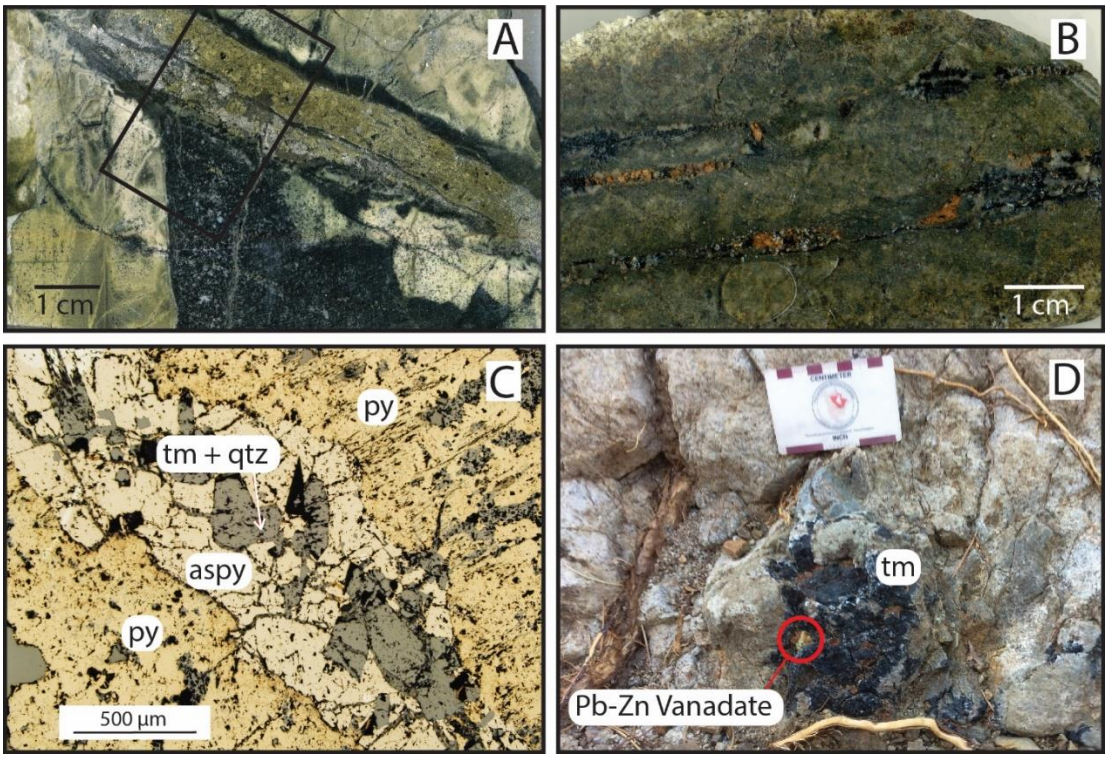

Fig. 21. Photos of showing key characteristics of tourmaline base metal sulfide veins. A) Sulfide-rich vein from core hole BCD-104-11, containing mostly pyrite. Sample also contains a patch of tm-qtz, whose temporal relationship with the vein is ambiguous. B) Hand sample of a typical Tbm veins on surface, which occur as thin veinlets containing tourmaline and quartz with oxidized sulfides (orange). C) Reflected light photomicrograph corresponding to the vein in A. Notice the arsenopyrite-tm-quartz cuts earlier pyrite. Galena and chalcopyrite occur with arsenopyrite elsewhere in the sample. D) Field photo of the face of a Tbm vein that contains pockets of oxidized sulfide (darker red) and a Pb-Zn vanadate mineral (bright green). Other vein samples contain hemimorphite and Pb-Zn vanadates (appendix B).

country rocks, tourmaline becomes more massive, forming along structures that extend into the host rocks. In drill core, sulfide rich veins cut Tm-qtz patches (Fig. 21). The abundance of tourmaline in both styles suggests they are related and tourmaline is formed during a single event.

Elemental correlations for TBM veins include Ag-Pb-Zn-Sb-As-(Au-Bi-Cu-Mo), and contain Ag>Au (Fig. 18). Sulfide minerals include pyrite with trace pyrrhotite, arsenopyrite, galena, sphalerite and chalcopyrite. Supergene Pb-Zn vanadates and hemimorphite are observed locally. Paragenetically, pyrite occurs early with an envelope

of tourmaline, and is cut by arsenopyrite-galena-sphalerite and chalcopyrite with minor tourmaline and quartz (Fig. 21). Most Tbm veins contain much less quartz than other vein types in the Buffalo Canyon area. Most quartz is prismatic with hosts abundant two-phase liquid-rich fluid inclusions. Tourmaline is subhedral to euhedral, with minor zoning that grades out from slightly dravitic compositions in the cores to slightly more schorl compositions near the rims of grains (see appendix B).

5.8. Propylitic Alteration (Prop)

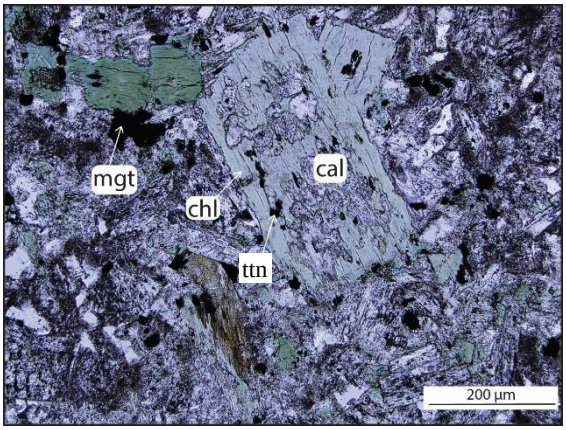

Fig. 22. PPl photomicrograph of propylitic alteration showing biotite grains altered to chlorite-calcite-titanite.

An assemblage consisting of chlorite + calcite + albite + titanite ± magnetite ± epidote ± apatite affects, to varying degrees, all intrusive rock types within the Buffalo Canyon area. Biotite and hornblende are variably altered to chlorite + calcite + epidote + magnetite + titanite, and plagioclase is variably altered to albite and calcite (Fig. 22). The amount of magnetite is variable. Intrusive rocks within hole BCD-101-11, including Kmd and Tqm, contain a greater abundance of magnetite compared to other occurrences.

These mineral assemblages, which are widespread, were originally interpreted by Silberling (1959) to be the result of lower greenschist regional metamorphism. Here they are interpreted as, propylitic alteration related to the intrusions of variable ages in the Buffalo Canyon area. This follows the interpretation of Barton and Hanson (1989) that much of what has been interpreted to be regional greenschist facies metamorphism in

western Nevada is likely overlapping halos of propylitic alteration associated with widespread, voluminous Mesozoic intrusions in western Nevada. The observation that Oligocene intrusive rocks in the Buffalo Canyon are propylitically altered further argues against this alteration being the result of regional metamorphism.

5.9. Sericitization (Ser)

Another distinct alteration type consists of muscovite/sericite + quartz ± tourmaline ± pyrite hosted primarily within younger intrusive rocks. Muscovite is the dominant mineral in this alteration style, and is locally coarser grained (up to 50 µm) near

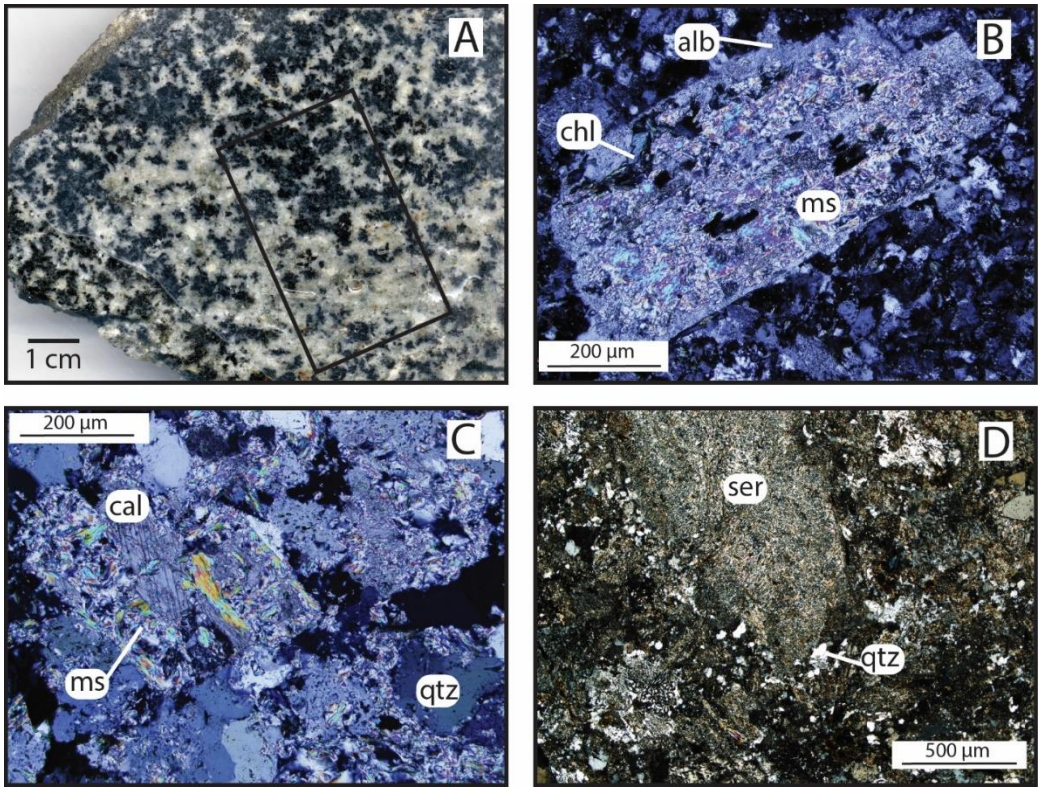

Fig. 23. Photos showing sericitization. A) Hand sample of a strongly altered dike of Td that is pervasively altered to muscovite and tourmaline. B) XPL photomicrograph of the alteration of a plagioclase phenocryst in Td. Muscovite (ms) is overprinting earlier chlorite (chl) and albite (alb). C) XPL photomicrograph of a plagioclase grain from the sample in A that has early calcite (cal) alteration, which is overprinted by muscovite. D) XPL photomicrograph of alteration in a sample of Tg. Muscovite is much finer grained compared to that in Td (B and C). Sericite pervasively replaces feldspar phenocrysts and matrix grains.

Buffalo Canyon, where it occurs in Td. Elsewhere muscovite is much finer grained and indistinguishable from illite, as indicated by EDS analyses. Textures and abundance of quartz is also variable, becoming coarser and more abundant where muscovite is also abundant. Tourmaline, often rimmed by muscovite, only occurs locally in the strongest areas of alteration and is minor elsewhere (Fig. 23).

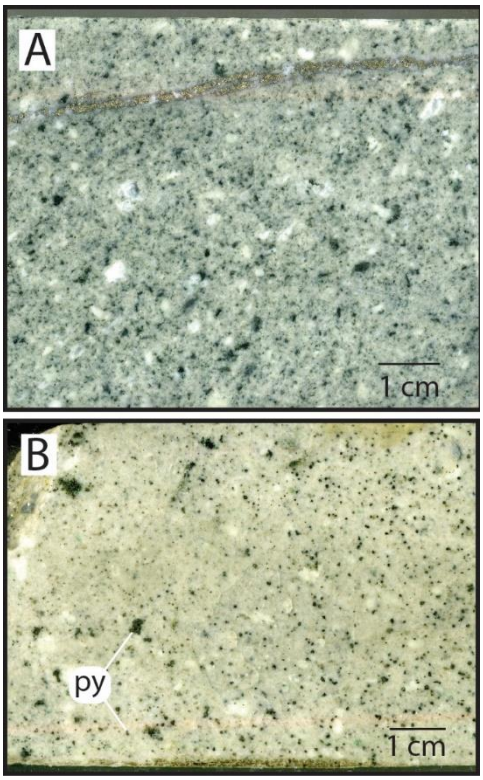

Fig. 24. Photos of hand samples from core hole BCD-101-11 showing variously sericitically altered intrusive rocks. A) Weaker sericitic alteration of Kmd, cut by a narrow pyrite-quartz-sericite vein. B) Strong sericitic alteration of either Kmd or Td. Sample contains disseminated, fine grained pyrite (py).

This alteration style is most common in Oligocene intrusive rocks (Td, Tg, Tqm), but also occurs within Klg. The sericitization is strongest in a 4-meter-thick dike of Td near Buffalo Canyon, as mentioned. Sericite is pervasive and finer grained in Tg north of the Everson. Sericitization is weaker in Tqm, Tqmd and Klg (Fig. 23). Muscovite primarily replaces plagioclase and orthoclase phenocrysts, and to a variable extent, groundmass feldspars. This alteration style overprints chlorite + calcite in both Tg and Td samples (Fig. 23). In Tqm and Klg, feldspar is weakly altered to muscovite, and in Tg feldspars are pervasively altered to finer grained muscovite + tourmaline (Fig. 23).

Additional quartz-sericite-pyrite (Qsp) alteration is observed in drill core BCD-101-11, affecting Kmd, Klg and potentially Td rocks. Due to the intensity of alteration, distinguishing between Td and Kmd is difficult. Intrusions are strongly bleached white by

quartz + sericite + pyrite alteration (Fig. 24). This alteration style is not observed on surface, and strongly occurs within a 30 meter, continuous interval within the core hole, and is associated with the only Au values, up to 0.9 ppm. The only significant veining within the hole is also associated with areas of alteration. Pyrite + quartz + sericite veinlets that are on average 2 mm thick and sheared, discontinuous veinlets of quartz + arsenopyrite + pyrite correspond to the highest gold values. Outside of Ser altered zones, no significant gold values were observed. Compared to other sericite occurrences previously mentioned, this sub-style contains finer grained sericite and more abundant pyrite.

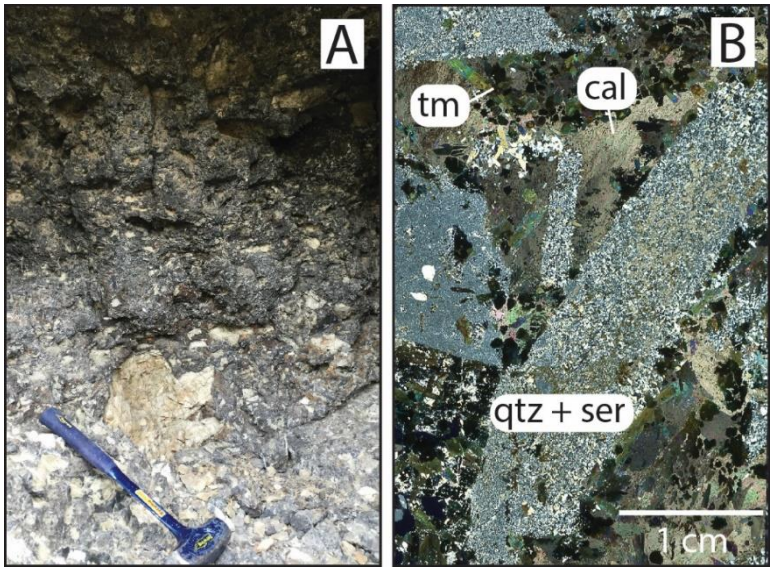

Fig. 25. Photos of tourmaline breccia (Tmbx), from a breccia pipe located just south of Buffalo Canyon. A) Field photo from inside a prospect within the breccia pipe. Light colored, quartz sericite altered, sub-angular, matrix supported monolithic clasts are hosted in a dark matrix of tourmaline and calcite. B) XPL photomicrograph of a breccia showing clasts altered to quartz (qtz) and sericite (ser). Tourmaline (tm) in the matrix is subhedral to euhedral and acicular.

A tourmaline breccia pipe located just south of Buffalo Canyon consists of sub-angular, monolithic, matrix supported fragments of meta-sediments (TRkc?) altered to quartz and sericite, hosted in a matrix of euhedral to subhedral medium-grained, acicular tourmaline and fine grained calcite and sericite (Fig. 25). The spatial and compositional similarities may indicate the breccia pipe is part of the same hydrothermal system that resulted in the sericitization.

5.10. Everson Quartz Veins (Eq)

A series of gold-bearing quartz veins that occur within the Everson deposit are grouped into a vein set called Everson quartz (Eq) veins (Fig. 13). Eq veins are easily distinguished in the field. They are predominantly composed of quartz. They occur as sheeted sets of <1-12 cm thick, continuous veins that are traceable for several meters until obscured by lack of exposure. Veins are straight to wavy with matching vein walls. Individual veins also show multiple periods of veining, indicated by multiple crack-sealing events, which creates laminated textures. Individual bands are generally <1-2 mm wide, but can be up to several cm thick in some cases (Fig. 26). Eq veins have a preferred orientation, striking to the WNW dipping steeply to the NE, which follows the same orientation as WNW-trending steeply dipping faults that cut through the Everson (Fig. 14).

Eq veins contain local free gold with <10% Ag, as determined by EDS. Sulfides are minor, but one sample included oxidized pyrite that contained small grains of gold. Tourmaline (~50-50 schorl and dravite based on EDS) and muscovite $\pm$ illite are both locally found within veins as <1-6 mm wide clots. Envelopes to Eq veins are locally developed, and are made up of $\leq$4 cm sericite halos with patches of tourmaline occurring next to veins or farther out into the host rock, up to 40cm away (Fig. 26). Sericite/muscovite and tourmaline occurring both within veins and as envelopes are similar to the alteration associated with sericitization mentioned above, which suggests the veining is part of the same hydrothermal system. Potassium feldspar has also been observed forming envelopes around thinner, wavy Eq veins, particularly in lower Knickerbocker (TRkvc) volcanic rocks. Fluorite is a common accessory mineral,

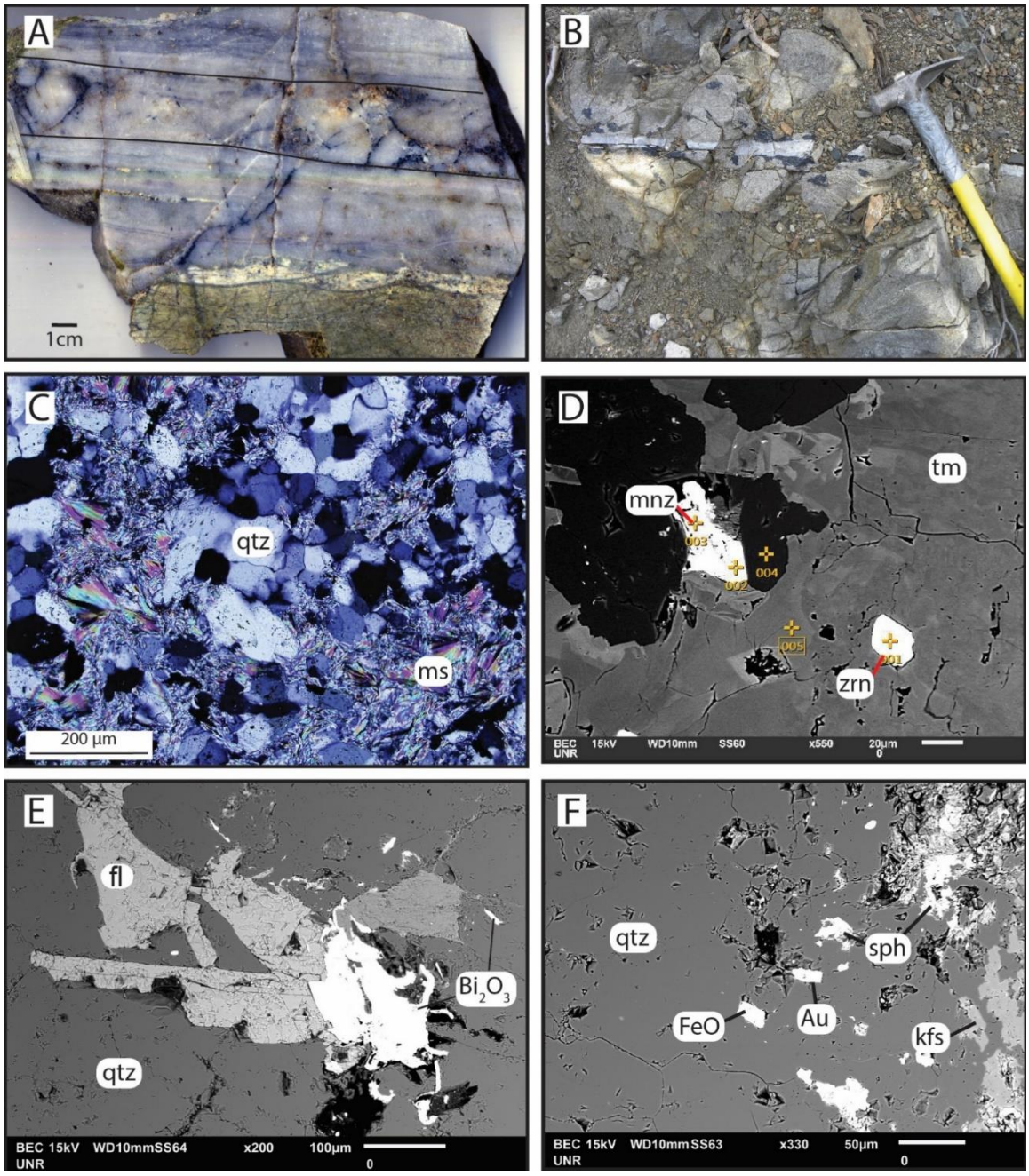

Fig. 26. Images showing mineralogy of Eq veins. A) Hand sample showing a thick Eq vein that contains early thinner crack sealing events and a later thick stage (outlined in black) that contains more tourmaline (dark mineral which also crosses earlier stages). Thick center stage contains free gold observed in thin section. Vein also contains a strong sericitic envelope. B) Photo of a typical Eq vein that shows a strong tourmaline selvage, which are common but not always present. C) XPL photomicrograph of relatively coarse-grained muscovite occurring in a blocky Eq vein. Muscovite is common mineral in Eq veins. D) Back-scattered electron (BSE) image of a clot of tourmaline (tm) and muscovite with accessory monazite (mnz) and zircon (zrn) locked within tourmaline (tm) in a thick center stage in an Eq vein. E) SEM back-scattered electron (BSE) image of fluorite occurring with bismuth oxide within a Eq vein. Fluorite is a common mineral in later paragenetic stages of Eq veins. F) BSE image of a native gold grain contained within an Eq vein, along with titanite (sph), hematite and a selvage of potassium feldspar.

occurring in later stages of veining often with oxidized bismuth minerals (Fig. 26). Local

hydrothermal monazite is intergrown with muscovite and tourmaline in later vein stages as well (Fig. 26).

The highest-grade vein assay samples contain 10-12 ppm Au, but vein samples typically assay <1ppm Au (Appendix B). Eq veins have a Au-Te-(Mo-Bi-Sn) elemental signature (Fig. 18). Ag is not correlated with Au, but rather with Pb and Sb. Zn is negatively correlated with Au, Te and Bi. This indicates that some veins lumped as Eq contain element associations more similar to Tbm veins.

An important aspect of Eq veins are their quartz textures, which are described and interpreted using the classification from Bons (2012) and Dong (1995) (Fig. 27). Eq textures are predominantly syntaxial, crack seal veins with both elongate-blocky and blocky morphologies with lesser comb-textured quartz (Fig. 28). Veins vary from single stage crack seal veins that are blocky and thinner (<1cm), to laminated veins that are made up of several distinguishable crack-seal events, that vary from fine blocky to elongate-blocky quartz. Individual stages are generally a few mm wide, but can be up to 2.5 cm thick. Later stages of veining tend to be thicker, including more elongate blocky quartz, with lesser examples of fine-grained blocky quartz (Fig. 28). Rare veins fall into an ataxial “stretching” category of quartz veining that is not associated with gold values (Fig. 28).

Comb textures are rare, and are more indicative of equilibrium conditions and open space crystallization (Dong, 1995). Within the Everson area, comb textures occur late in the paragenesis of Eq veins. The comb-textured quartz, overgrow earlier Eq veins and contain greater amounts of fluorite (Fig. 28). The primary distinguishing characteristics between comb textures and elongate blocky, syntaxial quartz is the growth

competition in syntaxial veins, whereas comb quartz does not show growth competition and has more euhedral, prismatic shapes (Fig. 28). Both types are associated with high

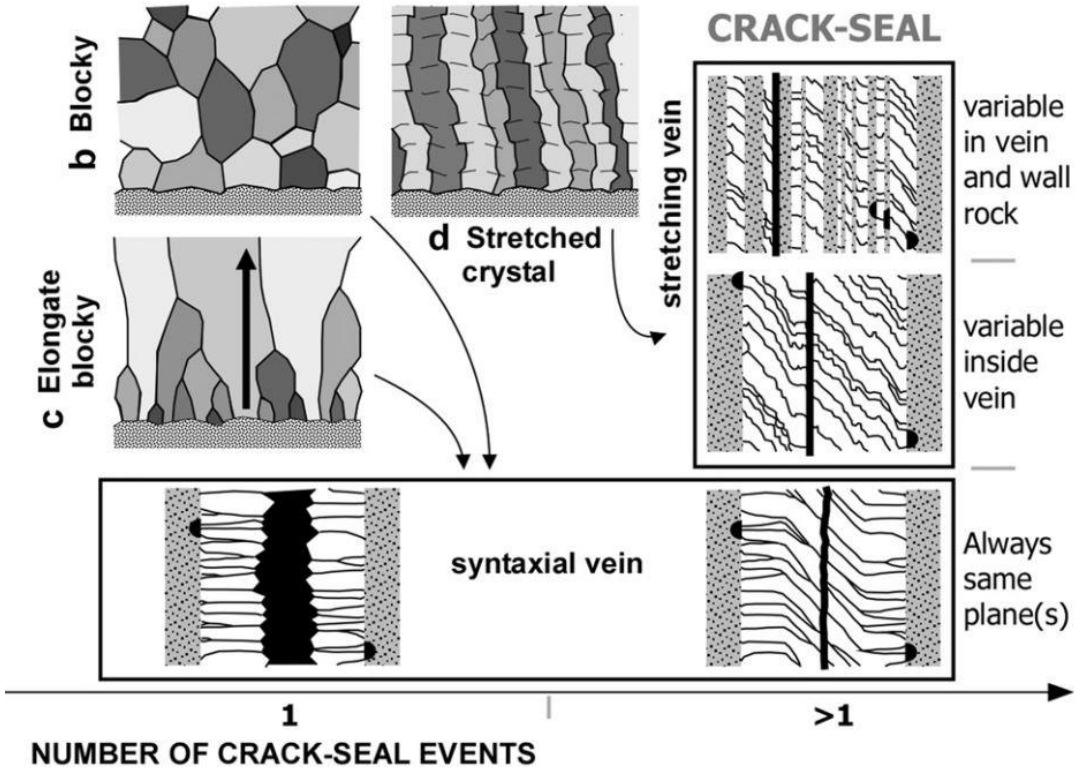

Fig. 27. Figure modified from Bons (2012) that shows crack-seal quartz textures that occur in tectonic veins. Eq veins show textures that indicate they are single crack seal events that are repeatedly occurring. Stretching "ataxial" veins are rare at Buffalo Canyon.

gold grades and similar trace metal associations.

There are multiple generations of Eq veins that are lumped together because there is insufficient evidence to subdivide them into distinct groups. Later stages of Eq veins either re-opened or obliquely cut earlier veins and are generally more narrow than earlier veins (Fig. 28). Wavier, thinner veins with fewer, or single crack sealing events most often cut earlier veins that are thicker with multiple stages.

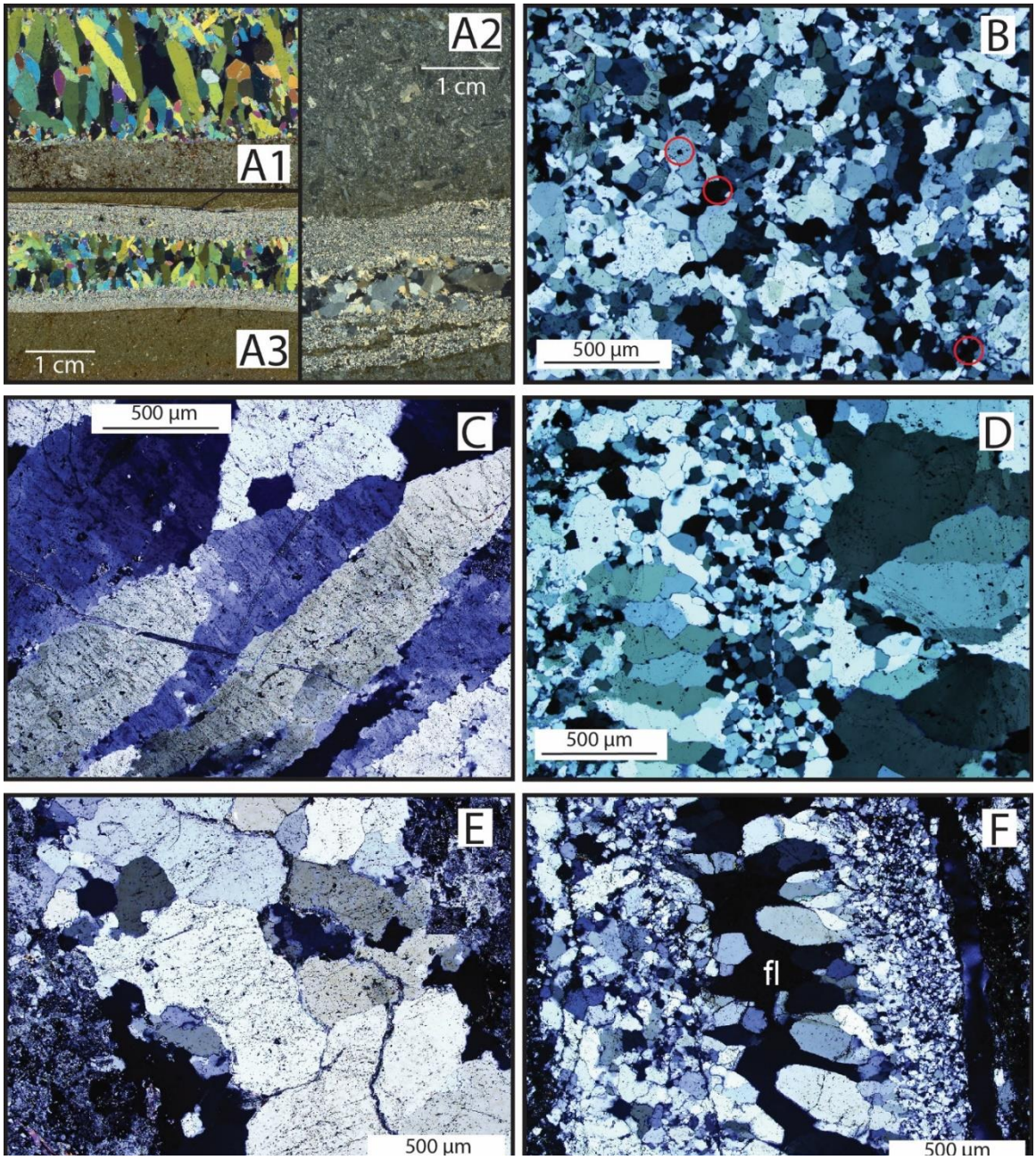

Fig. 28. Photographs showing the range of quartz textures in Eq veins. A) Three XPL thin section scans of various Eq veins showing a range of textures. A1 shows strong elongate blocky textures with strong growth competition hosted in Jd. A2 shows an early fine grained blocky stage of quartz re-opened by a coarser blocky stage hosted in Jgd. A3 shows an earlier blocky stage of quartz re-opened by a coarser elongate blocky stage hosted in TRkvc. B) XPL photomicrograph of a fine-grained blocky stage of quartz (from thick stage in Fig. 26) that hosts free gold, indicated by the red circles. Note quartz is much less deformed than Mq samples (Fig. 17). C) XPL photomicrograph of an elongate blocky quartz vein that has undergone more "stretching" as indicated by the serrated quartz boundaries. D) XPL photomicrograph from a fine laminated portion of an Eq vein. Notice the variation from more elongate blocky grains to fine blocky grains. This textural difference is what creates the laminations observed in most Eq veins. E) XPL photomicrograph of coarser, blocky, single stage of quartz that is hosted within a sample of Tg. F) XPL photomicrograph of an early fine grained blocky stage of quartz that is re-opened and filled by coarser "comb-textured" quartz that grew into open space, followed by later fluorite that filled the remaining open space in the vein center.

Quartz in Eq veins host common hypersaline fluid inclusions along with abundant two-phase liquid-rich inclusions and rare two-phase vapor-rich inclusions (Fig. 29). All thick sections of Everson veins contain hypersaline fluid inclusions with multiple daughter crystals, and in veins with multiple stages and types of quartz, hypersaline

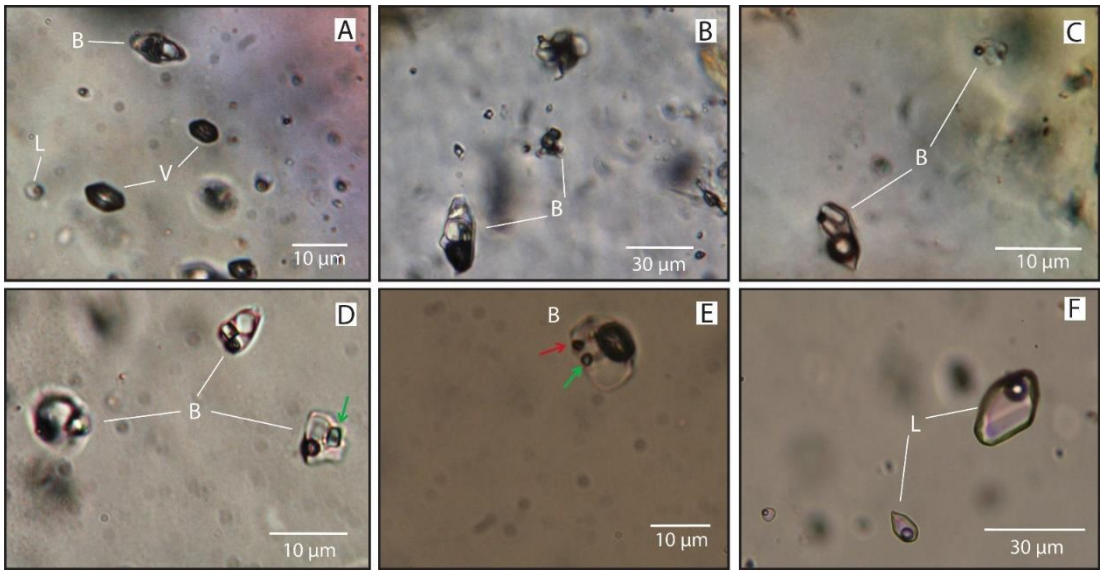

Fig. 29. Photomicrographs of fluid inclusions from Eq veins. All Eq veins and quartz textures within Eq veins contain hypersaline brine inclusions with daughter minerals. B=brine, V=vapor rich, L=liquid two phase A) PPl photomicrograph of co-existing daughter rich and vapor rich fluid inclusions, both with negative crystal shapes. Two-phase inclusions are also common. B) PPL photomicrograph of brine fluid inclusions. C) PPL photomicrograph of brine inclusions with negative crystal shapes. D) PPl photomicrograph of brine inclusions in an Eq hosted in Tg. Green arrow indicates an unknown green daughter mineral. All other inclusions hosted in clastic rocks E) PPL photomicrograph of a brine inclusion that contains hematite daughter crystal (red arrow) and an unknown green mineral (green arrow). F) PPl photomicrograph of a two-phase inclusion with moderately developed negative crystal shape. Two-phase, liquid-rich inclusions are the most common type of fluid inclusions in EQ veins, although many could be secondary in nature.

inclusions are found in both. Daughter minerals are difficult to identify, and there are often ≥four species co-existing. Identifiable minerals include ubiquitous halite and local hematite. Hypersaline inclusions are generally on the order of 10 µm in length, but can be as small as 2 µm and as large as 30 µm. In addition, many hypersaline inclusions show smooth, negative crystal shapes with lesser irregular shapes and have vapor bubbles that most often take up 15-30% of the inclusion, both of which indicate higher temperatures

of formation. Two-phase vapor-rich inclusions are common but less abundant than hypersaline inclusions and locally co-exist with hypersaline inclusions, suggestive of magmatic-hydrothermal fluids in the 2-phase field (Fig. 29). Vapor-rich and two-phase inclusions can also show negative crystal shapes, although not as commonly as hypersaline ones (Fig. 29). CL imaging was performed on one sample of Eq Veins, (Fig. 26A). More elongate blocky quartz showed distinct growth zoning while fine blocky quartz was more homogeneous. In certain samples with elongate blocky quartz, hypersaline inclusions occurred along growth zones, where others occurred as random 3D arrays. Liquid two-phase inclusions tend to cut across growth zones. Although two-phase liquid-rich inclusions make up the clear majority of fluid inclusions, many appear to be secondary in origin. More CL work of Eg veins is needed to better evaluate the paragenesis of the fluid inclusions and identity fluid inclusions suitable for microthermometry

Eq veins are the latest vein types mapped in the Buffalo Canyon area, based on cross cutting relationships. They clearly cut actinolite-albite veins, showing oblique extension with dominantly sinistral motion (Fig. 30). Many orientations show sinistral kinematic motion, with lesser examples of dextral motion (Fig. 30). Eq veins also cut both Jd and Jgd in the Everson area. Similar veins are observed in both Klg and Tg including single-stage, blocky quartz veins <1-cm-thick that contain tourmaline and hypersaline inclusions (Figs. 28 and 29). Assay data collected during previous sampling campaigns by Renaissance Gold indicate Tg hosts veins that contain up to 0.4 ppm Au. Eq veins have also been observed cutting Tbm veins where they overlap, in the drainage

north of the Everson. In one sample, an Eq vein with hypersaline inclusions was observed cutting a barren Mq vein.

Fig. 30. Selected field photographs showing cross-cutting relationships involving Eq veins: A) NS-striking earlier Eq vein that is offset left-laterally by a later SE striking set of sheeted Eq veins. B) Eq vein cutting and offsetting a Tbm vein in left lateral fashion (highlighted weakly in red). C) Field photos of Eq veins forming a ladder type structure, indicating left-lateral development. Scale indicates north direction. D) Single stage Eq vein offsetting a Sc vein in right lateral fashion. E) Wavy, bifurcating Eq veins with septums of wall rock, indicating extensional formation. F) Latest single stage Eq vein cuts an earlier Eq vein with right lateral offset, which cut a Sc vein.

5.11. District-Scale Observations

Although this work focused on the Buffalo Canyon area, important observations were made elsewhere in the district. Though reconnaissance in nature, they have significant implications. Jasperoid locally occurs throughout the district in limestone units, indicating cooler fluids, <300-350°C (Barton et al., 1997). Significant jasperoid bodies occur on Grantsville Ridge, (Nash, 1994), but small bodies of jasperoids, assaying up to 2 ppm Au, have also been observed in Knickerbocker limestone (TRkl) on the ridge north of Buffalo Canyon. Barite veins locally occur in TRkg above jasperoid bodies. In the Grantsville pit, silicified limestone containing Ag-bearing minerals with pyrite and lesser secondary copper minerals were observed, along with bladed quartz and calcite, indicative of shallow, boiling hydrothermal fluids. Float of quartz veins within Berlin Canyon also contain epithermal quartz textures, in hand sample, that differ from other veins, having a more banded, colloform texture.

6. DISCUSSION

6.1. Interpreted Geologic History

The mapping, petrography, and geochronology presented above indicate an intrusive history of Buffalo Canyon defined by distinct periods magmatism and hydrothermal alteration that spanned much of the Mesozoic and Tertiary. Due to the lack of surface exposure of intrusive rocks throughout the district, much needs to be inferred about the subsurface, which likely contains a large volume of intrusive rocks. At least three distinct periods of magmatism can be broken out based on geochronology, which includes a Late Jurassic intrusive event comprised of intermediate magmatism, a Late Cretaceous event that varies from intermediate to granitic in composition, and a complex Oligocene intrusive event that is also varied in composition from intermediate to felsic. The wide variety of ages and compositions of magmatism found within the small area presents a challenge in unraveling the timing of alteration and mineralization. Based on available data, an interpretation of the geologic history of the Buffalo Canyon is put forward, that makes a case for gold mineralization at the Everson deposit being genetically related to an evolving magmatic system in the late Oligocene.

6.1.1 Jurassic Geology

Jurassic rocks are the oldest, most voluminous intrusive units identified within the district. Jurassic magmatism is notably metaluminous and more oxidized compared to subsequent magmatic events. The ~1 km^2 Shamrock diorite (162.03 $\pm$ 0.91 Ma) is the only significantly exposed intrusive body within the district, and due to its more primitive geochemical signature and mineralogy, is interpreted to have a larger mantle component.

It likely represents an early fractionation product of a larger magma chamber at depth. Surface exposures of Jurassic intrusive rocks at Buffalo Canyon (Jd) have a similar mineralogy to the Shamrock diorite and chemically represent a slightly evolved phase that is interpreted to be related to the Jurassic event that produced the Shamrock plug. Jd is interpreted to be only partially unroofed, and is probably more extensive at depth (Fig. 31). Jgd dikes are also abundant in the Buffalo Canyon area. Dating suggests Jgd dikes are slightly younger (158.72 $\pm$ 0.98 Ma), and likely part of the same evolving magmatic event. Many late Jurassic intrusive rocks throughout Nevada have similar characteristics to those observed at Buffalo Canyon (du Bray, 2007). Dickinson (2006) attributed their mantle signature to be related to magmatism caused by breakoff off the Mezcalera slab.

Jurassic diorite intrusions are associated with hornfels throughout the project area. Biotite hornfels is overprinted by sodic-calcic alteration that is related to Jgd dikes, which indicates that the majority of contact metamorphism is related to underlying Jurassic (Jd) intrusions. Younger intrusions lack evidence of significant contact metamorphism, although the presence of pyrrhotite in both hornfels, other alteration styles (Tm-qtz) and Tmqd (all within the same area) suggests pyrrhotite in hornfels may be related to younger intrusions. The extent of hornfels that is associated with Jd suggests a larger volume of Jd in the shallow subsurface than crops out. Epidote-albite hornfels is interpreted as the distal part of the contact aureole. As previously mentioned, sodic-calcic alteration is strongly associated with Jgd dikes and is not documented within any Cretaceous or Oligocene intrusive units. Similar sodic-calcic alteration is found associated with many Jurassic intrusions throughout Nevada, such as in the Yerington mining district (Carten, 1986), the Stillwater Range and the Buena Vista Hills (Johnson and Barton, 2000). Iron-

oxide-apatite alteration has fewer spatial and temporal ties to Jurassic intrusive rocks in the Buffalo Canyon area, but other sodic-calcic alteration occurrences in Nevada are also associated with massive magnetite-apatite alteration (Johnson and Barton, 2000). Origins for sodic-calcic and Fe-oxide alteration styles are debated, though strong arguments have been made for convecting non-magmatic brines that are driven by the heat from Jurassic intrusions for sodic-calcic alteration zones in western Nevada (Barton and Johnson, 1996; Dilles et al., 2000).

6.1.2. Cretaceous Geology

Cretaceous intrusions are the most poorly exposed of the intrusive suites; however, evidence suggests significant Cretaceous intrusions are located at depth based on widespread Cretaceous U-Pb zircon ages obtained from Oligocene intrusions. Zircons yield a wide range of ages from approximately 95 to 72 Ma, though the largest concentration of ages is from 83 to 77 Ma. The largest volume of Cretaceous intrusive rock is a monzodiorite (Kmd) intercepted in drill hole BCD-101-11 in Berlin Canyon. This phase is more peraluminous and evolved than Jurassic diorites and contains rare miarolitic cavities. Kmd is cut by highly evolved, ilmenite bearing, peraluminous leucogranite (Klg) dikes in the same hole. The other exposure of Klg is found north of the Everson area and significantly contains micrographic textures, local pegmatite and a distinctive, coarse allotriomorphic groundmass. Miarolitic and other textures in both Kmd and Klg suggest Cretaceous intrusions were water rich and likely exsolved a volatile phase (Candela, 1997; London, 2009), although no significant alteration or mineralization is spatially or temporally associated with the intrusions. Nevertheless, the possibility exists that some mineralization related to Cretaceous magmatism may have been

overprinted by later magmatic-hydrothermal events. Geochemical data suggest some Cretaceous magmas were crustal-sourced, S-type granites that are more reduced in character compared to Jurassic intrusions. Late Cretaceous peraluminous, reduced magmatism occurs throughout Nevada, commonly expressed as two-mica granites (Barton, 1987). These intrusions commonly have associated lithophile element (Be, F, W, Mo, Sn, and Zn) mineralization (Barton, 1987; Barton and Trim, 1991). The abundant Late Cretaceous zircon xenocrysts in the Oligocene intrusions strongly suggests the presence of voluminous intrusive bodies at depth and that the highly evolved leucogranites may represent the apophysis of an underlying Late Cretaceous pluton (Fig. 31).

Several lines of evidence suggest mesothermal quartz (Mq) veins represent the oldest style of mineralization within the project area. Compared to other styles of veining, Mq veins contain deformed quartz and CO_2-bearing fluid inclusions, which indicate higher pressures and deeper depths of formation. Extensional veins and fault-fill veins associated with metamorphism are common and host mineralization in many orogenic gold deposits around the globe (Robert and Poulsen, 2001, Goldfarb et al., 2005). Mq veins bear a resemblance to these orogenic veins, but also contain differences. Similar to orogenic gold deposits, the Mq veins in the Buffalo Canyon area include deformed quartz textures, CO_2-bearing fluid inclusions, and if present, an alteration envelope of sericite $\pm$ calcite $\pm$ chl $\pm$ py. The mineralogy and element association of Au-Ag-(Sb-Pb-As-Cu) is also comparable to many orogenic deposits (Goldfarb et al., 2005). Differences include the lack of obvious, regional metamorphism and Mq veins contain greater Ag:Au ratios (~7-12:1) in the Buffalo Canyon area compared to most orogenic deposits (Goldfarb et

al., 2005). It is important to highlight that Mq veins are hosted within the apparently un-deformed Shamrock diorite, which indicates the veins cannot be related to Luning-Fencemaker deformation that lasted from the early Jurassic until the middle or late Jurassic (Wyld, 2002). ^{40}Ar-^{39}Ar sericite ages on similar quartz vein types hosted in Triassic rocks give ages that range from 118 to 55 Ma in the Humboldt Range, although many are dated between 90 and 70 Ma (Vikre, 1977, 1981, 2014; Cheong, 2000). Johnston et al., (2015) speculated that much of this mesothermal veining could be related to Sevier deformation due to slab flattening in the late Cretaceous. If Buffalo Canyon veins are of similar ages to veins dated elsewhere, they would be roughly coeval to the Late-Cretaceous magmatic system. Beyond being younger than 161 Ma, the age of Mq veining in the Buffalo Canyon area is speculative at this point. More work is needed to better constrain their age and evaluate a possible relationship to intrusive activity.

6.1.3. Tertiary Geology

Oligocene intrusions have the most chemical and petrographic variety of any intrusive group and represent a complex, diverse magmatic event at approximately 24.6 Ma. Exposed Oligocene intrusions are also volumetrically minor. The composition of the intrusions is variable, ranging from metaluminous to weakly peraluminous. The majority (Tg, Td, Tqm) are more evolved, but Tqmd and Tba represent more mafic components. Importantly, minor leucogranite dikes were observed cutting a dike of Td, indicating that a body of Oligocene leucogranite (Tlg) likely occurs in the subsurface. Tlg, like Klg, contains textures, including coarse graphic textures and unidirectional solidification textures (Candela, 1997), suggesting it exsolved a volatile phase. This volatile phase likely could have formed the greisen-type alteration and mineralization hosted in other

Oligocene intrusive rocks, which is related to Eq veining (Fig. 31). In most Oligocene intrusive phases, magmatic Fe-Ti-oxide phases were absent, making it difficult to assess the oxygen fugacity of the Oligocene intrusions. In one sample of Tqmd, magmatic ilmenite was found, suggesting they may be more reduced in nature. All phases that were dated have common ages that are within error each other (25.1 $\pm$ 0.29 to 24.6 $\pm$ 0.3 Ma), and are therefore inferred to come from the same source magma chamber.

Many of the Oligocene intrusions at Buffalo Canyon contain abundant Cretaceous zircon xenocrysts that lack Oligocene rims, and Oligocene zircons in the same samples had no inherited cores. This indicates that Oligocene dikes and small plugs intruded through a large Cretaceous granitic body, and xenocrysts did not have time equilibrate and dissolve or grow rims (Corfu, 2003). The lack of Cretaceous cores in Oligocene zircons either indicates that the Oligocene magmas did not significantly interact with underlying Cretaceous intrusions, or if they did, Cretaceous zircons were not preserved. The fine-grained nature of Oligocene intrusions supports that they were rapidly emplaced and xenocrysts did not have time to equilibrate. Oligocene leucogranite phases show textures that indicate volatile rich conditions, similar to Klg, which includes local pegmatite (Fig. 9, Appendix A). It is possible that all zircons analyzed in Klg are xenocrysts, as a late stage felsic melts could likely have been saturated in zirconium and crystalized zircon at an earlier stage, and not included primary zircons with the emplaced bodies, which is not uncommon for highly evolved intrusions (Corfu, 2003). This indicates that leucogranite phases dated to the Cretaceous do not necessarily have to be Cretaceous in age, and could instead be related to Oligocene leucogranite phases that

have only been locally identified. This is a purely speculative at this point, but is worth following up with more work.

Tertiary volcanic rocks that overlay the Mesozoic section were not in the scope of this work. These largely pyroclastic volcanic rocks bear similarities to Oligocene intrusive rocks described in this work, with similar compositions and ages. Published ages of volcanic cover in the range vary from 30-22 Ma (McKee and John, 1987; John, 1992). Tertiary cover in the southern Shoshone Mountains includes lava flows and ignimbrites that range from rhyolitic to basaltic in composition (Vitaliano, 1963; Whitebread et al., 1988). In addition, the thickness of Tertiary volcanic rocks in the southern Shoshone Mountains is determined to be >3,000 meters. Vitaliano (1963) also described intrusive dikes and plugs of rhyolite to trachyandesite composition that intrude the extrusive volcanic package in the Shoshones and a plug of diorite in the Paradise Range that is altered to sericite and tourmaline. Vitaliano and Vitaliano (1972) interpret many of these intrusive rocks to have fed overlying volcanic rocks. Tilted Tertiary rocks immediately overlying the Mesozoic section project up-dip about 0.3 to 0.4 km above the Everson deposit, assuming volcanic rocks were deposited horizontally.

Two K-Ar dates on biotite from the tuff of Ione Canyon/Sheep Canyon, including one from Ione by Armstrong (1970) and another by John (1992) give ages of 24.4 and 24.9 Ma, respectively and have no identified source (Henry and John, 2013). These ages are nearly identical to ages obtained on Oligocene intrusive rocks for this study, suggesting a potential link between the ages of mineralization and coeval volcanism, although at this point it is purely speculative and the tuffs could have a distal source. Most of the 3 km section of overlying volcanic rocks has been dated to 25 Ma or older,

including the tuff of Arc Dome, which caps most of the section (Vitaliano and Vitaliano, 1972; John, 1992; Henry and John, 2013). This suggests that the depths of formation of the Everson could be around 2-3 km assuming the age of mineralization is broadly contemporaneous with the Oligocene intrusions and coeval volcanic rocks. Vitaliano and Vitaliano (1972) indicate that several lower volcanic units are hydrothermally altered, including the lower Mission Spring formation, which contains quartz veinlets and the Third Canyon formation which is intensely propylitically altered, locally albitized and cut by related intrusive rocks.

Buffalo Canyon hosts a variety of alteration styles, many of which are interpreted to be related to Oligocene intrusions. These include skarn assemblages, patchy tourmaline-quartz (Tm-qtz), propylitic assemblages and sericitization. Skarn alteration is the most distinct assemblage, but relatively minor. The primary body of skarn in the Buffalo Canyon area is interpreted to form in the hanging wall of a north-trending fault that bounds the limestone protolith (Fig. 12). Retrograde skarn veins are found through most of the property, and overprint biotite hornfels, but no other cross-cutting relationships were observed to constrain the timing of their formation. Tm-qtz, propylitic and sericitization include similar mineralogies, with multiple assemblages containing tourmaline, sericite and or chlorite. Tm-qtz alteration is hosted in clastic rocks while propylitic and sericitization are hosted in Oligocene and older igneous rocks. Necessary relationships between alterations styles and their distribution are lacking to make definitive statements regarding the timing of various alteration assemblages, but are interpreted here as part of a single Tertiary intrusive event that evolved over time (Fig. 31).

Base metal mineralization (Tbm) is interpreted to be older than Everson mineralization based on cross-cutting relationships. These relationships are equivocal, and more observations are needed to better constrain temporal relationships. Base metal veins are likely related to other base metal features, such as those associated with Tm-qtz orbs and veins that contain pyrrhotite-pyrite and sphalerite. The presence of Ag-Pb-Zn base metal mineralization implies a distal environment (Fig. 31). Distal Ag-Pb-Zn are not uncommon in intrusion-related deposits (Fig. 32). The similarities between Grantsville mineralization and Tbm mineralization at Buffalo Canyon imply they could likely be related. This style of mineralization is interpreted to be an earlier, distal expression of a multi-phase Oligocene system that is cut by Eq veins. This relationship is supported by the presence of coarser muscovite that is overprinting earlier propylitic assemblages which are more related to base metal features.

The timing of Eq and Tbm veins is a key to interpreting the evolution of the hydrothermal system(s) at Buffalo Canyon. It would be unusual to see later gold bearing (Eq) veins cutting base metal mineralization (Tbm) that is part of the same hydrothermal system, which is what limited cross cutting relationships suggest. This leaves the possibility that, Tbm mineralization is in fact older than Eq veining and part of an older, related event, or that cross-cutting relationships observed are not representative of the entire system which may include later base metal mineralization, or perhaps both. Jasperoid scattered throughout the district also indicates more distal environments due to the cooling and an increase in pH of hydrothermal fluids to the point where they react with limestones, depositing quartz and dissolving calcite due to its retrograde solubility (Barton, et al., 1997). In addition, the presence of bladed quartz after calcite located in the

Grantsville pit and colloform quartz veins in Berlin Canyon indicate an epithermal overprint.

Eq veins variably contain muscovite, tourmaline and fluorite as common vein minerals, along with selvages of muscovite, tourmaline and rare potassium feldspar. Given the similarity between vein-related alteration styles and more pervasive wall rock alteration that both contain tourmaline-quartz-sericite-chlorite and variable sulfides, together resemble a greisen style of alteration and mineralization. Greisen-like alteration and mineralization hosted in Oligocene rocks imply that Eq vein formation is spatially and temporally tied to late stage, evolved magmatism in the Oligocene (Fig. 31). The presence of phases such as monazite and bismuth oxide (bismite) minerals also suggest a close link with magmatic-hydrothermal fluids.

Eq veins, which make up the bulk of Everson mineralization, are structurally controlled. As described above, Eq veins commonly strike WNW, which is the same orientation as faults that control drainages which cut through the Everson (Fig. 14). In addition, a separate series of faults has a dominant north strike, which, based on field mapping show both components of normal and strike-slip motion (Figs. 3, 4 and 14). WNW faults displace Jgd dikes with sinistral motion throughout the Everson deposit (Fig. 3), and the Eq veins at Everson show similar left-lateral motion, along with dilation that may have resulted in the characteristic crack-seal textures (Fig. 30). These WNW and N structural orientations persist throughout the district, and Silberling (1959) and Abrams (1979) suggest that these structures were coeval. Considering the left-lateral motion suggested by field relationships, it holds that WNW-trending, right step-over structures will be dilatant under left-lateral motion (Fig. 31). Left-lateral motion during

the late Oligocene has not been well documented, but authors such as Hardyman and Oldow (1991) suggest that there was possibly left-lateral motion along Walker Lane strike slip faults during early extension, from about 28-17 Ma. The southern Shoshone Mountains fall outside of the central Walker Lane, but are near its eastern boundary, indicating it may have experienced deformation related to the Walker Lane. Dilatant structural zones would be ideal for focusing hydrothermal fluids and intrusions from underlying magma chambers. WNW faults show both left-lateral and right-lateral motion,

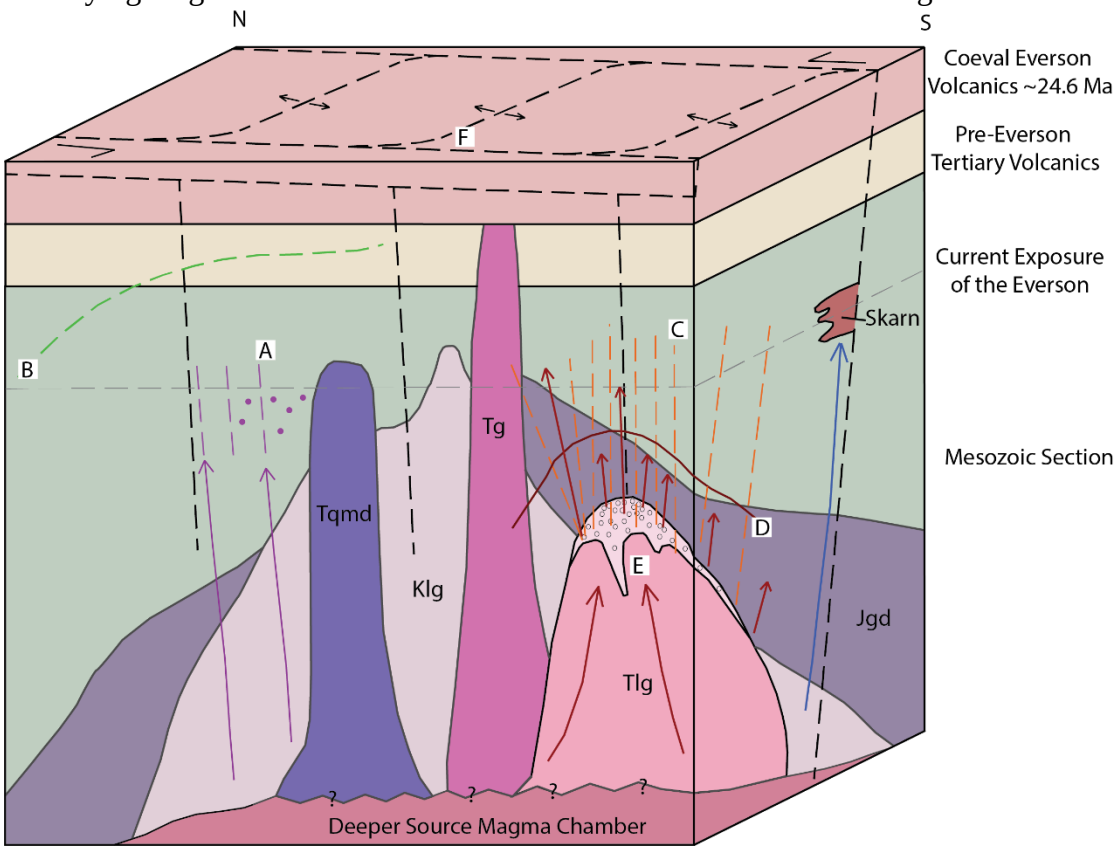

Fig. 31. Schematic diagram illustrating Everson formation during the late Oligocene. No specific scale is implied, but the paleodepth below the base of the Oligocene volcanic rocks to the top of the Tlg intrusions is interpreted to be <3 km. A) Distal tourmaline base metal sulfide (Tbm) mineralization that forms more distal to intrusive activity, and overlaps in space with, and is cut by Everson veins (C). B) Distal propylitic alteration that Vitaliano and Vitaliano (1972) described as affecting overlying volcanics. C) Everson quartz veins in orange and greisen like alteration fluids in dark red which are generally associated with veining, but can be locally pervasive. D) Interpreted uppermost extent of strong greisen-like alteration, overlying Tlg. E) Inferred causative intrusion that exsolved fluids responsible for Everson mineralization and greisen-like alteration. F) Interpreted fault controls on Everson mineralization that provided dilatational structures for focusing fluids from an underlying intrusion.

of which the latter is interpreted to be later overprinted by more typical, right lateral Walker Lane motion. Additional work, both regionally and at Buffalo Canyon, is needed to evaluate the structural setting of Everson mineralization during the Oligocene.

Petrographic characteristics are particularly useful for interpreting Eq veins. The abundance of hypersaline inclusions with multiple daughter minerals in all Eq vein stages further supports the close temporal association with magmatic-hydrothermal fluids. In addition, many inclusions of all types display negative crystal shapes, which suggest temperatures >270° (Goldstein, 2003). The presence of coexisting vapor-rich fluid inclusions suggests phase separation into a brine and vapor phase. Phase immiscibility of vapor and brine generally correspond to lower pressures (~500 bars), but depends on temperature and salinity; with addition of CO_2 increasing pressures at which un-mixing occurs can be as high as 2000 bars (Driesner and Heinrich, 2007; Audetat and Simon, 2012). Fluid inclusions observed within Everson veins resemble those documented by Baker (2002) in RIRG systems, which can include hypersaline inclusions and coexisting vapor dominant, CO_2-bearing inclusions (Fig. 32). Evidence for CO_2 was not identified in Eq veins, and additional work is needed to determine fluid trapping temperatures and salinities required for a more rigorous pressure estimate.

6.2. Comparison to Other Deposit Styles

Everson mineralization bears a strong resemblance to reduced intrusion related gold (RIRG) systems, which are common in Alaska and Yukon (Table 3). Features of some RIRG systems that are shared with Everson mineralization include: sheeted, low-sulfide, free gold-bearing quartz veins with hypersaline fluid inclusions, a strong Te $\pm$ Bi

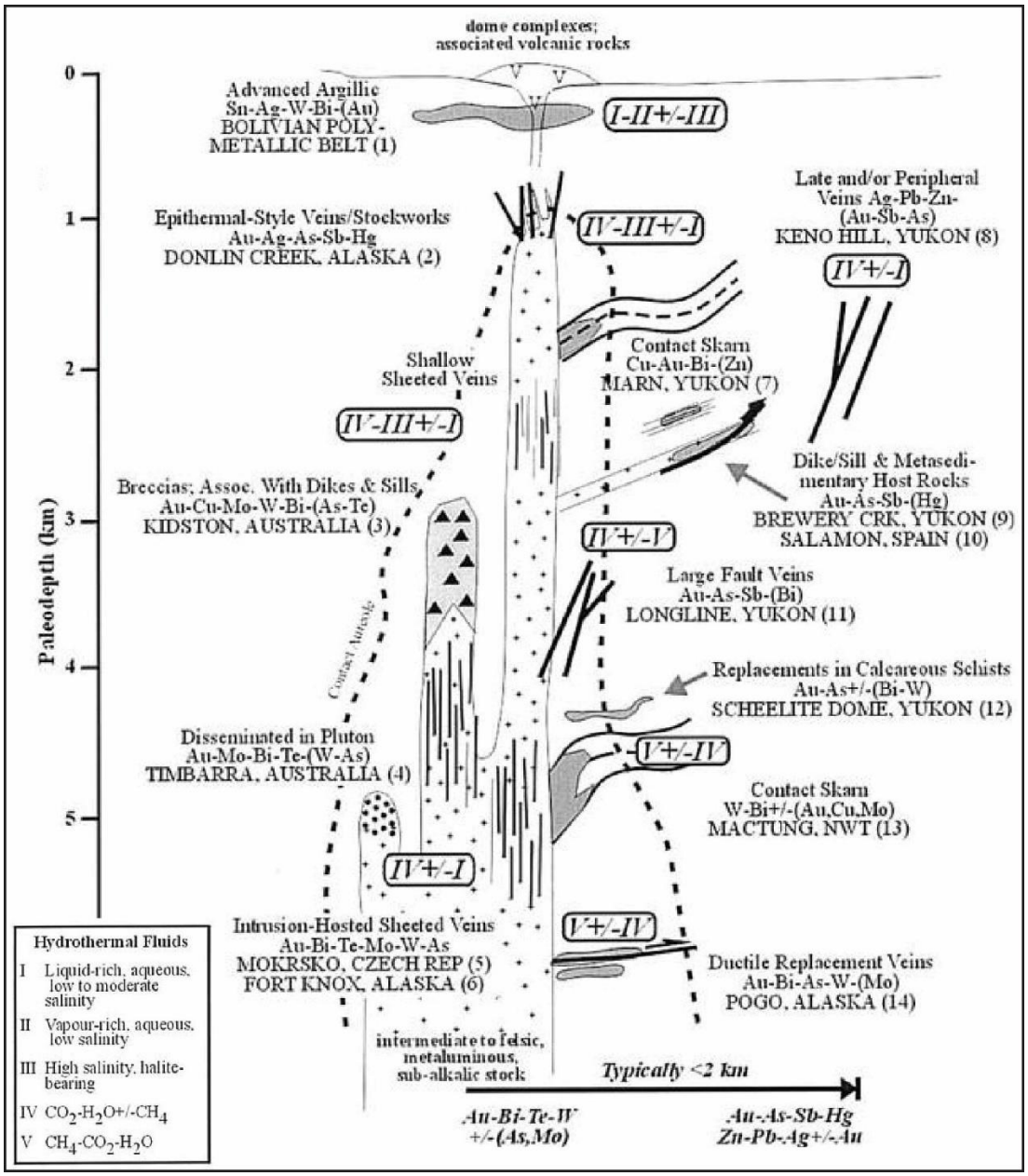

Fig. 32. Exploration model for RIRG deposits, modified from Lang and Baker (2001). Note the deposits have a typical proximal Au-Bi-Te-W signature that grades out into a distal Au-As-Sb-Zn-Pb-Ag signature, with some deposits such as Keno Hill containing late Ag-Pb-Zn veins. At Buffalo Canyon Ag-Pb-Zn veins and mineralization occur alongside Au-Te-(Mo-Bi-Sn) mineralization, with the former cutting the latter. Also, notice that deposits with high salinity inclusions (III) typically occur at interpreted paleodepths < 3 km.

± Mo association, and proximity to reduced granitic intrusions, (Hart, 2007). RIRG systems can also display metal zonation with cores of Au-Bi-Te ± W grading out into As-Sb-Au and distal Ag-Pb-Zn, resembling mineralization styles at Buffalo Canyon (Fig. 31;

Lang and Baker., 2001). At Buffalo Canyon, these proximal and distal associations occur together, indicating related, overprinting events. Typical RIRG deposits are found in a variety of environments, including, magmatic arc, back-arc, collisional and post-collisional tectonic settings, but commonly are hosted in thickened continental strata inboard of the active margin (Thompson et al., 1999). In addition, evidence suggests Buffalo Canyon formed at shallower depths (<3 km), and while some deposits such as Donlin Creek, Brewery Creek and Keno Hill formed at shallower depths, RIRG deposits commonly form at deeper (5-9 km), mesozonal depths (Lang and Baker, 2001). The depth of Eq vein formation is an important question. The thickness of the volcanic section that is older or coeval to Oligocene intrusions at Buffalo Canyon could be over 3 km of paleodepth, which wouldn't be out of the ordinary for RIRG deposits.

Few, if any deposits in Nevada share a similar age and deposit style to Buffalo Canyon. Precious-metal deposits of similar age include Majuba Hill, Paradise Peak, and the Round Mountain gold deposit. Majuba Hill, located north of Lovelock in Pershing County, is a Ag-Cu-Sn rich deposit with the only known Au values associated with nearby placers (MacKenzie and Bookstrom, 1976). Mineralization at Majuba Hill is associated with an Oligocene (24-25 Ma) rhyolitic intrusive complex with associated tourmaline and sericite alteration (MacKenzie and Bookstrom, 1976). High-sulfidation epithermal Au-Ag mineralization at Paradise Peak deposits and nearby Au-Ag-Cu mineralization is hosted at the Sullivan deposit, located ~30 km WSW of Buffalo Canyon, are both located across the Ione Valley to the southwest of Buffalo Canyon. Paradise Peak mineralization is a high sulfidation system hosted in Miocene rhyolite and andesite flows and tuffs with associated porphyry gold styles of mineralization, whereas

Sullivan is a skarn-like deposit hosted in Mesozoic, weakly metamorphosed host rocks with Au>Ag and highly anomalous values of Ag, As, Au, Bi, Cu, Sb, Zn and Hg (John et al., 1989; Nash, 1994, Sillitoe and Lorson, 1994). Sullivan has also been targeted as a porphyry system related to Cretaceous stocks mapped elsewhere in the district (Nash, 1994). The age of mineralization at Paradise Peak ranges from 22.1 to 18.0 Ma, and the age of Sullivan mineralization is unknown and lacks sufficient information to make a comparison with Buffalo Canyon (John et al., 1989). Nevertheless, the presence of Au>Ag, weak metamorphism, porphyry gold styles of mineralization, along with its relatively proximity are intriguing. The low-sulfidation epithermal Round Mountain deposit has a similar age (26 Ma), potentially representing a distal expression of a similar type of intrusion related setting.

Within Nevada, Buffalo Canyon bears the most similarity to intrusion-related gold deposits of older ages. Spring Valley and Bald Mountain contain the most similar styles of mineralization. Bald Mountain has been determined to be a Jurassic reduced intrusion related gold deposit with associated sericitic alteration (Nutt and Hofstra, 2007; Pace, 2009). Spring Valley, located in the Humboldt Range, contains several features similar to Buffalo Canyon. These include, but are not limited to, crack-seal Au-bearing quartz veins with little silver and minor sulfides, quartz-sericite-pyrite-tourmaline alteration and variable base metal sulfide mineralization. Significant differences include a lack of hypersaline fluid inclusions and predominance of liquid CO_2-bearing inclusions (Crosby and Thompson, 2015). Crosby and Thompson (2015) attributed Spring Valley mineralization to either a RIRGS or orogenic style of mineralization. Vikre (1981) suggested that mineralization in the Humboldt Range may be related to underlying

Cretaceous intrusions. The presence of CO_2-bearing inclusions at Spring Valley suggests much greater depths of formation.

6.3. Exploration Implications

Buffalo Canyon has significant implications for exploration in Nevada. Few deposits of this age and style are documented within the state. Results of this work can potentially open new areas for exploration. Magmatism related to slab rollback in the Great Basin represents a major event with important metallogenic implications. The long history of subduction along the Cordilleran margin may have led to a hydrated, metasomatised subcontinental lithospheric mantle that was the source of Au and other trace elements for deposits formed during slab rollback (Muntean et al., 2011). Most precious-metal deposits associated with slab rollback in the Great Basin formed early (Eocene) and late (Miocene) in the rollback history, with far fewer examples of Oligocene deposits. The important exception is the low-sulfidation epithermal Round Mountain deposit, which formed at ca. 26 Ma and has produced $\geq$16 million oz Au (Muntean and Davis, 2017; Henry et al., 1997). One potential difference is the style and composition of magmatism, with Eocene magmatism related to dome and lava fields and accompanying intermediate intrusions of dacitic and andesitic compositions, whereas Oligocene to early Miocene magmatism was more felsic and resulted in caldera-forming eruptions of predominantly rhyolitic ash-flow tuff (Henry and John,2013). Calderas occur over much of central Nevada, including parts of the Shoshone Mountains, with ash-flow tuffs and other volcanic rocks, perhaps covering earlier-formed deposits. Buffalo Canyon

Table 3. Comparison of Similar Deposits

	Buffalo Canyon	RIRGS deposits of Alaska and Yukon (i.e. Fort Knox)	Majuba Hill, Nevada	Spring Valley, Nevada
Temporally associated Intrusive Rocks	Intermediate to felsic dikes and small plugs (24-25 Ma), some ilmenite-bearing, metaluminous to peraluminous	Mostly felsic, ilmenite series, isolated plutons	Subvolcanic rhyolite complex (24-25 Ma)	Unknown. Spring Valley granodiorite (32 Ma) Rocky Canyon granodiorite (92-90 Ma)
Mineralization Styles	Sheeted, low-sulfide, free gold-bearing quartz veins hosted in hornfels clastic rocks	Intrusion-hosted, sheeted, low-sulfide quartz veins that form bulk tonnage low grade Au deposits. Also skarns, disseminations, stock-works, replacements and breccias	Veinlets of chalcopyrite with arsenopyrite, pyrrhotite, minor Ag- and Sn-bearing mineralization. Quartz-molybdenite stockworks	Crack-seal, gold bearing quartz veins with variable pyrite and late sphalerite-galena,
Geochemical Signature	Au-Te-(Mo-Bi-Sn), Au>Ag, early? Ag-Pb-Zn-Sb-As-(Au-Bi-Cu-Mo)	Au-Bi-(Te-As-Mo-W), Au>Ag, distal As-Sb-Au and Ag-Pb-Zn	Ag-Cu-Sn-(Mo-Au-As-Pb-Zn)	Au>Ag, minor Zn-Pb-As
Associated Alteration/Gangue Mineralogy	Muscovite, tourmaline, quartz, fluorite, propylitic, skarn, pyrrhotite-pyrite	K-feldspar, albitic, sericitic-muscovite, tourmaline, chlorite and carbonate often form vein selvages, Biotite-quartz $\pm$ pyrrhotite hornfels	K-feldspar, silicification, sericitic, argillic, propylitic, tourmaline	quartz-sericite+-pyrite $\pm$ tourmaline; quartz-hematite
Age of Mineralization	Oligocene (~24 Ma?)	Late Cretaceous	Oligocene	Cretaceous?
Fluid Inclusion Characteristics	Common co-existing hypersaline liquid and vapor-rich inclusions. Common, late two-phase liquid-rich inclusions	Liquid CO_2 and CH_4 bearing three-phase inclusions, low salinity (<10 wt % NaCl equiv.), 150-500°C trapping temperature. Local high-salinity inclusions (>30% NaCl equiv.)	Unknown	liquid CO_2-bearing, three-phase, 330-520°C trapping temperatures
Depths of formation	< 3km?	Commonly mesozonal (5-9 km), locally epizonal (<3-5 km)	<2 km?	> 5 km?
Tectono-Magmatic Setting During Mineralization	Slab rollback related magmatism and abundant volcanism emplaced into fine grained siliciclastic rocks during early Walker Lane development	Variable. Often emplaced into tectonically thickened continental strata, inboard from the active continental margin associated with various magma chemistries	Slab rollback related magmatism.	Associated with subduction related magmatism, hosted in Triassic volcanic and sedimentary rocks
Sources	This work	Lang and Baker, 2001; Hart, 2007	MacKenzie and Bookstrom, 1976	Crosby, 2012; Vikre, 2012; Crosby and Thompson, 2015

mineralization opens the possibility of additional intrusion-related gold deposits of Oligocene age.

Intrusion-related gold deposits of either Mesozoic or Tertiary age represent an underexplored target within the state. Spring Valley and Bald Mountain suggest that such deposits are viable exploration targets. Geophysical exploration methods can lend themselves to exploring for reduced intrusions, which often form pyrrhotite halos that give doughnut-shaped magnetic anomalies (Hart, 2007). Geochemical targeting of typical intrusion-related elements such as Au, Bi, Te or W are also important. Due to the expanse of volcanic cover that exists in much of central Nevada, regional-scale structural targeting of potential dilatant zones is likely the best first-order selection criteria, followed up by detailed field work and data collection focusing in on the characteristics of intrusion related gold deposits.

6.4. Future Work

There are many unresolved questions with regards to the timing of intrusive activity, alteration and mineralization at Buffalo Canyon. No single model can completely explain the variety of observed hydrothermal mineralization and alteration features.

Future work that could help further constrain the temporal and spatial development of intrusive and hydrothermal activity at Buffalo Canyon include the identification of additional cross-cutting relationships, which are needed for a more precise history of intrusive events and their relationship to alteration and mineralization. Ultimately, further exploration of the property is the best way to test hypotheses and

gather new information about the distribution and extent of mineralization. More core drilling proximal to Everson mineralization and intrusions could reveal additional cross-cutting relationships that would solidify temporal relationships between mineralization and intrusive phases. Both Eq veins and sericitic alteration contain muscovite that could be dated using $^{40}Ar/^{39}Ar$, and Eq veins also contain monazite that could be dated using U-Pb. Dating Eq veins would constrain the timing of alteration and mineralization more directly and immediately test the hypothesis laid out in this work. Another important remaining task is better constraining the depth of formation for the system. An additional question revolves around determining whether there are any temporal links between the intrusion-related mineralization and the lower temperature epithermal mineralization observed in the district. Reconnaissance fluid inclusion petrography has been performed on several samples of Mq and Eq veins, but a detailed fluid inclusion study would be extremely informative. Quantitative fluid inclusion data would help in constraining temperature, salinity, and depths, which would help constrain sources of the hydrothermal fluids and the operative ore-forming processes at the Everson deposits and in the Buffalo Canyon area. Additional mapping would greatly help in better understanding the structural setting that focused gold mineralization and where additional targets of gold mineralization are located. Additional field work involves looking at the Union district as a whole, in order to put other mineralization occurrences into perspective, including base metal sulfide replacement and epithermal styles of mineralization located in the Grantsville area. In addition, a broader scope field work would help correlate the overlying Tertiary volcanic rocks to Oligocene intrusions at Buffalo Canyon and build a comprehensive magmatic story.

8. CONCLUSIONS

The Buffalo Canyon prospect hosts a complex history of magmatism spanning the Mesozoic to mid-Tertiary. At least three pulses of intrusive activity were recognized including Late Jurassic, Late Cretaceous, and Oligocene. Intrusions vary from diorite to granite and magnetite- to ilmenite-bearing, and are poorly exposed on surface. Jurassic (162-158 Ma) intrusions are intermediate, magnetite bearing and are associated with sodic-calcic alteration and contact metamorphism. Cretaceous (83-77 Ma) peraluminous granites are ilmenite-bearing and larger Cretaceous intrusions at depth are inferred based on zircon xenocrysts in Oligocene intrusions. Oligocene (24-25 Ma) ilmenite-bearing intrusions that vary in composition are potentially coeval with overlying volcanic rocks, and are likely responsible for most hydrothermal alteration and gold mineralization at Buffalo Canyon.

The Everson deposit, interpreted to be Oligocene in age, contains abundant crack-seal, free gold bearing, low sulfide, sheeted quartz veins that are defined by a Au-Te-(Mo-Bi-Sn) signature. Coexisting hypersaline brine inclusions with multiple daughter minerals and vapor-rich rich inclusions in the veins strongly suggest trapping of magmatic-hydrothermal fluids in the two-phase vapor + brine field, which suggests ore formation at depths less than approximately 5 km. Greisen-like alteration associated with veining includes tourmaline, muscovite and fluorite. Fluid inclusions in these veins consist of hypersaline brine, vapor-dominant and liquid-rich assemblages, which suggest mineralization formed under epizonal conditions. Earlier, tourmaline base-metal sulfide rich veins represent a distal part of an earlier intrusion related system of interpreted Oligocene age. Historically produced mesothermal quartz veins, mainly in the Berlin area

to the south, contain liquid CO_2-bearing inclusions and predate other styles of Everson mineralization. Mineralization styles at Buffalo Canyon strongly resembles RIRG systems that are common in Alaska and Yukon. However, these deposits have not been widely documented in Nevada, and Buffalo Canyon is the only known RIRG deposit of Oligocene age or younger documented in Nevada.

References

Abrams, G.J., 1979, Geology and Ore Deposits of the Union District Southern Shoshone Mountains, Nye County Nevada: University of Nevada Reno, 100 p.

Armstrong, R.L., 1970, Geochronology of Tertiary igneous rocks, eastern Basin and Range Province, western Utah, eastern Nevada, and vicinity, U.S.A.: Geochimica et Cosmochimica Acta, v. 34, p. 203-232.

Audetat, A., and Simon, A.C., 2012, Magmatic Controls on Porphyry Copper Genesis: Society of Economic Geologists Special Publication, v. 16, p. 553–572.

Baker, T., 2002, Emplacement depth and carbon dioxide-rich fluid inclusions in intrusion-related gold deposits: Economic Geology, v. 97, no. 5, p. 1111–1117.

Barton, M.D., 1987, Lithophile-element mineralization associated with late Cretaceous two-mica granites in the Great Basin.: Geology, v. 15, no. 4, p. 337–340.

Barton, M.D., 1990, Cretaceous magmatism, mineralization and metamorphism in the east-central Great Basin: in J. L. Anderson, The Nature and Origin of Cordilleran Magmatism, Geological Society of America Memoir 174, p. 283-302.

Barton, M.D., and Hanson, R.B., 1989, Magmatism and the development of low-pressure metamorphic belts: Implications from the western United Sates and thermal modeling: Geological Society of America Bulletin, v. 101, p. 1051–1065.

Barton, M.D., and Johnson, D.A., 1996, Evaporitic-source model for igneous-related Fe oxide-(REE-Cu-Au-U) mineralization: Geology, v. 24, no. 3, p. 259–262.

Barton, M.D., and Trim, H.E., 1991, Late Cretaceous Two-Mica Granites and Lithophile Element Mineralization in the Great Basin: in Schafer, R.W., and Wilkinson, W.H., eds., Geology and Ore Deposits of the Great Basin, Geological Society of Nevada Symposium Proceedings, Geological Society of Nevada, p. 529–538.

Barton, M.D., and Young, S., 2002, Non-pegmatitic Deposits of Beryllium: Mineralogy, Geology, Phase Equilibria and Origin: Reviews in Mineralogy and Geochemistry, v. 50, no. 1, p. 591–691.

Barton, M.D., Girardi, J.D., Kreiner, D.C., Seedorff, E., Zurcher, L., Dilles, J.H., Haxel, G.B., and Johnson, D. a, 2011, Jurassic igneous-related metallogeny of southwestern North America: Great Basin Evolution and Metallogeny, p. 373–396.

Barton, M.D., Seedorff, E., Ilchik, R.P., and Ghidotti, G., 1997, Contrasting siliceous replacement mineralization, east-central Nevada [extended abs.]: Society of Economic Geologists Guidebook Series, v. 28, p. 131-134.

Bons, P.D., Elburg, M.A., and Gomez-Rivas, E., 2012, A review of the formation of tectonic veins and their microstructures: Journal of Structural Geology, v. 43, p. 33–62.

Bowring, J.F., McLean, N.M. and Bowring, S.A., 2011, Engineering cyber infrastructure for U-Pb geochronology: Tripoli and U-Pb_Redux, Geochem. Geophys. Geosyst., 12.

Candela, P.A., 1997, A Review of Shallow, Ore-related Granites: Textures, Volatiles, and Ore Metals: Journal of Petrology, v. 38, no. 12, p. 1619–1633.

Carten, R.B., 1986, Sodium-calcium metasomatism: chemical, temporal, and spatial relationships at the Yerington, Nevada porphyry copper deposit: Economic Geology, v. 81, no. 6, p. 1495–1519.

Cheong, S., 2000, General characteristics and structural evolution of metamorphic gold-quartz veins in northwestern Nevada, U.S.A.: Geosciences Journal, v. 4, no. 2, p. 135–152.

Colgan, J.P., Henry, C.D., and John, D.A., 2014, Evidence for Large-Magnitude, Post-Eocene Extension in the Northern Shoshone Range, Nevada, and Its Implications for the Structural Setting of Carlin-Type Gold Deposits in the Lower Plate of the Roberts Mountains Allochthon: Economic Geology, v. 109, no. 7, p. 1843–1862.

Corfu, F., Hanchar, J.M., Hoskin, P.W.O., and Kinny, P., 2003, Atlas of Zircon Textures: Reviews in Mineralogy and Geochemistry, v. 53, no. 1, p. 469–500.

Crosby, B.L., 2012, Gold and Base Metal Mineralization, Hydrothermal Alteration and Vein Paragenesis in the Spring Valley Deposit, Pershing County, Nevada: University of Nevada Reno, 172 p.

Crosby, B.L., and Thompson, T.B., 2015, Vein Textures, Mineralization and Hydrothermal Alteration of the Spring Valley Deposit, Pershing County, Nevada: in Pennell, W.M., and Garside, L.J., eds., New Concepts and Discoveries, Geological Society of Nevada Symposium Proceedings, Geological Society of Nevada, p. 551–582.

Daggett, E., 1907, The Extraordinary Faulting at the Berlin Mine: The Engineering and Mining Journal, v. 83, p. 617–621.

Davis, D.A., Muntean, J. L., 2016, Metals, in The Nevada mineral industry 2016: Nevada Bureau of Mines and Geology Special Publication MI-2016.

Dickinson, W., 2006, Geotectonic evolution of the Great Basin: Geosphere, v. 2, no. 7, p. 353–368.

Dilles, J. H., Einaudi, M. T., Proffett, J. M., and Barton, M. D., 2000, Overview of the Yerington porphyry copper district: Magmatic to non-magmatic sources of hydrothermal fluids, their flow paths, alteration affects on rocks, and Cu-Mo-Fe-Au ores: in Dilles, J. H., Barton, M. D., Johnson, D. A., Proffett, J. M., and Einaudi, M. T., editors, 2000, Contrasting Styles of Intrusion Associated Hydrothermal Systems: Society of Economic Geologists Guide Book Series, v. 32, p. 55-66.

Dong, G., Morrison, G., and Jaireth, S., 1995, Quartz textures in epithermal veins, Queensland - classification, origin, and implication: Economic Geology, v. 90, no. 6, p. 1841–1856.

Driesner, T., and Heinrich, C.A., 2007, The system H2O-NaCl. Part I: Cor- relation formulae for phase relations in temperature-pressure-composition space from 0° to 1000°C, 0 to 5000 bars, and 0 to 1 X-NaCl: Geochimica et Cosmochimica Acta, v. 71, p. 4880−4901.

du Bray, E.A., 2007, Time, space, and composition relations among northern Nevada intrusive rocks and their metallogenic implications: Geosphere, v. 3, no. 5, p. 381.

Dube, B., and Gosselin, P., 2007, Greenstone hosted quartz-carbonate vein deposits: in Goodfellow, W.D., ed., Mineral Deposits of Canada: A synthesis of Major Deposit-Types, District Metallogeny, the Evolution of Geological Provinces, an Exploration Methods: Geological Association of Canada, Mineral Deposits Division, Special Publication, no. 5, p. 49–73.

Dube, B., and Guha, J., 1993, Factors Controlling the Occurrence of Ferro-Axinite within Archean Gold-Copper-Rich Quartz Veins: Cooke Mine, Chibougamau Area, Abitibi Greenstone Belt: The Canadian Mineralogist, v. 31, p. 905–916.

Goldfarb, R.J., Baker, T., Dube, B., Groves, D.I., Hart, C.J.R., and Gosselin, P., 2005, Distribution , Character , and Genesis of Gold Deposits in Metamorphic Terranes: Economic Geology, v. 100th Anni, p. 407–450.

Goldfarb, R.J., Snee, L.W., Miller, L.D., and Newberry, R.J., 1991, Rapid dewatering of the crust deduced from ages of mesothermal gold deposits: Nature, v. 354, p. 296–298.

Goldstein, R., 2003, Petrographic analysis of fluid inclusions: in Samson, I., Anderson, A., and Marshall, D., eds, Fluid Inclusions: Analysis and Interpretation. Mineral. Assoc. Can., Short Ser. 32, 9-53

Hardyman, R.F., and Oldow, J.S., 1991, Tertiary Tectonic Framework and Cenozoic History of the Central Walker Lane, Nevada: in Schafer, R.W., and Wilkinson, W.H., eds., Geology and Ore Deposits of the Great Basin, Geological Society of Nevada Symposium Proceedings, Geological Society of Nevada, p. 279–301.

Hart, C.J.R., and Goldfarb, R., 2005, Distinguishing intrusion-related from orogenic gold systems: Proceedings of the 2005 New Zealand Minerals Conference, Auckland, November 13-16, p. 125–133.

Hart, C.J.R., 2007, Reduced intrusion-related gold systems, in Goodfellow, W.D., ed., Mineral deposits of Canada: A Synthesis of Major Deposit Types, District Metallogeny, the Evolution of Geological Provinces, and Exploration Methods: Geological Association of Canada, Mineral Deposits Division, Special Publication No. 5, p. 95-112.

Henry, C.D., Elson, H.B., McIntosh, W.C., Heizler, M.T., and Castor, S.B., 1997, Brief duration of hydrothermal activity at Round Mountain, Nevada, determined from 40Ar/ 39Ar geochronology: Economic Geology, v. 92, no. 7–8, p. 807–826.

Henry, C.D., and John, D.A., 2013, Magmatism, ash-flow tuffs, and calderas of the ignimbrite flareup in the western Nevada volcanic field , Great Basin , USA: Geosphere, v. 9, no. 3, p. 951–1008.

Humphreys, E.D., 1995, Post-Laramide removal of the Farallon slab, western United States: Geology, v. 23, no. 11, p. 987–990.

John, D.A., 1992, Stratigraphy, Regional Distribution, and Reconnaissance Geochemistry of Oligocene and Miocene Volcanic Rocks in the Paradise Range and Northern Pactolus Hills, Nye County, Nevada U.S.: Geological Survey Bulletin 1974, p. 67.

John, D.A., Henry, C.D., and Colgan, J.P., 2008, Magmatic and tectonic evolution of the Caetano caldera, north-central Nevada : A tilted , mid-Tertiary eruptive center and source of the Caetano Tuff: Geosphere, v. 4, no. 1, p. 75–106.

John, D.A., Thomason, R.E., McKee, E.H., 1989, Geology and K-Ar Geochronology of the Paradise Peak Mine and the Relationship of Pre-Basin and Range Extension to Early Miocene Precious Metal Mineralization in West-Central Nevada: Economic Geology, v. 84, p. 631-649.

Johnson, D. A. and Barton, M. D., 2000, Time-Space Development of an external-brine-dominated, igneous-driven hydrothermal system: Humboldt mafic complex, western

Nevada: in Dilles, J. H., Barton, M. D., Johnson, D. A., Proffett, J. M., and Einaudi, M. T., editors, 2000, Contrasting Styles of Intrusion Associated Hydrothermal Systems: Society of Economic Geologists Guide Book Series, v. 32, no. 3, p. 145-162.

Johnson, M.G., 1973, Placer Gold Deposits of Nevada: Geological Survey Bulletin 1556, U.S. Geological Survey, p. 1–118.

Johnston, M.K., Coleman, K.N., and Ressel, M.W., 2015, Late Cretaceous Orogenic Au-Ag Vein Deposits of Western and North-Central Nevada: Consequences of Sevier Flat-Slab Subduction, and Links with Other Cordilleran Orogenic Deposits: in Pennell, W.M., and Garside, L.J., eds., New Concepts and Discoveries, Geological Society of Nevada Symposium Proceedings, Geological Society of Nevada, p. 583–610.

Kleinhampl, F.J., and Ziony, J.I., 1984, Mineral Resources of Northern Nye County, Nevada: Nevada Bureau of Mines and Geology, Bulletin 99B, 243 p.

Kral, V.E., 1951, Mineral Resources of Nye County, Nevada: Nevada Bureau of Mines and Geology Bulletin 50, p. 223.

Lang, J.R., Baker, T., Hart, C.J.R., and Mortensen, J.K., 2000, An exploration model for Intrusion-Related Gold Systems: SEG Newsletter, v. 40, p. 6–15.

Lang, J.R., and Baker, T., 2001, Intrusion-related gold systems: The present level of understanding: Mineralium Deposita, v. 36, no. 6, p. 477–489.

London, D., 2009, The origin of primary textures in granitic pegmatites: Canadian Mineralogist, v. 47, no. 4, p. 697–724.

MacKenzie, W.B., and Bookstrom, A.A., 1976, Geology of the Majuba Hill area, Pershing County, Nevada: Nevada Bureau of Mines and Geology Bulletin 86, 23 p.

Mcdonough, W.F., and Sun, S.S., 1995, The composition of the Earth: Chemical Geology, v. 120, no. 3, p. 223–253.

McDowell, F.W., and Kulp, J.L., 1967, Age of Intrusion and Ore Deposition in the Robinson Mining District of Nevada: Economic Geology, v. 62, p. 905–909.

McKee, E.H., and John, D.A., 1987, Sample locality map and potassium-argon ages and data for Cenozoic igneous rocks in the Tonopah 1 by 2 quadrangle, central Nevada: U.S. Geological Survey Miscellaneous Field Studies Map, MF 1877-I.

Meeuwig, D., 1988, The Nevada Mineral Industry 1987: Nevada Bureau of Mines and Geology, Special Publication MI-1987, 54p.

Middlemost, E.A.K., 2006, Naming materials in the magma-igneous rock system: Earth-Science Reviews, v. 37, no. 1994, p. 215–224.

Muntean, J.L., Cline, J.S., Simon, A.C., and Longo, A.A., 2011, Magmatic–hydrothermal origin of Nevada's Carlin-type gold deposits: Nature Geoscience, v. 4, no. 2, p. 122–127.

Nash, T.J., 1994, Geochemical signatures of silver and gold deposits, Tonopah 1x2 degree quadrangle, Nevada-description and applications to exploration: U.S. Geological Survey Bulletin 2077, p. 46.

Nutt, C.J., and Hofstra, A.H., 2007, Bald Mountain gold mining district, Nevada: A Jurassic reduced intrusion-related gold system: Economic Geology, v. 102, no. 6, p. 1129–1155.

Oldow, J.S., 1984, Evolution of a Late Mesozoic Back-Arc Fold and Thrust Belt, Northwestern Great Basin, U.S.A.: Tectonophysics, v. 102, p. 245–274.

Oldow, J.S., and Bartel, R.L., 1987, Early to Middle (?) Jurassic extensional tectonism in the western Great Basin : Growth faulting and synorogenic deposition of the Dunlap Formation: Geology, v. 15, no. August, p. 740–743.

Pace, D.W., 2009, Relationship Between Magmatism and Mineralization in the RBM Gold Deposit, White Pine County, Nevada: University of Nevada Reno, 172p.

Paces, J.B., and Miller, J.D., 1993, Precise U-Pb Ages of Duluth Complex and Related Mafic Intrusions, Northeastern Minnesota: Geochronological Insights to Physical, Petrogenetic, and Tectonomagmatic Processes Associated With the 1.1 Ga Midcontinent Rift System: Journal of Geophysical Research, v. 98, no. B8, p. 13997–14013.

Robert, F., and Poulsen, K.H., 2001, Vein Formation and Deformation in Greenstone Gold Deposits: Reviews in Economic Geology vol. 14; Structural Controls on ore genesis, p. 111–155.

Silberling, N.J., 1959, Pre-Tertiary stratigraphy and Upper Triassic paleontology of the Union district, Shoshone Mountains, Nevada: Nevada: U.S. Geological Survey Professional Paper 332, p. 67.

Sillitoe, R.H., Lorson, R.C., 1994, Epithermal Gold-Silver-Mercury Deposits at Paradise Peak, Nevada: Ore Controls, Porphyry Gold Association, Detachment Faulting, and Supergene Oxidation: Economic Geology, v. 89, p. 1228–1248.

Slama, J., Kosler, J., Condon, D.J., Crowley, J.L., Gerdes, A., Hanchar, J.M., Horstwood, M.S.A., Morris, G.A., Nasdala, L., Norberg, N., Schaltegger, U., Schoene, B.,

Tubrett, M.N., and Whitehouse, M.J., 2008, Plesovice zircon - A new natural reference material for U-Pb and Hf isotopic microanalysis: Chemical Geology, v. 249, no. 1–2, p. 1–35.

Thompson, J.F.H., and Newberry, R.J., 2000, Gold deposits related to reduced granitic intrusions:in Hagemann, S.G., Brown, P.E., eds. Gold in 2000, Reviews in Economic Geology, v. 13, p. 377-400.

Thompson, J.F.H., Sillitoe, R.H., Baker, T., Lang, J.R., and Mortensen, J.K., 1999, Intrusion-related gold deposits associated with tungsten-tin provinces: Mineralium Deposita, v. 34, no. 4, p. 323–334.

Vikre, P.G., 1977, Geology and silver mineralization of the Rochester district, Pershing County, Nevada: Unpublished Ph.D. dissertation, Stanford University, 404 p.

Vikre, P.G., 1981, Silver mineralization in the Rochester district, Pershing County, Nevada: Economic Geology, v. 76, no. 3, p. 580–609.

Vikre, P.G., 2014, Magmatism, metasomatism, tectonism, and mineralization in the Humboldt Range, Pershing County, Nevada: Geological Society of Nevada 2014 Spring Field Trip Guidebook, spec. pub. no. 58, p. 179-204.

Vitaliano, C.J., 1963, Cenozoic geology and sections of the Ione quadrangle, Nye County, Nevada: U.S. Geological Survey Mineral Investigations Field Studies Map, MF-255, scale 1: 62,500.

Vitaliano, C.J., and Vitaliano, D.B., 1972, Cenozoic Volcanic Rocks in the Southern Shoshone Mountains and Paradise Range, Nevada: Geological Society of America Bulletin, v. 83, no. November, p. 3269–3280.

Weir, R.H., and Kerrick, D.M., 1987, Mineralogic, fluid inclusion, and stable isotope studies of several gold mines in the Mother Lode, Tuolumne and Mariposa Counties, California, USA: Economic Geology, v. 82, no. 2, p. 328–344.

Whitebread, D.H., Silberling, N.J., Brem, G.F., and Andrews, T.D., 1988, Preliminary Geologic Map of the Eastern Half of the Ione Quadrange, Nye County, Nevada: U.S. Geological Survey Open File Report 88-48, scale 1:62500.

Wiedenbeck, M., Hanchar, J.M., Peck, W.H., Sylvester, P., Valley, J., Whitehouse, M., Kronz, A., Morishita, Y., Nasdala, L., Fiebig, J., Franchi, I., Girard, J.P., Greenwood, R.C., Hinton, R., et al., 2004, Further characterization of the 91500 Zircon Crystal: Geostandards and Geoanalytical Research, v. 28, p. 9–39.

Wright, J.E., and Wooden, J.L., 1991, New Sr , Nd , and Pb isotopic data from plutons in the northern Great Basin : Implications for crustal structure and granite pedogenesis in the hinterland of the Sevier thrust belt: Geology, v. 19, no. May, p. 457–460.

Wyld, S.J., 2002, Structural evolution of a Mesozoic backarc fold-and-thrust belt in the U.S. Cordillera: New evidence from northern Nevada: GSA Bulletin, v. 114, no. 11, p. 1452–1468.

Wyld, S.J., Rogers, J.W., Wright, J.E., 2001, Structural evolution within the Luning-Fencemaker fold-thrust belt, Nevada: progression from back-arc basin closure to intra-arc shortening: Journal of Structural Geology, v. 23, p. 1971-1995.

Appendix A: Supplemental Material for Intrusive Rocks

Appendix A contains additional hand sample/thin section images, photomicrographs and SEM-BSE data/images for intrusive rocks.

Jd Jurassic Diorite

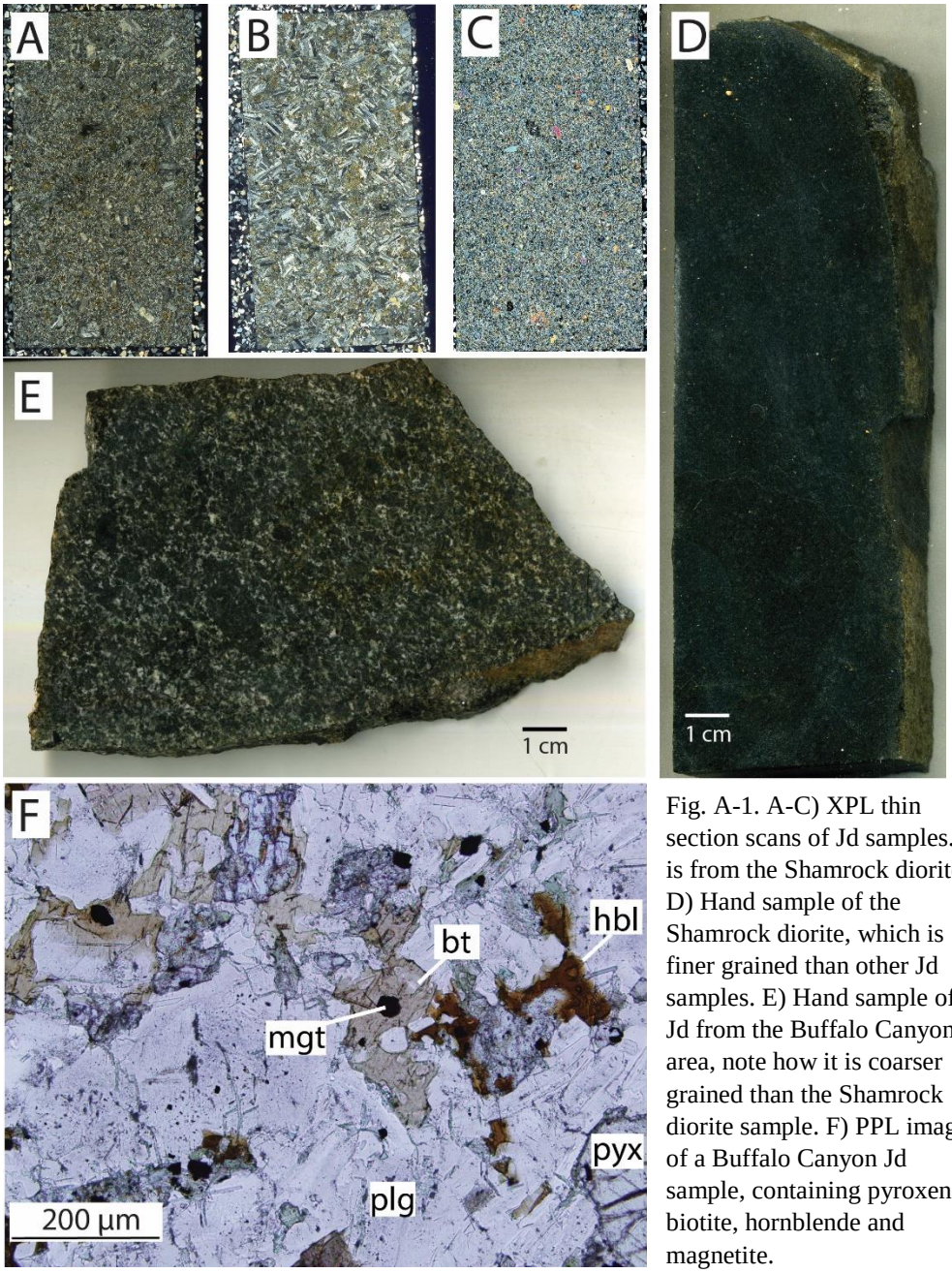

Fig. A-1. A-C) XPL thin section scans of Jd samples. C is from the Shamrock diorite. D) Hand sample of the Shamrock diorite, which is finer grained than other Jd samples. E) Hand sample of Jd from the Buffalo Canyon area, note how it is coarser grained than the Shamrock diorite sample. F) PPL image of a Buffalo Canyon Jd sample, containing pyroxene, biotite, hornblende and magnetite.

RBCPQ035 Pyroxene and biotite with actinolite alteration in Jd

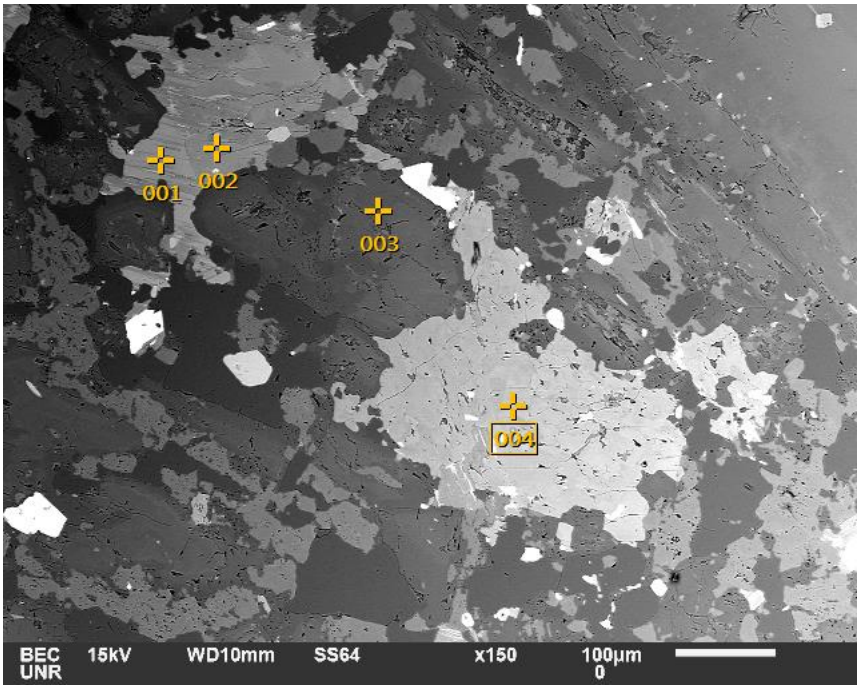

Volt : 15.00 kV
Mag. : x 150
Date : 2016/11/12
Pixel : 1280 x 960

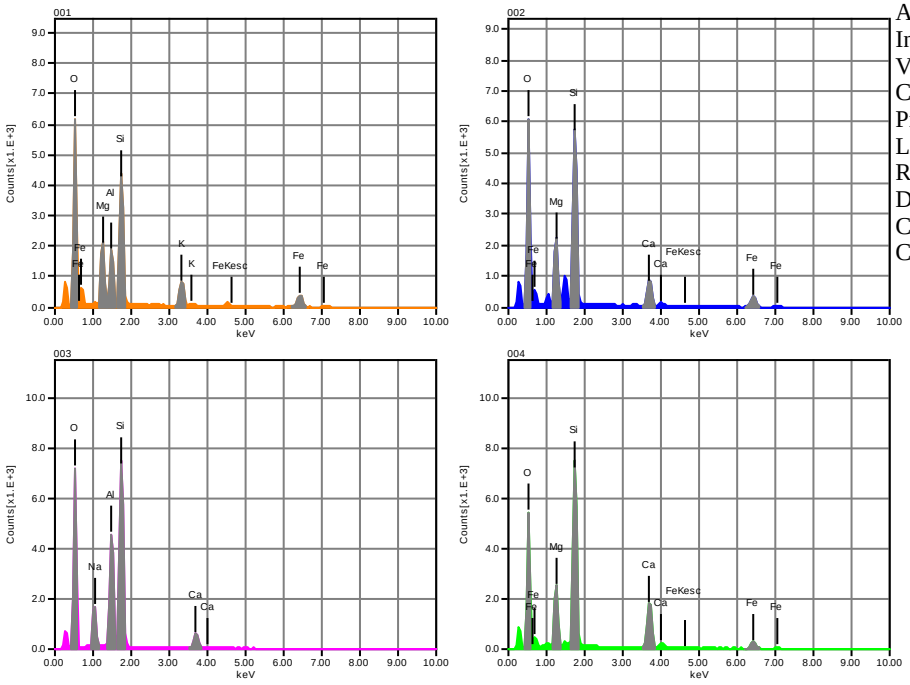

Acquisition Condition
Instrument : 6510(LA)
Volt : 15.00 kV
Current : ---
Process Time : T4
Live time : 11.46 sec.
Real Time : 15.00 sec.
DeadTime : 24.00 %
Count Rate : 17277.00 CPS

	CaO	O	Na2O	MgO	Al2O3	SiO2	K2O	FeO		Likely Mineral
001		0.00		15.83	14.37	41.79	8.96	19.04		Biotite
002	12.31	0.00		17.44		54.33		15.92		Actinolite
003	6.75	0.00	8.86		25.82	58.56				Andesine
004	21.28	0.00		15.32		53.02		10.39		Augite
Average	13.45	0.00	8.86	16.20	20.10	51.93	8.96	15.11		
Standard deviation	7.33	0.00	0.00	1.11	8.09	7.16	0.00		4.38	

RBCPQ035 Andesine plagioclase in Jd

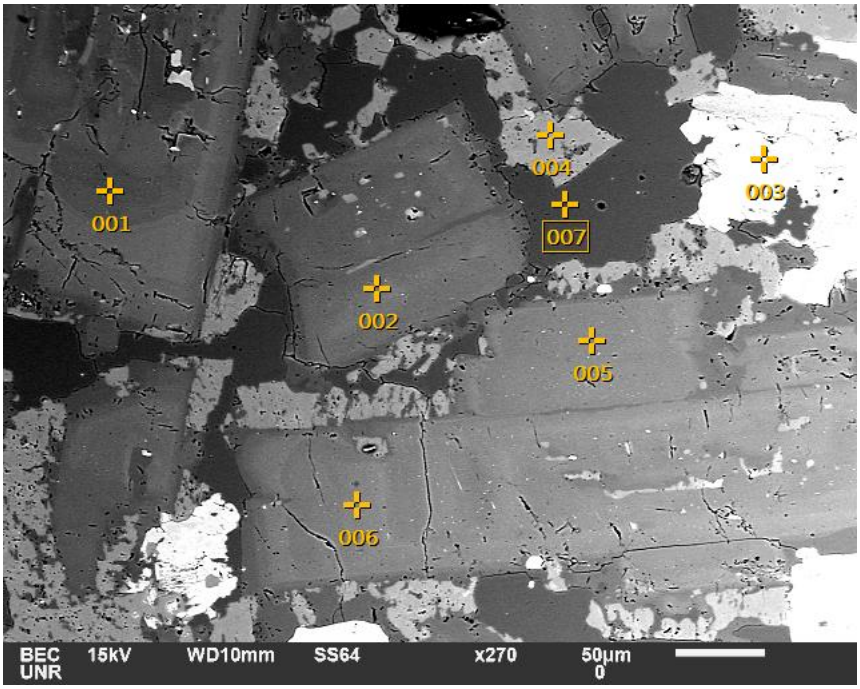

Volt : 15.00 kV
Mag. : x 270
Date : 2016/11/12
Pixel : 1280 x 960

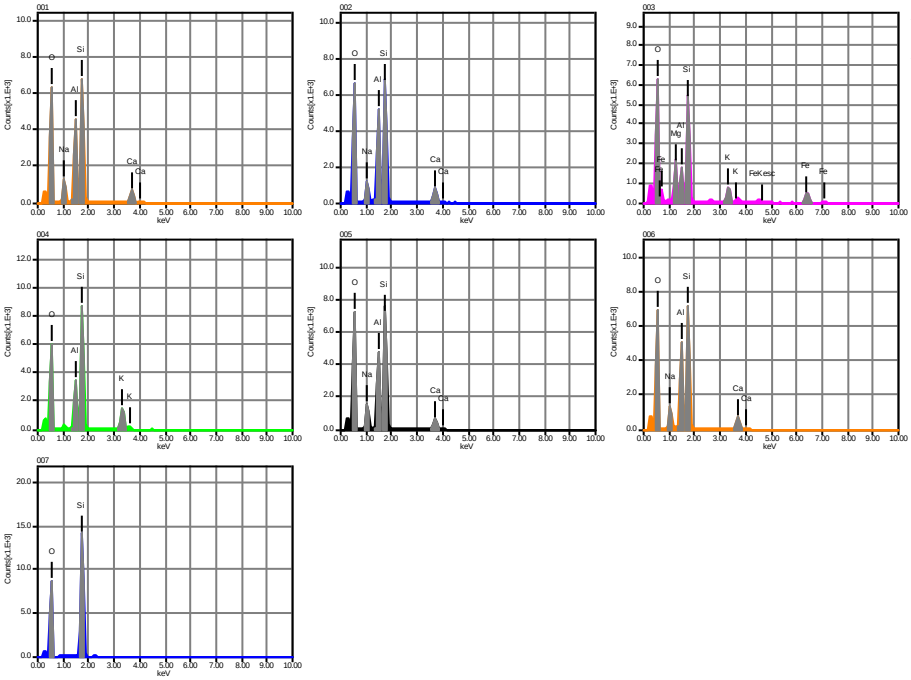

Acquisition Condition
Instrument : 6510(LA)
Volt : 15.00 kV
Current : ---
Process Time : T4
Live time : 11.08 sec.
Real Time : 15.00 sec.
DeadTime : 26.00 %
Count Rate : 19868.00 CPS

	CaO	O	Na2O	MgO	Al2O3	SiO2	K2O	FeO		Likely Mineral
001	9.25	0.00	7.06		27.91	55.78				Andesine
002	10.44	0.00	6.38		29.48	53.70				Andesine
003		0.00		14.61	11.97	46.03	7.64	19.74		Biotite
004		0.00			19.27	65.48	15.26			K-Feldspar
005	7.84	0.00	8.05		27.14	56.97				Andesine
006	8.94	0.00	7.12		28.30	55.65				Andesine
007		0.00				100.00				
Average	9.11	0.00	7.15	14.61	24.01	61.94	11.45	19.74		
Standard deviation	1.07	0.00	0.69	0.00	6.94	17.72	5.38	0.00		

RBCPQ035 Magnetite bearing Jd

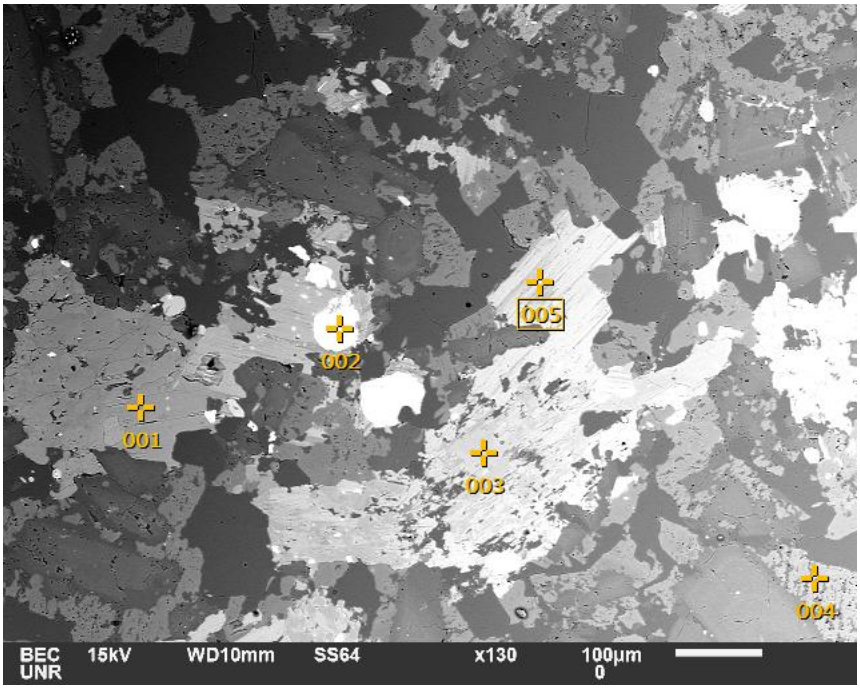

Volt : 15.00 kV
Mag. : x 130
Date : 2016/11/12
Pixel : 1280 x 960

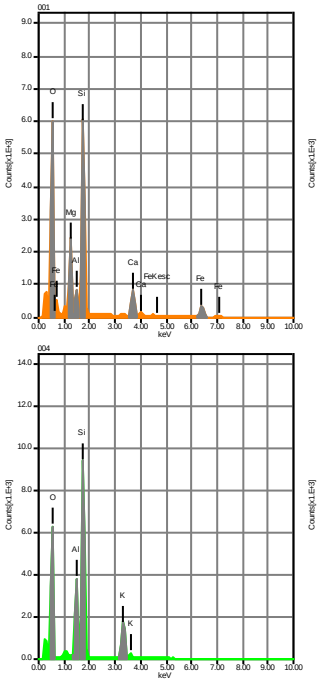

Acquisition Condition
Instrument : 6510(LA)
Volt : 15.00 kV
Current : ---
Process Time : T4
Live time : 11.66 sec.
Real Time : 15.00 sec.
DeadTime : 22.00 %
Count Rate : 16412.00 CPS

	CaO	O	MgO	Al2O3	SiO2	K2O	FeO		Likely Mineral
001	11.25	0.00	16.78	5.40	51.73		14.83		Actinolite?
002		0.00					100.00		Magnetite
003	11.46	0.00	17.19	6.30	51.48		13.56		Actinolite
004		0.00		19.26	64.80	15.94			K-Feldspar
005		0.00	19.04	16.25	37.93	1.47	25.31		Biotite
Average	11.36	0.00	17.67	11.80	51.49	8.70	38.43		
Standard deviation	0.15	0.00	1.21	6.99	10.97	10.23		41.38	

Jgd: Jurassic Granodiorite

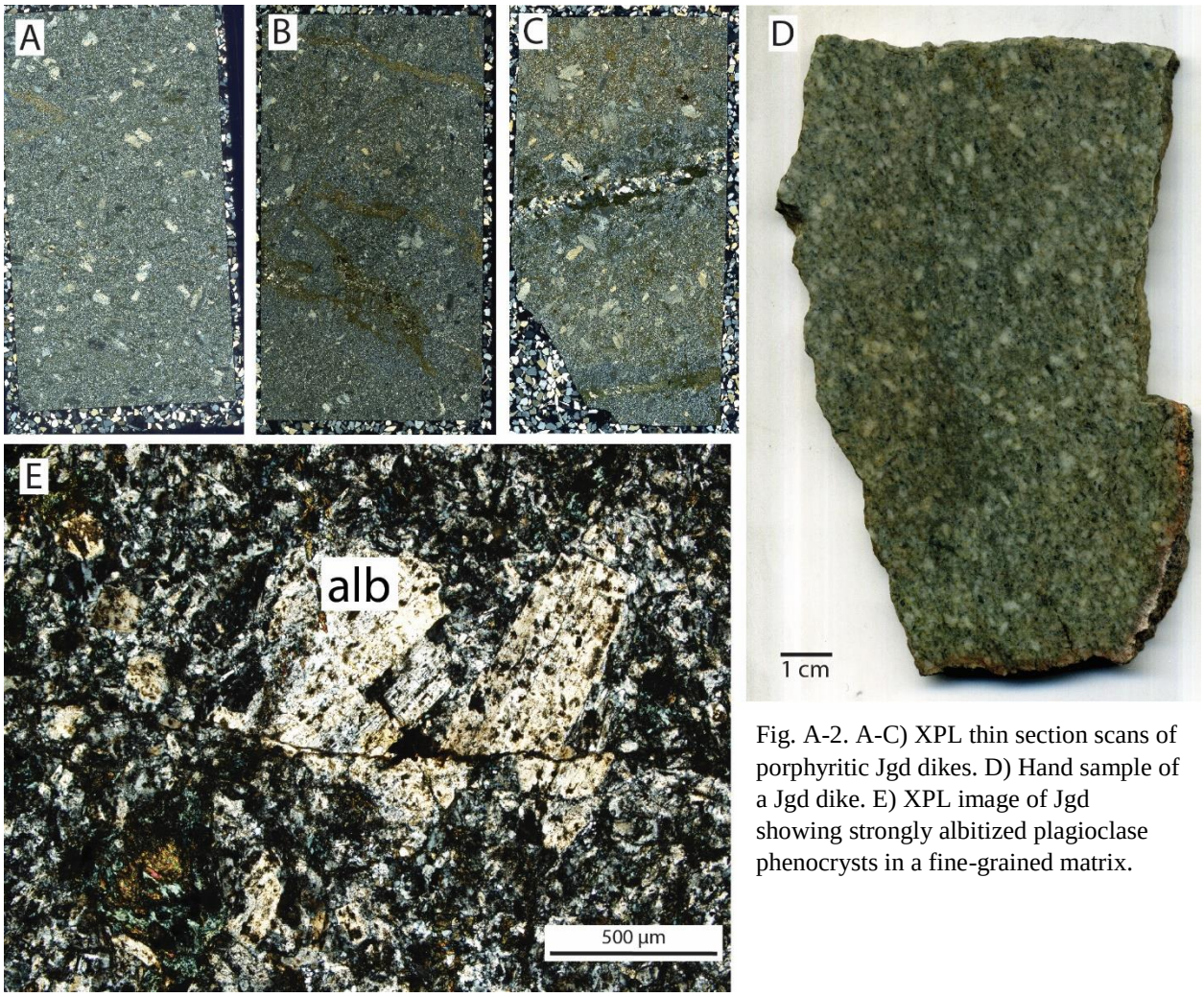

Fig. A-2. A-C) XPL thin section scans of porphyritic Jgd dikes. D) Hand sample of a Jgd dike. E) XPL image of Jgd showing strongly albitized plagioclase phenocrysts in a fine-grained matrix.

RBCPQ014D K-feldspar altering to albite in Jgd

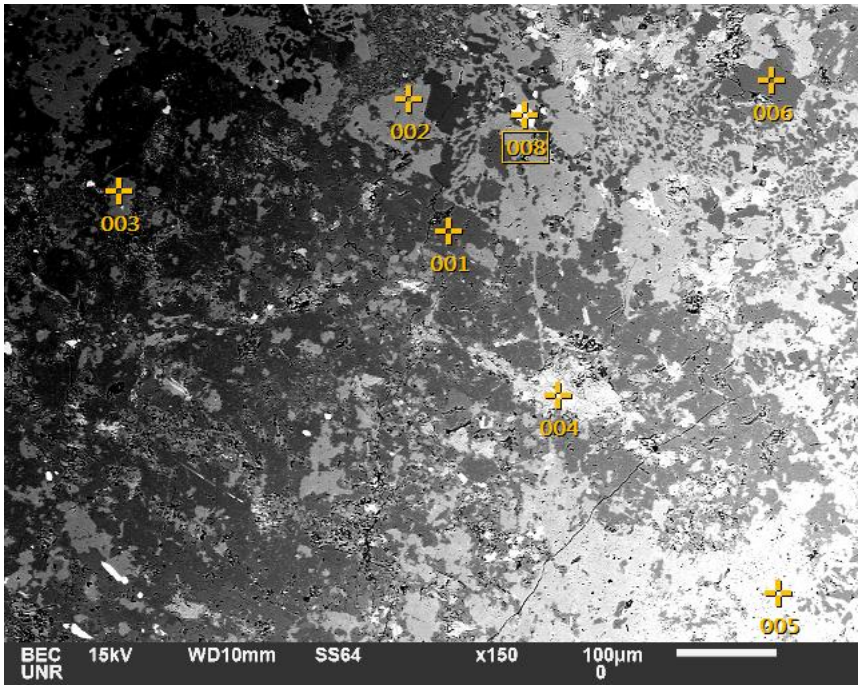

Volt : 15.00 kV
Mag. : x 150
Date : 2016/11/12
Pixel : 1280 x 960

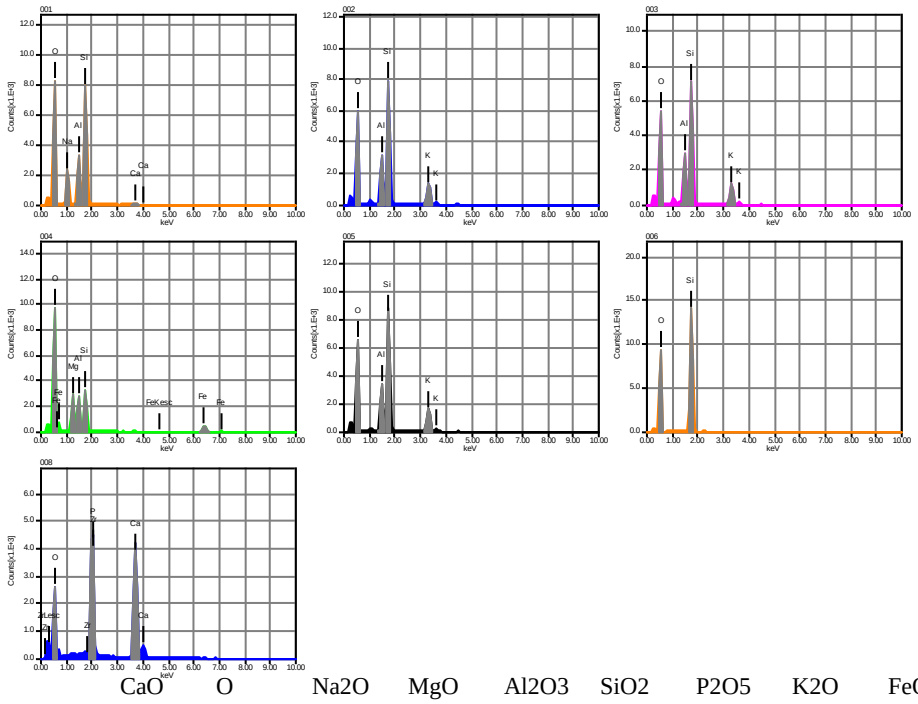

Acquisition Condition
Instrument : 6510(LA)
Volt : 15.00 kV
Current : ---
Process Time : T4
Live time : 12.00 sec.
Real Time : 15.00 sec.
DeadTime : 20.00 %
Count Rate : 14135.00 CPS

	CaO	O	Na2O	MgO	Al2O3	SiO2	P2O5	K2O	FeO	ZrO2	Likely Mineral
001	0.94	0.00	13.05		20.60	65.40					Albite
002		0.00			19.82	65.27		14.91			K-Feldspar
003		0.00			19.85	65.40		14.75			K-Feldspar
004		0.00		21.89	23.19	34.16			20.75		Chlorite?
005		0.00			19.62	64.57		15.81			K-Feldspar
008	46.52	0.00					40.67			12.81	Apatite
Average	23.73	0.00	13.05	21.89	20.62	58.96	40.67	15.16	20.75	12.81	
Standard deviation	32.23	0.00	0.00	0.00	1.49	13.87	0.00	0.57	0.00	0.00	

Kmd: Cretaceous Monzodiorite

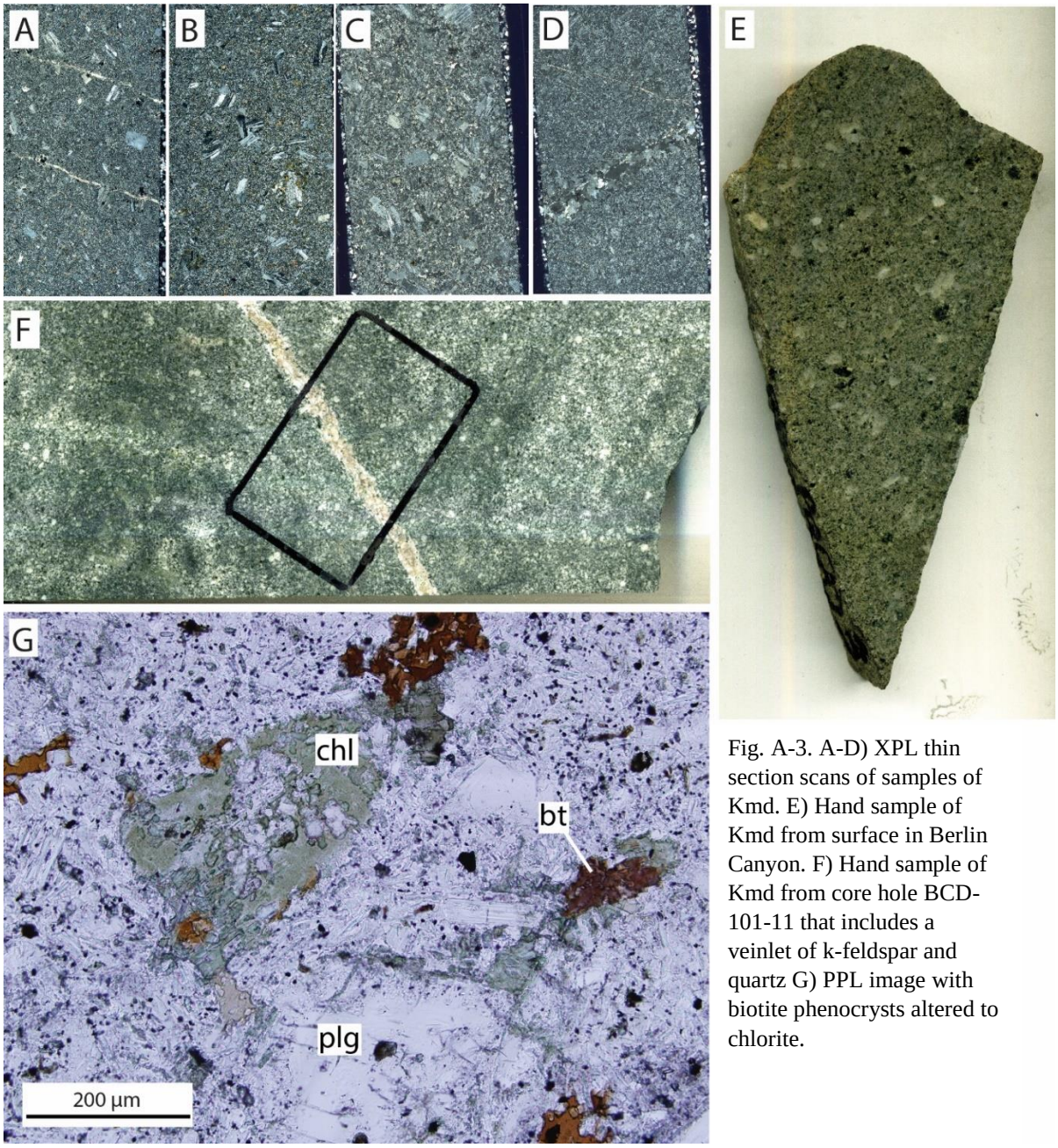

Fig. A-3. A-D) XPL thin section scans of samples of Kmd. E) Hand sample of Kmd from surface in Berlin Canyon. F) Hand sample of Kmd from core hole BCD-101-11 that includes a veinlet of k-feldspar and quartz G) PPL image with biotite phenocrysts altered to chlorite.

Klg: Cretaceous Leucogranite

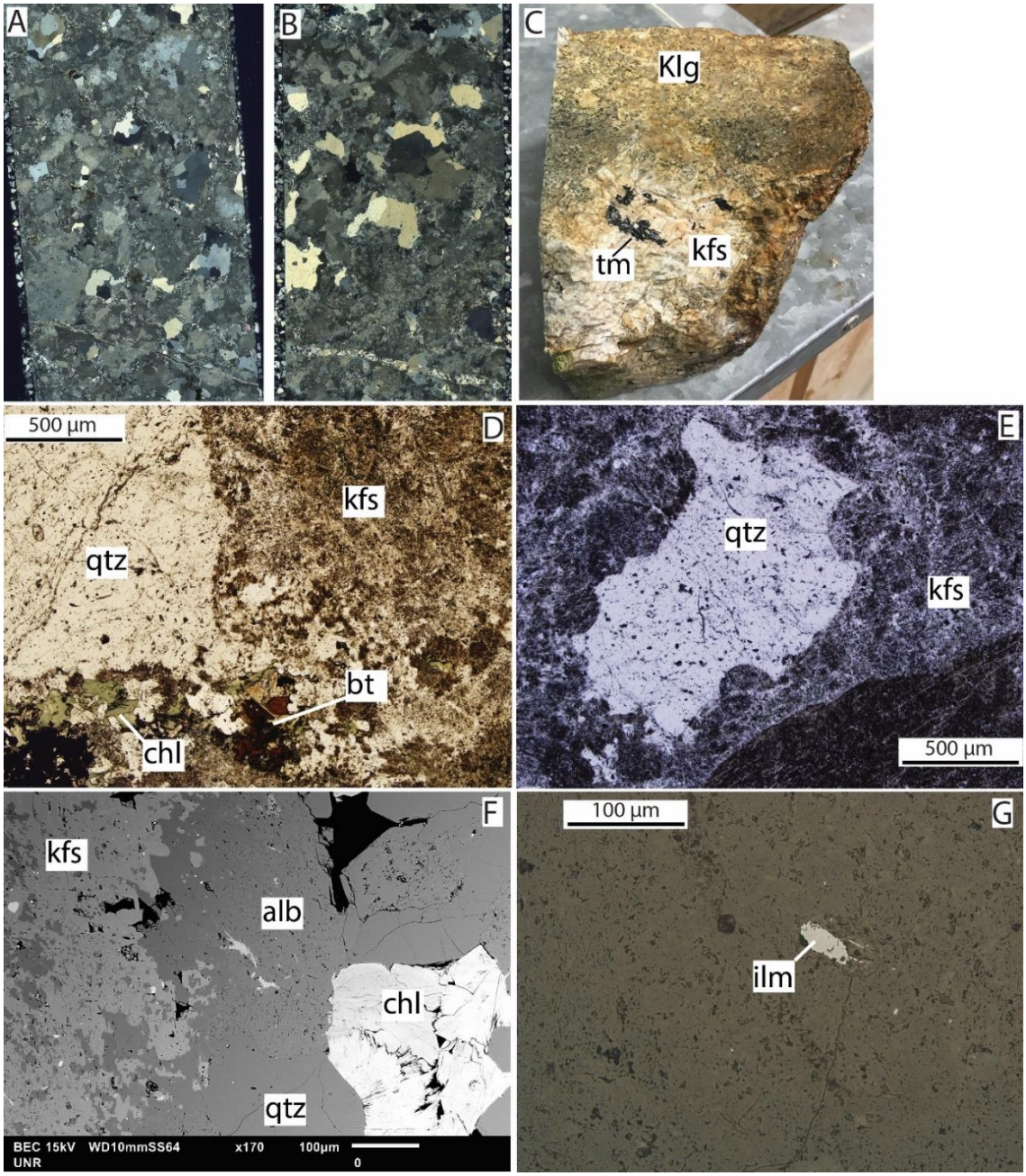

Fig. A-4. A-B) XPL thin section scans for samples of Klg. C) Sample of pegmatitic Klg containing a large, several cm wide, crystal of k-feldspar with tourmaline. D) PPl image of a large, resorbed, quartz eye surrounded by k-feldspar and with biotite partially altered to chlorite. E) PPl photomicrograph of a resorbed quartz grain. F) SEM image of chlorite surrounded by quartz and albite, surrounded by k-feldspar. G) Reflected light image of an ilmenite grain in a sample of Klg.

RBCPQ021A Typical Klg mineralogy

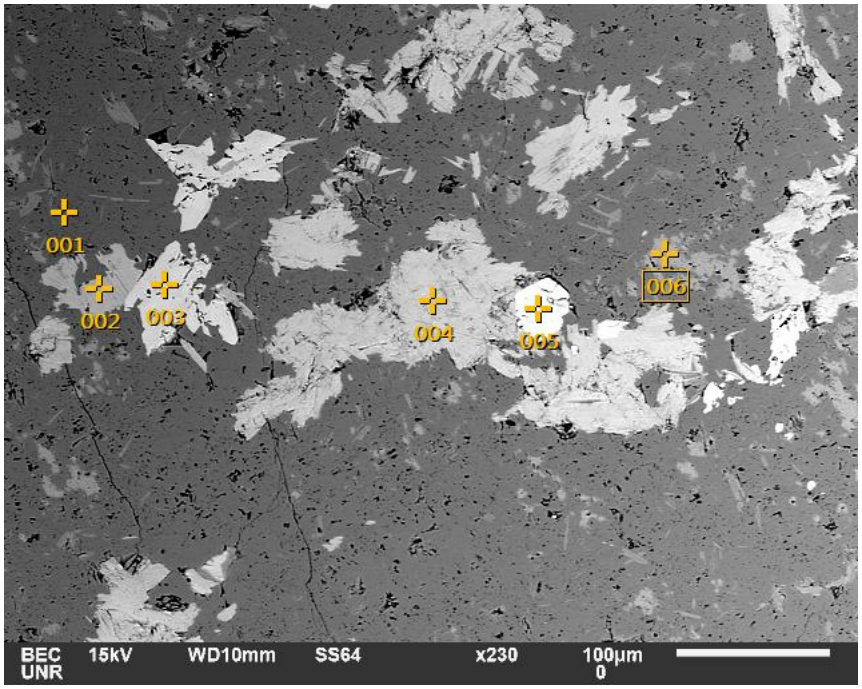

Volt : 15.00 kV
Mag. : x 230
Date : 2016/11/12
Pixel : 1280 x 960

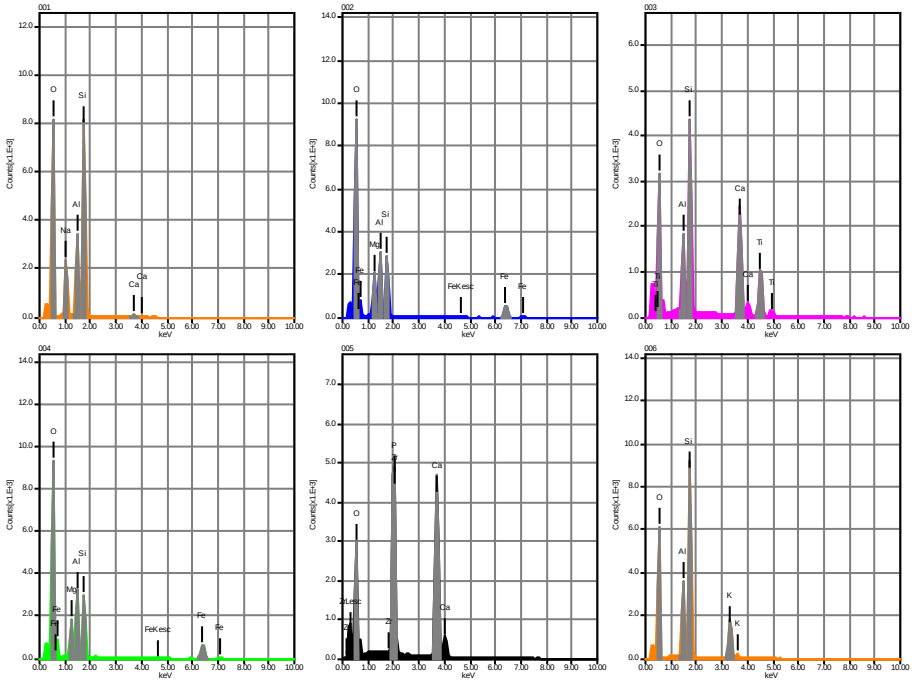

Acquisition Condition
Instrument : 6510(LA)
Volt : 15.00 kV
Current : ---
Process Time : T4
Live time : 11.16 sec.
Real Time : 15.00 sec.
DeadTime : 25.00 %
Count Rate : 18995.00 CPS

	CaO	O	Na2O	MgO	Al2O3	SiO2	P2O5	K2O	TiO2	FeO	ZrO2	Likely Mineral
001	1.15	0.00	12.93		20.84	65.08						Albite
002		0.00		16.88	26.13	30.15				26.84		Chlorite
003	29.82	0.00			10.80	33.53			25.86			Titanite
004		0.00		14.39	25.61	29.99				30.01		Chlorite
005	46.31	0.00					40.12				13.57	Apatite
006		0.00			19.11	64.39		16.51				K-feldspar
Average	25.76	0.00	12.93	15.63	20.50	44.63	40.12	16.51	25.86	28.42	13.57	
Standard deviation	22.85	0.00	0.00	1.76	6.20	18.41	0.00	0.00	0.00	2.24	0.00	

RBCPQ021A Abundant zircon, apatite and allanite in groundmass of Klg

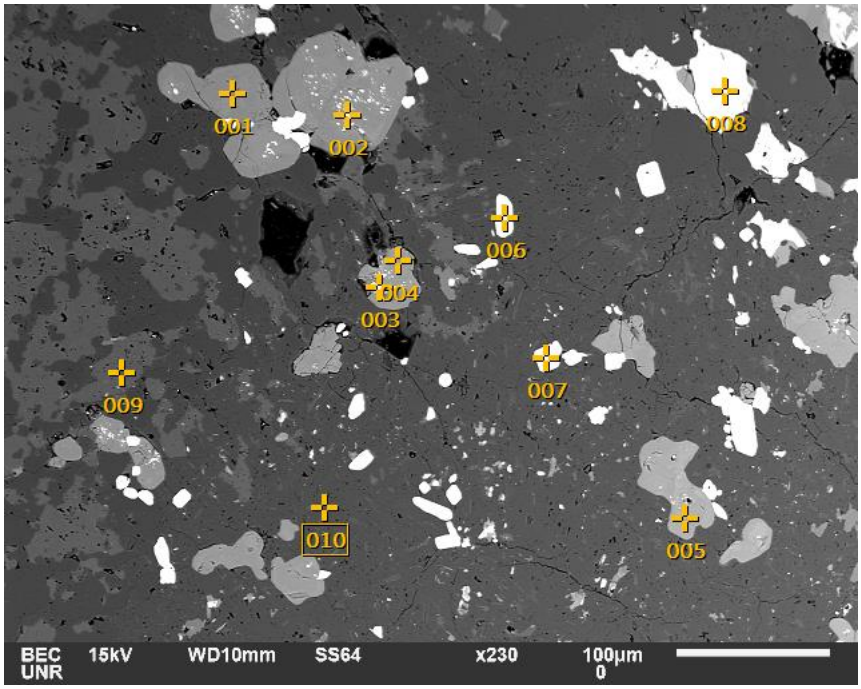

Volt : 15.00 kV
Mag. : x 230
Date : 2016/11/12
Pixel : 1280 x 960

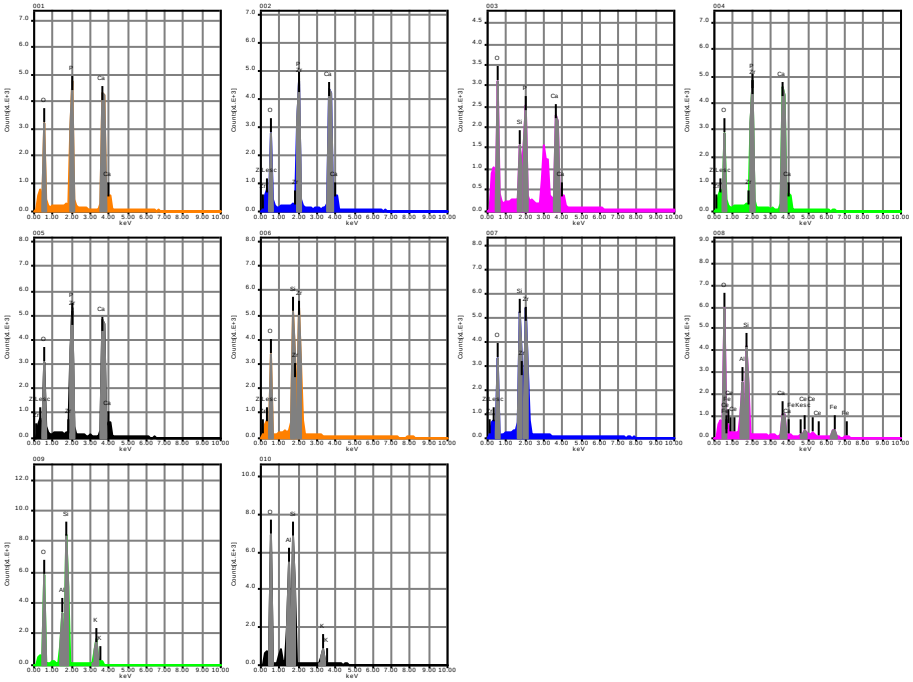

Acquisition Condition
Instrument : 6510(LA)
Volt : 15.00 kV
Current : ---
Process Time : T4
Live time : 11.45 sec.
Real Time : 15.00 sec.
DeadTime : 24.00 %
Count Rate : 17971.00 CPS

	CaO	O	Al2O3	SiO2	P2O5	K2O	FeO	ZrO2	CeO2	Likely Mineral
001	50.55	0.00			49.45					Apatite
002	46.82	0.00			40.12			13.06		Apatite
003	42.48	0.00		14.52	43.00					Apatite
006		0.00		29.70				70.30		Zircon
007		0.00		29.45				70.55		Zircon
008	14.04	0.00	18.78	38.16			16.06		12.96	Allanite
009		0.00	19.09	64.78		16.14				K-feldspar
010		0.00	33.05	58.38		8.57				K-feldspar
Average	41.18	0.00	23.64	39.16	42.51	12.35	16.06	36.15	12.96	
Standard deviation	13.54	0.00	8.15	19.07	4.09	5.35	0.00	31.29	0.00	

Tqmd: Tertiary Quartz Monzodiorite and Tqm: Tertiary Quartz Monzonite

Tqmd

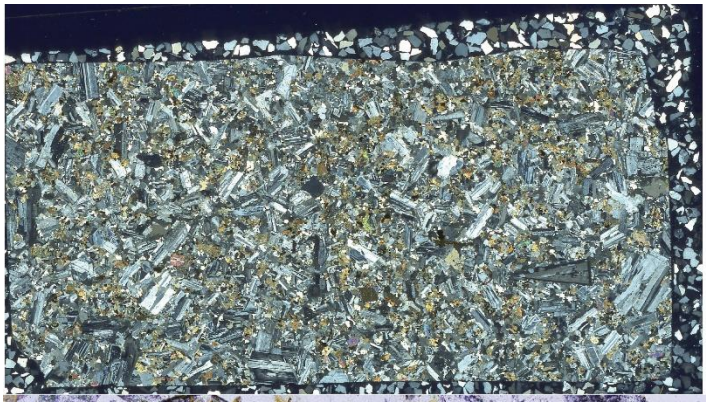

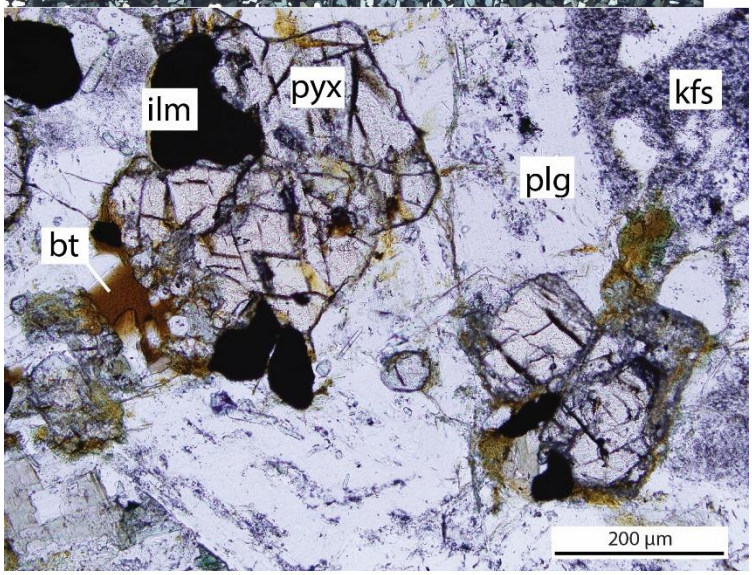

Fig. A-5. XPL thin section scan and PPL image of a sample of Tqmd. Photomicrograph shows pyroxene, ilmenite and biotite as common mafic minerals hosted in a plagioclase with lesser k-feldspar matrix.

Tqm

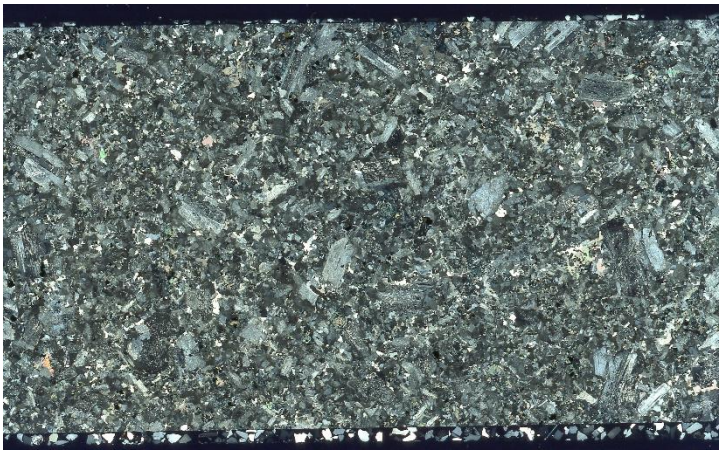

Fig. A-6. XPL thin section scan of a sample of Tqm

RBCPQ113 Ilmenite, pigeonite bearing quartz monzodiorite (Tqmd)

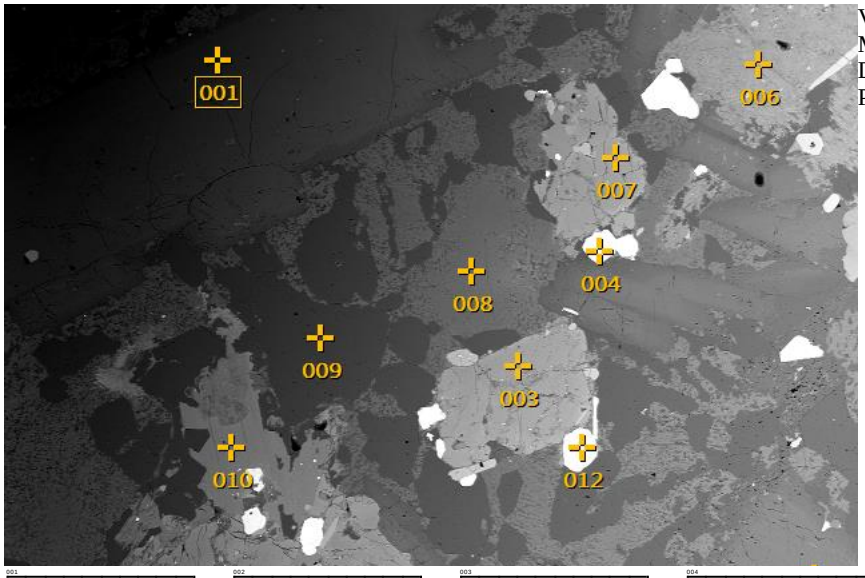

Volt : 15.00 kV
Mag. : x 70
Date : 2016/11/19
Pixel : 1280 x 960

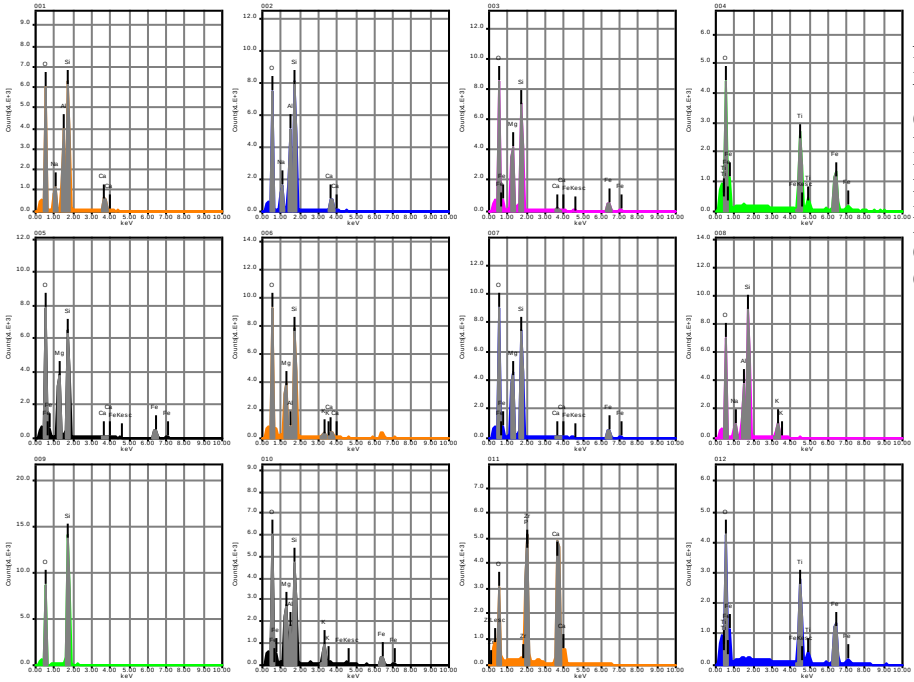

Acquisition Condition
Instrument : 6510(LA)
Volt : 15.00 kV
Current : ---
Process Time : T4
Live time : 12.07 sec.
Real Time : 15.00 sec.
DeadTime : 20.00 %
Count Rate : 14460.00 CPS

	CaO	O	Na2O	MgO	Al2O3	SiO2	P2O5	K2O	TiO2	FeO	ZrO2	Likely Mineral
001	8.56	0.00	7.42		26.81	57.21						Andesine
003	1.64	0.00		26.13		52.79				19.43		Pigeonite
004		0.00							52.99	47.01		Ilmenite
006	4.51	0.00		24.23	5.16	63.38		2.72				unknown clay?
007	1.27	0.00		26.40		53.61				18.72		Pigeonite
008		0.00	4.83		19.78	65.10		10.29				Alkali Feldspar
009		0.00				100.00						Quartz
010		0.00		18.76	13.24	42.68		10.29		15.01		Biotite
012		0.00							52.67	47.33		Ilmenite
Average	10.26	0.00	6.58	24.41	18.37	60.61	39.38	7.77	52.83	27.68	14.58	
Standard deviation		16.07	0.00	1.52	3.29	9.30	16.15	0.00	4.37	0.23	15.17	0.00

RBCPQ113 Hornblende, alkali feldspar, ilmenite, pigeonite apatite bearing (Tmqd)

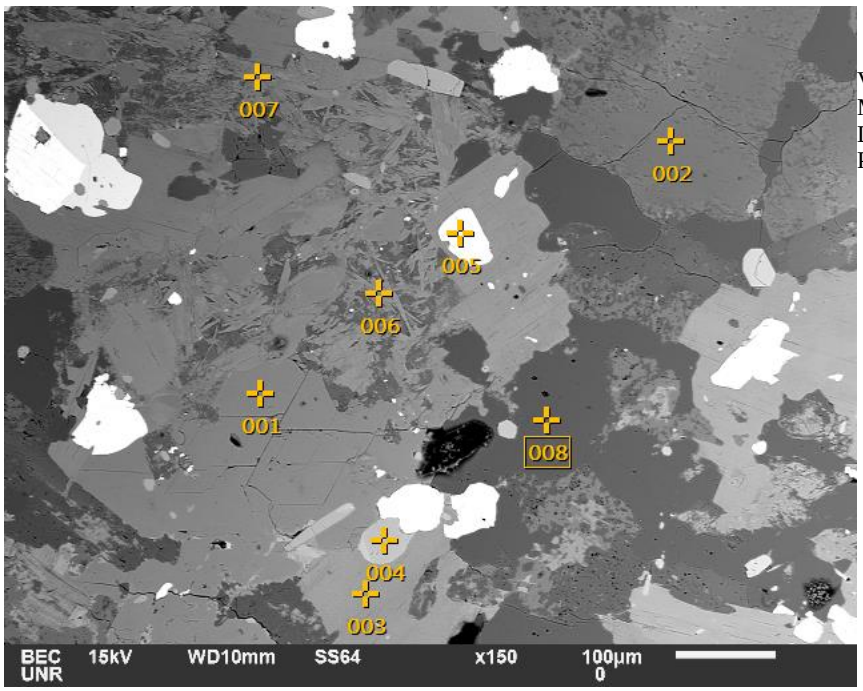

Volt : 15.00 kV
Mag. : x 150
Date : 2016/11/19
Pixel : 1280 x 960

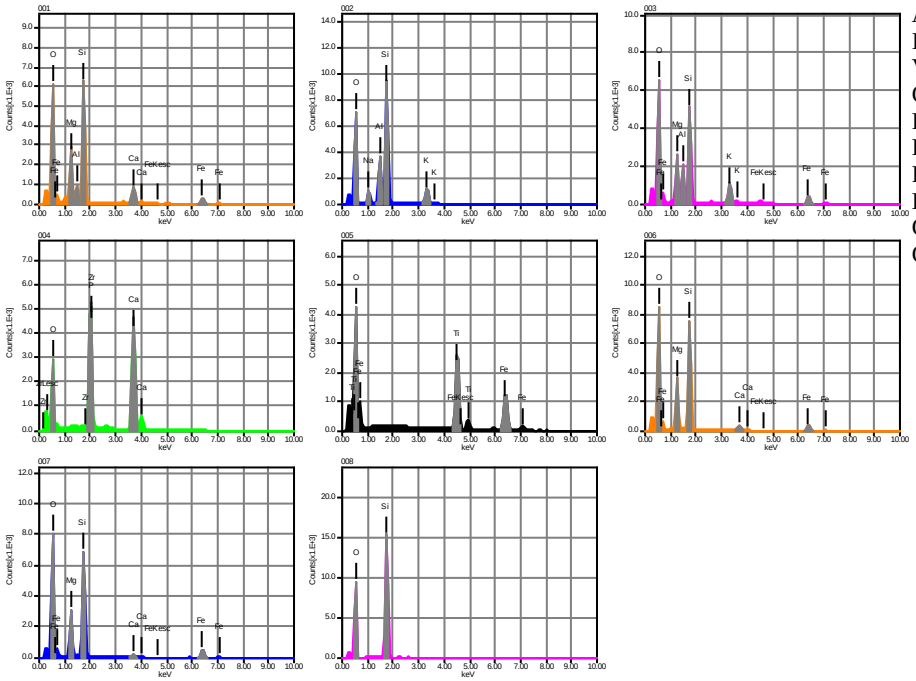

Acquisition Condition
Instrument : 6510(LA)
Volt : 15.00 kV
Current : ---
Process Time : T4
Live time : 10.78 sec.
Real Time : 15.00 sec.
DeadTime : 28.00 %
Count Rate : 21486.00 CPS

	CaO	O	Na2O	MgO	Al2O3	SiO2	P2O5	K2O	TiO2	FeO	ZrO2	Likely Mineral
001	11.21	0.00		18.68	6.05	51.31				12.75		Hornblende?
002		0.00	4.75		19.23	65.09		10.93				Alkali Feldspar
003		0.00		16.93	13.81	42.26		9.97		17.03		Biotite
004	45.67	0.00					39.51				14.82	Apatite
005		0.00							53.59	46.41		Ilmenite
006	4.78	0.00		23.59		57.88				13.74		Pigeonite
007	2.26	0.00		21.58		56.95				19.22		Pigeonite
008		0.00				100.00						Quartz
Average	15.98	0.00	4.75	20.19	13.03	62.25	39.51	10.45	53.59	21.83	14.82	
Standard deviation	20.15	0.00	0.00	2.97	6.63	20.00	0.00	0.68	0.00	13.98	0.00	

Td: Tertiary Dacite

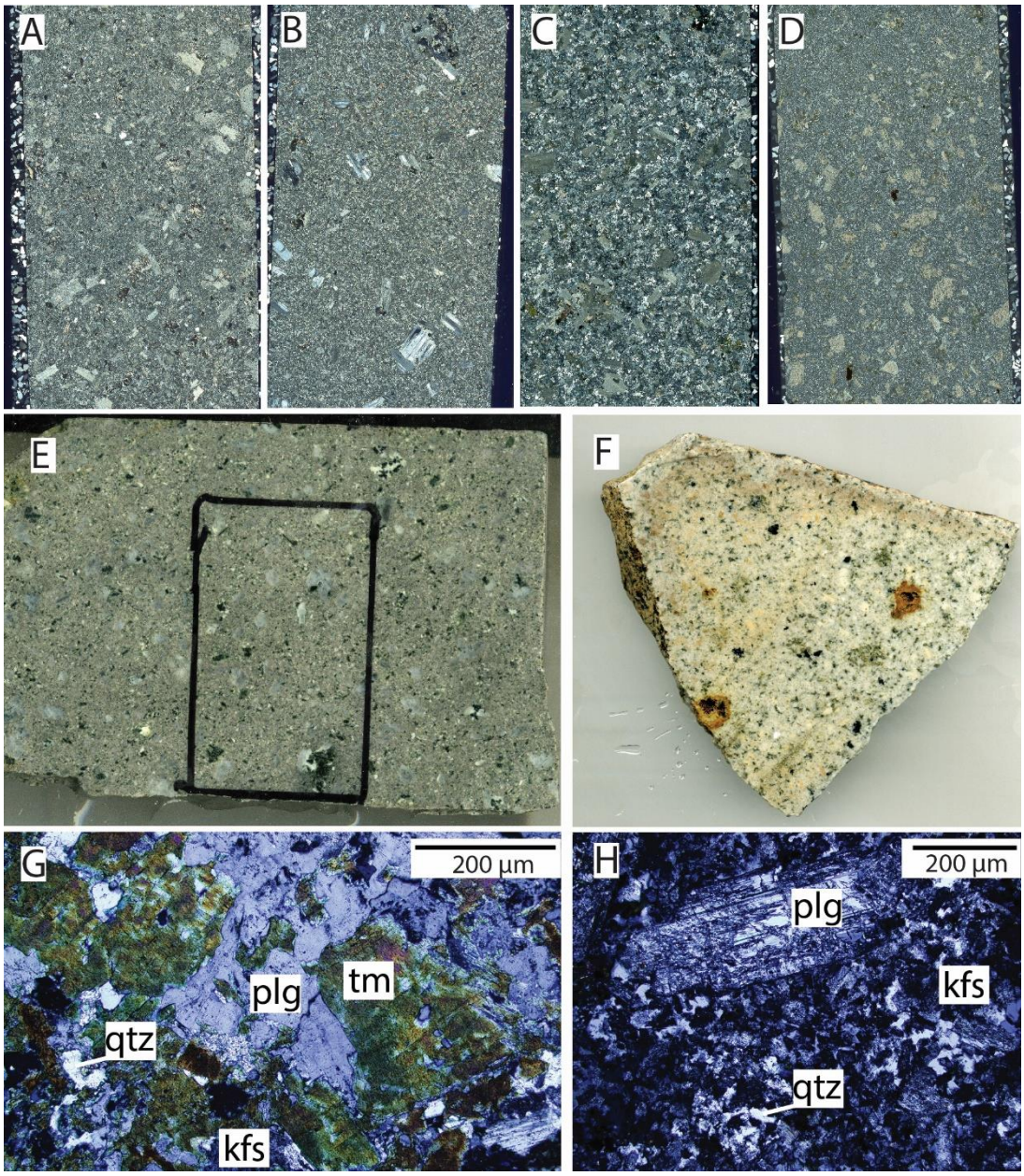

Fig. A-7. A-D) XPL thin section scans for samples of Td. C represents an altered version with strong sericitic-quartz alteration. E) Hand sample of Td from core hole BCD-101-11, corresponds to thin section from B. F) Hand sample of Td from Buffalo Canyon, containing small dark tourmaline clots. G) XPL image of Td containing magmatic tourmaline. H) XPL image of Td with fragmented plagioclase phenocrysts.

Tg-Tlg: Tertiary Granite/Tertiary Leucogranite

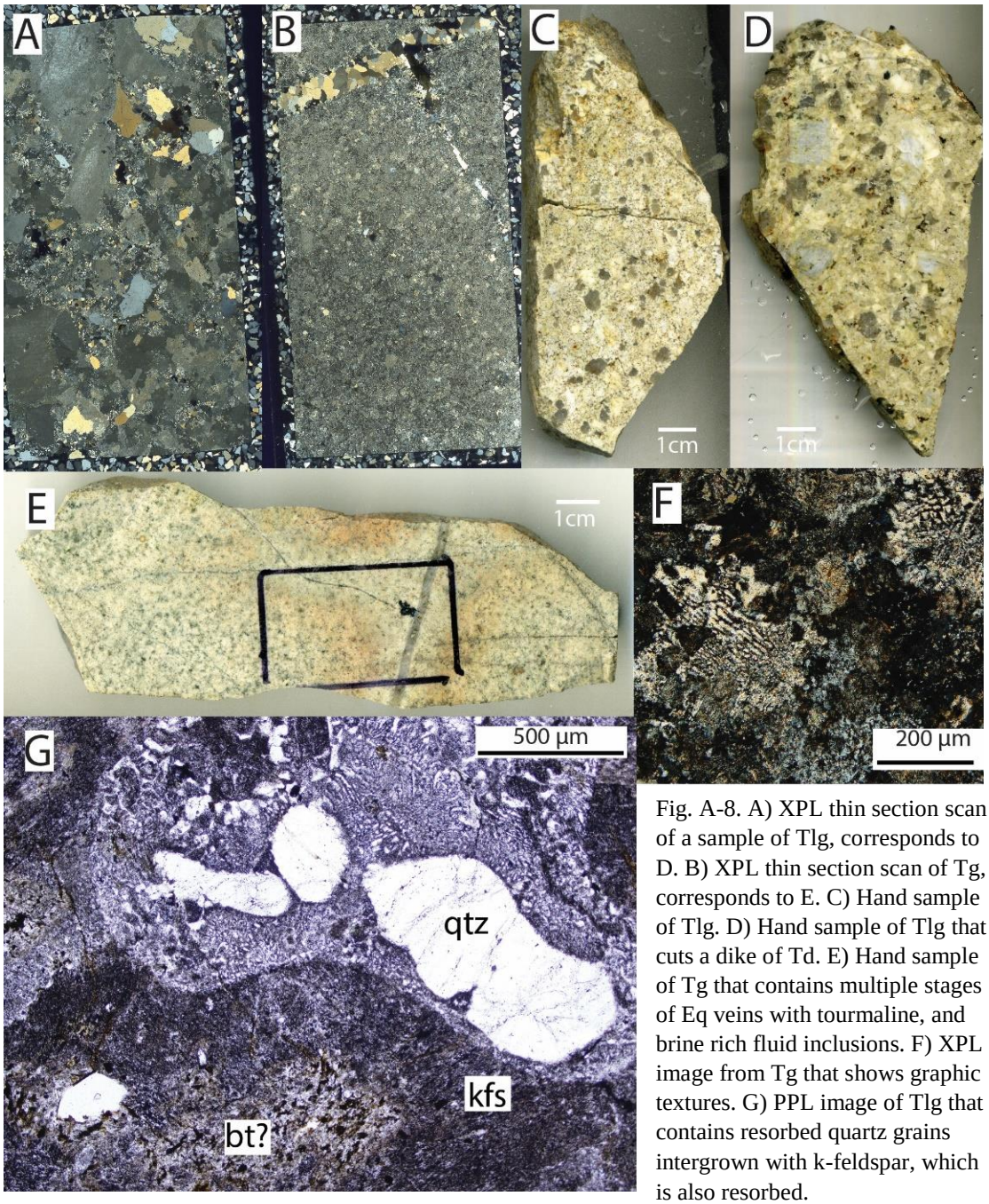

Fig. A-8. A) XPL thin section scan of a sample of Tlg, corresponds to D. B) XPL thin section scan of Tg, corresponds to E. C) Hand sample of Tlg. D) Hand sample of Tlg that cuts a dike of Td. E) Hand sample of Tg that contains multiple stages of Eq veins with tourmaline, and brine rich fluid inclusions. F) XPL image from Tg that shows graphic textures. G) PPL image of Tlg that contains resorbed quartz grains intergrown with k-feldspar, which is also resorbed.

RBCPQ054B Tertiary leucogranite with graphic textures (Tlg)

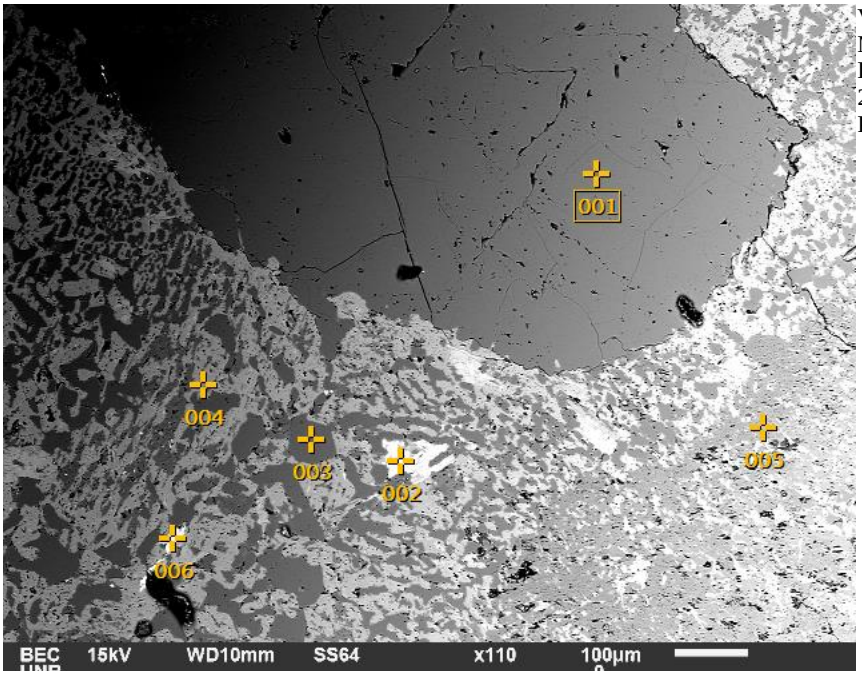

Volt : 15.00 kV
Mag. : x 110
Date : 2016/11/19
Pixel : 1280 x 960

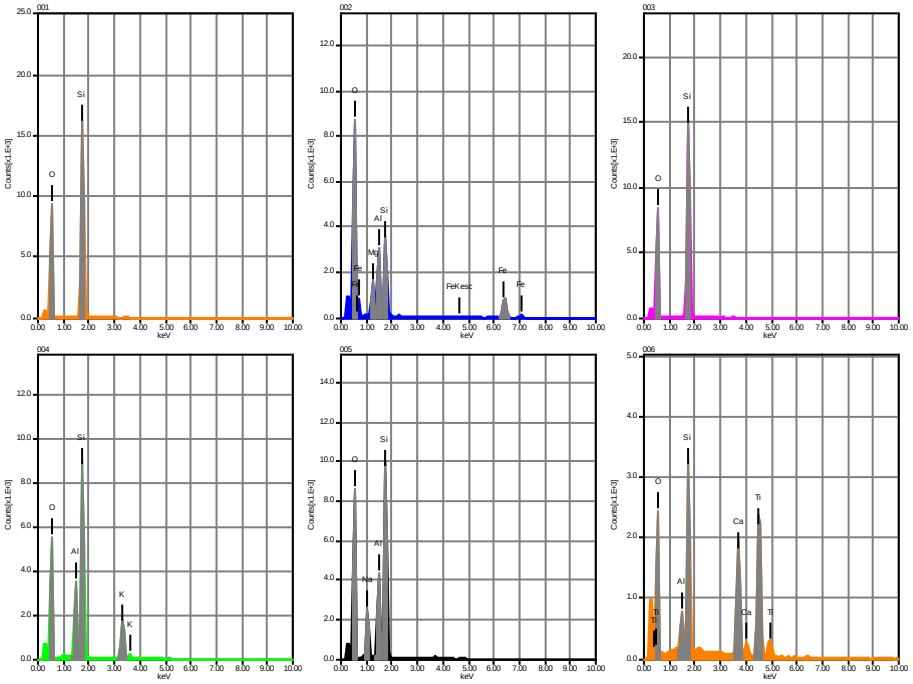

Acquisition Condition
Instrument : 6510(LA)
Volt : 15.00 kV
Current : ---
Process Time : T4
Live time : 10.63 sec.
Real Time : 15.00 sec.
DeadTime : 29.00 %
Count Rate : 22326.00 CPS

	CaO	O	Na2O	MgO	Al2O3	SiO2	K2O	TiO2	FeO	Likely Mineral
001		0.00				100.00				Quartz
002		0.00		11.60	22.77	31.96			33.67	Chlorite
003		0.00				100.00				Quartz
004		0.00			18.99	64.16	16.84			K-feldspar
005		0.00	11.61		21.83	66.56				Albite
006	21.43	0.00			3.96	23.34		51.27		Titanite
Average	21.43	0.00	11.61	11.60	16.89	64.34	16.84	51.27	33.67	
Standard deviation		0.00	0.00	0.00	0.00	8.77	32.49	0.00	0.00	0.00

Tba: Tertiary Basaltic Andesite

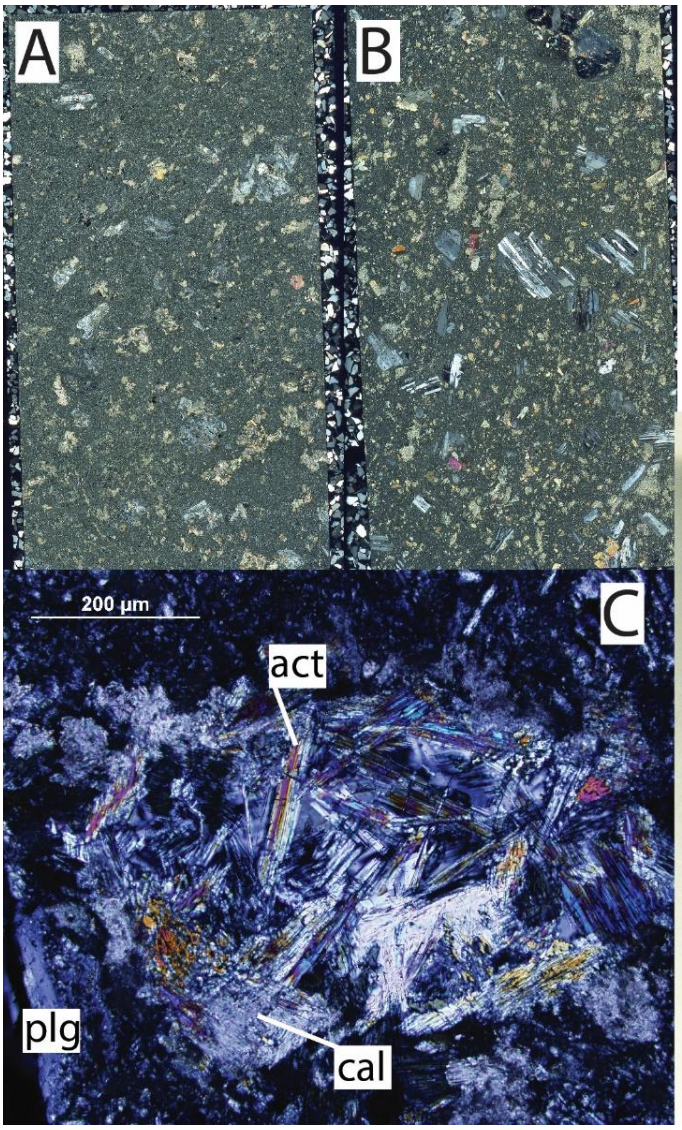

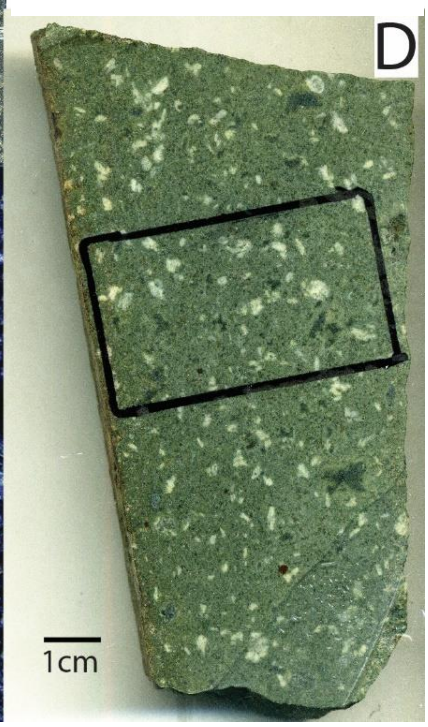

Fig. A-9. A-B) XPL thin section scans of Tba samples, pyroxene is mostly altered (tan calcite patches). C) XPL image of a relict pyroxene grained altered to actinolite and calcite. D) Hand sample of Tba that corresponds to A.

Appendix B: Supplemental Material for Alteration and Mineralization

Appendix contains additional field photos, thin section scans, hand samples images, photomicrographs and SEM-BSE data for altered and mineralized samples. Styles are listed from interpreted youngest to oldest, except for epithermal overprint images, which are at the end.

Everson quartz (Eq) veins

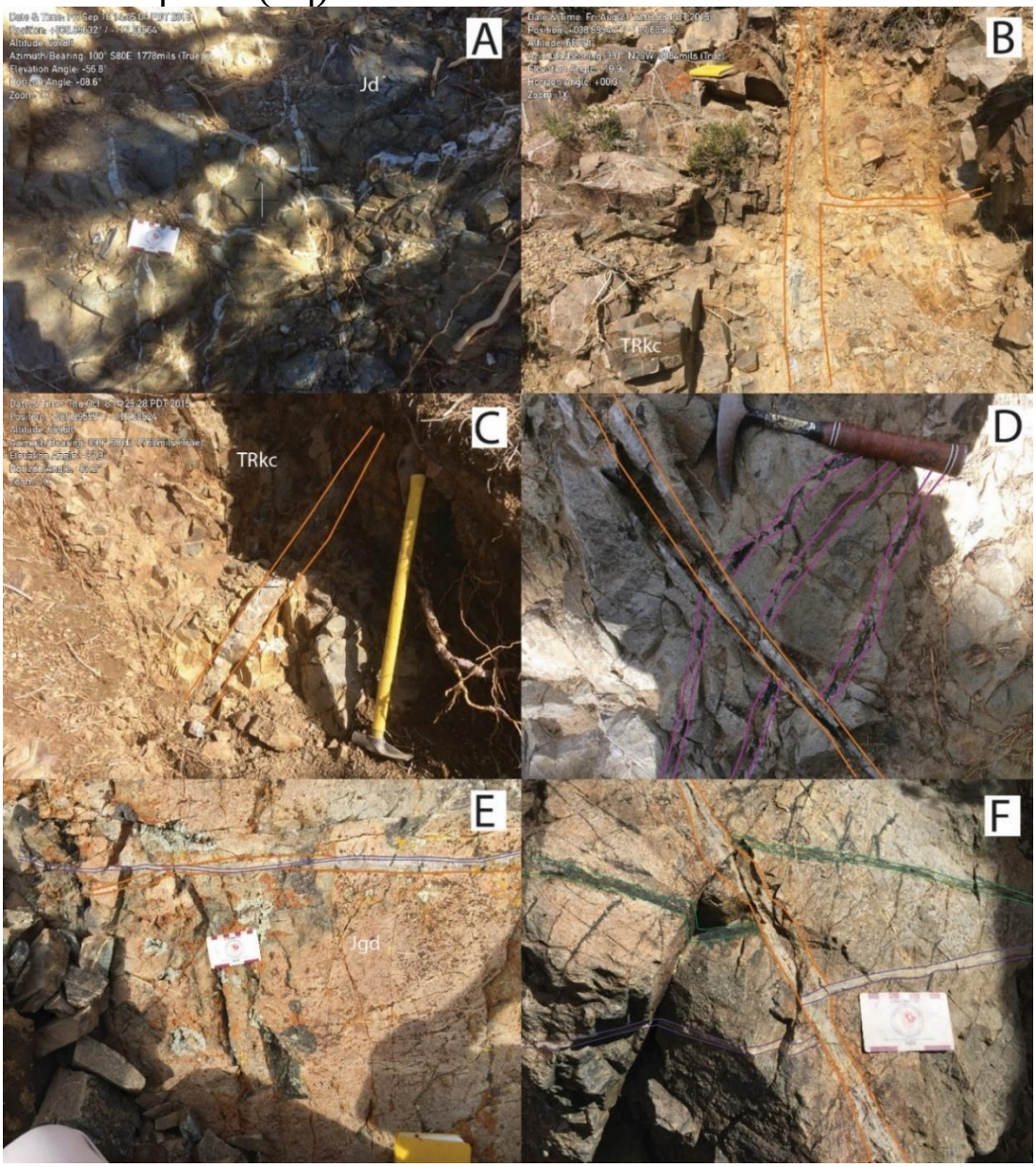

Fig. B-1. Field photos of Eq veins. A) Eq veins hosted in Jd that have a more stockwork style of veining. B) Thick 10cm, sheeted style of Eq veins outlined in orange, with smaller stockwork veinst. C) 8cm thick Eq vein hosted in TRkc. D) Eq vein (orange) cutting several Tbm veins (purple). E) Two stages of Eq veins hosted in Jgd, with a thinner, wavy Eq vein (blue) cutting an earlier thicker Eq vein (orange). F) Eq vein (orange) cutting an earlier Eq vein (blue), which also cuts a Sc vein (green).

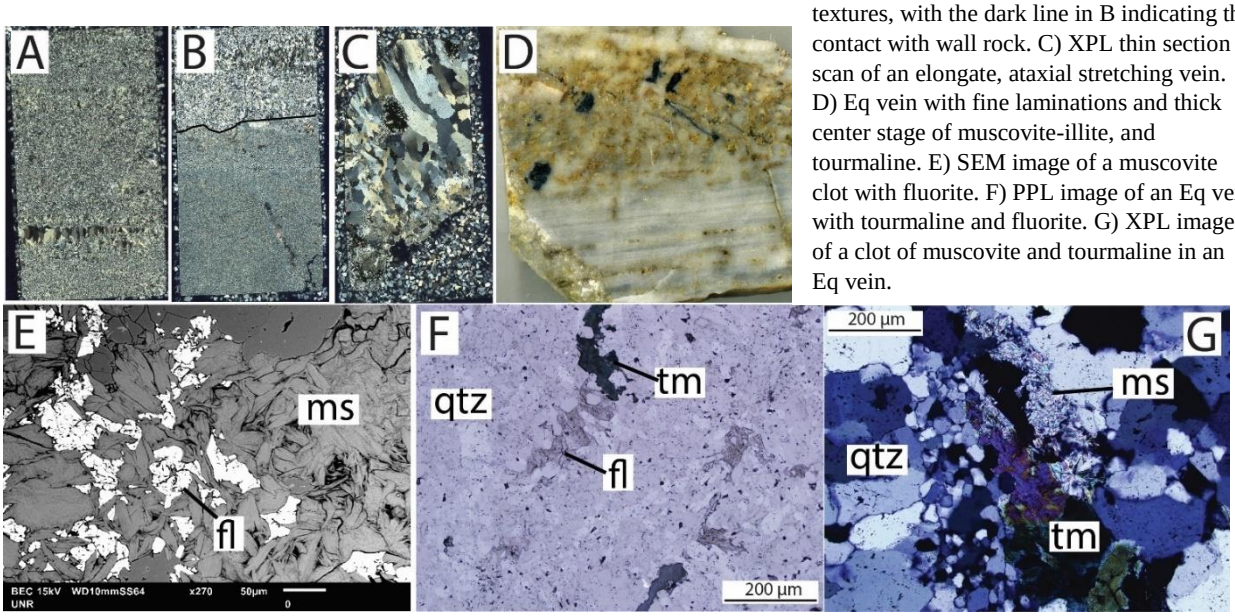

Fig. B-2. A-B) Two XPL thin section scans from a 10cm thick Eq vein illustrating typical textures, with the dark line in B indicating the contact with wall rock. C) XPL thin section scan of an elongate, ataxial stretching vein. D) Eq vein with fine laminations and thick center stage of muscovite-illite, and tourmaline. E) SEM image of a muscovite clot with fluorite. F) PPL image of an Eq vein with tourmaline and fluorite. G) XPL image of a clot of muscovite and tourmaline in an Eq vein.

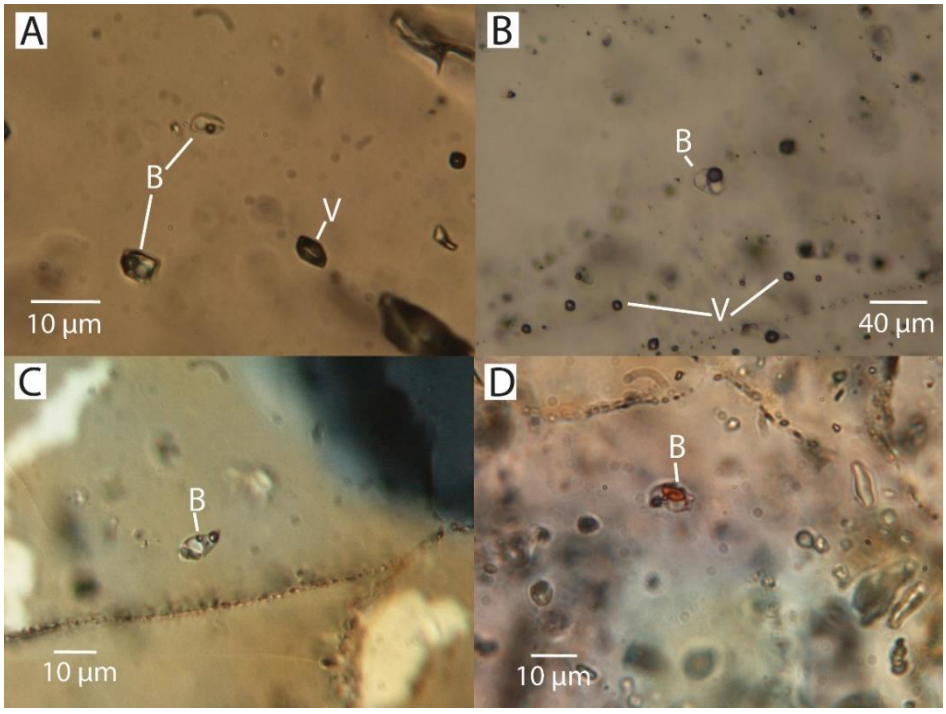

Fig. B-3. Additional photomicrographs of fluid inclusions from Eq veins. A) Hypersaline brine rich inclusions coexisting with negative crystal shape two phase vapor rich inclusions. B) Hypersaline brine rich inclusions and small two phase vapor rich inclusions. C) Brine rich inclusions with small vapor bubble in an Eq vein hosted Tg. D) Hypersaline brine rich inclusion with red hematite daughter mineral.

RBCPQ022E Au in Eq quartz vein

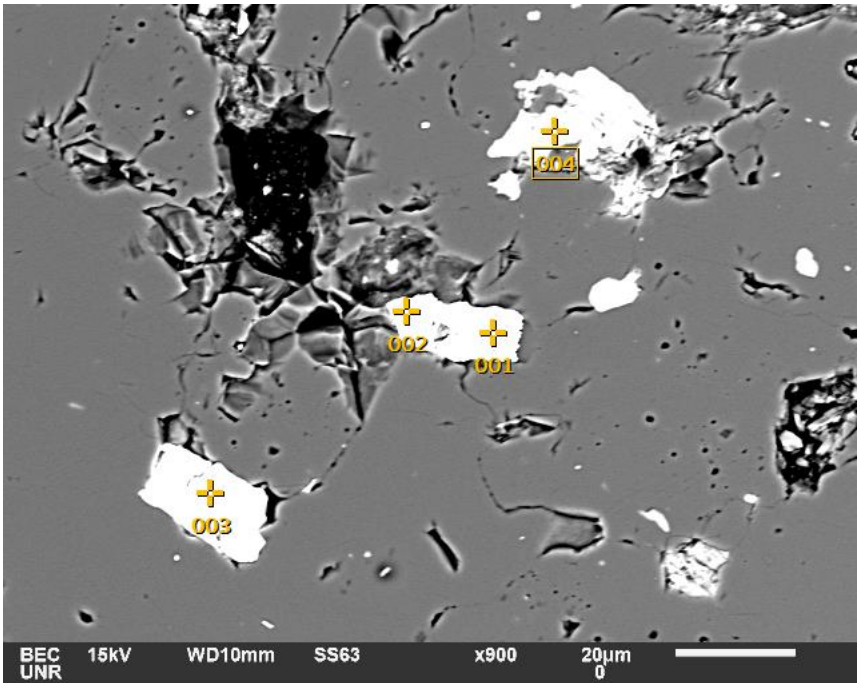

Volt : 15.00 kV
Mag. : x 900
Date : 2016/01/16
Pixel : 1280 x 960

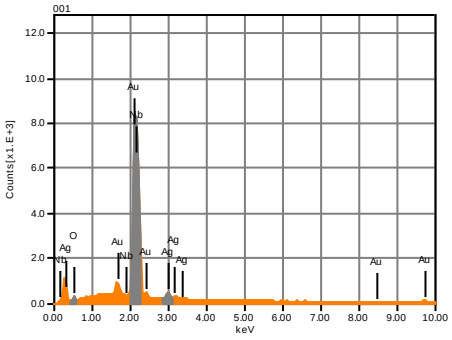

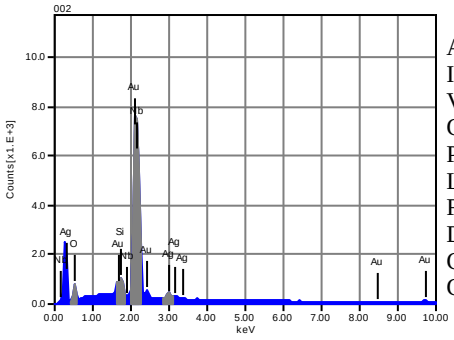

Acquisition Condition
Instrument : 6510(LA)
Volt : 15.00 kV
Current : ---
Process Time : T4
Live time : 11.33 sec.
Real Time : 15.00 sec.
DeadTime : 24.00 %
Count Rate : 17584.00 CPS

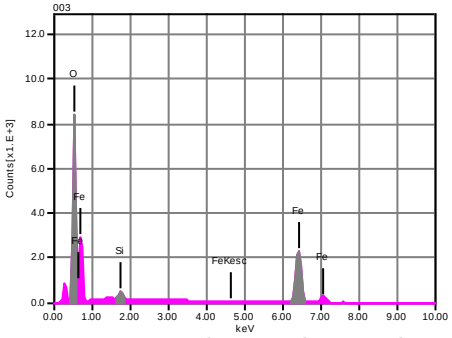

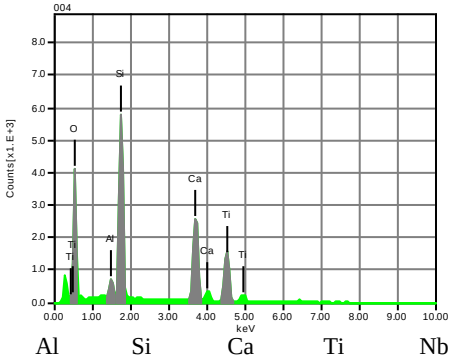

	Fe	O	Au	Ag	Al	Si	Ca	Ti	Nb	Likely Mineral
001		1.34	90.58	5.24					2.85	Free Gold
002		5.67	84.60	4.93		1.41			3.39	Free Gold
003	67.26	31.40				1.34				Limonite
004		45.46			1.39	16.09	18.56	18.49		Titanite
Average	67.26	20.97	87.59	5.08	1.39	6.28	18.56	18.49	3.12	
Standard deviation		0.00	21.04	4.23	0.22	0.00	8.49	0.00	0.00	0.38

RBCPQ091x Free gold in an oxidized pyrite grain of an Eq vein

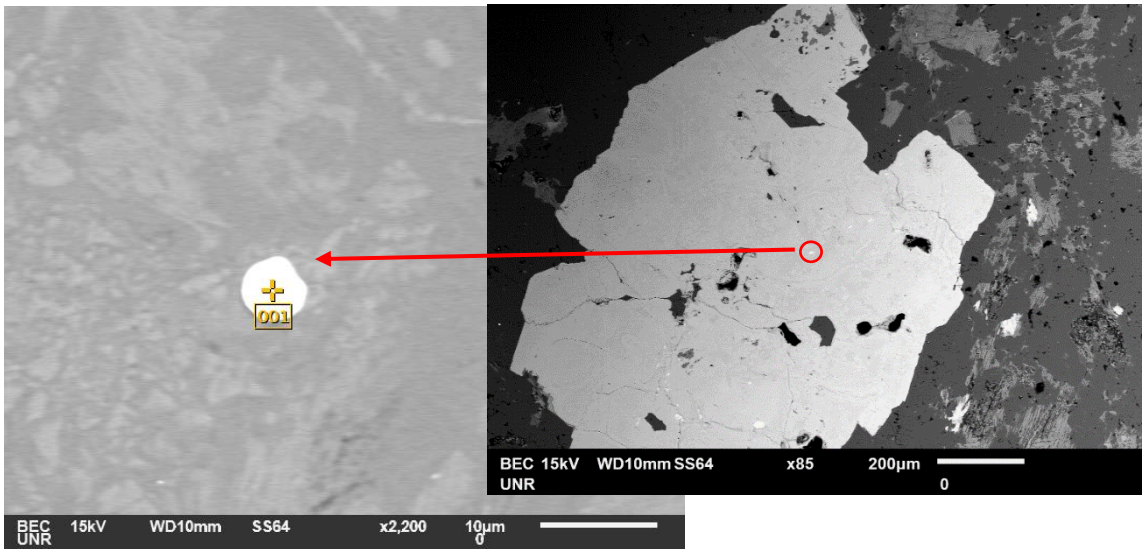

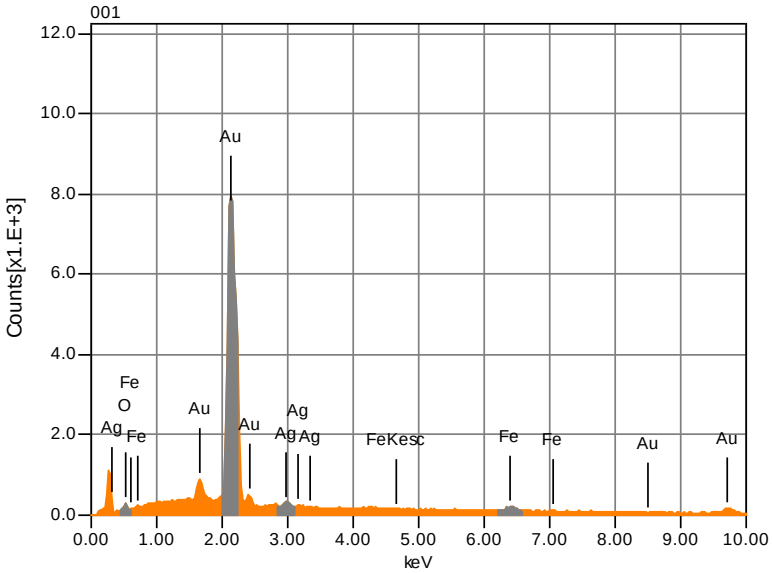

Volt : 15.00 kV
Mag. : x 2,200
Date : 2016/11/12
Pixel : 640 x 480

Acquisition Condition
Instrument : 6510(LA)
Volt : 15.00 kV
Current : ---
Process Time : T4
Live time : 8.54 sec.
Real Time : 15.00 sec.
DeadTime : 43.00 %
Count Rate : 34564.00 CPS

Chemical formula	mass%	Atom%	Sigma	Net	K ratio	Line
O	1.20	12.16	0.02	4052	0.0341992	K
Fe	2.50	7.24	0.07	7151	0.2030381	K
Ag	2.39	3.59	0.08	11455	0.1143622	L
Au	93.90	77.01	0.24	530598	5.1908817	M
Total	100.00	100.00				

Likely Mineral
Free Gold

JEOL EDS System JEOL

RBCPQ081A Gold, and Pb minerals in a thick (10cm) Eq vein

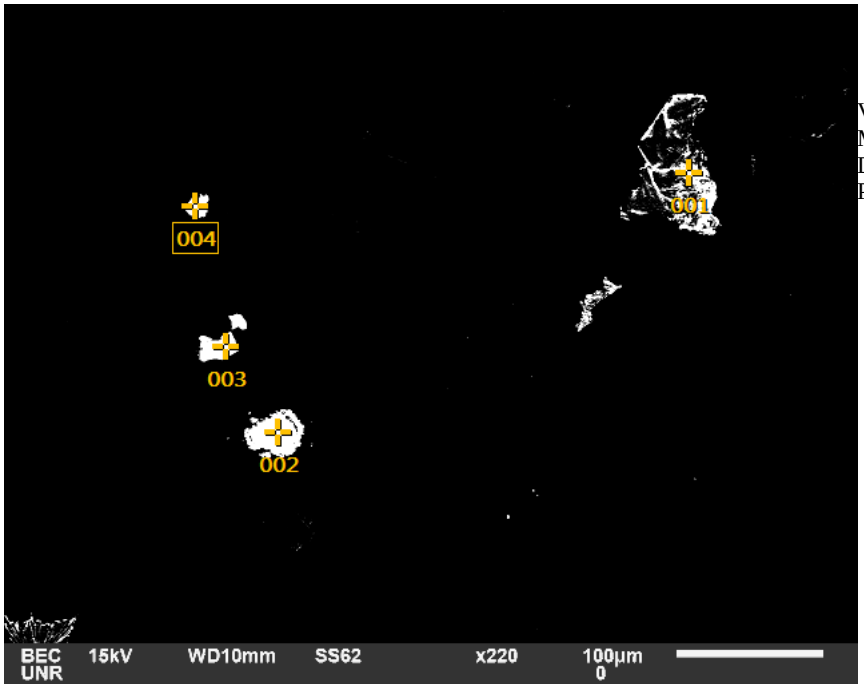

Volt : 15.00 kV
Mag. : x 220
Date : 2016/02/04
Pixel : 1280 x 960

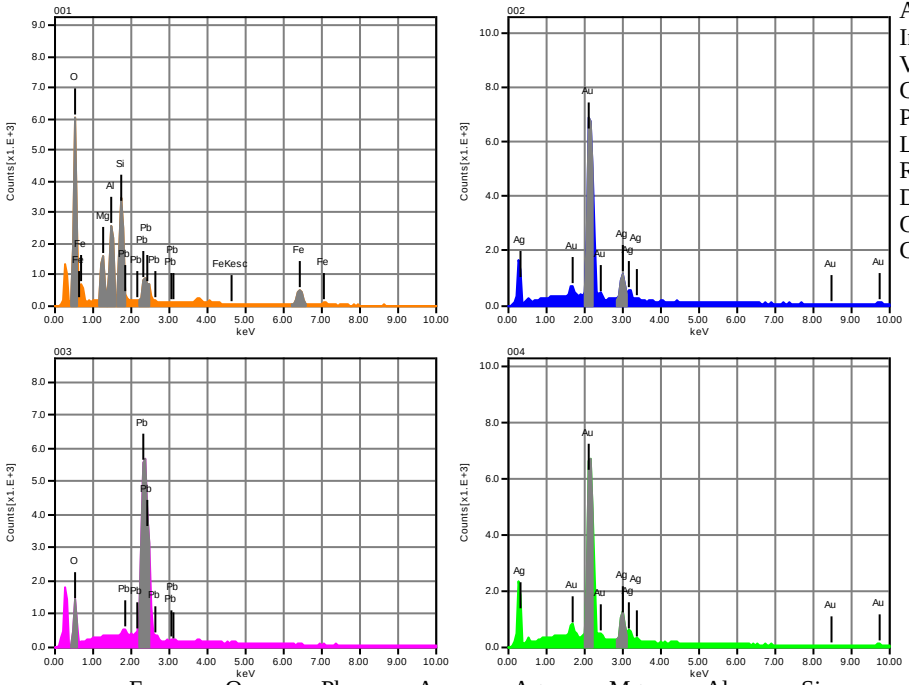

Acquisition Condition
Instrument : 6510(LA)
Volt : 15.00 kV
Current : ---
Process Time : T4
Live time : 8.85 sec.
Real Time : 15.00 sec.
DeadTime : 41.00 %
Count Rate : 33294.00 CPS

	Fe	O	Pb	Au	Ag	Mg	Al	Si		Likely Mineral
001	16.95	36.13	16.16			6.52	9.97	14.28		Unknown
002				84.02	15.98					Gold
003		9.91	90.09							litharge?
004				82.61	17.39					Gold
Average	16.95	23.02	53.12	83.31	16.69	6.52	9.97	14.28		
Standard deviation		0.00	18.54	52.28	0.99	0.99	0.00	0.00	0.00	

RBCPQ081A Bismuth minerals in Eq vein

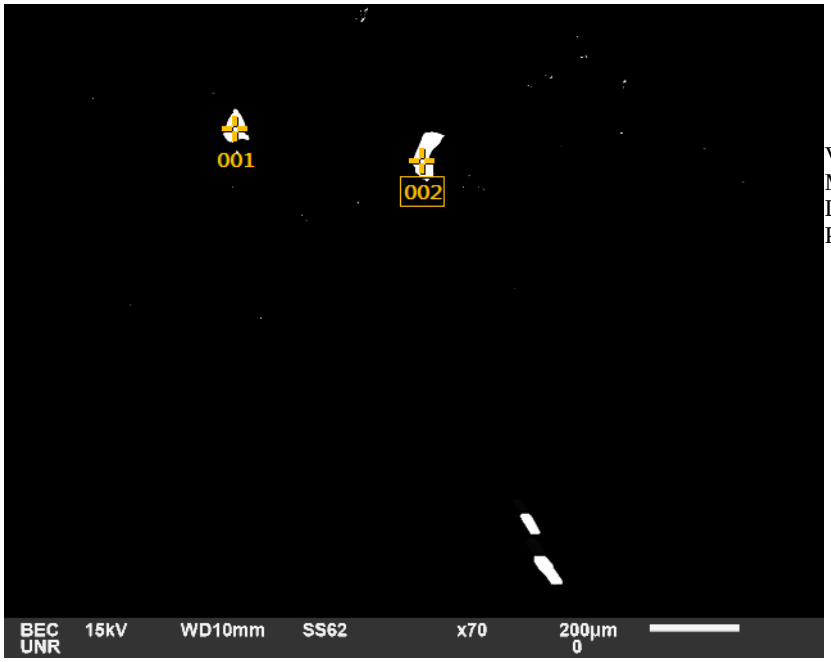

Volt : 15.00 kV
Mag. : x 70
Date : 2016/02/04
Pixel : 1280 x 960

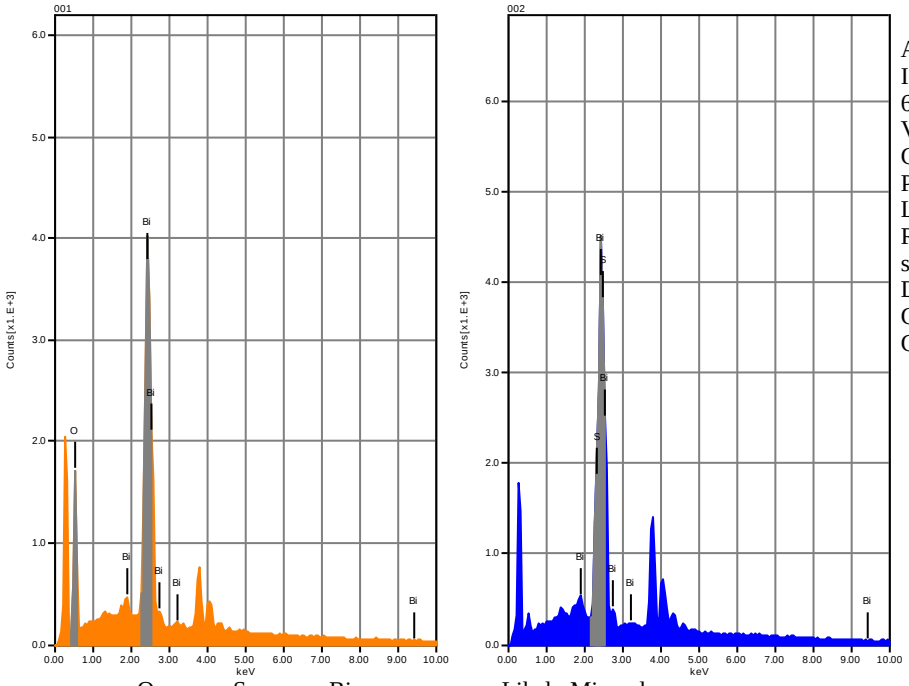

Acquisition Condition
Instrument : 6510(LA)
Volt : 15.00 kV
Current : ---
Process Time : T4
Live time : 9.44 sec.
Real Time : 15.00 sec.
DeadTime : 37.00 %
Count Rate : 28536.00 CPS

	O	S	Bi		Likely Mineral
001	11.92		88.08		Bismite
002		9.32	90.68		Bismuthinite?
Average	11.92	9.32	89.38		
Standard deviation	0.00	0.00	0.00	1.83	

JEOL EDS System JEOL

RBCPQ081A Rare-earth minerals in Eq vein

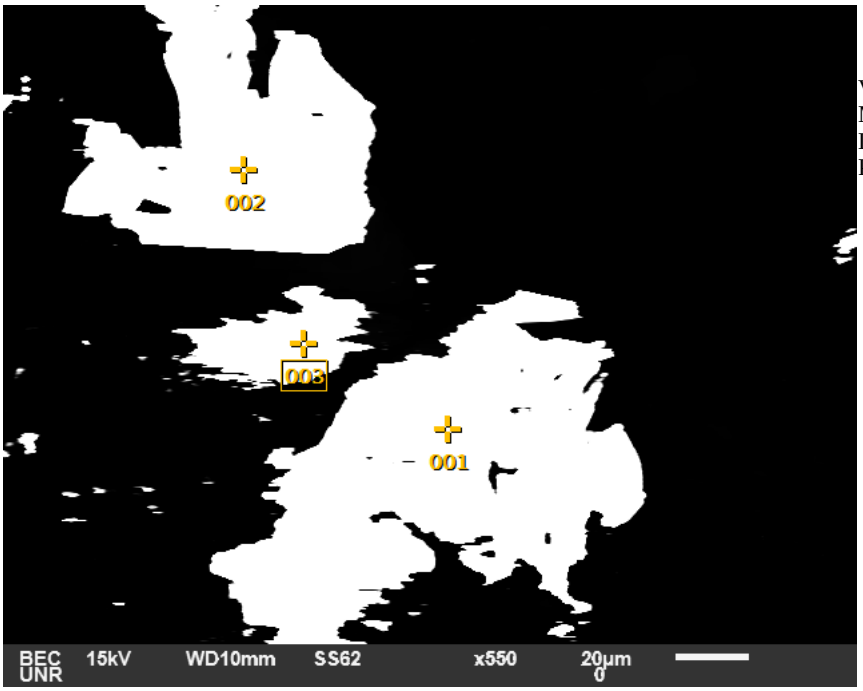

Volt : 15.00 kV
Mag. : x 550
Date : 2016/02/04
Pixel : 640 x 480

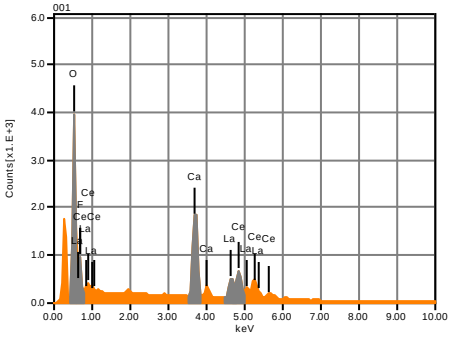

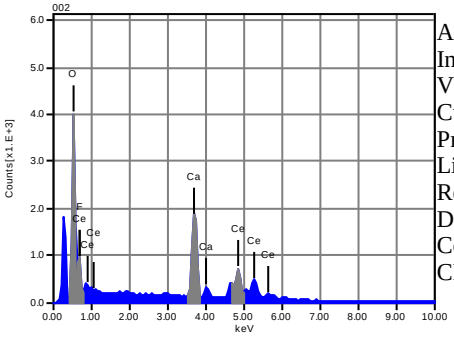

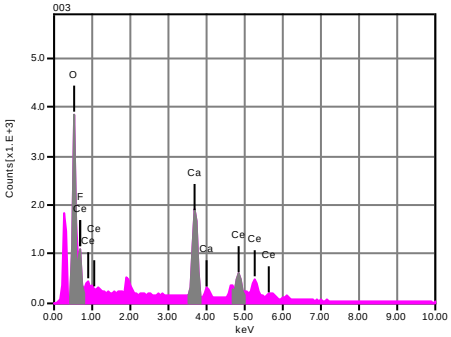

Acquisition Condition
Instrument : 6510(LA)
Volt : 15.00 kV
Current : ---
Process Time : T4
Live time : 11.57 sec.
Real Time : 15.00 sec.
DeadTime : 23.00 %
Count Rate : 15763.00 CPS

	CaO	O	F	La2O3	CeO2		Likely Mineral
001	28.07	0.00	7.40	25.87	38.66		Parisite????
002	38.25	0.00	11.80		49.95		“ “
003	38.72	0.00	13.80		47.48		“ “
Average	35.01	0.00	11.00	25.87	45.36		
Standard deviation	6.02	0.00	3.27	0.00		5.94	

JEOL EDS System JEOL

RBCPQ018 K-feldspar alteration near Eq vein

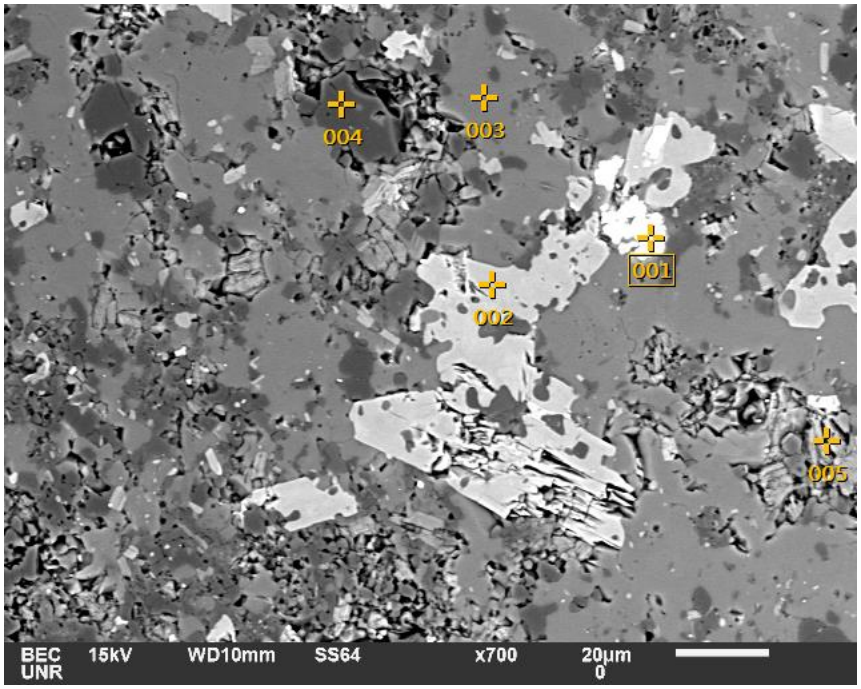

Volt : 15.00 kV
Mag. : x 700
Date : 2016/11/19
Pixel : 1280 x 960

Acquisition Condition
Instrument : 6510(LA)
Volt : 15.00 kV
Current : ---
Process Time : T4
Live time : 11.61 sec.
Real Time : 15.00 sec.
DeadTime : 23.00 %
Count Rate : 16351.00 CPS

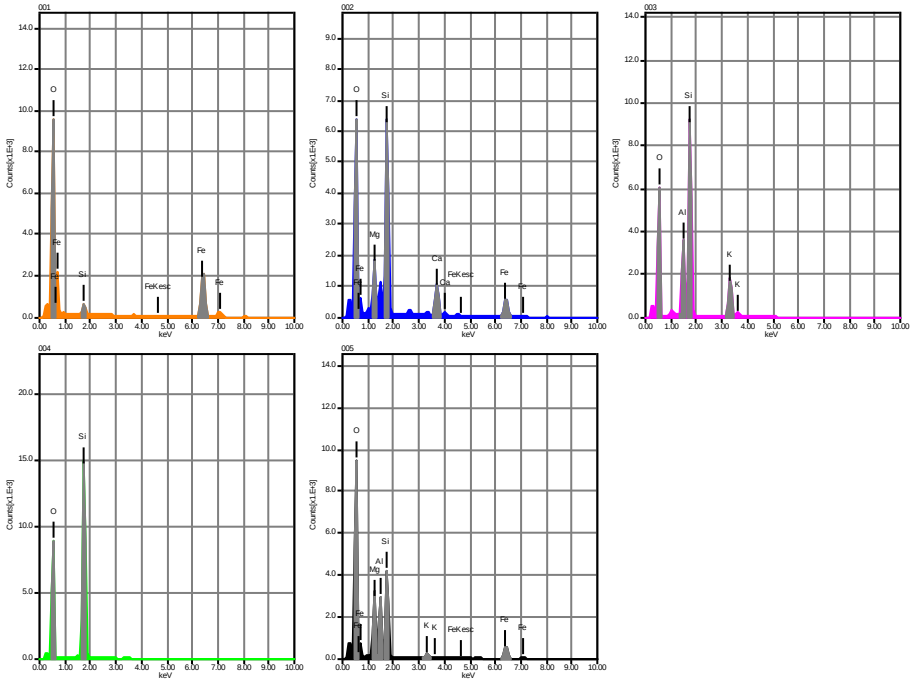

	CaO	O	MgO	Al2O3	SiO2	K2O	FeO	Likely Mineral
001		0.00			5.85		94.15	Pyrite
002	13.36	0.00	12.90		51.46		22.28	Actinolite?
003		0.00		19.26	64.39	16.35		K-feldspar
004		0.00			100.00			Quartz
Average	13.36	0.00	16.41	19.72	51.57	8.99	46.19	
Standard deviation		0.00	0.00	4.97	0.65	34.78	10.41	41.54

RBCPQ018 Fluorite in Eq quartz vein

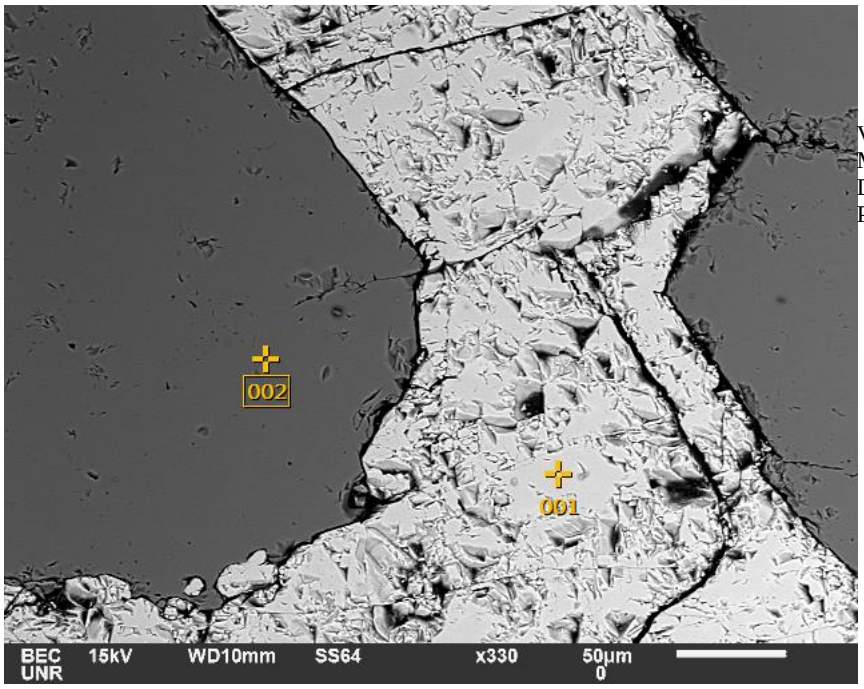

Volt : 15.00 kV
Mag. : x 330
Date : 2016/11/19
Pixel : 1280 x 960

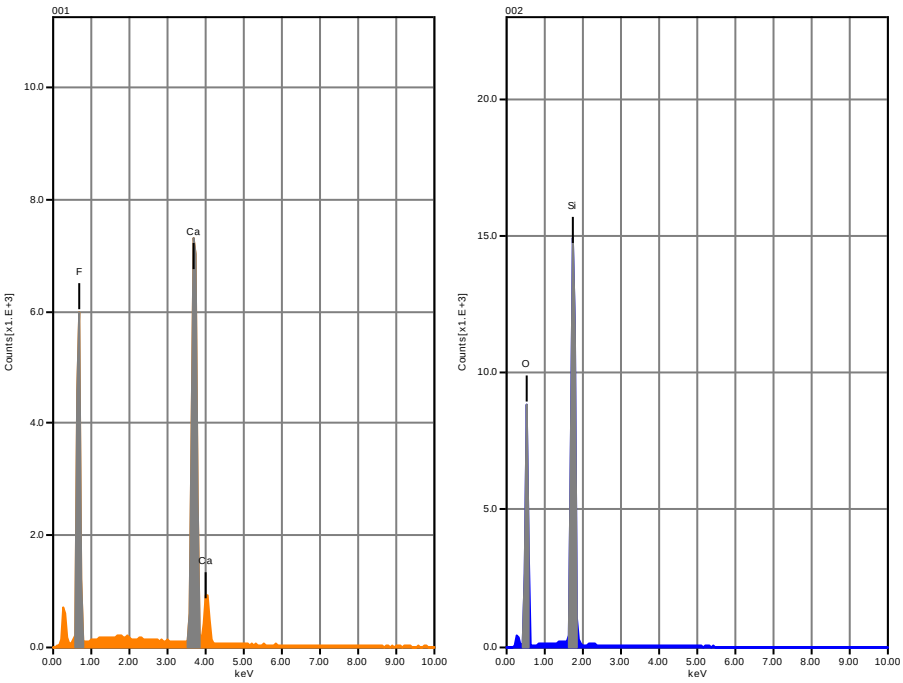

Acquisition Condition
Instrument : 6510(LA)
Volt : 15.00 kV
Current : ---
Process Time : T4
Live time : 11.03 sec.
Real Time : 15.00 sec.
DeadTime : 26.00 %
Count Rate : 20304.00 CPS

	CaO	O	F	SiO2		
001	56.55		43.45			
002		0.00		100.00		Fluorite
Average	56.55	0.00	43.45	100.00		Quartz
Standard deviation	0.00	0.00	0.00	0.00		

Sericitization (Ser)

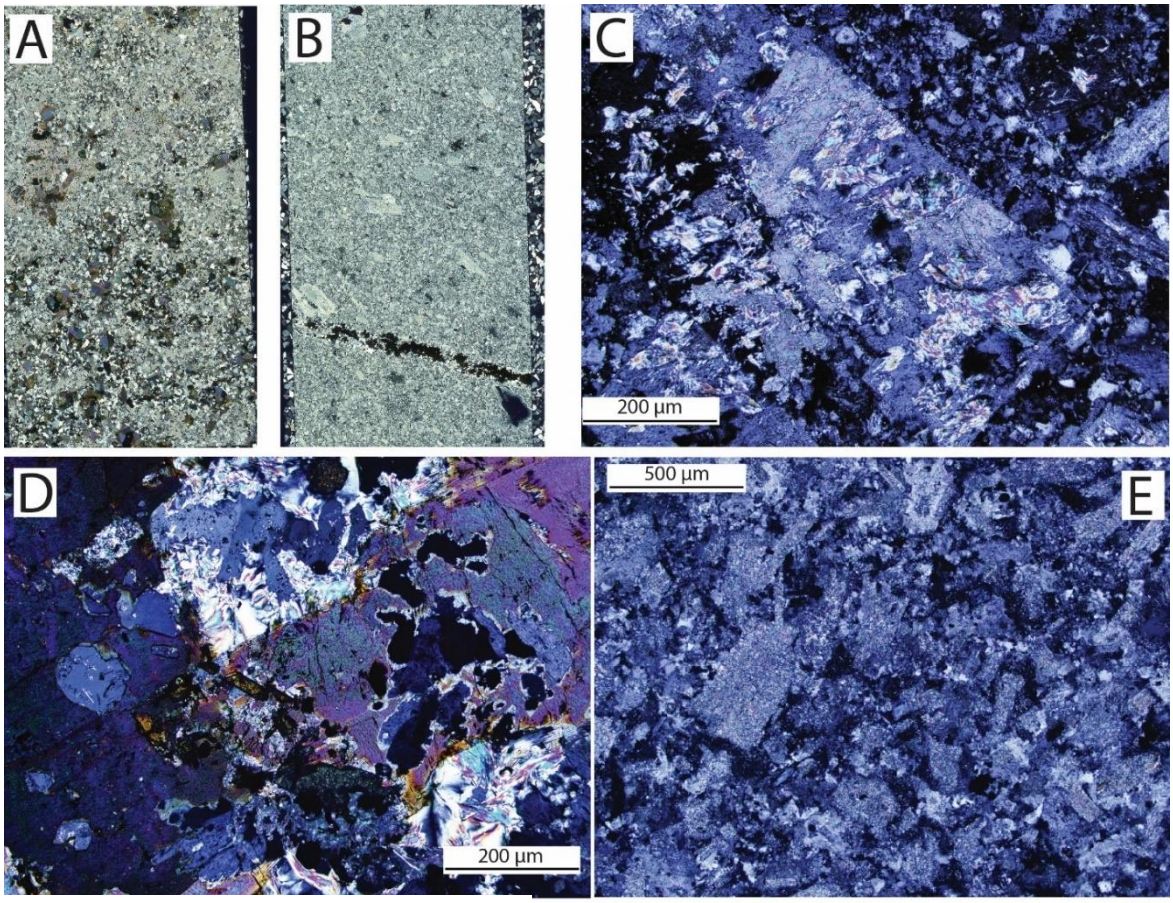

Fig. B-4. Images of sericitic alteration. A) XPL thin section scan of a highly altered sample of Td with strong sericite and tourmaline. B) Moderate to strong sericitic alteration in a dike of Td. C) Muscovite altering a plagioclase phenocryst and overprinting calcite. D) Muscovite surrounding a tourmaline grain. E) Moderate sericitic alteration with feldspars being completely altered. F) Sericitically altered core sample (Kmd? Or Td?) in BCD-101-11 with a quartz-calcite-arsenopyrite vein.

Tourmaline base-metal sulfide (Tbm) veins

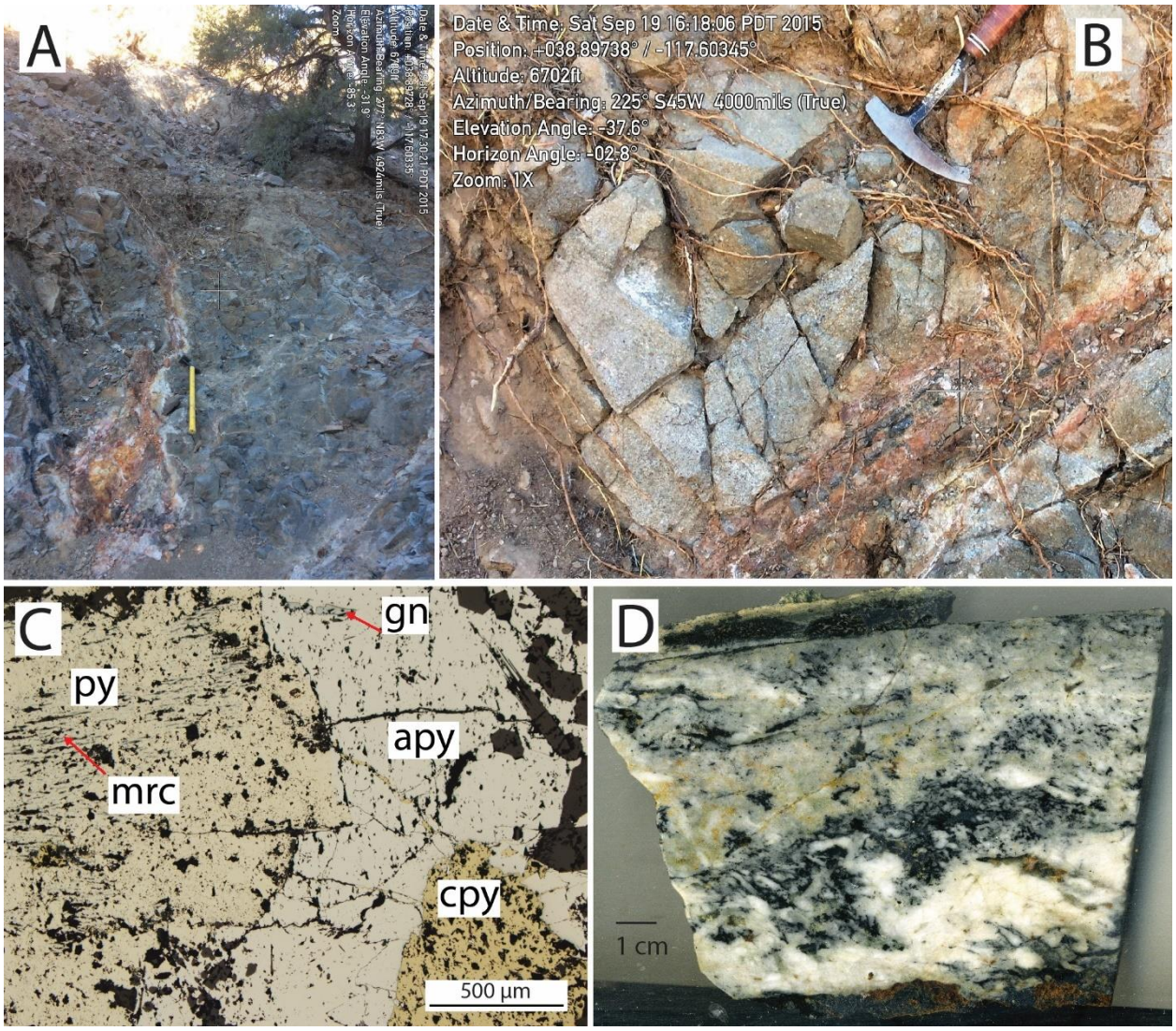

Fig. B-5. A) Highly oxidized structure that contains material of a sulfide rich Tbm vein. B) Typical surface expression of a Tbm vein, with reddish orange oxidation. C) Reflected light image of a sulfide rich Tbm vein that contains earlier pyrite/marcasite, arsenopyrite, galena and chalcopyrite. D) Thicker, more quartz rich style of Tbm vein that contains abundant tourmaline (black) and is Zn and Pb rich.

BCD-104-257 Tourmaline composition associated with arsenopyrite Tbm vein

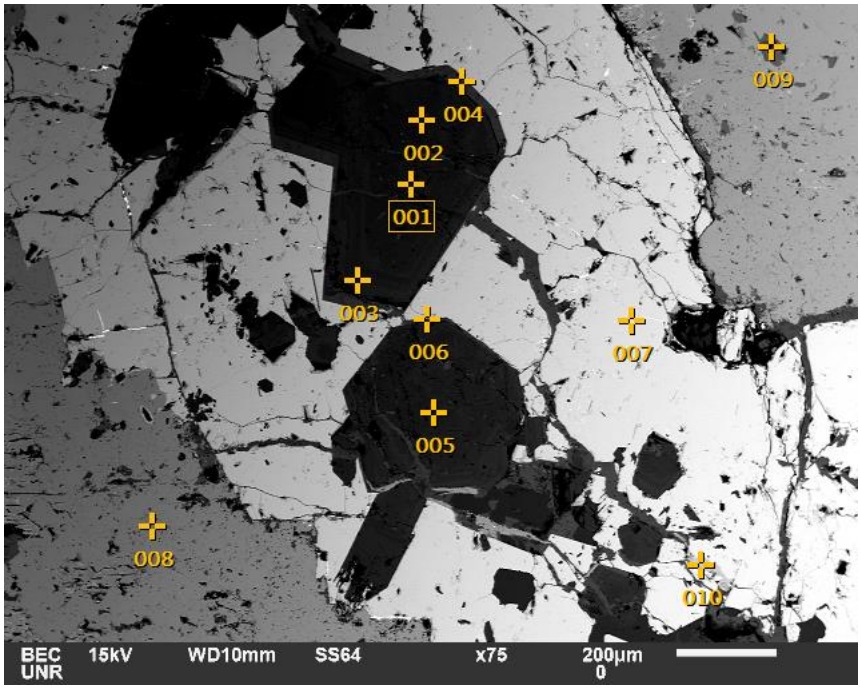

Volt : 15.00 kV
Mag. : x 75
Date : 2016/11/12
Pixel : 1280 x 960

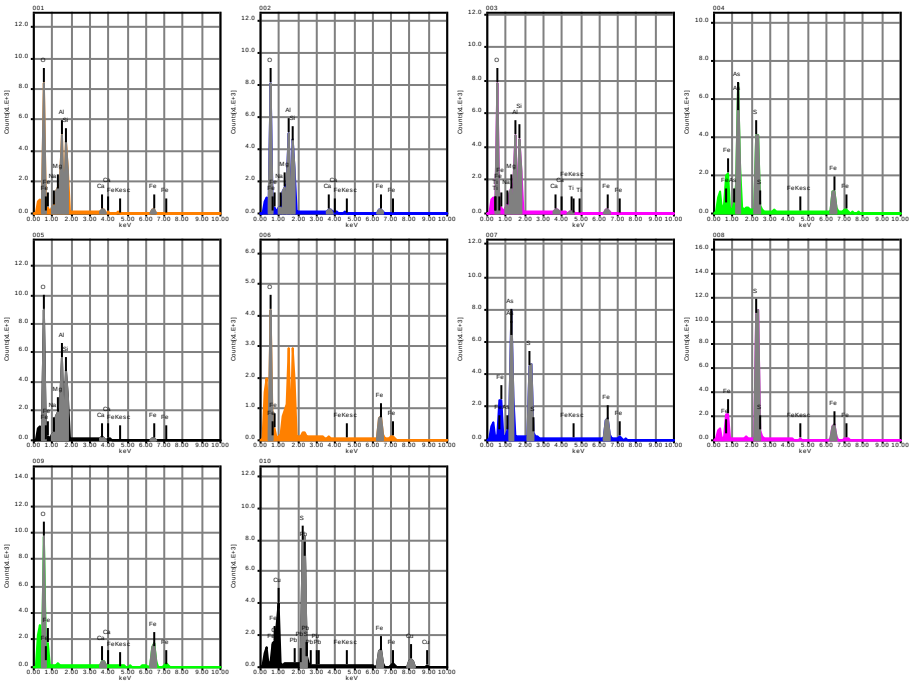

Acquisition Condition
Instrument : 6510(LA)
Volt : 15.00 kV
Current : ---
Process Time : T4
Live time : 11.59 sec.
Real Time : 15.00 sec.
DeadTime : 22.00 %
Count Rate : 16871.00 CPS

	CaO	O	Na2O	MgO	Al2O3	SiO2	SO3	TiO2	FeO	CuO	As2O3	PbO	Likely Mineral
001	2.19	0.00	2.27	10.04	34.25	42.06			9.19				Tourmaline
002	2.73	0.00	1.74	10.22	33.95	41.76			9.60				" "
003	2.56	0.00	1.93	9.44	32.20	40.90		2.31	10.66				" "
004							31.29		25.39		43.32		Arsenopyrite
007							31.44		24.25		44.32		" "
008							70.84		29.16				Pyrite
010							48.11		20.97	21.53		9.39	Chalcopyrite
Average	3.00	0.00	2.08	10.15	34.33	41.71	45.42	2.31	32.94	21.53	43.82	9.39	
Standard deviation	1.61	0.00	0.30	0.61	1.95	0.56	18.70	0.00	34.76	0.00	0.70	0.00	

BCD-104-257 Tourmaline zonation from envelope of sulfide rich Tbm vein

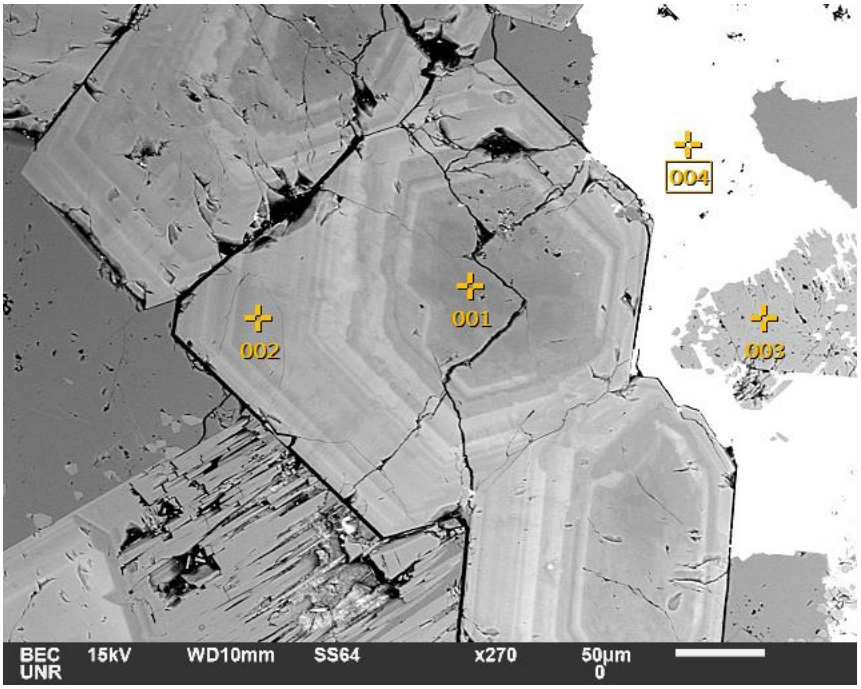

Volt : 15.00 kV
Mag. : x 270
Date : 2016/11/12
Pixel : 1280 x 960

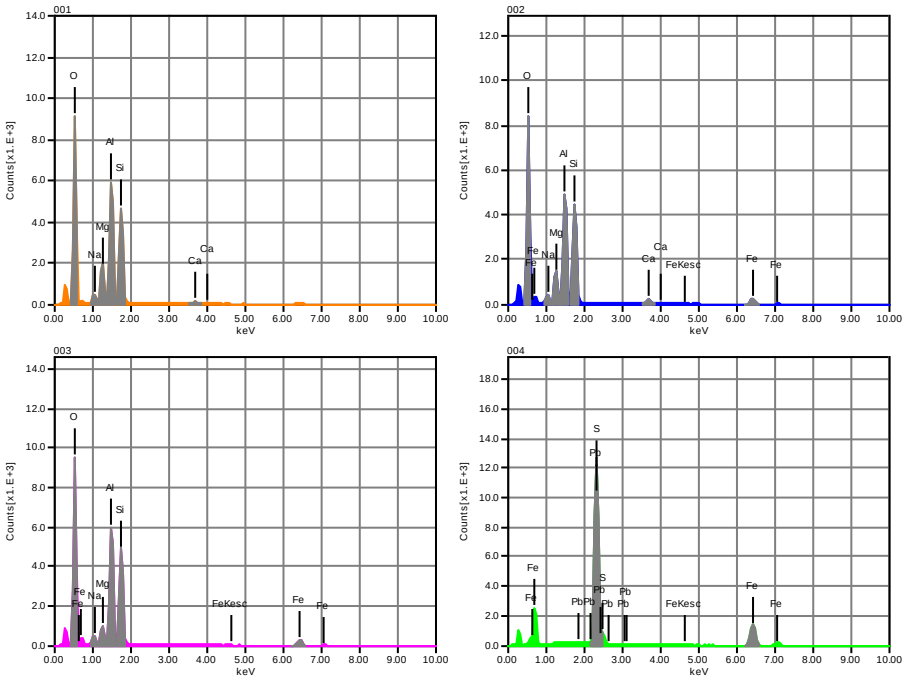

Acquisition Condition
Instrument : 6510(LA)
Volt : 15.00 kV
Current : ---
Process Time : T4
Live time : 10.12 sec.
Real Time : 15.00 sec.
DeadTime : 32.00 %
Count Rate : 24466.00 CPS

	CaO	O	Na2O	MgO	Al2O3	SiO2	SO3	FeO	PbO	Likely Mineral
001	1.26	0.00	2.27	11.79	39.60	45.08				Tourmaline
002	2.48	0.00	2.16	9.23	33.78	41.41		10.94		Tourmaline
003		0.00	2.54	5.49	37.78	42.73		11.46		Tourmaline
004							63.85	26.16	9.99	Galena
Average	1.87	0.00	2.32	8.84	37.05	43.07	63.85	16.18	9.99	
Standard deviation	0.86	0.00	0.20	3.17	2.98	1.86	0.00	8.64	0.00	

RBCPQ099 Hemimorphite, Pb-Zn vanadate and tourmaline in a Tbm vein

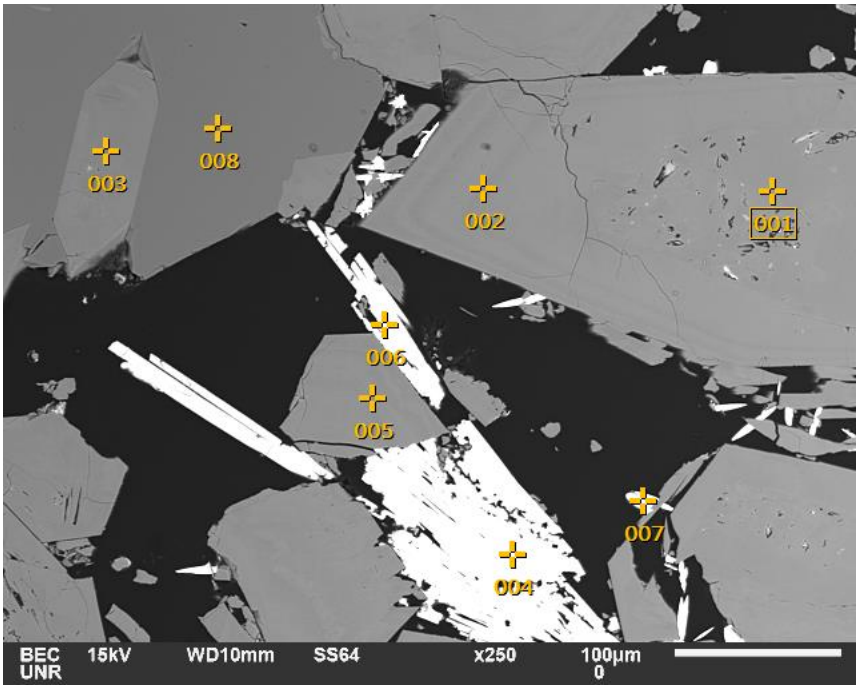

Volt : 15.00 kV
Mag. : x 250
Date : 2016/11/19
Pixel : 1280 x 960

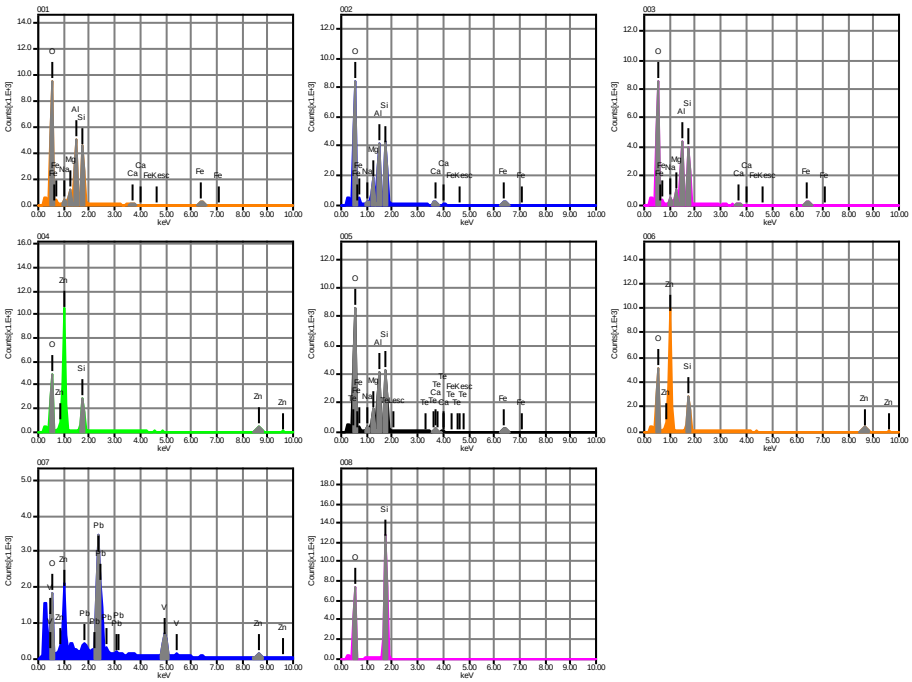

Acquisition Condition
Instrument : 6510(LA)
Volt : 15.00 kV
Current : ---
Process Time : T4
Live time : 11.56 sec.
Real Time : 15.00 sec.
DeadTime : 22.00 %
Count Rate : 17167.00 CPS

	CaO	O	Na2O	MgO	Al2O3	SiO2	V2O5	FeO	ZnO	TeO2	PbO	Likely Mineral
001	1.32	0.00	2.75	7.40	35.32	42.34		10.88				Tourmaline
002	3.55	0.00	1.34	12.06	30.13	41.44		11.48				Tourmaline
003	1.30	0.00	2.86	7.11	33.57	41.41		13.75				Tourmaline
004		0.00				33.50			66.50			Hemimorphite
005	3.19	0.00	1.71	10.87	29.58	40.92		12.41		1.32		Tourmaline
006		0.00				35.34			64.66			Hemimorphite
007		0.00					19.97		13.80		66.23	Pb-Zn Vanadate
008		0.00				100.00						Quartz
Average	2.34	0.00	2.16	9.36	32.15	47.85	19.97	12.13	48.32	1.32	66.23	
Standard deviation	1.20	0.00	0.75	2.48	2.76	23.25	0.00	1.25	29.91	0.00	0.00	

Tourmaline-quartz-chlorite (Tm-qtz) alteration

BCD-104-65 Tourmaline composition in patchy quartz tourmaline style, next three SEM images correspond to image A from figure 20

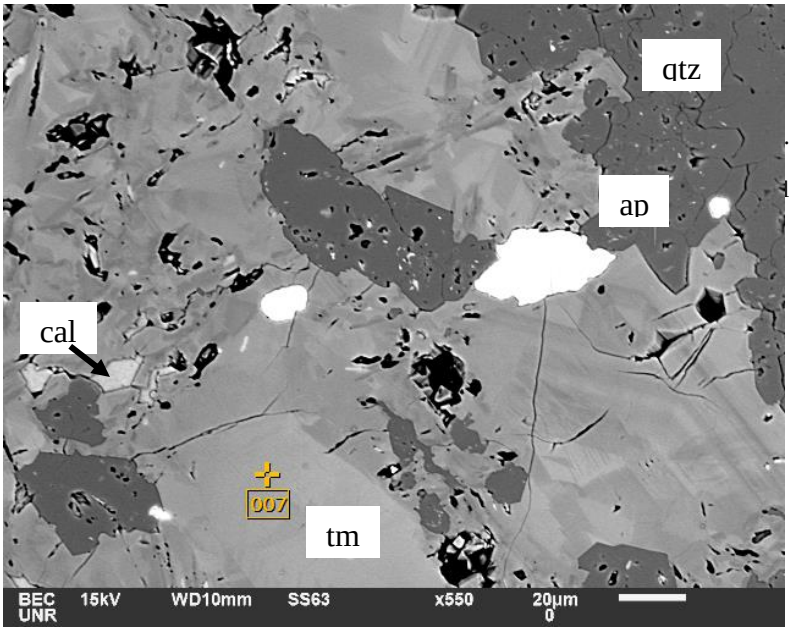

: 15.00 kV
: x 550
: 2016/01/16
: 1280 x 960

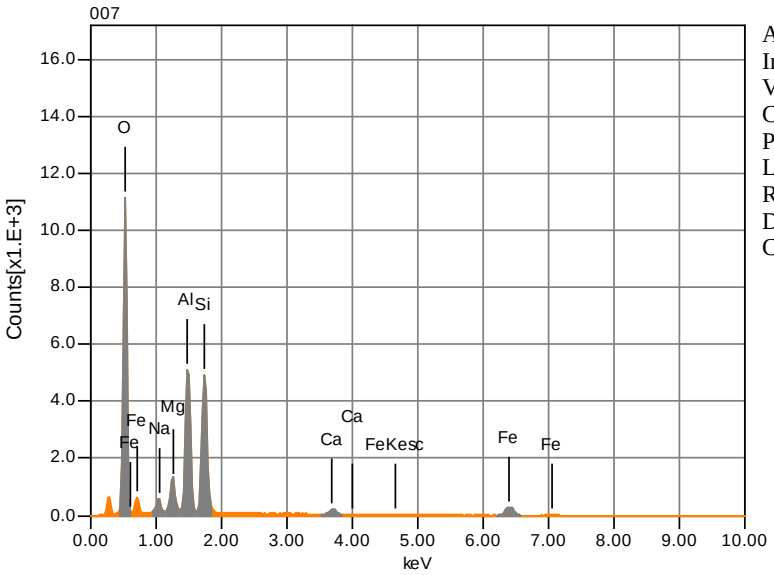

Acquisition Condition
Instrument : 6510(LA)
Volt : 15.00 kV
Current : ---
Process Time : T4
Live time : 11.04 sec.
Real Time : 15.00 sec.
DeadTime : 27.00 %
Count Rate : 20214.00 CPS

Chemical formula	mass%	mol%	Cation	Sigma	Net	K ratio	Line
O							
Na2O	2.51	2.76	0.69	0.04	13612	0.0569184	K
MgO	7.37	12.49	1.57	0.06	40536	0.1370893	K
Al2O3	32.78	21.94	5.51	0.12	173661	0.6070454	K
SiO2	41.71	47.39	5.95	0.17	176517	0.6885172	K
CaO	2.10	2.56	0.32	0.05	9290	0.0750427	K
FeO	13.52	12.85	1.61	0.12	21006	0.4613800	K
Total	100.00	100.00	15.65				

BCD-104-65 Chlorite outside of tourmaline zone in Tm-qtz alteration (Fig 20 A)

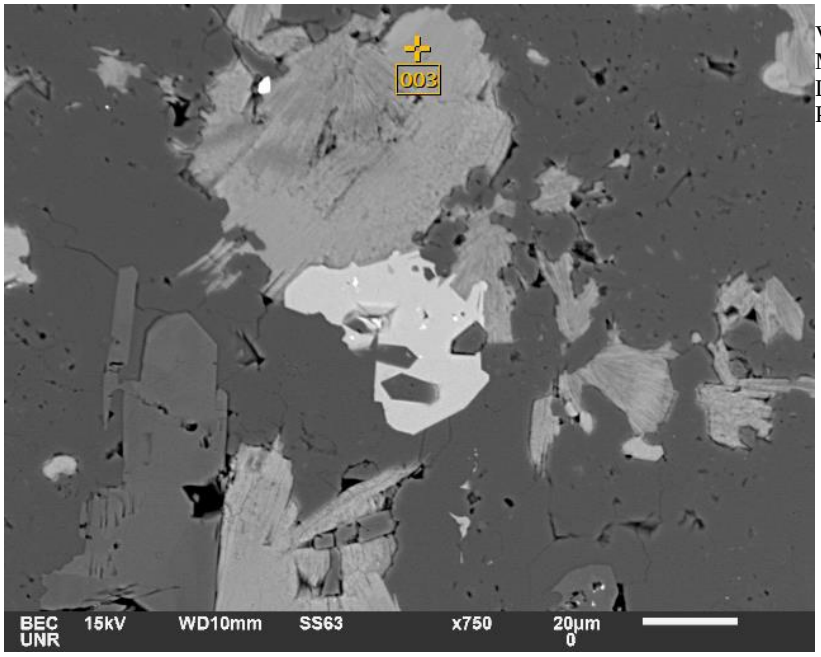

Volt : 15.00 kV
Mag. : x 750
Date : 2016/01/16
Pixel : 1280 x 960

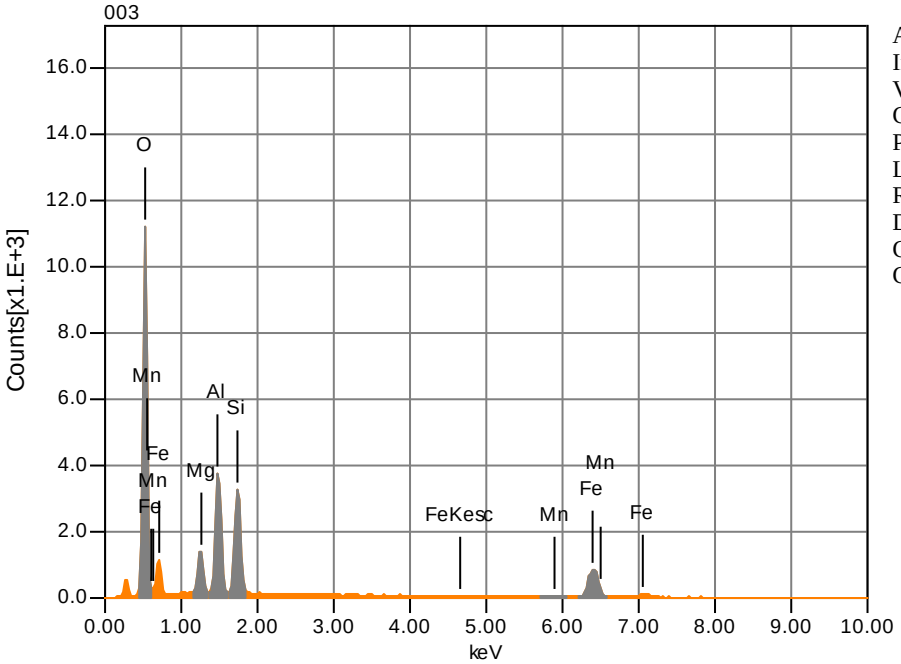

Acquisition Condition
Instrument : 6510(LA)
Volt : 15.00 kV
Current : ---
Process Time : T4
Live time : 11.23 sec.
Real Time : 15.00 sec.
DeadTime : 26.00 %
Count Rate : 18711.00 CPS

Chemical formula	mass%	mol%	Cation	Sigma	Net	K ratio	Line	
O								
MgO	9.22	15.63	2.26	0.07	45489	0.1512349	K	
Al2O3	25.45	17.06	4.94	0.12	124240	0.4269406	K	Likely Mineral
SiO2	27.71	31.52	4.57	0.14	115996	0.4447945	K	Chamosite (chlorite)
MnO	1.65	1.59	0.23	0.07	3164	0.0563912	K	
FeO	35.97	34.21	4.96	0.17	58356	1.2600664	K	
Total	100.00	100.00	16.96					

BCD-104-65 K-feldspar alteration on outer zone of Tm-qtz alteration (Fig. 20 A)

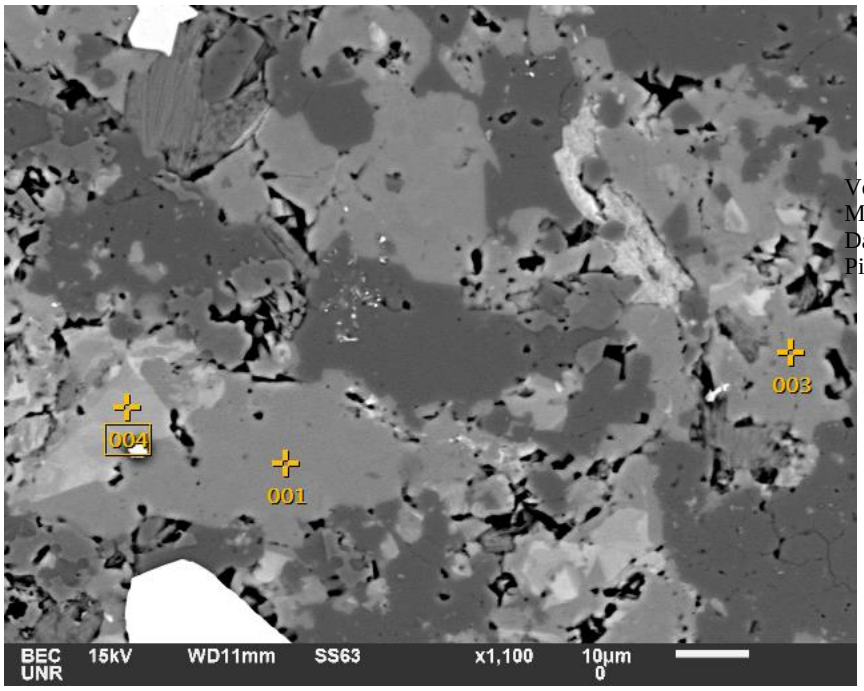

Volt : 15.00 kV
Mag. : x 1,100
Date : 2016/01/16
Pixel : 1280 x 960

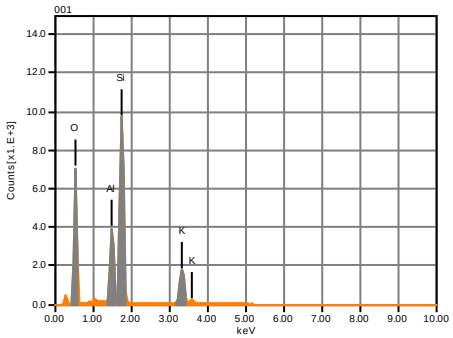

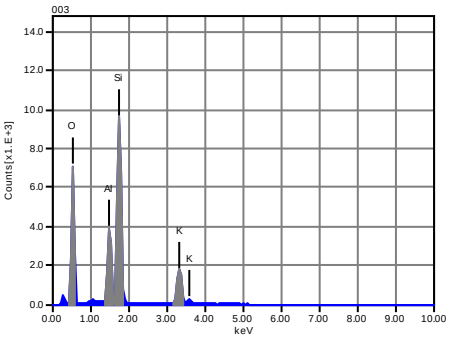

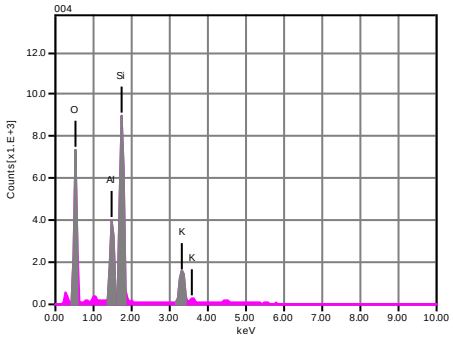

Acquisition Condition
Instrument : 6510(LA)
Volt : 15.00 kV
Current : ---
Process Time : T4
Live time : 10.83 sec.
Real Time : 15.00 sec.
DeadTime : 28.00 %
Count Rate : 21221.00 CPS

	O	Al2O3	SiO2	K2O		
001	0.00	19.26	64.72	16.02		K-feldspar
003	0.00	19.10	64.86	16.04		
004	0.00	21.22	63.99	14.79		
Average	0.00	19.86	64.52	15.61		
Standard deviation	0.00	1.18	0.47	0.72		

JEOL EDS System JEOL

BCD-104-97 Allanite, arsenopyrite, tourmaline, calcite, galena from a qtz-tm veinlet

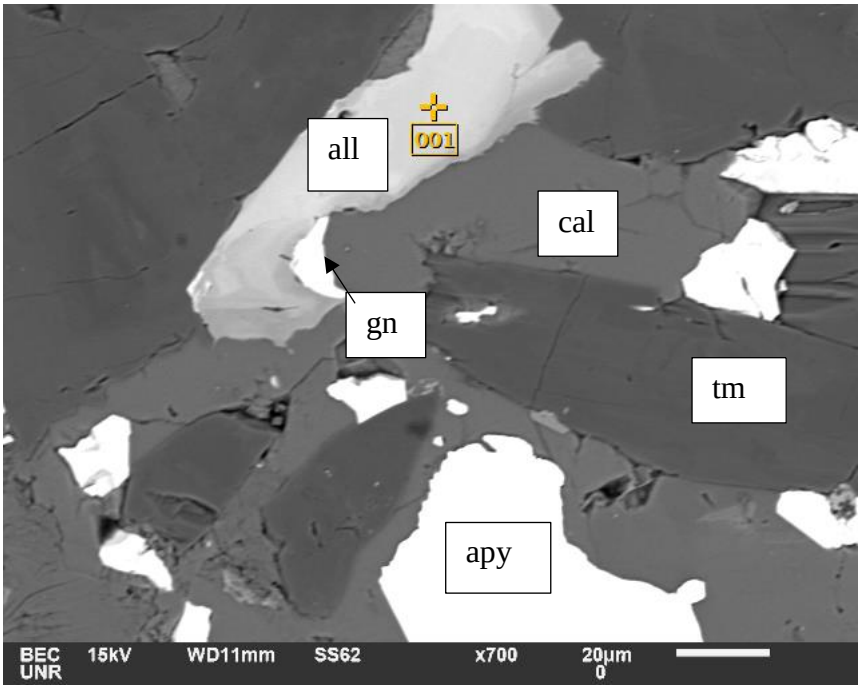

Volt : 15.00 kV
Mag. : x 700
Date : 2016/01/12
Pixel : 1280 x 960

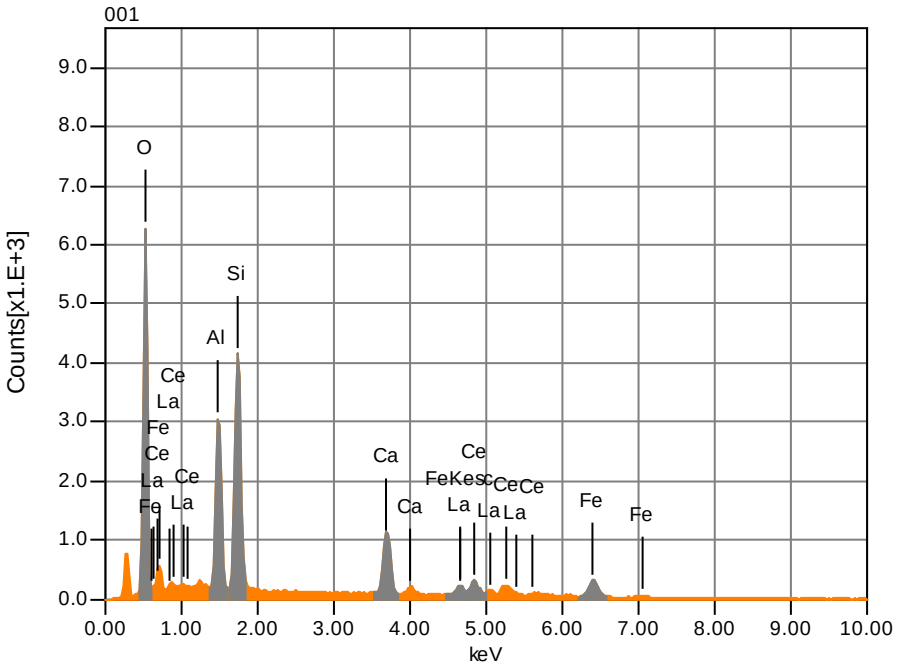

Acquisition Condition
Instrument : 6510(LA)
Volt : 15.00 kV
Current : ---
Process Time : T4
Live time : 11.22 sec.
Real Time : 15.00 sec.
DeadTime : 24.00 %
Count Rate : 18258.00 CPS

Chemical formula	mass%	mol%	Cation	Sigma	Net	K ratio	Line
O							
Al2O3	20.11	15.67	4.03	0.11	99175	0.3411120	K
SiO2	34.42	45.52	5.85	0.16	148460	0.5697866	K
CaO	12.52	17.74	2.28	0.09	59527	0.4731394	K
FeO	11.71	12.95	1.66	0.12	19078	0.4123054	K
La2O3	7.75	1.89	0.49	0.15	16965	0.2719353	L
CeO2	13.49	6.23	0.80	0.18	25475	0.4565923	L
Total	100.00	100.00	15.10				

Likely Mineral: Allanite

BCD-104-751 Pyrrhotite, intergrown with chlorite, sphalerite in Tm-qtz orbicular feature

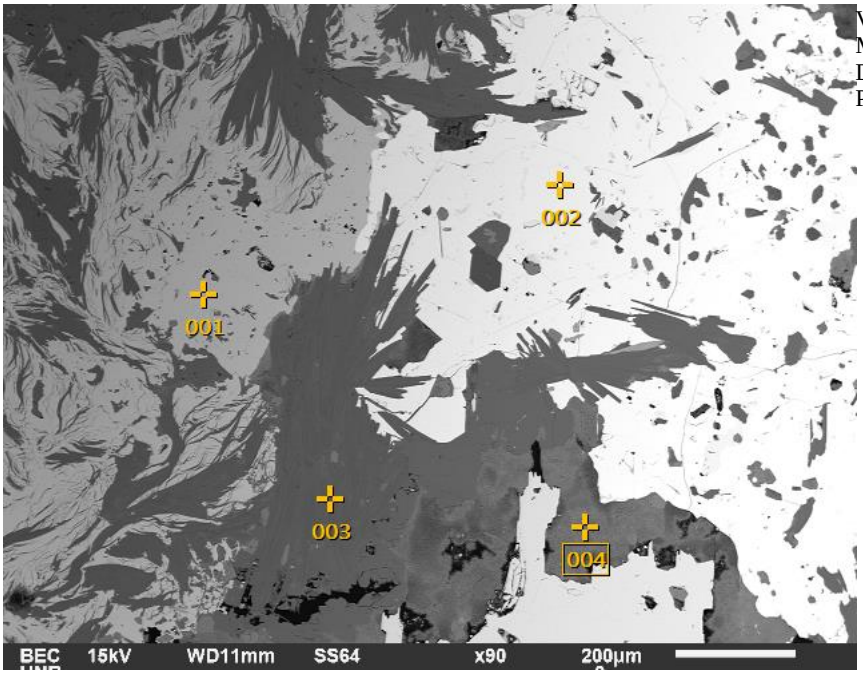

Volt : 15.00 kV
Mag. : x 90
Date : 2016/11/05
Pixel : 1280 x 960

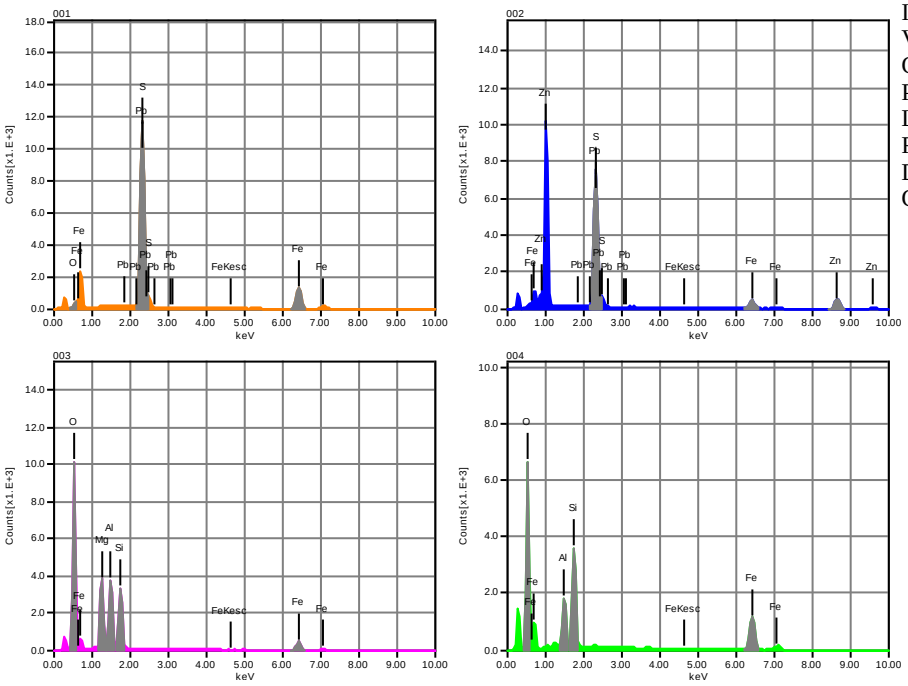

Acquisition Condition
Instrument : 6510(LA)
Volt : 15.00 kV
Current : ---
Process Time : T4
Live time : 11.84 sec.
Real Time : 15.00 sec.
DeadTime : 21.00 %
Count Rate : 14993.00 CPS

	Fe	O	Pb	Mg	Al	Si	S	Zn	Likely Mineral
001	35.31	2.52	16.23				45.93		Pyrrhotite+Galena
002	12.07		15.39				32.93	39.61	Sphalerite
003	12.55	48.35		13.64	12.70	12.76			Chlorite
004	39.95	37.25			7.16	15.65			Unknown
Average	24.97	29.37	15.81	13.64	9.93	14.20	39.43	39.61	
Standard deviation	14.74	23.91	0.60	0.00	3.92	2.04	9.19	0.00	

Skarn

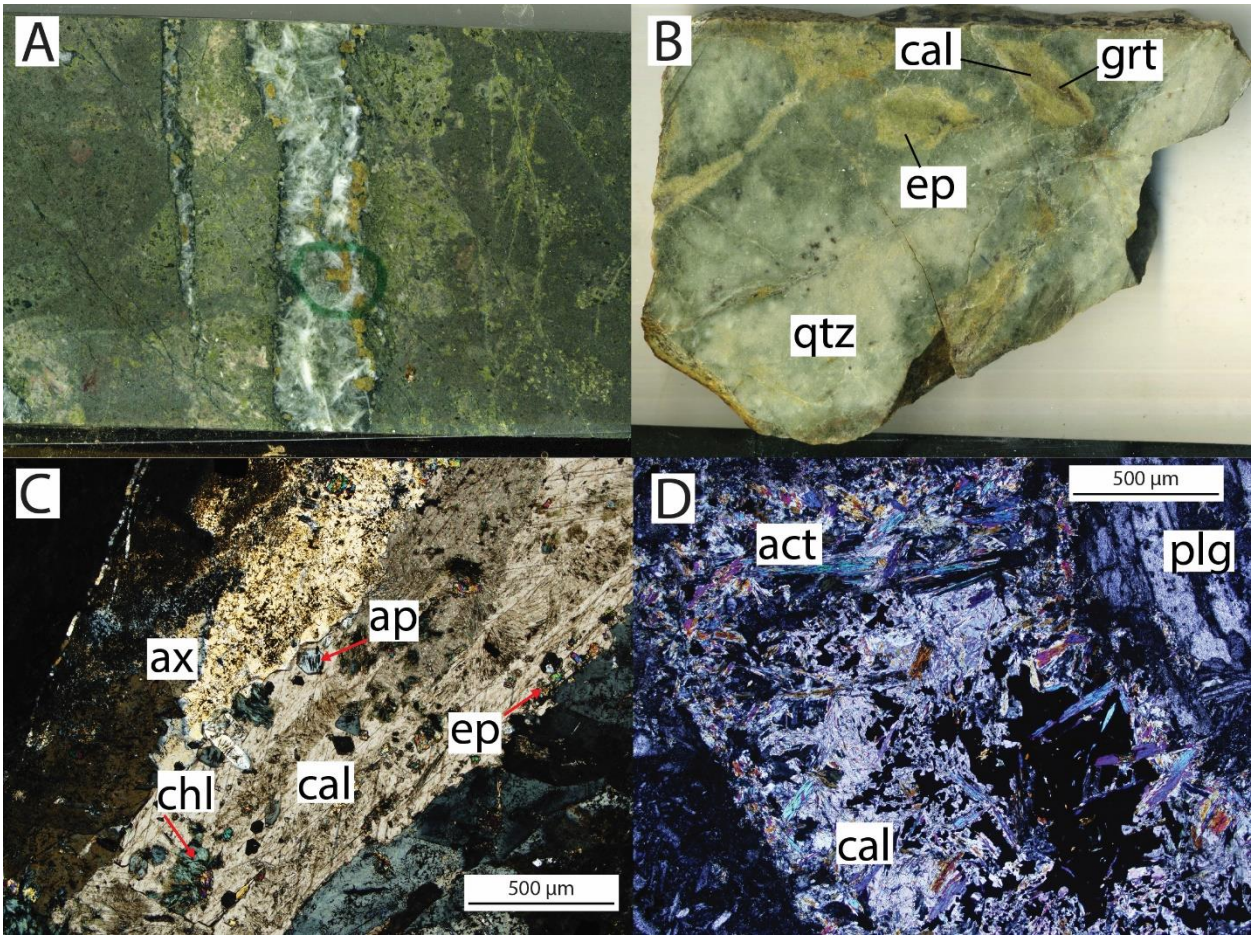

Fig. B-6. A) Retrograde skarn vein composed of mostly calcite with a weak envelope of chlorite. Primary skarn minerals include garnet (yellow) and quartz. B) Exoskarn hosted in TRkl composed of clots of garnet, overprinted by epidote and calcite. C) Retrograde skarn vein composed mostly of calcite with an envelope of axinite. Lesser minerals include epidote, chlorite and apatite. D) Retrograde minerals also include calcite and actinolite.

RBCPQ036B Andradite in skarn grading out to vesuvianite (B-6B)

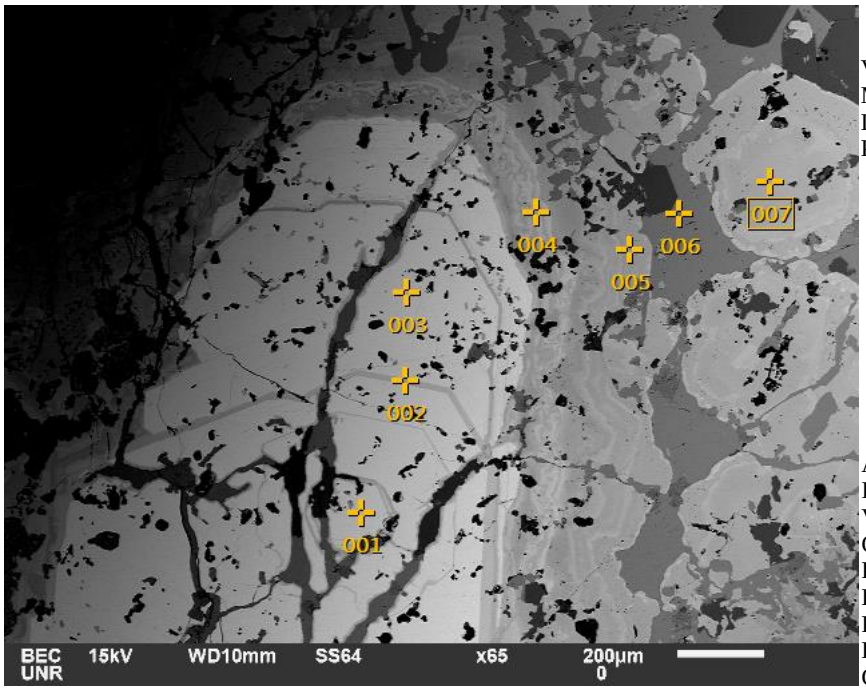

Volt : 15.00 kV
Mag. : x 65
Date : 2016/11/05
Pixel : 1280 x 960

Acquisition Condition
Instrument : 6510(LA)
Volt : 15.00 kV
Current : ---
Process Time : T4
Live time : 10.79 sec.
Real Time : 15.00 sec.
DeadTime : 29.00 %
Count Rate : 21074.00 CPS

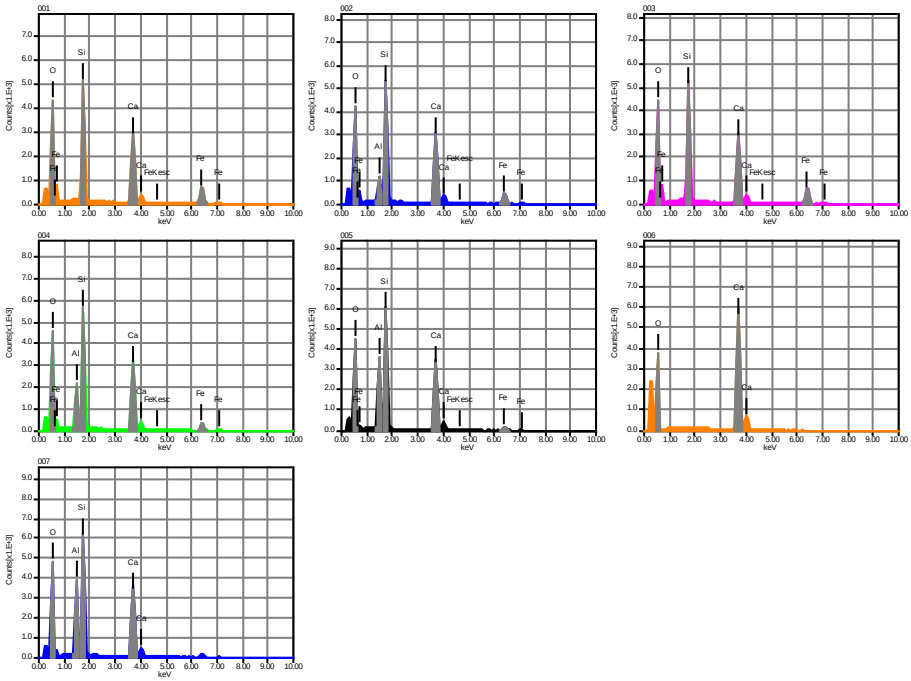

	CaO	O	Al2O3	SiO2	FeO		Likely Mineral
001	35.40	0.00		37.27	27.34		Andradite
002	35.77	0.00	6.57	38.12	19.55		Andradite
003	34.99	0.00		38.00	27.01		Andradite
004	35.65	0.00	11.43	39.12	13.80		Vesuvianite
005	36.42	0.00	18.63	39.48	5.48		Vesuvianite
006	100.00	0.00					Calcite
Average	45.35	0.00	14.02	38.88	18.63		
Standard deviation	24.14	0.00	6.14	1.43	9.26		

RBCPQ076 Diopside, anorthite, quartz, chlorite, apatite in skarn of TRkvc protolith

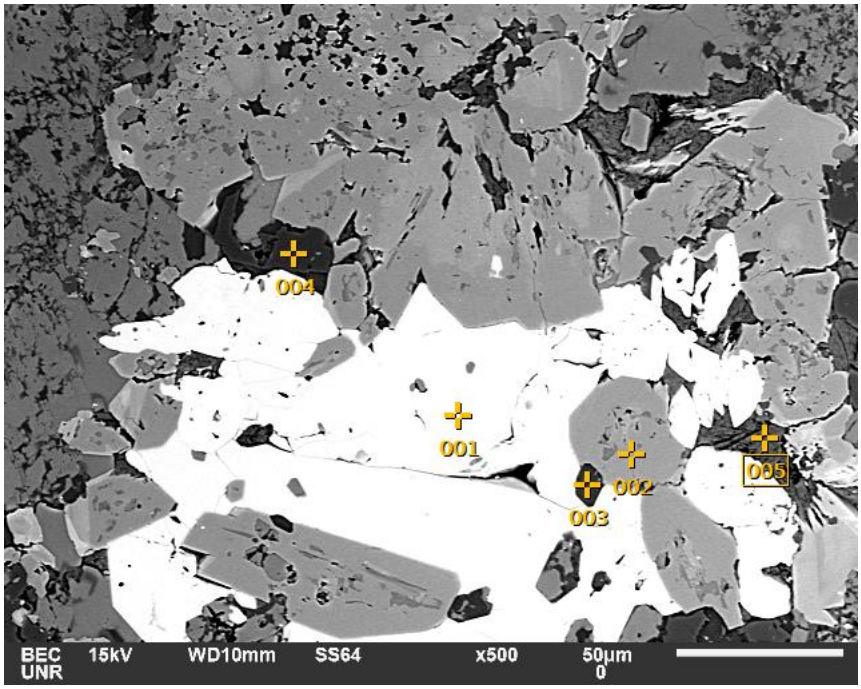

Volt : 15.00 kV
Mag. : x 500
Date : 2016/11/05
Pixel : 1280 x 960

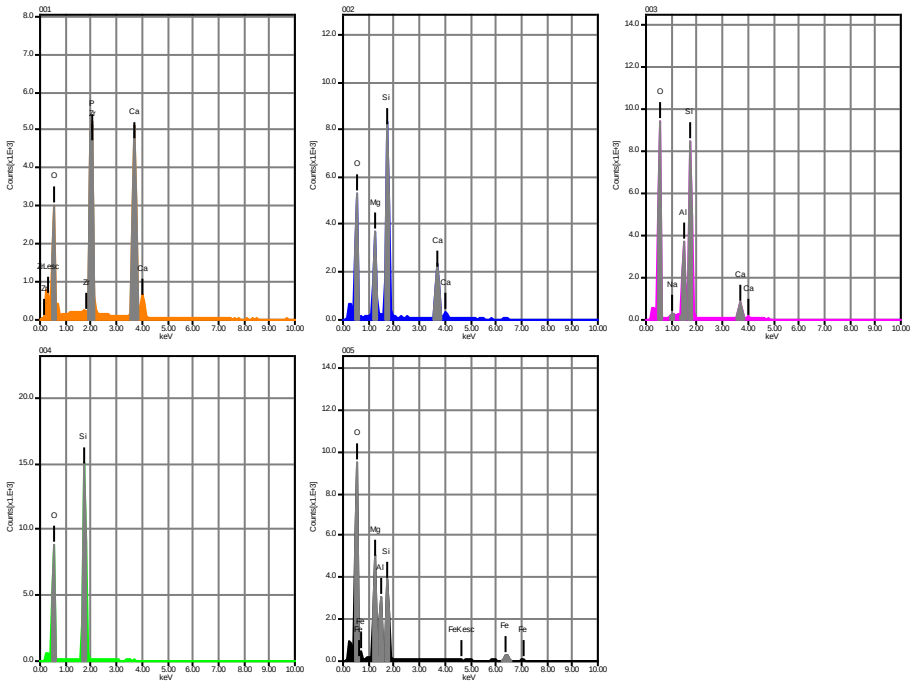

Acquisition Condition
Instrument : 6510(LA)
Volt : 15.00 kV
Current : ---
Process Time : T4
Live time : 11.39 sec.
Real Time : 15.00 sec.
DeadTime : 24.00 %
Count Rate : 18220.00 CPS

	CaO	O	Na2O	MgO	Al2O3	SiO2	P2O5	FeO	ZrO2	Likely Mineral
001	47.59	0.00					39.10		13.32	Apatite
002	25.38	0.00		20.03		54.60				Diopside
003	10.58	0.00	1.10		21.58	66.73				Anorthite
004		0.00				100.00				Quartz
005		0.00		30.75	22.26	35.09		11.90		Chlorite?
Average	27.85	0.00	1.10	25.39	21.92	64.10	39.10	11.90	13.32	
Standard deviation	18.63	0.00	0.00	7.59	0.48	27.25	0.00	0.00	0.00	

BCD-102-262 Garnet with quartz in a retrograde calcite vein (B-6A)

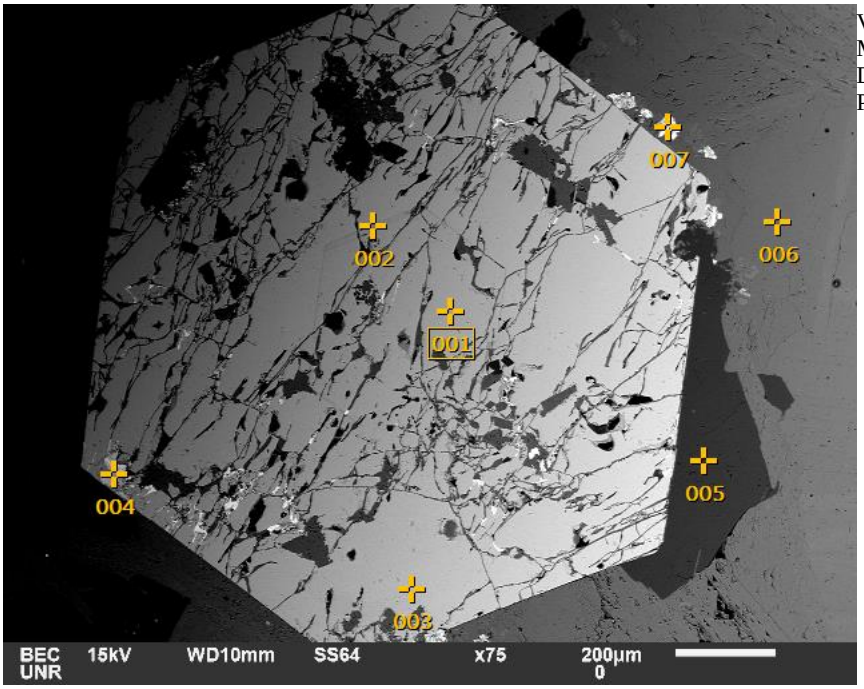

Volt : 15.00 kV
Mag. : x 75
Date : 2016/11/19
Pixel : 1280 x 960

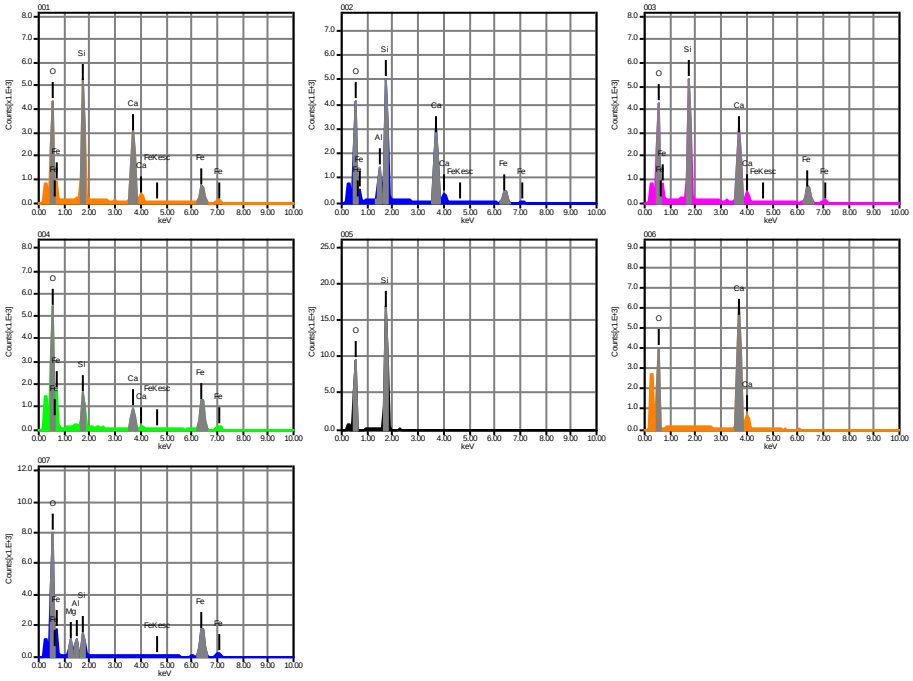

Acquisition Condition
Instrument : 6510(LA)
Volt : 15.00 kV
Current : ---
Process Time : T4
Live time : 11.49 sec.
Real Time : 15.00 sec.
DeadTime : 24.00 %
Count Rate : 16966.00 CPS

	CaO	O	MgO	Al2O3	SiO2	FeO	
001	35.61	0.00			37.48	26.90	
002	35.69	0.00		8.49	38.31	17.51	
003	35.37	0.00			37.25	27.38	
004	14.98	0.00			17.25	67.77	
005		0.00			100.00		
006	100.00	0.00					
007		0.00	8.95	8.35	12.59	70.12	
Average	44.33	0.00	8.95	8.42	40.48	41.94	
Standard deviation	32.37	0.00	0.00	0.10	31.25	24.98	

Mesothermal quartz (Mq) veins

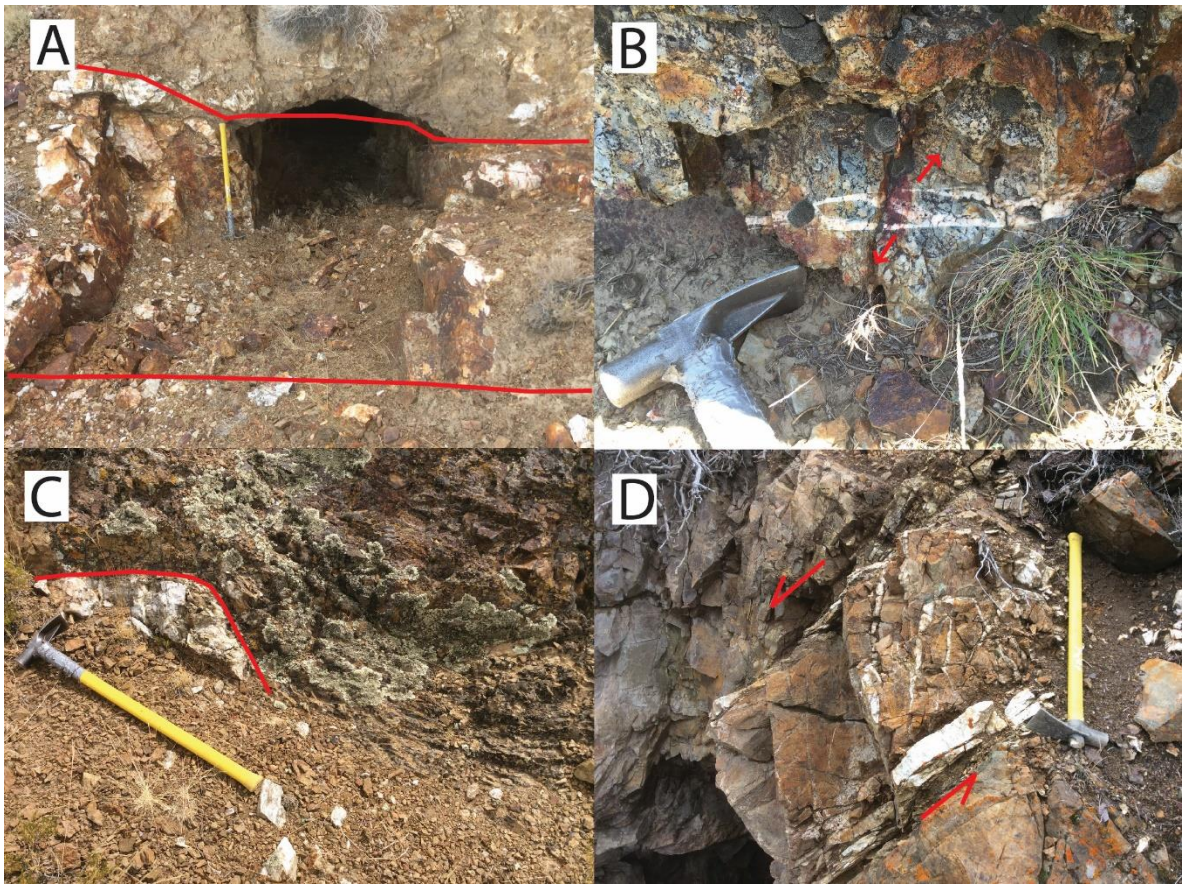

Fig. B-7. A) Surface exposure of a >1m thick, shallowly dipping Mq vein from the Good Luck Mine workings. B) Small offshoot of an Mq vein with rock septums, indicating extension. C) Boudinaged Mq vein, which locally occur. D) Steeply dipping offshoots of the Richmond vein mine that form a ladder vein, indicating sinistral motion.

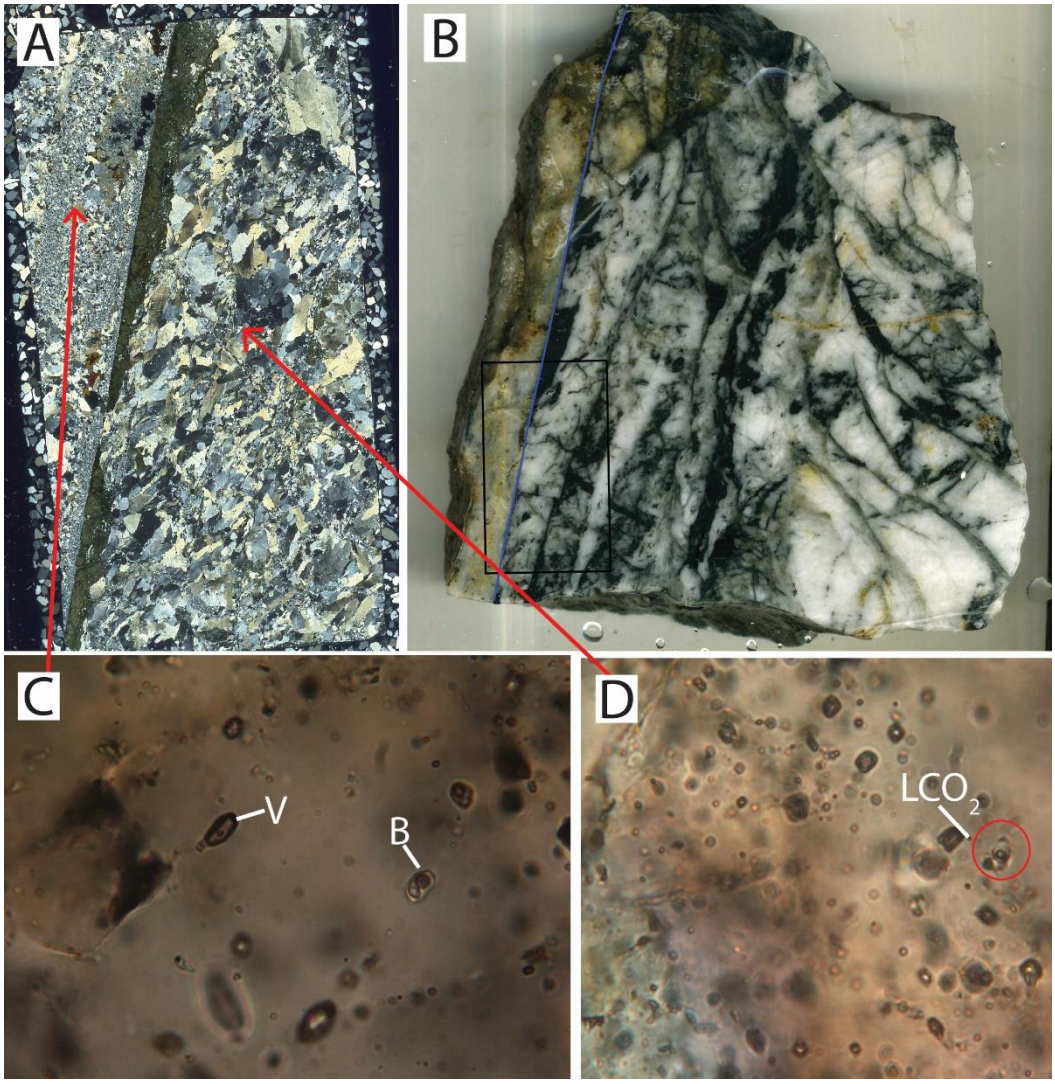

Fig. B-8. Example of a later Eq vein cutting and older Mq vein. A) XPL thin section scan showing an Eq vein (left) cutting an Mq vein (right). B) Hand sample, noting where the thin section from A comes from. C) Fluid inclusions from the Eq vein, which contains hypersaline brine rich inclusions and two-phase vapor rich inclusions. D) Fluid inclusions from the Mq part of the vein. One 3-phase liquid CO_2 bearing inclusions is highlighted in red.

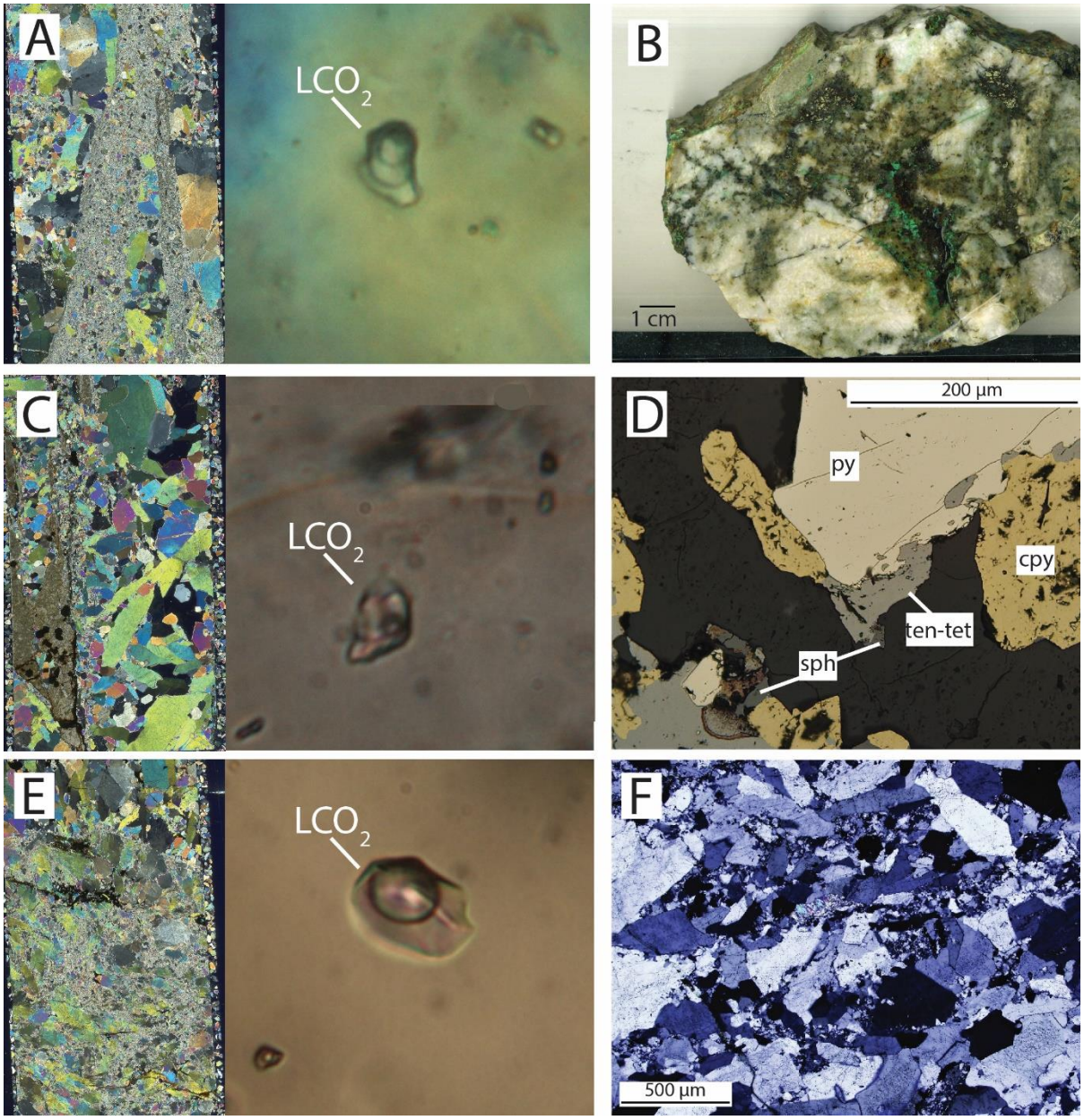

Fig. B-9. A) XPL thick section scan from the Berlin Mine that contains 3-phase liquid CO_2 inclusions. B) Hand sample of a Mq vein that contains secondary copper minerals (malachite). C) XPL thick section scan from the Richmond Mine that contains a liquid CO_2 bearing fluid inclusion. D) Reflected light image of a sample from the Richmond Mine. Contains pyrite, chalcopyrite, tennantite-tetrahedrite and minor sphalerite. E) XPL thick section scan from a sample from the Shamrock Mine workings. Contains 3-phase liquid CO_2 fluid inclusions. F) XPL image of recrystallized quartz commonly found in Mq veins.

Sodic-calcic (Sc) alteration

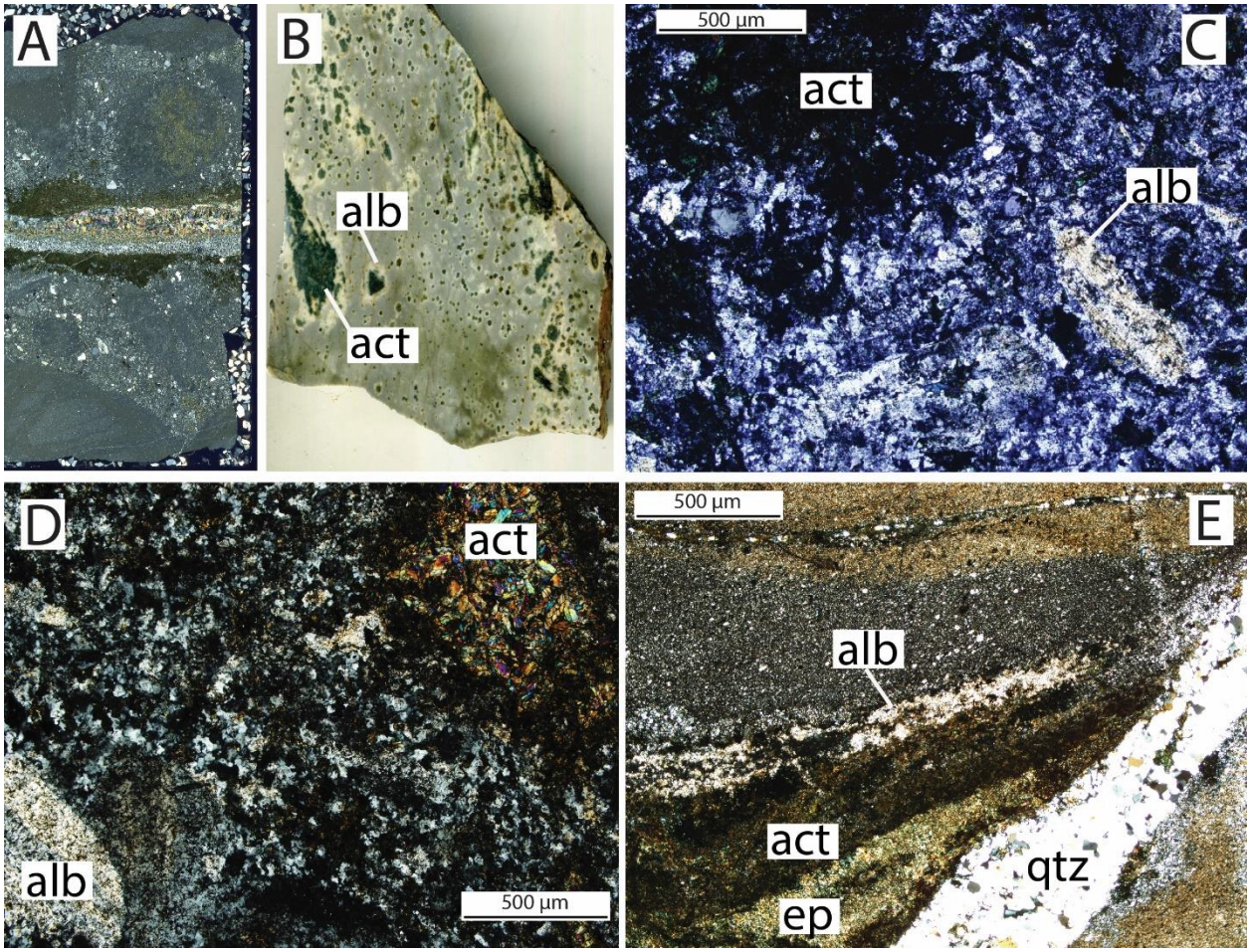

Fig. B-10. A) XPL thin section scan of a Sc vein that contains actinolite, albite, epidote, quartz and apatite. B) Hand sample of TRkvc that contains phenocrysts and clasts altered to actinolite with rims of albite. C-D) XPL images of a Jgd dikes that contains clots of actinolite and phenocrysts strongly altered to albite. E) XPL image of a Sc vein composed of act-ep-alb that is cut by a later quartz veinlet.

RBCPQ057 Actinolite, albite epidote alteration envelope around Sc vein

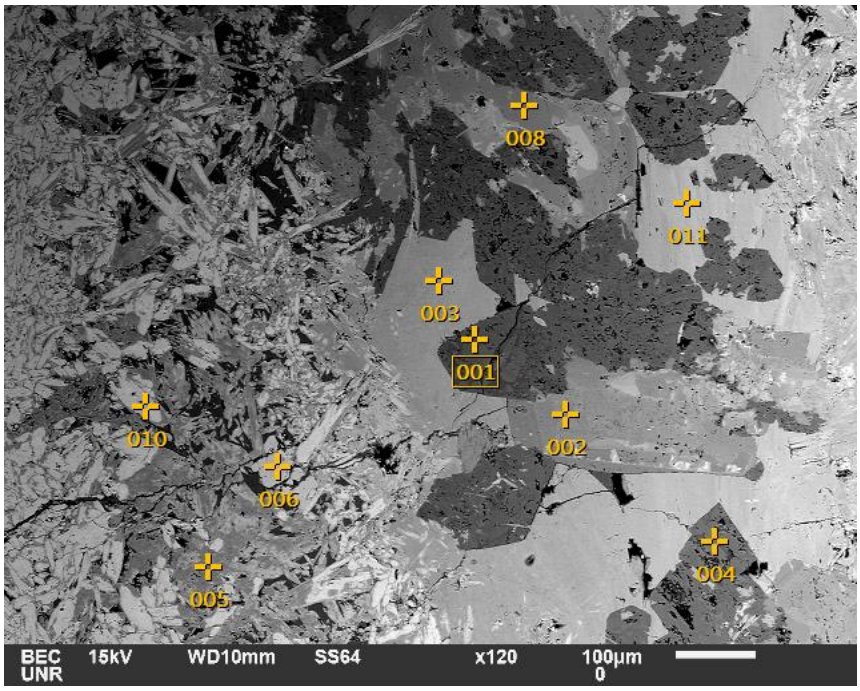

Volt : 15.00 kV
Mag. : x 120
Date : 2016/11/19
Pixel : 1280 x 960

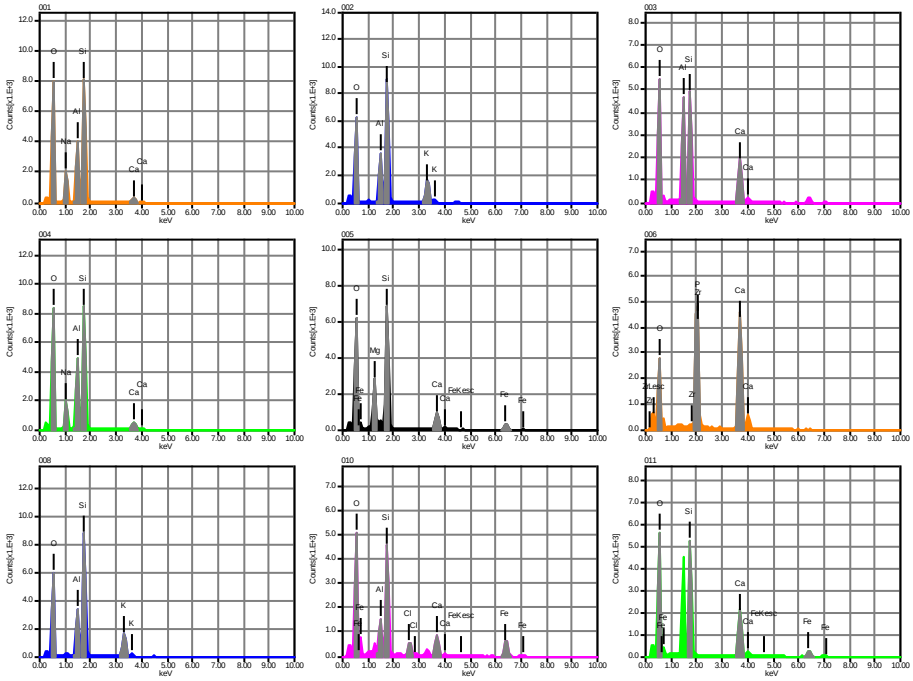

Acquisition Condition
Instrument : 6510(LA)
Volt : 15.00 kV
Current : ---
Process Time : T4
Live time : 11.26 sec.
Real Time : 15.00 sec.
DeadTime : 25.00 %
Count Rate : 18904.00 CPS

	CaO	O	Na2O	MgO	Al2O3	SiO2	P2O5	Cl	K2O	FeO	ZrO2	Likely Mienral
001	3.86	0.00	11.07		23.03	62.03						Albite/Oligoclase
003	26.82	0.00			29.80	43.38						Epidote (clinozoisite)?
004	6.13	0.00	9.35		25.37	59.14						Albite/Oligoclase
005	12.66	0.00		19.10		55.84				12.41		Actinolite
006	46.77	0.00					39.27				13.95	Apatite
010	12.38	0.00			11.53	42.94		3.67		29.48		Epidote
Average	20.39	0.00	10.21	19.10	21.40	55.46	39.27	3.67	16.36	18.69	13.95	
Standard deviation	15.94	0.00	1.22	0.00	6.25	8.70	0.00	0.00	0.30	9.39	0.00	

RBCPQ014D Actinolite, albite altering k-feldspar

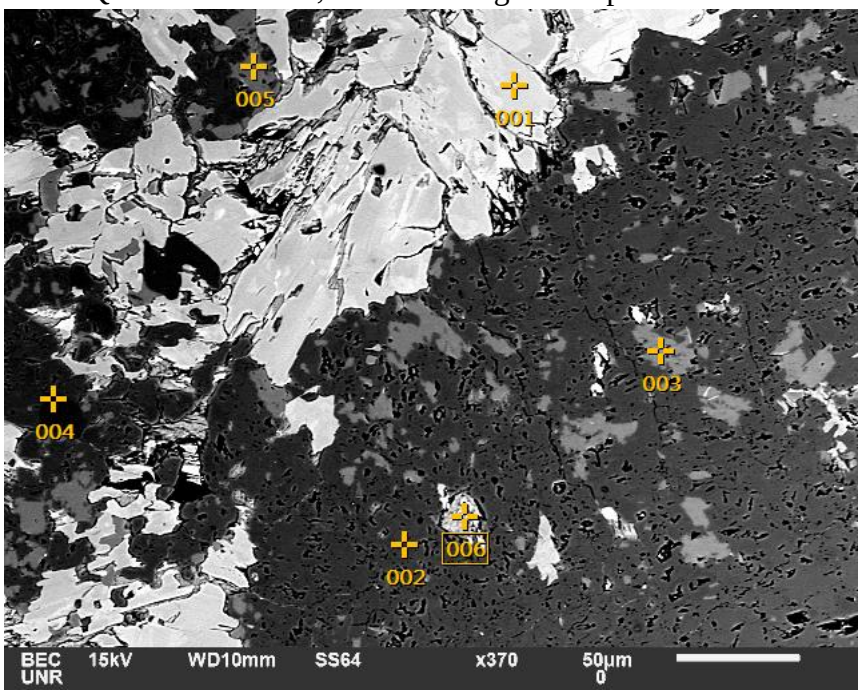

Volt : 15.00 kV
Mag. : x 370
Date : 2016/11/12
Pixel : 1280 x 960

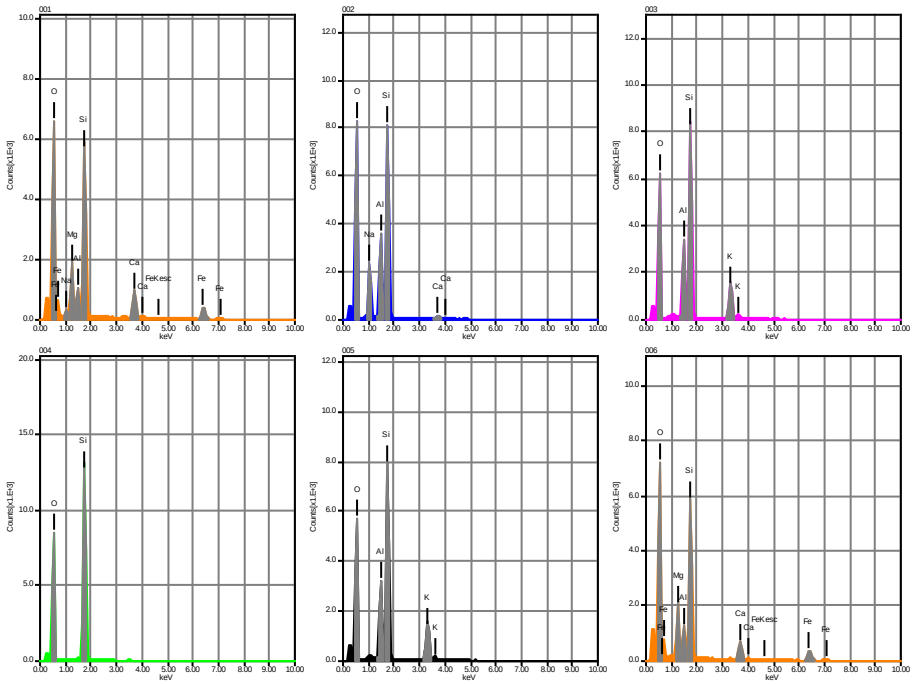

Acquisition Condition
Instrument : 6510(LA)
Volt : 15.00 kV
Current : ---
Process Time : T4
Live time : 11.67 sec.
Real Time : 15.00 sec.
DeadTime : 22.00 %
Count Rate : 16482.00 CPS

	CaO	O	Na2O	MgO	Al2O3	SiO2	K2O	FeO	Likely Mineral
001	11.86	0.00	1.32	13.31	6.69	49.87		16.95	Actinolite
002	1.78	0.00	12.69		21.12	64.41			Albite
003		0.00			19.42	64.68	15.90		K-Feldspar
004									
005		0.00			19.28	64.86	15.86		K-Felspar
006	9.22	0.00		14.59	8.43	51.37		16.38	Actinolite
Average	7.62	0.00	7.00	13.95	14.99	59.04	15.88	16.67	
Standard deviation	5.23	0.00	8.04	0.90	6.85	7.70	0.03	0.40	

RBCPQ035 Sc vein in Jd

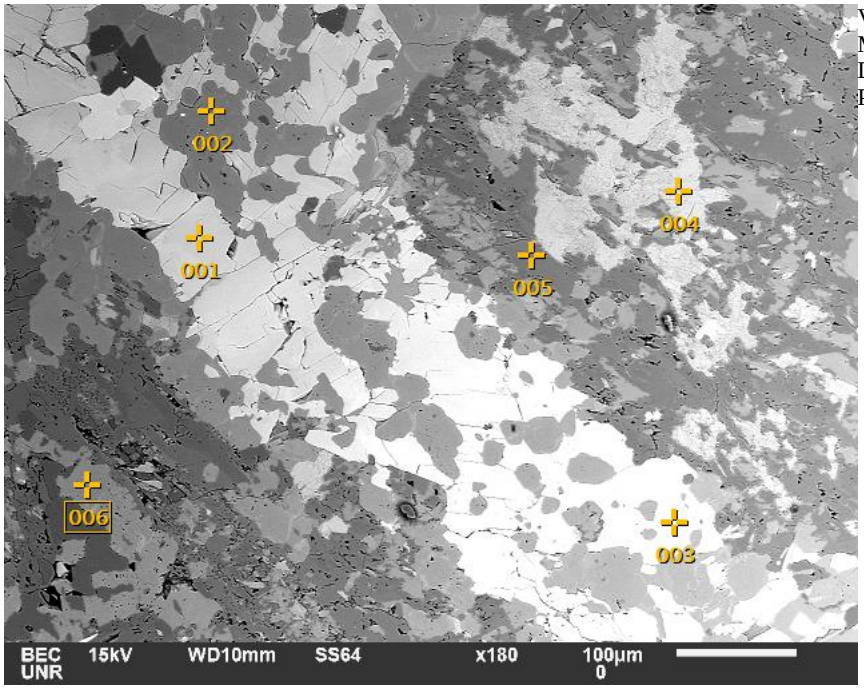

Volt : 15.00 kV
Mag. : x 180
Date : 2016/11/12
Pixel : 1280 x 960

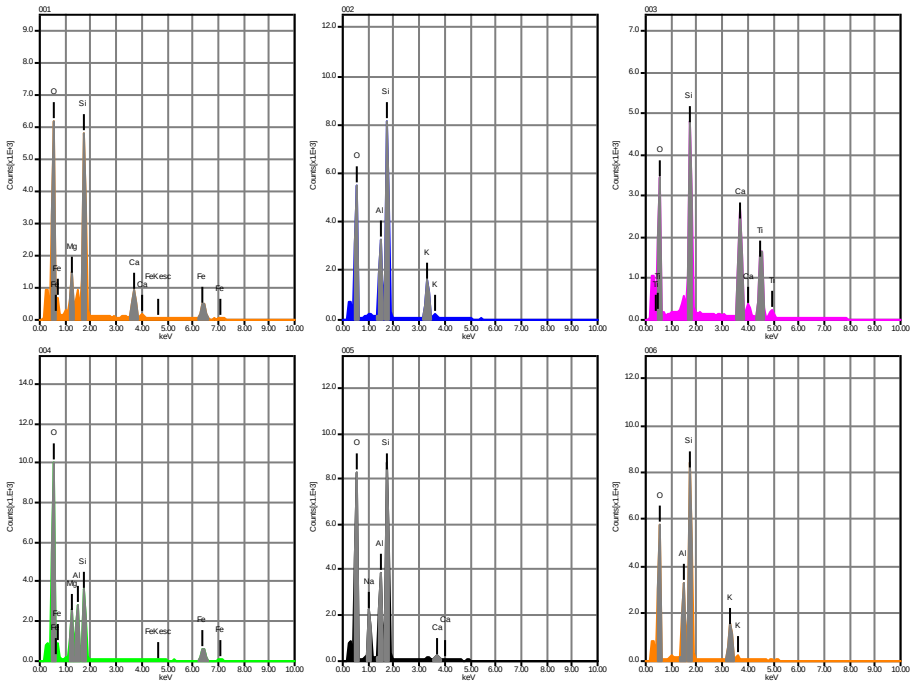

Acquisition Condition
Instrument : 6510(LA)
Volt : 15.00 kV
Current : ---
Process Time : T4
Live time : 11.58 sec.
Real Time : 15.00 sec.
DeadTime : 23.00 %
Count Rate : 16796.00 CPS

	CaO	O	Na2O	MgO	Al2O3	SiO2	K2O	TiO2	FeO	Likely Mineral
001	13.29	0.00		10.92		53.57			22.22	Actinolite
002		0.00			18.92	64.65	16.43			K-feldspar
003	29.94	0.00				33.29		36.77		Titanite
004		0.00		18.01	21.32	33.99			26.69	Chlorite
005	2.45	0.00	11.19		21.98	64.39				Albite
Average	15.23	0.00	11.19	14.46	20.74	49.98	16.43	36.77	24.45	
Standard deviation	13.85	0.00	0.00	5.01	1.61	15.57	0.00	0.00	3.16	

Evidence of Epithermal Overprint

Fig. B-11. Images that indicate overprinting epithermal features. Top left is a sample of quartz vein from Berlin Canyon that contains banded, colloform vein textures (indicated by red arrow). Bottom is an image of bladed quartz and calcite, which indicates boiling conditions. Found in the Grantsville pit.

Appendix C: Whole Rock Geochemical Data for Intrusive Rocks

	Sample ID	RBCPQ088	RBCPQ035	RBCPQ051	RBCPQ016	RBCPQ083	RBCPQ061	RBCPQ021B	BCD-101-241	RBCPQ002	RBCPQ003	BCD-101-331	RBCPQ021A	RBCPQ004
	Rock Type	Jd (Sham.)	Jd	Jd	Jgd	Jgd	Jgd	Kmd	Kmd	Kmd	Kmd	Klg	Klg	Klg
	Easting (NAD83)	449744	447653	447738	447375	447898	447470	447722	448535	448709	448710	447722	447722	448740
	Northing (Z11)	4310427	4305477	4305574	4305168	4304960	4304734	4305788	4304046	4304034	4304024	4305788	4305788	4303975
Method														
ME-XRF26	Al2O3 %	15.9	16.34	16.48	16.58	15.84	15.8	16.05	16.55	15.75	16.1	15	14.55	14.64
ME-XRF26	BaO %	0.13	0.13	0.12	0.17	0.19	0.19	0.14	0.15	0.21	0.19	0.27	0.21	0.14
ME-XRF26	CaO %	8.09	5.27	5.73	2.74	3.39	3.62	3.12	4.79	3.41	3.7	2.47	1.03	1.53
ME-XRF26	Cr2O3 %	0.03	0.01	0.01	<0.01	<0.01	0.01	<0.01	<0.01	<0.01	<0.01	<0.01	<0.01	<0.01
ME-XRF26	Fe2O3 %	8.2	5.94	6.47	4.9	3.78	3.62	4.33	5.06	4.19	4.59	1.47	1.18	1.5
ME-XRF26	K2O %	2.11	2.76	2.54	3.3	3.83	2.91	3.07	2.77	3.54	3.28	5.05	5.34	3.92
ME-XRF26	MgO %	6.09	2.94	3.24	2.25	2.05	1.76	1.3	2.41	1.87	2.18	0.62	0.28	0.39
ME-XRF26	MnO %	0.13	0.1	0.09	0.04	0.06	0.05	0.05	0.09	0.07	0.08	0.05	0.02	0.04
ME-XRF26	Na2O %	3.08	3.86	3.68	4.42	4.11	5.04	4.06	3.68	3.65	3.77	1.72	4.09	4.15
ME-XRF26	P2O5 %	0.27	0.26	0.26	0.22	0.17	0.18	0.19	0.24	0.21	0.25	0.06	0.05	0.05
ME-XRF26	SiO2 %	54.63	60.84	59.46	63.43	64.05	64.22	65.1	61.8	64.7	62.9	68.5	72.3	72.61
ME-XRF26	SrO %	0.08	0.08	0.07	0.06	0.07	0.09	0.08	0.08	0.07	0.07	0.04	0.05	0.06
ME-XRF26	TiO2 %	0.75	0.77	0.8	0.48	0.45	0.42	0.56	0.7	0.62	0.67	0.21	0.19	0.17
OA-GRA05x	LOI 1000 %	0.47	0.55	0.66	1.46	1.94	2.07	1.43	0.95	1.98	2.24	3.49	0.59	0.59
ME-XRF26	Total %	100.05	99.91	99.67	100.1	100	100.05	99.57	99.56	100.45	100.15	99.81	99.97	100.1
ME-MS81	Ba ppm	1255	1195	1095	1715	1885	1720	1295	1390	1985	1850	2630	2110	1250
ME-MS81	Ce ppm	42.2	49.9	49.8	56.9	62.1	46.5	53.4	54.8	57.4	58.2	46.4	43.7	41
ME-MS81	Cr ppm	190	50	30	30	30	30	10	50	30	40	20	10	<10
ME-MS81	Cs ppm	5.49	7.07	5.95	6.45	3.31	2.84	7.07	4.58	8.2	5.5	14	3.03	5.22
ME-MS81	Dy ppm	3.09	2.75	3.17	2	2.09	1.65	2.99	3.15	2.88	2.97	1.29	1.52	1.41
ME-MS81	Er ppm	1.54	1.78	1.71	1.07	1.16	0.91	1.79	1.73	1.54	1.61	0.7	0.78	0.77
ME-MS81	Eu ppm	1.17	1.08	1.12	0.67	1.09	0.77	0.91	1.16	0.99	1.13	0.68	0.68	0.47
ME-MS81	Ga ppm	16.4	19.5	19.2	16.2	15.8	17.6	20	20.1	18.7	19.1	19.8	17.7	17.1
ME-MS81	Gd ppm	3.47	3.66	3.76	2.42	2.79	2.35	4.04	3.99	3.73	4.15	1.97	2.08	2.24
ME-MS81	Hf ppm	2.7	4.7	4.2	4.1	4.6	3.1	4.3	5.1	5	4.8	3.6	3.5	2.9
ME-MS81	Ho ppm	0.59	0.55	0.61	0.37	0.41	0.3	0.63	0.61	0.58	0.62	0.24	0.3	0.27
ME-MS81	La ppm	20.7	24.7	24.4	30.5	33.1	25.1	26.7	28	29.5	30.1	23.9	23.8	25
ME-MS81	Lu ppm	0.23	0.25	0.24	0.17	0.17	0.13	0.22	0.25	0.22	0.23	0.09	0.13	0.1
ME-MS81	Nb ppm	5.8	8.7	8.6	8.7	9.7	7	11.2	10.6	11	10.6	7.9	7.5	7.8
ME-MS81	Nd ppm	20.3	24.9	24.5	20.7	23	19	24.6	24.1	25.1	25.6	17.9	17	15.6
ME-MS81	Pr ppm	5.12	5.97	6.05	5.97	6.59	5.11	6.31	6.48	6.43	6.78	5.06	4.86	4.44
ME-MS81	Rb ppm	58.8	79.8	77.8	87.5	90.7	89.9	114.5	83.9	127	117.5	218	189	141.5
ME-MS81	Sm ppm	3.97	4.93	4.8	3.44	4.08	3.16	4.89	4.85	4.72	4.61	3.04	2.97	3.01
ME-MS81	Sn ppm	1	2	1	3	6	1	2	1	1	2	1	1	1
ME-MS81	Sr ppm	729	675	667	525	626	787	640	684	578	652	330	483	476
ME-MS81	Ta ppm	0.3	0.5	0.4	0.6	0.7	0.4	0.8	0.7	0.7	0.7	0.8	0.8	0.8
ME-MS81	Tb ppm	0.51	0.5	0.54	0.35	0.37	0.34	0.56	0.62	0.51	0.58	0.29	0.29	0.29
ME-MS81	Th ppm	5.51	7.11	7.46	14.15	18.45	8.88	10.3	8.34	10.9	9.27	19.15	13.8	14.35
ME-MS81	Tm ppm	0.24	0.23	0.26	0.15	0.17	0.11	0.28	0.24	0.24	0.25	0.09	0.14	0.12
ME-MS81	U ppm	1.97	2.46	2.29	4.39	5.27	3.72	4.89	3.06	3.7	3.07	9.59	5.56	1.91
ME-MS81	V ppm	209	131	148	109	78	76	68	110	85	96	18	20	18
ME-MS81	W ppm	1	1	1	1	1	1	1	2	2	2	1	1	1
ME-MS81	Y ppm	16.3	15.9	16.8	10.2	11.5	8.8	16.9	16.2	15.1	15.4	6.6	8	8.5
ME-MS81	Yb ppm	1.65	1.52	1.68	1.06	1.07	1.03	1.82	1.58	1.56	1.43	0.64	0.77	0.77
ME-MS81	Zr ppm	98	165	143	147	167	100	167	197	203	199	124	115	99
ME-4ACD81	Ag ppm	<0.5	<0.5	<0.5	<0.5	<0.5	<0.5	<0.5	<0.5	<0.5	<0.5	<0.5	<0.5	<0.5
ME-4ACD81	Cd ppm	<0.5	0.5	<0.5	0.8	<0.5	<0.5	<0.5	<0.5	<0.5	<0.5	<0.5	<0.5	<0.5
ME-4ACD81	Co ppm	29	13	13	6	6	8	5	11	8	9	1	1	2
ME-4ACD81	Cu ppm	41	26	15	48	26	25	16	11	11	8	2	15	10
ME-4ACD81	Li ppm	10	20	30	40	40	30	40	20	30	30	20	10	10
ME-4ACD81	Mo ppm	1	<1	<1	1	<1	<1	2	1	1	<1	<1	<1	2
ME-4ACD81	Ni ppm	73	15	12	10	16	19	3	6	7	6	<1	2	5
ME-4ACD81	Pb ppm	9	17	10	19	6	9	39	16	12	14	22	17	31
ME-4ACD81	Sc ppm	18	13	13	8	7	7	7	11	8	9	2	2	2
ME-4ACD81	Zn ppm	77	95	66	58	40	35	92	83	68	77	63	34	41
ME-MS42	As ppm	1.8	5.8	6.4	13.9	5	16	4.3	1.9	3.9	1.7	96	2.6	14.3
ME-MS42	Bi ppm	0.07	0.12	0.08	0.37	0.74	0.1	0.59	0.35	0.24	0.13	0.23	0.51	0.05
ME-MS42	Hg ppm	<0.005	0.011	0.007	<0.005	<0.005	0.021	<0.005	0.018	0.009	<0.005	0.031	<0.005	0.066
ME-MS42	Sb ppm	0.18	0.27	0.33	0.32	1.08	1.03	0.85	0.39	0.77	0.96	2.49	0.48	0.89
ME-MS42	Se ppm	0.4	0.2	0.2	0.4	0.4	0.2	0.4	0.4	0.4	0.3	0.2	0.2	0.2
ME-MS42	Te ppm	<0.01	0.01	0.01	0.13	0.03	<0.01	0.02	0.01	<0.01	<0.01	0.01	0.03	0.04
ME-MS42	Tl ppm	0.26	0.21	0.39	0.09	0.05	0.02	0.06	0.07	0.02	<0.02	0.1	0.07	0.03
S-IR08	S %	0.01	<0.01	0.04	<0.01	0.01	0.02	<0.01	0.07	0.04	0.02	0.29	<0.01	0.1
C-IR07	C %	0.05	0.03	0.01	0.02	0.25	0.28	0.07	0.09	0.22	0.24	0.48	0.07	0.04

	Sample ID	RBCPQ054A	BCD-101-66	RBCPQ029	RBCPQ027	BCD-101-457	RBCPQ102	RBCPQ020	RBCPQ114	RBCPQ054B	RBCPQ023	RBCPQ026	RBCPQ117A
	Rock Type	**Tqmd**	**Tqm**	**Td**	**Td**	**Td**	**Td**	**Tg**	**Tlg**	**Tlg**	**Tba**	**Tba**	**Tba**
	Easting (NAD83)	448344	447722	448338	448043	447722	448351	447662	448348	448344	448203	448066	448350
	Northing (Z11)	4305874	4305788	4305856	4305915	4305788	4305862	4305705	4305876	4305874	4305253	4305356	4305901
Method													
ME-XRF26	Al2O3 %	15.95	15.75	14.65	14.83	15.3	14.82	14.29	13.04	14.1	15	15.75	16.96
ME-XRF26	BaO %	0.13	0.16	0.16	0.16	0.21	0.16	0.15	0.09	0.15	0.11	0.09	0.11
ME-XRF26	CaO %	4.68	3.23	1.87	2.8	2.7	1.95	0.69	0.42	1.02	8.25	7.84	6.41
ME-XRF26	Cr2O3 %	0.01	<0.01	<0.01	<0.01	<0.01	<0.01	0.01	<0.01	0.01	0.02	0.03	0.01
ME-XRF26	Fe2O3 %	5.43	4.55	2.38	4.07	3.67	2.18	1.79	0.51	1.09	7.23	7.45	7.08
ME-XRF26	K2O %	3.14	3.94	4.49	4.28	4	4.09	4.21	4.66	3.86	1.26	1.45	1.92
ME-XRF26	MgO %	2.57	1.6	1.39	1.69	1.61	1.43	0.78	0.11	0.38	5.04	5.58	4.02
ME-XRF26	MnO %	0.09	0.07	0.06	0.07	0.07	0.06	0.03	0.01	0.02	0.18	0.12	0.12
ME-XRF26	Na2O %	3.76	4.05	3.39	3.35	3.81	3.81	3.79	4.01	4.3	2.51	2.41	3.7
ME-XRF26	P2O5 %	0.23	0.21	0.14	0.17	0.17	0.14	0.09	<0.01	0.06	0.23	0.24	0.26
ME-XRF26	SiO2 %	62.76	62.4	67.1	64.82	66.4	68.71	72.64	76.59	73.88	53.3	55.6	57.72
ME-XRF26	SrO %	0.07	0.06	0.04	0.04	0.07	0.06	0.04	0.03	0.07	0.08	0.07	0.09
ME-XRF26	TiO2 %	0.72	0.7	0.48	0.5	0.54	0.47	0.26	0.06	0.2	0.8	0.82	0.89
OA-GRA05x	LOI 1000 %	0.29	2.23	2.48	2.99	1.5	2.11	0.94	0.21	0.42	5.4	2.11	0.4
ME-XRF26	Total %	99.89	99.14	98.75	99.86	100.15	100.1	99.77	99.8	99.6	99.5	99.66	99.8
ME-MS81	Ba ppm	1120	1505	1545	1500	2030	1405	1370	716	1295	962	796	1005
ME-MS81	Ce ppm	56.5	55.6	61.4	50.2	58.3	55.5	33.4	14.9	35.6	42.9	41.3	45.7
ME-MS81	Cr ppm	40	30	30	30	30	20	10	<10	<10	200	200	60
ME-MS81	Cs ppm	3.9	5.35	4.43	3.37	8.41	6.55	5.57	2.5	3.2	2.7	4.87	6.44
ME-MS81	Dy ppm	2.87	3.69	2.86	2.91	2.77	2.8	1.36	0.42	1.18	3.31	4.4	3.13
ME-MS81	Er ppm	1.67	2.15	1.61	1.59	1.65	1.5	0.79	0.21	0.6	1.85	2.64	1.68
ME-MS81	Eu ppm	0.97	1.1	0.88	0.75	0.96	0.71	0.47	0.21	0.41	1.22	1.17	1.27
ME-MS81	Ga ppm	19	19.4	18.3	17.2	18.4	17.9	18	20.7	20.3	17.2	18	20
ME-MS81	Gd ppm	3.71	4.52	3.58	3.28	3.54	3.2	1.48	0.55	1.51	4.19	4.5	3.92
ME-MS81	Hf ppm	4.9	4.8	5.4	4.2	5.5	4.8	4.8	3.9	3.9	3.7	3.5	4
ME-MS81	Ho ppm	0.59	0.75	0.58	0.58	0.55	0.54	0.26	0.04	0.23	0.7	0.93	0.63
ME-MS81	La ppm	28	28.3	33	25.4	30.4	29.7	16.8	9.8	18.7	20.9	21	23.9
ME-MS81	Lu ppm	0.25	0.28	0.29	0.27	0.24	0.25	0.18	0.06	0.1	0.25	0.36	0.25
ME-MS81	Nb ppm	10.1	13.4	13.2	11.5	11.2	12.5	10.3	3.3	8.7	7.4	6.5	8
ME-MS81	Nd ppm	26.5	25.9	25.1	21.1	24.1	22.8	12.5	5.3	14.7	21.3	20.9	22.7
ME-MS81	Pr ppm	6.62	6.72	7.03	5.81	6.6	6.4	3.49	1.65	4.06	5.3	5.13	5.75
ME-MS81	Rb ppm	109	174	155.5	146	152.5	146	132.5	161.5	118.5	31.4	66.5	81.3
ME-MS81	Sm ppm	5.35	5.11	4.71	4.14	4.66	4.25	2.38	1	2.64	4.68	4.75	4.78
ME-MS81	Sn ppm	1	1	4	11	1	6	1	1	2	3	10	1
ME-MS81	Sr ppm	575	523	345	323	597	433	324	180.5	563	702	608	702
ME-MS81	Ta ppm	0.6	0.9	1.2	0.9	0.8	1.2	0.9	0.3	1.1	0.4	0.4	0.6
ME-MS81	Tb ppm	0.59	0.67	0.53	0.54	0.53	0.51	0.23	0.07	0.21	0.59	0.69	0.55
ME-MS81	Th ppm	10.4	10	16.8	15.15	12.95	16.7	16.55	22.7	22.1	5.54	5.24	7.24
ME-MS81	Tm ppm	0.27	0.28	0.27	0.23	0.24	0.24	0.14	0.02	0.11	0.3	0.38	0.27
ME-MS81	U ppm	3.3	3.5	5.73	5.76	4.47	4.45	4.94	12.55	7.27	2.14	2.17	2.23
ME-MS81	V ppm	125	92	70	76	71	59	31	5	19	175	179	158
ME-MS81	W ppm	2	1	2	1	2	1	1	1	1	2	1	3
ME-MS81	Y ppm	16.5	18.9	15.7	16.1	14.7	15.4	8.1	2.6	7.8	17.2	22.9	16.6
ME-MS81	Yb ppm	1.64	1.9	1.81	1.6	1.4	1.68	1.1	0.29	0.73	1.72	2.12	1.52
ME-MS81	Zr ppm	156	193	208	148	217	188	146	80	95	140	138	152
ME-4ACD81	Ag ppm	<0.5	<0.5	<0.5	<0.5	<0.5	<0.5	<0.5	<0.5	<0.5	<0.5	<0.5	<0.5
ME-4ACD81	Cd ppm	<0.5	<0.5	<0.5	<0.5	<0.5	<0.5	<0.5	<0.5	<0.5	<0.5	<0.5	<0.5
ME-4ACD81	Co ppm	11	8	1	3	7	1	2	2	4	21	7	19
ME-4ACD81	Cu ppm	12	13	1	31	8	4	9	3	4	2	4	13
ME-4ACD81	Li ppm	20	20	30	30	30	40	40	10	10	80	40	30
ME-4ACD81	Mo ppm	<1	<1	<1	<1	1	<1	1	<1	1	<1	<1	2
ME-4ACD81	Ni ppm	10	5	2	4	5	5	3	2	1	23	19	18
ME-4ACD81	Pb ppm	15	10	7	30	19	15	31	20	23	13	5	15
ME-4ACD81	Sc ppm	12	9	6	7	7	6	3	1	3	19	19	15
ME-4ACD81	Zn ppm	80	68	36	90	67	68	72	26	26	116	81	98
ME-MS42	As ppm	3.3	1.8	22.5	40.3	1.1	36.5	4.1	48.5	111.5	10.4	3.9	2.9
ME-MS42	Bi ppm	0.09	0.58	1.63	0.33	0.19	0.11	0.26	0.1	0.11	0.42	1.29	0.07
ME-MS42	Hg ppm	<0.005	0.005	0.008	0.011	<0.005	0.019	0.011	0.073	0.032	<0.005	0.007	0.008
ME-MS42	Sb ppm	0.26	0.48	0.25	0.54	0.51	0.54	0.19	0.4	2.57	0.69	0.81	0.33
ME-MS42	Se ppm	0.3	0.6	0.3	0.5	0.2	0.3	0.2	0.2	0.2	0.2	<0.2	<0.2
ME-MS42	Te ppm	<0.01	0.02	0.05	0.08	0.01	0.02	0.01	0.06	0.04	0.26	0.05	<0.01
ME-MS42	Tl ppm	0.2	0.02	0.05	0.09	0.02	0.03	0.06	0.04	0.03	0.02	0.12	0.3
S-IR08	S %	0.01	0.02	<0.01	0.01	0.02	0.01	0.01	0.01	<0.01	0.01	0.01	0.01
C-IR07	C %	0.01	0.34	0.37	0.48	0.15	0.3	0.05	0.02	0.02	0.71	0.13	0.01

Appendix D: Geochemical Data for Veining

Sample_ID	BC5-07	360957	BC5-13	360963	FSBC9673	FSBC9668	RBCPQ118	BC20161012	14081608	16081602	12081601	18081603
X_UTM84	447467	447432	447426	447516	448714	448574	447798	447667	447675	447586	447841	447478
Y_UTM84	4305474	4305354	4305441	4305393	4304038	4304116	4305824	4305731	4305560	4305166	4305354	4305231
Vein Type	Eq	Eq	Eq	Eq	Eq	Eq	Eq	Eq	Eq	Eq	Eq	Eq
Au_ppm	0.45	0.43	0.289	0.05	1.635	0.009	0.019	0.018	0.013	5.57	2.3	2.18
Ag_ppm	0.13	0.19	0.14	0.29	9.67	0.26	0.65	0.2	0.71	1.25	0.48	0.4
Al_%	1.06	2.84	1.07	6.45	2.91	7.36	7.1	5.88	7.18	4.75	4.51	5.91
As_ppm	29.3	7.3	23.4	69.1	576	37.1	10	48.5	17.4	22.9	52.3	46.4
Ba_ppm	30	380	70	1670	320	1150	1420	520	820	970	1040	1820
Be_ppm	0.38	0.75	0.43	1.07	0.99	0.88	2.27	2	1.53	1.52	1.04	1.6
Bi_ppm	1.58	3.02	0.46	2.16	0.02	0.12	2.02	0.72	1.27	48.2	0.8	1.52
Ca_%	1.27	1.8	1.04	2.02	0.11	0.75	0.87	1.59	2.07	0.31	0.56	0.63
Cd_ppm	0.49	0.22	0.51	0.56	0.04	0.13	0.21	0.57	0.6	0.43	0.41	0.98
Ce_ppm	51	19.3	27.8	34.7	13.95	31.1	65.7	23.6	39.7	47	30.5	80.9
Co_ppm	4.7	5	6.3	8.5	0.8	7.6	4.5	1.6	8.7	0.8	4.6	4.9
Cr_ppm	62	46	66	75	13	7	11	13	40	16	65	14
Cs_ppm	1.3	3.12	1.57	3.75	10.95	2.26	3.41	7.29	6.4	3.17	3.73	1.6
Cu_ppm	67.8	43.5	48.9	82.2	11.5	13.6	198	7.2	17.8	31.3	41.7	160.5
Fe_%	3.3	1.46	3.1	3.61	0.74	3.4	1.59	1.01	3.2	0.59	1.85	2.31
Ga_ppm	5.4	6.78	5.69	14.8	8.56	8.69	17.95	15.65	17.85	12.45	10.15	15.7
Ge_ppm	0.17	0.11	0.14	0.13	0.05	0.06	0.17	0.14	0.13	0.09	0.13	0.14
Hf_ppm	0.08	0.3	0.09	0.2	0.5	0.5	0.4	0.3	0.3	1.3	0.3	1.5
Hg_ppm	0.05	null	0.03	null	0.07	0.03	null	null	null	null	null	null
In_ppm	0.231	0.038	0.325	0.178	null	null	0.138	0.078	0.095	0.048	0.088	0.195
K_%	0.08	0.69	0.17	1.53	1.07	0.74	3.39	1.86	1.83	1.77	1.3	3.26
La_ppm	21.1	10	11.2	17.9	7.9	16.4	35.1	12.4	18.5	22.6	15.5	43.2
Li_ppm	27.5	40.3	27.7	63.3	164	19	46.1	24.4	65.5	16.1	32.6	30.9
Mg_%	0.66	0.61	0.76	1.27	0.08	0.66	0.46	0.28	1.49	0.17	0.67	0.4
Mn_ppm	348	207	463	607	34	748	294	365	593	139	359	245
Mo_ppm	2.11	4.12	3.75	3.73	1.54	0.77	1.43	3.48	1.55	3.64	4.75	6.52
Na_%	0.03	0.82	0.03	2.17	0.03	4.57	2.27	1.84	2.31	1.76	1.17	2.03
Nb_ppm	0.23	2.4	0.23	6.1	1.9	5.9	11.1	7.1	7.2	13.2	4.1	17.1
Ni_ppm	10.9	10.7	15.7	23.4	2.2	3.5	3.5	1.8	10.5	1.1	19.9	2.7
P_ppm	1310	520	1000	1370	60	1310	460	320	1060	700	900	890
Pb_ppm	13.3	7.8	19.2	29.2	11.9	9.9	26.2	24.7	27.3	31.1	14.6	18.7
Rb_ppm	5.1	52.3	11.8	85.5	97.8	26.8	136	113	119.5	80	75.7	101.5
Re_ppm	0.001	0.003	0.001	-0.002	0.001	0.002	<0.002	<0.002	0.003	-0.002	0.005	-0.002
S_%	0.005	-0.01	0.005	0.01	0.06	0.01	0.01	<0.01	-0.01	0.01	-0.01	0.01
Sb_ppm	0.4	1.39	0.47	1.61	56.1	4.84	1.78	1.37	1.48	2.93	1.57	2.97
Sc_ppm	4.8	4	5.7	12.2	2	4.3	4.2	3	11.3	5	7.3	6.7
Se_ppm	0.3	-1	0.3	1	1	1	1	<1	-1	1	1	1
Sn_ppm	2.9	7	4	4.9	0.4	0.8	2.4	2.4	4.2	9.5	2	7.4
Sr_ppm	26.9	99.6	28	326	36	499	302	135.5	448	95.6	188	281
Ta_ppm	0.005	0.15	0.005	0.39	0.14	0.33	0.84	0.62	0.47	0.79	0.25	1
Te_ppm	0.09	1.27	0.07	0.14	0.05	0.11	0.09	0.09	-0.05	9.95	0.5	0.16
Th_ppm	6.5	2.9	3.6	6.3	2.4	6.2	18.7	13.85	5.74	16.7	3.62	19.75
Ti_%	0.063	0.111	0.065	0.299	0.045	0.203	0.178	0.102	0.393	0.283	0.197	0.367
Tl_ppm	0.08	0.65	0.1	1.17	0.47	0.12	1.39	1.18	1.52	0.68	0.78	0.92
U_ppm	1.15	0.5	0.7	0.9	0.7	1.6	3.8	2.6	1.4	3.4	0.8	4.5
V_ppm	70	52	83	128	14	45	32	22	101	25	82	35
W_ppm	0.55	0.9	0.55	1.9	2.1	1.7	1.1	1.3	1.5	2.5	1.9	4.6
Y_ppm	13	8.5	11.95	17.5	2.2	5.4	12.7	7.1	14.4	14.8	14.1	18.6
Zn_ppm	61	28	73	90	6	36	55	53	135	21	55	52
Zr_ppm	1.2	4.7	2	3.7	15.2	15.5	9.4	10.1	5.8	47.1	11.2	51.4

Sample_ID	16081603	18081604	16081609	14081603	18081607	18081615	18081605	RBCPQ112	16081608	18081614	14081604	14081602
X_UTM84	447581	447467	447514	447703	447440	447378	447461	447525	447515	447381	447699	447704
Y_UTM84	4305167	4305236	4305200	4305517	4305228	4305244	4305235	4305338	4305194	4305242	4305529	4305517
Vein Type	Eq	Eq	Eq	Eq	Eq	Eq	Eq	Eq	Eq	Eq	Eq	Eq
Au_ppm	2.15	2.09	1.75	1.455	0.983	0.795	0.71	0.592	0.43	0.333	0.326	0.047
Ag_ppm	0.45	0.59	0.3	0.88	0.24	0.15	0.19	0.17	0.15	0.05	0.43	0.37
Al_%	6.86	5.85	6.79	4.66	4.69	5.86	5.5	0.54	7.56	7.87	5.63	7.17
As_ppm	47.1	21.5	118.5	14.8	22.7	16.1	19.6	6.4	25.8	12.7	23.9	29.5
Ba_ppm	1700	1980	750	340	990	1960	2170	40	2190	2070	700	640
Be_ppm	2.46	1.2	3.26	1.1	1.36	1.84	1.39	0.22	2.69	1.6	1.08	1.56
Bi_ppm	6.7	2.04	6.12	1.69	0.49	0.96	0.69	1.69	3.88	0.2	1.03	0.63
Ca_%	0.61	2.06	1.1	0.35	0.58	1.64	1.26	0.09	0.95	2.53	1.01	1.18
Cd_ppm	0.62	1.47	0.99	0.78	0.62	0.63	1.4	0.31	0.56	0.46	0.8	1.17
Ce_ppm	90.1	38.8	78.5	31.1	35.3	79.5	32.3	3.7	108	42.8	34.9	33.7
Co_ppm	4.9	11.6	4.6	6.7	7.2	3.9	8.2	0.9	4.2	10.2	7.7	10.3
Cr_ppm	10	54	5	30	62	11	51	18	4	5	35	41
Cs_ppm	3.55	6.53	3.3	3.45	9.28	6.44	3.95	1.11	1.43	10.85	3.64	6.33
Cu_ppm	209	297	203	8.9	132	56.8	98.3	16.2	168	60.6	21.9	14.1
Fe_%	2.65	2.92	3.67	2.42	3.21	1.89	2.85	0.47	2.74	4.46	2.97	4.08
Ga_ppm	19.05	13.05	21.7	11.4	12.95	14.3	13.35	1.89	20.5	18.4	14	18.2
Ge_ppm	0.15	0.12	0.14	0.11	0.1	0.14	0.15	0.08	0.17	0.12	0.09	0.11
Hf_ppm	2.6	0.4	1.5	0.1	0.7	1.5	0.5	<0.1	1.9	0.3	0.2	0.2
Hg_ppm	null	null	null	null	null	null	null	null	null	null	null	null
In_ppm	0.342	0.308	0.67	0.126	0.219	0.666	0.447	0.074	0.326	0.215	0.145	0.197
K_%	3.27	3.48	1.52	1.19	2.02	2.53	4.18	0.18	3.94	2.21	1.38	1.8
La_ppm	44.7	21.7	36	13.9	18.7	41.3	16.9	1.8	55.6	20.1	17.1	15.9
Li_ppm	33.4	32.4	30.7	62.2	35.5	20.8	30	11.4	31.6	57.5	53.9	73.2
Mg_%	0.42	0.8	0.37	0.96	0.95	0.4	0.58	0.07	0.46	1.66	1.12	1.43
Mn_ppm	215	388	271	884	335	339	381	100	269	243	786	1290
Mo_ppm	3.76	13.1	5.89	2.9	3.4	5.48	16.35	4.16	3.32	2.82	2.43	1.65
Na_%	2.93	1.14	3.5	1.26	1.2	1.77	0.98	0.03	3.05	2.57	1.52	1.53
Nb_ppm	20.2	4.9	20.5	3.8	6.7	18.3	4.6	0.9	23.2	11.7	5.2	6.9
Ni_ppm	1.3	15.3	2.1	6.5	22.8	3.2	13.1	2.9	1.1	7.6	7.7	9.3
P_ppm	1030	1140	1060	660	800	970	1110	120	1150	2080	810	1060
Pb_ppm	18.3	28.9	14	151.5	8.1	29.4	16.1	7.5	12.3	6.1	33	228
Rb_ppm	106	145.5	49.6	98.5	124.5	115	158.5	16.4	129	135.5	88.9	138.5
Re_ppm	0.004	0.007	-0.002	0.005	-0.002	-0.002	0.007	0.002	-0.002	-0.002	-0.002	-0.002
S_%	-0.01	0.03	-0.01	-0.01	-0.01	-0.01	0.01	<0.01	-0.01	-0.01	-0.01	-0.01
Sb_ppm	5.56	1.6	6.66	1.53	1.32	6.97	1.41	0.65	4.67	0.75	1.96	2.45
Sc_ppm	8.2	9.8	8.2	7.4	10.3	7	8.7	0.8	9.3	8.5	9.2	11.8
Se_ppm	1	1	1	-1	-1	1	-1	<1	1	1	-1	1
Sn_ppm	9.3	6.3	15.5	6.1	5.6	25.1	9.3	2.8	9.2	8.9	4.2	7.4
Sr_ppm	218	335	282	107	166	339	391	12.3	300	511	261	289
Ta_ppm	1.22	0.3	1.21	0.23	0.44	1.08	0.26	<0.05	1.38	0.64	0.34	0.44
Te_ppm	0.65	0.29	2.17	0.1	0.19	0.16	0.22	0.38	1.83	0.05	0.05	0.05
Th_ppm	24	4.42	24.3	3.31	5.67	20.9	3.69	0.81	27.2	7.7	4.34	5.35
Ti_%	0.428	0.244	0.43	0.222	0.259	0.379	0.236	0.027	0.495	0.402	0.283	0.367
Tl_ppm	0.89	1.35	0.48	1.08	1.29	1.44	1.26	0.2	0.98	2.14	1	1.44
U_ppm	4.8	1.1	5	0.6	1.1	4.5	1	0.1	5.8	1.4	0.9	1.1
V_ppm	38	117	47	76	133	35	105	15	43	125	80	108
W_ppm	3.2	2.3	4.1	2.4	1.5	5.9	1.7	1	2.4	1.1	2.2	2.8
Y_ppm	21.8	15.4	24.8	7.9	15.6	19	15.1	1.2	23.8	16.4	10.1	13.5
Zn_ppm	55	99	55	187	71	65	101	26	53	42	90	273
Zr_ppm	91.1	9.5	43.5	3.4	20.4	51.5	16.4	1.1	62.9	10.6	4.6	5.3

Sample_ID	RBCPQ106	18081609	14081611	14081607	16081605	18081602	18081613	16081604	18081606	16081610	13081601	13081607
X_UTM84	447810	447425	447641	447678	447557	447502	447384	447568	447458	447510	447765	447721
Y_UTM84	4305396	4305230	4305603	4305549	4305169	4305215	4305238	4305171	4305232	4305205	4305442	4305489
Vein Type	Eq	Eq	Eq	Eq	Eq	Eq	Eq	Eq	Eq	Eq	Eq	Eq
Au_ppm	0.143	0.311	0.068	0.356	0.882	0.788	0.591	0.129	0.076	0.063	0.766	0.51
Ag_ppm	0.79	0.13	0.32	1.08	0.09	0.14	0.17	0.17	0.45	0.37	0.27	0.17
Al_%	5.82	6.19	7.32	7.72	7.87	7.02	6.78	8.31	7.27	7.51	7.47	5.92
As_ppm	106.5	21	18.7	52.1	14.8	9.9	16.8	24.5	55.6	63.8	74.3	31.2
Ba_ppm	1750	950	860	870	2810	270	1620	1870	2800	920	2530	360
Be_ppm	1.62	1.71	1.56	1.62	3.1	2.3	1.52	2.84	1.26	2.1	2.92	1.25
Bi_ppm	0.72	0.22	0.41	2.7	3.02	0.96	0.27	5.68	0.65	0.27	1.09	0.36
Ca_%	1.24	1.75	2.86	2.24	1.31	0.74	2.01	1.33	2.72	1.13	0.88	0.53
Cd_ppm	0.49	0.35	0.77	1.57	0.23	0.1	0.49	0.53	1.44	1.3	0.97	0.52
Ce_ppm	55.7	49.5	42.7	43.9	114.5	36.8	52.6	113	43.8	52.4	86.7	33.7
Co_ppm	10.6	8.3	12.1	12.4	1.3	2.1	7.7	3.7	13.5	6.6	6.2	7.7
Cr_ppm	54	86	41	57	3	27	70	3	71	31	6	39
Cs_ppm	7.55	9.55	5.87	7.63	4.81	4.47	7.21	3.02	5.35	6.11	4.49	4.17
Cu_ppm	113	139	16.5	29	21	5.8	270	105	166.5	14.7	184.5	7.5
Fe_%	3.04	4.68	4.01	4.84	1.03	1.18	3.11	2.78	3.77	2.94	5.8	2.75
Ga_ppm	12.15	17.1	18.35	20.8	21.6	18.9	13.8	22.2	15.55	21.4	21.6	14.85
Ge_ppm	0.16	0.14	0.12	0.11	0.22	0.08	0.16	0.19	0.12	0.1	0.16	0.08
Hf_ppm	0.2	0.5	0.3	0.3	2	0.8	0.3	3.3	0.4	0.5	2	0.2
Hg_ppm	null	null	null	null	null	null	null	null	null	null	null	null
In_ppm	0.072	0.367	0.161	0.33	0.082	0.025	0.344	0.151	0.279	0.106	0.507	0.106
K_%	1.67	1.91	1.68	2.1	3.9	1.22	2.35	3.49	3.89	2.01	5.15	1.31
La_ppm	30.5	26.6	19.8	21.1	54.8	19.9	28.1	58.5	23.1	27.7	44.4	16.8
Li_ppm	33.9	56.7	52.9	76.3	20.4	49	51.2	21	22	50.3	31.5	62
Mg_%	0.95	1.87	1.72	1.79	0.34	1.03	1.21	0.37	0.75	1.24	0.52	1.15
Mn_ppm	366	443	934	1240	156	134	257	288	573	553	344	657
Mo_ppm	3.53	5.66	2.06	2.3	1.11	0.83	9.67	2.45	6.01	0.96	5.16	2.09
Na_%	1.66	2.16	2.41	1.68	2.61	3.28	2.41	3.88	2.11	2.18	2.05	1.87
Nb_ppm	6.2	9	6.7	7.9	24.1	8.5	5.9	24.9	6.3	8.8	21.5	6
Ni_ppm	23.2	34.1	11.7	14.5	1	8.3	22.3	1	19.1	8.5	2.1	9
P_ppm	1200	960	1180	1240	1260	710	1520	1240	1560	940	1180	850
Pb_ppm	23.7	9.8	38.6	210	7.2	3.9	11.3	21.7	34.8	53.9	59.5	8.2
Rb_ppm	104	127	86.8	128.5	134.5	93.1	129.5	125.5	166	122	135.5	124
Re_ppm	0.002	0.005	0.003	-0.002	0.003	-0.002	0.006	-0.002	-0.002	-0.002	-0.002	-0.002
S_%	0.01	-0.01	-0.01	-0.01	-0.01	-0.01	-0.01	0.01	0.06	0.01	0.01	-0.01
Sb_ppm	1.87	1.01	1.18	3.65	3.92	1.31	1.27	7.12	3.03	1.88	5.09	1.59
Sc_ppm	10.3	14.1	13.3	15.3	8.5	6.8	12.6	10.1	13.6	10	9.5	9
Se_ppm	1	1	1	1	1	-1	1	1	1	1	1	1
Sn_ppm	1.8	9.5	3.4	7.7	9.9	4.7	10.1	8.2	5.4	4.7	8.4	6.1
Sr_ppm	332	303	627	423	299	210	491	320	799	368	279	143.5
Ta_ppm	0.34	0.56	0.44	0.52	1.32	0.65	0.36	1.48	0.39	0.68	1.3	0.41
Te_ppm	0.21	0.07	-0.05	-0.05	1.21	0.34	0.06	2.55	0.09	0.06	0.18	0.11
Th_ppm	5.42	6.42	5.52	5.02	29.2	17.9	4.85	28.9	5.28	11.1	26.3	5.05
Ti_%	0.253	0.348	0.432	0.451	0.504	0.208	0.326	0.532	0.335	0.334	0.477	0.293
Tl_ppm	1.48	1.69	1	1.68	1.05	0.86	1.68	1.05	1.43	1.48	1.36	1.36
U_ppm	1	1.1	1.2	1.3	4.9	3.3	1	6.8	1.3	2	5.4	1
V_ppm	118	136	128	130	44	61	138	45	120	84	50	85
W_ppm	1.3	0.9	2.1	4.3	3.6	1	1.6	3.4	1.5	1.2	7.3	1.9
Y_ppm	20.3	19.7	14.2	16.2	25.1	9.8	21.9	25.9	21.5	15.5	24.3	10.2
Zn_ppm	127	85	162	323	24	27	62	51	137	152	133	66
Zr_ppm	5.9	14.6	6.5	5.7	83.4	24.9	7.5	123	10.6	12.2	64	3.5

Sample_ID	13081608	13081609	360961	360957	360961	RBCPQ014A	RBCPQ081A	RBCPQ091A	360964	360956	360954	1033982
X_UTM84	447720	447717	447525	447432	447525	447375	447845	447553	447678	447431	447608	448037
Y_UTM84	4305492	4305497	4305342	4305354	4305342	4305168	4305320	4305164	4305543	4305354	4304890	4305885
Vein Type	Eq	Eq	Eq	Eq	Eq	Eq	Eq	Eq	Tbm	Tbm	Tbm	Tbm
Au_ppm	0.435	0.066	0.529	0.43	0.529	0.688	13.2	5.23	12.5	1.245	0.009	1.34
Ag_ppm	1.49	0.17	0.31	0.19	0.31	0.23	2	0.46	100	2.14	0.47	17.1
Al_%	5.1	7.1	1.4	2.84	1.4	5.15	0.78	6.66	3.65	6.43	2.94	0.39
As_ppm	87	32.7	9	7.3	9	29.2	4.2	7	10000	11	45.7	777
Ba_ppm	190	840	80	380	80	600	80	2590	160	370	180	60
Be_ppm	1.46	1.51	0.36	0.75	0.36	1.42	0.24	2.53	1.82	1.59	1.55	0.25
Bi_ppm	2.08	0.42	32.3	3.02	32.3	0.7	18.2	8.62	884	535	98.6	41
Ca_%	0.45	1.97	0.13	1.8	0.13	1.92	0.46	0.77	0.66	3.84	4.76	0.36
Cd_ppm	1.82	0.88	0.28	0.22	0.28	0.95	0.34	0.31	52.1	0.33	0.06	2.6
Ce_ppm	22.9	44.3	5.8	19.3	5.8	30	6.42	78.1	14.65	29.2	195	null
Co_ppm	4.6	9.9	1	5	1	9.4	0.9	2.8	2.6	5.9	4.7	3
Cr_ppm	34	43	54	46	54	18	23	8	32	67	25	22
Cs_ppm	6.67	4.7	1.95	3.12	1.95	3.46	1.01	2.3	7.75	6.01	5.2	null
Cu_ppm	13.5	15.3	18.4	43.5	18.4	190.5	9.8	119	1310	44	4	354
Fe_%	3.29	3.42	0.6	1.46	0.6	3.24	0.5	3.33	17.35	3.16	1.4	1.98
Ga_ppm	12.55	17.9	3.9	6.78	3.9	12.3	2.06	16.35	13.85	16.95	9.99	5
Ge_ppm	0.09	0.1	0.09	0.11	0.09	0.17	0.15	0.29	0.13	0.11	0.26	null
Hf_ppm	0.1	0.2	0.1	0.3	0.1	0.6	0.1	1.5	0.1	0.3	1.3	null
Hg_ppm	null	null	null	null	null	null	null	null	null	null	null	0.5
In_ppm	0.504	0.12	0.066	0.038	0.066	0.706	0.028	0.788	31	0.257	0.13	null
K_%	1.86	1.65	0.34	0.69	0.34	1.31	0.22	4.31	0.96	1.14	1.21	0.1
La_ppm	10	22.8	3.4	10	3.4	14.9	3	36	8.2	15	82.5	10
Li_ppm	67.4	57.8	19.5	40.3	19.5	24.5	13.3	26.2	43.5	69.9	44.6	null
Mg_%	0.83	1.39	0.17	0.61	0.17	0.81	0.11	0.39	0.57	1.4	0.5	0.18
Mn_ppm	1070	536	135	207	135	427	146	343	148	344	1100	241
Mo_ppm	3.27	1.69	6.46	4.12	6.46	6.78	5.32	3.51	131.5	1.66	1.93	4
Na_%	0.09	2.28	0.19	0.82	0.19	2.18	0.19	1.84	0.2	1.77	0.03	0.02
Nb_ppm	4.8	7.7	1.6	2.4	1.6	5.4	1.5	18.6	2.3	6.6	5.6	null
Ni_ppm	6.8	10.1	4.4	10.7	4.4	9	2.5	1.4	4.1	26.3	4.8	6
P_ppm	710	1090	240	520	240	620	80	980	560	1150	400	1340
Pb_ppm	299	22.8	6.9	7.8	6.9	18	32.6	11.4	42700	13	12.1	1425
Rb_ppm	176	103	32.6	52.3	32.6	63.3	15.3	121	74.1	107.5	77.7	null
Re_ppm	-0.002	-0.002	0.003	0.003	0.003	<0.002	<0.002	<0.002	-0.002	-0.002	-0.002	null
S_%	-0.01	-0.01	-0.01	<0.01	<0.01	<0.01	<0.01	<0.01	0.9	-0.01	0.01	0.07
Sb_ppm	4.08	1.44	2.06	1.39	2.06	1.53	1.14	10.6	195.5	2.3	12.85	6
Sc_ppm	6.7	12.4	3	4	3	7.5	0.5	7.7	5.5	11.3	15.4	1
Se_ppm	1	1	-1	<1	<1	1	1	1	7	2	3	null
Sn_ppm	8.6	4.3	7.3	7	7.3	18.7	1.5	14.2	8	15.2	1.4	null
Sr_ppm	29	490	26.5	99.6	26.5	350	19.8	309	1680	286	109.5	49
Ta_ppm	0.3	0.53	0.09	0.15	0.09	0.39	0.08	1.01	0.16	0.43	0.35	null
Te_ppm	0.14	0.06	19	1.27	19	0.1	9.63	2.76	0.08	227	55.2	null
Th_ppm	4.19	6.32	1.6	2.9	1.6	8.21	1.56	22.2	3	6.7	7.7	10
Ti_%	0.24	0.403	0.063	0.111	0.063	0.182	0.037	0.408	0.142	0.281	0.154	0.01
Tl_ppm	1.61	1.2	0.37	0.65	0.37	0.88	0.25	1	0.68	1.21	0.55	5
U_ppm	1	1.3	0.4	0.5	0.4	2	0.2	3.6	18.5	2.2	2.2	5
V_ppm	83	102	37	52	37	68	8	38	673	133	48	55
W_ppm	5.6	1.3	1.1	0.9	1.1	1.4	0.6	2	6.1	1.5	1.4	5
Y_ppm	9.9	15	3.3	8.5	3.3	13.4	1.8	21.3	5.9	20.7	26.8	null
Zn_ppm	567	89	15	28	15	70	16	43	3510	44	35	254
Zr_ppm	3.1	5.4	2.7	4.7	2.7	16.2	1.2	46.5	2.9	6.9	50	null

Sample_ID	BC5-05	FSBC17995	BC5-10	70570	1033975	70582	1033957	FSBC18007	1033968	BC006	FSBC9629	70581
X_UTM84	447496	448389	447689	447998	447869	447675	447556	448021	447957	449410	448010	447723
Y_UTM84	4305352	4305800	4305544	4305113	4305813	4305217	4305173	4305030	4305622	4307210	4305101	4305298
Vein Type	Tbm	Tbm	Tbm	Tbm	Tbm	Tbm	Tbm	Tbm	Tbm	Tbm	Tbm	Tbm
Au_ppm	0.935	0.706	3.64	0.01	0.06	0.205	0.192	0.0025	0.614	0.04	0.007	0.221
Ag_ppm	0.09	8.4	1.54	0.3	0.2	0.1	0.1	0.5	18.7	0.2	0.15	0.1
Al_%	0.74	1.19	1.05	0.96	3.08	1.76	0.6	0.52	1.38	0.69	0.856	1.2
As_ppm	10.4	583	1250	13	11	35	3	29	15000	448	13	17
Ba_ppm	20	60	70	70	690	60	60	70	20	210	78	50
Be_ppm	0.29	0.25	1.06	0.25	0.6	0.25	1	0.8	0.25	0.5	0	0.7
Bi_ppm	14.7	13	12.1	12	11	5	4	4	2	2	1.5	1
Ca_%	2.6	0.28	0.63	1.62	1.8	1.04	1.89	1.87	0.73	0.61	1.351	1.12
Cd_ppm	0.27	2.1	2.26	0.25	0.25	0.25	0.25	0.25	170	0.25	0.25	0.25
Ce_ppm	31	null	24.2	null	null	null	null	null	null	null	null	null
Co_ppm	5.8	5	3.5	3	8	7	1	1	7	3	3	3
Cr_ppm	48	29	18	16	51	49	2	5	20	111	17	3
Cs_ppm	2.37	null	3.33	null	null	null	null	null	null	null	null	null
Cu_ppm	18.8	57	473	10	395	162	4	3	320	16	28	100
Fe_%	1.12	2.44	3.52	1.89	2.78	3.49	0.64	0.62	3.88	2.66	1.86	1.98
Ga_ppm	2.66	5	4.64	5	10	10	5	5	5	5	5	10
Ge_ppm	0.05	null	0.05	null	null	null	null	null	null	null	null	null
Hf_ppm	0.03	null	0.03	null	null	null	null	null	null	null	null	null
Hg_ppm	0.05	0.03	0.05	0.01	1	null	0.5	0.02	3	0.15	0.5	null
In_ppm	0.066	null	1.3	null	null	null	null	null	null	null	null	null
K_%	0.12	0.17	0.22	0.19	0.6	0.21	0.18	0.29	0.14	0.28	0.198	0.17
La_ppm	13.6	10	12.6	10	10	10	50	50	10	10	9	20
Li_ppm	20.8	null	15	null	null	null	null	null	null	null	null	null
Mg_%	0.42	0.54	0.28	0.51	0.89	1.12	0.25	0.08	0.85	0.19	0.501	0.43
Mn_ppm	255	885	289	725	247	191	217	411	1130	405	796	113
Mo_ppm	4.33	1	11.45	2	1	5	0.5	2	45	16	9	2
Na_%	0.02	0.01	0.04	0.03	0.17	0.12	0.04	0.01	0.01	0.01	0.0275	0.1
Nb_ppm	0.025	null	0.025	null	null	null	null	null	null	null	null	null
Ni_ppm	10.7	17	4.9	8	18	26	0.5	1	12	5	16	2
P_ppm	680	1060	860	830	1360	960	1120	970	1160	580	663	1210
Pb_ppm	7.3	608	573	26	16	14	4	39	7200	20	6	11
Rb_ppm	10.9	null	22.1	null	null	null	null	null	null	null	null	null
Re_ppm	0.0005	null	0.0005	null	null	null	null	null	null	null	null	null
S_%	0.005	0.04	0.03	0.005	0.07	0.01	0.005	0.03	0.01	0.005	0.00025	0.005
Sb_ppm	0.35	8	14.45	1	1	2	1	1	62	8	1.5	2
Sc_ppm	2	1	2.1	2	7	4	3	1	2	1	2.5	3
Se_ppm	0.2	null	1.1	null	null	null	null	null	null	null	2.5	null
Sn_ppm	0.7	null	1.6	null	null	null	null	null	null	null	null	null
Sr_ppm	73.1	13	153.5	64	114	35	105	48	24	18	31	61
Ta_ppm	0.005	null	0.005	null	null	null	null	null	null	null	null	null
Te_ppm	3.45	null	0.07	null	null	null	null	null	null	null	null	null
Th_ppm	2.9	10	5	null	10	null	20	20	10	null	1.5	null
Ti_%	0.005	0.01	0.005	0.02	0.15	0.14	0.01	0.01	0.01	0.005	0.005	0.19
Tl_ppm	0.14	5	0.26	5	5	10	5	5	5	5	2.5	10
U_ppm	0.39	5	2.23	5	5	5	5	5	5	5	4	5
V_ppm	22	39	81	28	84	57	10	6	56	9	12	23
W_ppm	0.19	5	1.3	5	5	5	5	5	5	5	1	5
Y_ppm	9.31	null	11.55	null	null	null	null	null	null	null	null	null
Zn_ppm	18	322	286	27	49	49	20	10	32500	54	19	23
Zr_ppm	0.6	null	1	null	null	null	null	null	null	null	null	null

Sample_ID	FSBC9654	1033990	1033989	13081605	13081603	RBCPQ107	14081606	16081601	14081601	14081609	14081613	RBCPQ099
X_UTM84	447628	447984	447839	447729	447756	447728	447681	447597	447704	447672	447621	448051
Y_UTM84	4305301	4305614	4305693	4305477	4305451	4305479	4305545	4305164	4305518	4305566	4305617	4305400
Vein Type	Tbm	Tbm	Tbm	Tbm	Tbm	Tbm	Tbm	Tbm	Tbm	Tbm	Tbm	Tbm
Au_ppm	0.148	2.42	0.186	0.131	0.284	0.734	0.022	0.08	0.243	0.067	0.062	0.051
Ag_ppm	0.1	50.8	0.1	3.37	7.86	3.5	1.03	0.07	0.94	1.11	0.25	2.95
Al_%	1.63	2.11	1.85	7.5	6.25	7.53	8.15	7.61	7.02	6.14	7.83	1.64
As_ppm	18	4380	18	102.5	682	119.5	40.5	75	155	377	27.9	42.1
Ba_ppm	100	30	540	560	270	590	1070	1970	210	130	1120	30
Be_ppm	0.25	1	0.25	1.63	1.88	1.8	1.69	3.1	1.54	1.55	1.53	0.84
Bi_ppm	1	39	3	2.83	8.24	3.18	1.58	1.44	1.4	0.96	0.63	4.5
Ca_%	0.95	0.4	0.73	0.44	0.51	0.44	1.93	0.81	0.55	0.65	3.13	0.48
Cd_ppm	0.25	60.9	0.25	2.59	1.75	3.45	1.45	0.33	1.74	1.24	0.57	8.94
Ce_ppm	null	null	null	44.2	32.3	50.1	50.6	104.5	37.6	32.1	42.8	11.05
Co_ppm	7	5	12	8	13.5	8.8	11.9	2	5.9	6.4	13.6	2.4
Cr_ppm	30	31	73	21	56	20	47	2	44	41	41	27
Cs_ppm	null	null	null	7.31	7.32	7.8	7.42	5.22	8.31	4.12	6.27	0.73
Cu_ppm	108	478	135	36.2	209	37.1	19.2	59.4	7.8	33.7	17.2	42.7
Fe_%	3.27	6.24	3.43	5.43	3.29	4.56	4.21	2.05	5.3	4.64	4.13	1.44
Ga_ppm	10	10	10	19.85	14.55	20.1	20.7	20.6	17.35	16.3	20.1	4.93
Ge_ppm	null	null	null	0.13	0.09	0.13	0.16	0.16	0.12	0.1	0.11	0.12
Hf_ppm	null	null	null	0.3	0.6	0.4	0.3	3.3	0.3	0.2	0.4	0.1
Hg_ppm	0.01	2	1	null	null	null	null	null	null	null	null	null
In_ppm	null	null	null	4.5	0.528	1.88	0.31	0.416	0.576	0.499	0.177	0.764
K_%	0.44	0.11	0.89	2.77	2.23	2.94	2.42	3.53	1.89	0.95	1.9	0.16
La_ppm	10	5	10	20.2	17.8	23.1	23.5	53.8	17.5	15.6	20.7	6.2
Li_ppm	null	null	null	94.2	47.4	76.2	66.3	35.1	85.4	49	41	6.6
Mg_%	0.91	0.81	1.16	1.05	0.74	0.92	1.6	0.35	1.47	1.25	1.84	0.33
Mn_ppm	486	1075	346	1640	552	1530	1200	276	1740	641	834	181
Mo_ppm	1	19	0.5	2.01	28.3	2.05	1.42	0.94	1.71	2.28	0.9	1.12
Na_%	0.05	0.01	0.1	0.14	0.14	0.24	1.97	2.93	0.24	0.45	2.48	0.12
Nb_ppm	null	null	null	7.6	4.1	9.1	7.8	23.4	5.8	5.2	8.5	0.5
Ni_ppm	16	27	23	7.3	18.8	8.2	12.5	1.8	8.5	10.1	11.5	9.2
P_ppm	680	1100	1240	1030	1200	1030	1250	1170	1080	950	1210	140
Pb_ppm	6	8320	35	259	1890	259	183.5	8	235	131.5	32.9	425
Rb_ppm	null	null	null	229	201	233	138.5	141	182.5	89.2	76.8	12.6
Re_ppm	null	null	null	0.003	-0.002	<0.002	0.004	-0.002	0.005	-0.002	-0.002	<0.002
S_%	0.005	0.1	0.02	-0.01	-0.01	<0.01	-0.01	-0.01	-0.01	-0.01	-0.01	0.01
Sb_ppm	1	71	1	6.95	13.85	7.24	3.32	5.85	4.83	6.81	1.95	2.98
Sc_ppm	8	9	9	8.8	9.7	9.2	13.5	9.1	11.4	9.6	14.1	5.2
Se_ppm	null	null	null	1	1	1	-1	1	-1	-1	1	1
Sn_ppm	null	null	null	16.5	11.3	14.5	6.2	11.9	17.4	18.6	3.8	7.5
Sr_ppm	28	131	29	74.5	73.6	70.5	464	234	115.5	204	633	79.7
Ta_ppm	null	null	null	0.52	0.28	0.57	0.53	1.4	0.37	0.35	0.57	<0.05
Te_ppm	null	null	null	0.18	1.07	0.1	-0.05	0.47	0.09	-0.05	-0.05	0.76
Th_ppm	null	10	10	7.72	5.34	9.11	6.61	27.8	5.05	4.63	6.37	0.42
Ti_%	0.07	0.005	0.23	0.305	0.204	0.31	0.443	0.489	0.352	0.29	0.465	0.021
Tl_ppm	5	5	5	1.95	1.94	2.32	1.35	1.4	1.59	0.84	1.16	0.17
U_ppm	5	5	5	1.8	1.7	1.8	1.5	7.3	1.1	1.3	1.4	0.2
V_ppm	89	116	131	86	230	84	122	43	118	100	124	66
W_ppm	5	5	5	10.8	7.1	11.6	2.9	4.5	7.5	9.7	2.4	0.4
Y_ppm	null	null	null	14.1	16.5	14.9	16.7	24.3	12.8	10.5	14.4	3.5
Zn_ppm	53	17150	78	1300	1110	1620	343	29	493	344	119	1380
Zr_ppm	null	null	null	7.4	14.6	7.2	7.5	121	7.8	4.7	6.9	1.6

Sample_ID	1033986	FSBC17967	FSBC18019	RB052903-4	FSBC9609	SRBC20760	FSBC9681	FSBC18045	FSBC9625	70572	70574	70575
X_UTM84	448104	448428	447481	448366	449512	447843	447570	448139	448485	448379	448566	448591
Y_UTM84	4305808	4305547	4304935	4304443	4307223	4304243	4304620	4303874	4304395	4304932	4304830	4304854
Vein Type	Mq	Mq	Mq	Mq	Mq	Mq	Mq	Mq	Mq	Mq	Mq	Mq
Au_ppm	5.6	0.425	0.017	0.314	0.172	0.109	0.431	0.919	0.238	0.015	0.318	1.485
Ag_ppm	357	77.8	7.7	59.3	1.6	1.6	7.72	76.7	44.8	1.1	4.6	83.6
Al_%	0.32	1.66	0.65	0.78	0.74	0.33	0.73	0.2	0.263	0.41	0.17	0.52
As_ppm	15000	3840	270	144	241	231	272	330	713	88	50	25
Ba_ppm	30	40	20	1330	401	470	100	20	2210	20	400	70
Be_ppm	0.6	0.25	0.6	0.25	0	0.25	0.85	0.25	0	0.25	0.25	0.25
Bi_ppm	68	46	39	14	8	7	6.51	3	1.5	<1	<1	<1
Ca_%	0.34	0.25	0.2	0.67	7.5	0.21	0.71	0.03	0.362	0.13	0.07	1.98
Cd_ppm	687	32.5	1	20.6	2.7	0.25	0.11	0.25	116.1	0.25	0.25	1.9
Ce_ppm	null	null	null	null	null	null	7.85	null	null	null	null	null
Co_ppm	16	0.5	51	8	4	8	4.4	2	20	5	5	6
Cr_ppm	12	2	39	65	3	9	19	18	17	7	10	7
Cs_ppm	null	null	null	null	null	null	5.03	null	null	null	null	null
Cu_ppm	4600	369	10450	15500	173	517	733	326	28300	3440	116	2760
Fe_%	12	14.2	2.22	1.67	2.41	7.59	1.39	3.03	1.83	2.71	2.17	2.45
Ga_ppm	5	10	5	5	8	5	2.24	5	5	5	5	5
Ge_ppm	null	null	null	null	null	null	0.025	null	null	null	null	null
Hf_ppm	null	null	null	null	null	null	0.4	null	null	null	null	null
Hg_ppm	9	1.96	0.5	5.82	0.09	0.5	0.1	0.68	68	0.26	0.13	1.28
In_ppm	null	null	null	null	null	null	null	null	null	null	null	null
K_%	0.05	0.07	0.08	0.16	0.21	0.13	0.19	0.04	0.0894	0.04	0.02	0.06
La_ppm	10	5	30	20	14	5	4.5	5	5	10	5	10
Li_ppm	null	null	null	null	null	null	244	null	null	null	null	null
Mg_%	0.07	0.68	0.38	0.47	0.75	0.06	0.07	0.02	0.126	0.3	0.04	0.36
Mn_ppm	403	1045	172	173	1315	134	83	60	157	121	208	600
Mo_ppm	40	35	2	1	3	136	4.55	3	18	9	2	2
Na_%	0.01	0.01	0.02	0.02	0.03	0.005	0.01	0.01	0.0312	0.01	0.005	0.005
Nb_ppm	null	null	null	null	null	null	1.4	null	null	null	null	null
Ni_ppm	14	2	40	5	5	5	9.6	0.5	18	2	5	5
P_ppm	950	290	350	320	300	300	280	400	119	330	210	510
Pb_ppm	200000	8510	14	3	33	26	22.4	2	1.5	1	16	4
Rb_ppm	null	null	null	null	null	0.01	16.1	null	null	null	null	null
Re_ppm	null	null	null	null	null	21	0.001	null	null	null	null	null
S_%	0.2	0.3	0.06	0.07	0	1	0.18	0.24	0.175	0.01	0.02	0.04
Sb_ppm	2540	136	5	2890	1	null	48.2	958	17800	4	12	130
Sc_ppm	0.5	4	1	1	0	null	0.9	2	2.5	0.5	1	2
Se_ppm	null	null	null	null	1	null	1	null	2.5	null	null	null
Sn_ppm	null	null	null	null	null	null	0.3	null	null	null	null	null
Sr_ppm	41	33	14	52	309	16	63.5	7	71	6	7	35
Ta_ppm	null	null	null	null	null	null	0.07	null	null	null	null	null
Te_ppm	null	null	null	null	null	null	3.64	null	null	null	null	null
Th_ppm	10	10	10	null	null	10	1.5	10	1.5	null	null	null
Ti_%	0.005	0.01	0.005	0.005	0.005	0.005	0.048	0.005	0.005	0.005	0.005	0.005
Tl_ppm	null	null	null	null	20.7	null	0.12	null	2.5	null	null	null
U_ppm	40	null	null	null	null	null	2.2	null	null	null	null	null
V_ppm	48	26	13	29	10	41	18	10	13	14	7	23
W_ppm	20	-2	-2	-2	-2	-2	8.8	-2	-2	-2	-2	-2
Y_ppm	null	null	null	null	null	null	1.5	null	null	null	null	null
Zn_ppm	43500	3570	38	240	22	4	11	18	438	12	28	95
Zr_ppm	null	null	null	null	null	null	12.8	null	null	null	null	null

Sample_ID	FSBC17953	FSBC17980	FSBC18014	FSBC18017	FSBC18018	FSBC18030	FSBC18042	FSBC20869	FSBC9698	FSBC9700
X_UTM84	449071	449060	448183	447469	447403	448253	448006	449370	448661	448667
Y_UTM84	4307078	4306826	4305053	4304701	4304686	4303941	4303890	4307428	4304904	4304766
Vein Type	Mq	Mq	Mq	Mq	Mq	Mq	Mq	Mq	Mq	Mq
Au_ppm	0.007	0.102	0.0025	0.01	4.37	11.6	0.187	0.034	0.031	0.124
Ag_ppm	0.1	2.1	0.1	0.1	1	0.8	0.2	1.1	0.5	0.5
Al_%	0.61	0.2	0.06	0.07	0.05	0.23	0.07	0.25	0.28	0.37
As_ppm	65	96	4	75	695	31	53	407	4	49
Ba_ppm	120	60	10	10	10	40	130	2310	60	170
Be_ppm	0.25	0.25	0.25	0.25	0.25	0.25	0.25	0.25	0.25	0.25
Bi_ppm	<1	<1	<1	<1	<1	<1	<1	<1	<1	<1
Ca_%	0.86	2.61	0.42	0.04	0.01	0.07	0.02	4.45	0.38	0.2
Cd_ppm	0.25	0.25	0.25	0.25	2.3	0.25	0.25	0.25	0.25	0.7
Ce_ppm	null	null	null	null	null	null	null	null	null	null
Co_ppm	5	4	1	0.5	0.5	2	3	57	4	7
Cr_ppm	23	18	13	11	10	19	16	24	18	21
Cs_ppm	null	null	null	null	null	null	null	null	null	null
Cu_ppm	10	24	78	4	8	62	7	163	111	62
Fe_%	1.46	0.98	0.36	0.57	1.36	0.77	1.29	6.34	0.77	2.08
Ga_ppm	5	5	5	5	5	5	5	5	5	5
Ge_ppm	null	null	null	null	null	null	null	null	null	null
Hf_ppm	null	null	null	null	null	null	null	null	null	null
Hg_ppm	0.06	0.06	0.02	0.02	0.07	0.5	0.01	0.22	0.16	0.11
In_ppm	null	null	null	null	null	null	null	null	null	null
K_%	0.09	0.03	0.01	0.03	0.02	0.08	0.03	0.09	0.06	0.05
La_ppm	10	10	5	5	5	5	5	10	10	5
Li_ppm	null	null	null	null	null	null	null	null	null	null
Mg_%	0.26	0.2	0.08	0.01	0.005	0.04	0.01	0.12	0.09	0.08
Mn_ppm	832	201	155	73	28	196	47	1195	297	729
Mo_ppm	1	4	0.5	0.5	2	0.5	1	24	0.5	2
Na_%	0.01	0.01	0.005	0.01	0.01	0.01	0.01	0.04	0.01	0.005
Nb_ppm	null	null	null	null	null	null	null	null	null	null
Ni_ppm	9	3	4	2	1	3	0.5	44	4	6
P_ppm	480	410	30	10	30	150	50	410	1580	250
Pb_ppm	9	24	3	1	241	5	6	42	8	36
Rb_ppm	null	null	null	null	null	null	null	null	null	null
Re_ppm	null	null	null	null	null	null	null	null	null	null
S_%	0.01	0.01	0.005	0.01	0.31	0.02	0.38	0.12	0.005	0.02
Sb_ppm	2	7	1	6	10	2	1	7	8	3
Sc_ppm	1	1	0.5	0.5	0.5	0.5	0.5	4	1	2
Se_ppm	null	null	null	null	null	null	null	null	null	null
Sn_ppm	null	null	null	null	null	null	null	null	null	null
Sr_ppm	23	51	9	2	3	5	10	51	39	15
Ta_ppm	null	null	null	null	null	null	null	null	null	null
Te_ppm	null	null	null	null	null	null	null	null	null	null
Th_ppm	0.005	10	10	10	10	10	10	10	0.01	0.005
Ti_%	10	0.005	0.005	0.005	0.005	0.005	0.005	0.005	10	10
Tl_ppm	null	null	null	null	null	null	null	null	null	null
U_ppm	null	null	null	null	null	null	null	null	null	null
V_ppm	8	5	2	2	1	4	2	26	9	27
W_ppm	-2	-2	-2	-2	-2	-2	-2	-2	-2	-2
Y_ppm	null	null	null	null	null	null	null	null	null	null
Zn_ppm	19	12	5	13	158	9	3	58	19	37
Zr_ppm	null	null	null	null	null	null	null	null	null	null

Sample_ID	RB021103-1	RB052903-10	RB052903-11	RB052903-2	RB052903-3	RB052903-5	RB052903-6	RB110602-3	RLP102402-3	SRBC20757
X_UTM84	447464	448360	448395	448495	448419	448326	448079	448591	448915	447926
Y_UTM84	4304704	4304474	4304493	4304453	4304460	4304381	4304443	4304901	4305590	4304067
Vein Type	Mq	Mq	Mq	Mq	Mq	Mq	Mq	Mq	Mq	Mq
Au_ppm	0.877	0.466	0.04	0.512	0.15	0.407	0.0025	8.26	0.045	0.0025
Ag_ppm	0.7	0.5	6.1	0.4	2.1	0.4	0.1	10.8	0.2	0.1
Al_%	0.19	0.17	0.14	0.05	0.09	0.08	0.47	0.21	0.12	0.87
As_ppm	2780	13	9	11	17	13	4	10	258	5
Ba_ppm	40	20	1280	120	1040	20	30	60	30	1110
Be_ppm	0.25	0.25	0.25	0.25	0.25	0.25	0.25	0.25	0.25	0.25
Bi_ppm	<1	<1	<1	<1	<1	<1	<1	<1	<1	<1
Ca_%	0.07	1.38	0.11	0.03	0.04	0.04	3.17	3.34	0.59	1.38
Cd_ppm	0.25	0.25	0.25	0.25	0.25	0.25	0.25	0.25	0.25	0.25
Ce_ppm	null	null	null	null	null	null	null	null	null	null
Co_ppm	1	5	3	2	6	3	3	6	14	6
Cr_ppm	9	94	131	116	154	120	66	14	8	15
Cs_ppm	null	null	null	null	null	null	null	null	null	null
Cu_ppm	12	21	82	4	65	25	37	300	3	42
Fe_%	1.93	1.08	0.78	0.74	1	0.79	1.1	1.59	4.73	1.35
Ga_ppm	5	5	5	5	5	5	5	5	5	5
Ge_ppm	null	null	null	null	null	null	null	null	null	null
Hf_ppm	null	null	null	null	null	null	null	null	null	null
Hg_ppm	0.00005	0.01	0.08	0.03	0.05	0.04	0.03	0.09	0.15	0.5
In_ppm	null	null	null	null	null	null	null	null	null	null
K_%	0.15	0.06	0.03	0.02	0.03	0.03	0.03	0.01	0.03	0.15
La_ppm	10	5	5	5	5	5	5	5	5	10
Li_ppm	null	null	null	null	null	null	null	null	null	null
Mg_%	0.01	0.1	0.07	0.01	0.02	0.03	0.41	0.12	0.05	0.56
Mn_ppm	67	267	94	15	214	106	621	650	855	389
Mo_ppm	2	1	2	3	2	2	0.5	2	0.5	0.5
Na_%	0.005	0.005	0.02	0.01	0.02	0.005	0.005	0.005	0.005	0.02
Nb_ppm	null	null	null	null	null	null	null	null	null	null
Ni_ppm	2	5	6	5	4	5	4	5	3	12
P_ppm	270	190	90	110	40	90	170	320	40	530
Pb_ppm	53	1	4	1	45	8	1	2	6	3
Rb_ppm	null	null	null	null	null	null	null	null	null	0.005
Re_ppm	null	null	null	null	null	null	null	null	null	1
S_%	0.23	0.005	0.04	0.15	0.15	0.005	0.005	0.005	0.1	1
Sb_ppm	5	3	14	2	7	7	1	12	6	null
Sc_ppm	0.5	1	0.5	0.5	0.5	0.5	1	1	0.5	null
Se_ppm	null	null	null	null	null	null	null	null	null	null
Sn_ppm	null	null	null	null	null	null	null	null	null	null
Sr_ppm	15	16	9	8	14	5	32	48	11	86
Ta_ppm	null	null	null	null	null	null	null	null	null	null
Te_ppm	null	null	null	null	null	null	null	null	null	null
Th_ppm	null	null	null	null	null	null	null	null	null	10
Ti_%	0.005	0.005	0.005	0.005	0.005	0.005	0.005	0.005	0.005	0.005
Tl_ppm	null	null	null	null	null	null	null	null	null	null
U_ppm	null	null	null	null	null	null	null	null	null	null
V_ppm	2	6	6	3	5	5	12	13	25	12
W_ppm	-2	-2	-2	-2	-2	-2	-2	-2	-2	-2
Y_ppm	null	null	null	null	null	null	null	null	null	null
Zn_ppm	11	6	11	2	9	7	18	38	16	29
Zr_ppm	null	null	null	null	null	null	null	null	null	null

Sample_ID	SRBC20758	SRBC20762	SRBC20763	FSBC9670	FSBC9678	FSBC9669	360955	Richmond Vein	Berlin Vein	Shamrock Vein
X_UTM84	448059	448110	448135	448423	448595	448328	447434	449732	447409	450002
Y_UTM84	4303949	4304555	4304583	4304127	4303813	4304379	4304960	4302989	4303699	4310655
Vein Type	Mq	Mq	Mq	Mq	Mq	Mq	Mq	Mq	Mq	Mq
Au_ppm	0.006	0.0025	17.9	0.717	0.017	0.025	0.005	1.19	303	0.254
Ag_ppm	0.1	0.2	2.5	22	0.21	0.27	0.11	85.4	150	7.23
Al_%	0.48	2.18	0.74	0.29	1.33	0.52	1.46	0.25	1.2	0.55
As_ppm	17	13	122	33.2	323	11.9	34.5	68.9	72.1	124
Ba_ppm	190	130	120	40	130	40	20	100	130	20
Be_ppm	0.25	0.5	0.25	0.14	1.93	0.23	0.65	0.09	0.53	0.12
Bi_ppm	<1	<1	<1	0.09	0.06	0.02	1.01	0.34	0.23	0.02
Ca_%	1.92	3.97	0.58	0.91	0.13	0.06	1.21	0.03	0.05	0.35
Cd_ppm	0.25	0.25	0.25	1.01	0.07	0.03	0.15	1.75	1.75	0.28
Ce_ppm	null	null	null	2.11	28.9	4.32	33.2	0.94	10.1	1.31
Co_ppm	8	21	13	4.8	6.3	4	3.3	2.9	1.7	2.4
Cr_ppm	7	5	5	14	54	15	45	42	34	25
Cs_ppm	null	null	null	0.58	6.98	2.35	2.11	0.54	2.86	0.6
Cu_ppm	6	326	345	494	30.8	5.7	46.8	772	63.1	7.8
Fe_%	1.83	3.24	3.14	1.3	4.99	0.92	1.58	0.87	0.82	0.77
Ga_ppm	5	10	5	0.88	4.95	1.39	5.45	0.58	2.55	1.21
Ge_ppm	null	null	null	0.025	0.11	0.025	0.1	0.44	0.13	0.11
Hf_ppm	null	null	null	0.1	0.3	0.1	0.2	<0.1	0.3	0.1
Hg_ppm	0.5	0.5	0.5	0.04	0.03	0.05	null	null	null	null
In_ppm	null	null	null	null	null	null	0.155	0.013	0.084	<0.005
K_%	0.06	0.15	0.2	0.05	0.35	0.07	0.05	0.07	0.51	0.13
La_ppm	5	10	10	1.2	24.1	2.2	18.7	0.6	5	0.7
Li_ppm	null	null	null	6.4	15.9	13.4	20.1	7.4	25.6	9.5
Mg_%	0.23	1.99	0.19	0.12	0.09	0.12	0.23	0.02	0.1	0.07
Mn_ppm	490	942	222	248	69	204	128	54	93	78
Mo_ppm	0.5	0.5	2	2.97	6.68	1.82	2.89	2	0.47	1.21
Na_%	0.005	0.05	0.02	0.02	0.02	0.06	0.1	0.03	0.02	0.04
Nb_ppm	null	null	null	0.3	1.9	0.5	0.8	0.1	1.9	0.3
Ni_ppm	3	6	5	3.4	15.8	6.6	5.1	2.3	1.3	3
P_ppm	200	1070	1110	50	980	110	400	30	60	30
Pb_ppm	1	1	7	15.9	7	4.5	4.6	3.9	128	11.1
Rb_ppm	0.005	0.01	0.01	2.7	20.5	3.4	3	4.3	33.2	5.4
Re_ppm	5	3	14	0.001	0.003	0.001	-0.002	<0.002	<0.002	<0.002
S_%	3	4	3	0.13	0.01	0.005	-0.01	0.35	0.01	0.01
Sb_ppm	null	null	null	14.05	33.2	12.3	6.43	425	25.2	19.9
Sc_ppm	null	null	null	0.9	3	1.3	1.6	0.2	0.8	1.3
Se_ppm	null	null	null	0.5	7	0.5	-1	1	<1	<1
Sn_ppm	null	null	null	0.1	0.3	0.1	3.5	0.2	0.3	<0.2
Sr_ppm	44	103	42	17.5	24.1	23	73.4	8.8	11.5	19.9
Ta_ppm	null	null	null	0.0025	0.12	0.0025	0.06	<0.05	0.12	<0.05
Te_ppm	null	null	null	0.0025	0.47	0.0025	0.45	<0.05	0.16	<0.05
Th_ppm	10	10	10	0.3	1.9	0.4	1.8	0.18	1.53	0.15
Ti_%	0.005	0.22	0.01	0.012	0.059	0.022	0.035	0.007	0.034	0.028
Tl_ppm	null	null	null	0.02	0.26	0.02	0.04	0.05	0.14	0.04
U_ppm	null	null	null	0.2	3.8	0.2	0.3	0.1	1.7	0.5
V_ppm	17	105	40	11	38	19	15	4	20	16
W_ppm	10	-2	-2	1.2	1.8	1.9	0.7	0.2	2.7	1.8
Y_ppm	null	null	null	1	11.4	1	7.4	0.3	1.9	0.5
Zn_ppm	19	62	33	24	69	12	37	95	533	25
Zr_ppm	null	null	null	2.3	11.2	2.3	6.6	1.1	15.4	3

Table D-1: Multi-element geochemical data that was used to calculate element correlations between vein types. Vein descriptions are found in the text. Dataset consists of different sample suites that were analyzed prior to and during this study. Discrepancies between analytical methods results in null values for certain sample groups, where certain elements were not analyzed. The data included here only includes samples that can directly be tied to certain vein types. A larger assay geochemical database was also used for other geochemical interpretations, including those not directly related to veining.

Appendix E: LA-ICPMS and CL Data

Appendix contains geochronologic data and additional SEM-CL images for zircons analyzed. Each table includes all the analyses for each sample. One cell represents one laser spot.

RBCPQ088	238U	1 sigma	207Pb	1 sigma	Th	206/238	1 sigma	207/206	1 sigma
Jd (Shamrock)	206Pb	% error	206Pb	% error	U	age	abs err	age	abs err
1103AZ1_15	40.9431	3.56%	0.0506	3.91%	0.860	155.6	5.5	221.4	93.0
1103AZ1_16	40.5326	1.71%	0.0495	2.38%	1.112	157.1	2.7	171.9	56.5
1103AZ1_11	40.2412	2.08%	0.0498	2.94%	1.100	158.2	3.3	183.6	70.0
1103AZ1_6	40.0297	2.80%	0.0506	3.44%	0.489	159.1	4.4	221.7	81.5
1103AZ1_28	40.0123	1.11%	0.0503	2.70%	0.963	159.1	1.7	209.1	63.8
1103AZ1_3	39.9142	2.82%	0.0511	3.49%	1.020	159.5	4.4	244.1	82.3
1103AZ1_5	39.8213	1.31%	0.0501	2.09%	0.546	159.9	2.1	200.6	49.3
1103AZ1_10	39.8112	3.40%	0.0498	4.34%	0.893	159.9	5.4	186.0	104.4
1103AZ1_26	39.7261	1.29%	0.0494	1.66%	1.052	160.3	2.0	166.3	39.3
1103AZ1_24	39.5576	1.10%	0.0496	1.69%	1.394	160.9	1.7	175.2	40.0
1103AZ1_29	39.4147	0.95%	0.0506	2.02%	1.112	161.5	1.5	221.6	47.4
1103AZ1_17	39.3532	2.15%	0.0507	3.03%	1.002	161.8	3.4	225.5	71.6
1103AZ1_8	39.3496	1.09%	0.0496	1.79%	0.738	161.8	1.7	178.0	42.4
1103AZ1_4	39.3490	3.85%	0.0501	4.45%	0.721	161.8	6.2	201.6	106.7
1103AZ1_27	39.3298	1.01%	0.0501	2.80%	0.994	161.9	1.6	200.0	66.2
1103AZ1_1	39.3099	2.54%	0.0482	2.89%	1.058	161.9	4.1	107.5	69.8
1103AZ1_22	39.1321	1.46%	0.0493	2.30%	0.756	162.7	2.3	160.3	54.8
1103AZ1_25	39.0995	0.97%	0.0491	1.64%	1.283	162.8	1.6	153.3	39.0
1103AZ1_19	39.0358	1.73%	0.0496	2.03%	1.168	163.1	2.8	176.7	48.0
1103AZ1_20	38.9567	1.94%	0.0488	2.62%	1.367	163.4	3.1	137.0	62.7
1103AZ1_21	38.9488	2.60%	0.0501	3.13%	1.182	163.4	4.2	199.8	74.3
1103AZ1_18	38.9186	2.62%	0.0490	2.96%	1.122	163.5	4.2	145.6	71.0
1103AZ1_7	38.8540	2.46%	0.0490	2.81%	1.069	163.8	4.0	149.7	67.3
1103AZ1_30	38.7706	1.09%	0.0506	2.29%	1.294	164.2	1.8	221.0	53.8
1103AZ1_12	38.5916	1.61%	0.0506	2.29%	0.743	164.9	2.6	223.8	53.9
1103AZ1_23	38.3931	1.07%	0.0495	2.16%	1.089	165.8	1.7	170.5	51.2
1103AZ1_9	38.3139	1.62%	0.0499	3.33%	0.671	166.1	2.7	188.5	79.3
1103AZ1_14	37.4710	2.77%	0.0526	4.02%	0.817	169.8	4.6	312.6	94.1
1103AZ1_13	39.1323	3.73%	0.0525	4.50%	0.921	162.7	6.0	305.2	105.9
1103AZ1_2	36.7323	5.14%	0.0547	5.58%	0.856	173.2	8.8	399.5	130.1

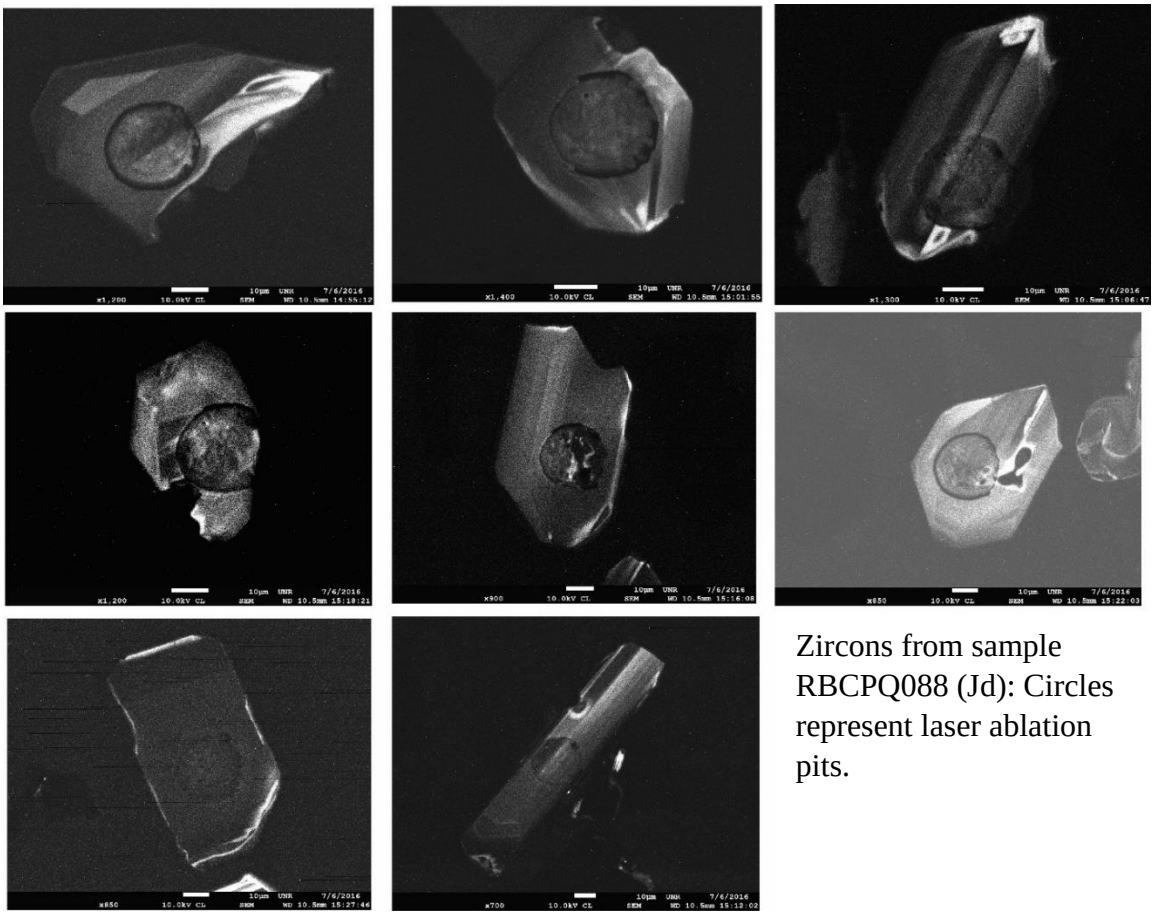

Zircons from sample RBCPQ088 (Jd): Circles represent laser ablation pits.

RBCPQ016	238U	1 sigma	207Pb	1 sigma	Th	206/238	1 sigma	207/206	1 sigma
Jgd	206Pb	% error	206Pb	% error	U	age	abs err	age	abs err
0491AZ1_1	39.3145	1.63%	0.0500	3.29%	0.504	161.9	2.6	193.3	78.4
0491AZ1_2	39.1051	1.60%	0.0501	2.65%	0.477	162.8	2.6	198.1	62.7
0491AZ1_3	39.2805	1.84%	0.0504	3.16%	0.532	162.1	2.9	212.4	75.0
0491AZ1_4	40.0808	2.00%	0.0498	2.84%	0.566	158.9	3.1	183.6	67.5
0491AZ1_5	40.4485	1.51%	0.0497	2.28%	0.550	157.4	2.3	182.5	54.0
0491AZ1_6	39.8258	1.35%	0.0492	3.49%	0.685	159.9	2.1	157.2	83.9
0491AZ1_7	39.1634	1.51%	0.0527	5.12%	0.720	162.5	2.4	316.5	120.7
0491AZ1_8	40.0645	1.10%	0.0498	2.90%	0.425	158.9	1.7	187.0	69.0
0491AZ1_9	40.3175	1.23%	0.0498	1.98%	0.723	157.9	1.9	183.5	46.9
0491AZ1_10	39.5128	1.13%	0.0496	1.96%	0.792	161.1	1.8	176.6	46.4
0491AZ1_11	38.2331	1.04%	0.0492	2.17%	0.571	166.4	1.7	157.0	51.5
0491AZ1_12	39.1992	1.49%	0.0503	2.26%	0.506	162.4	2.4	207.2	53.3
0491AZ1_14	40.1434	3.50%	0.0510	3.76%	0.766	158.6	5.5	241.1	89.1
0491AZ1_15	40.2799	2.13%	0.0514	4.97%	0.813	158.1	3.3	261.0	118.5
0491AZ1_16	40.7363	1.19%	0.0500	2.50%	0.415	156.3	1.8	197.3	59.2
0491AZ1_17	40.3110	2.18%	0.0511	4.37%	0.789	158.0	3.4	247.4	103.9
0491AZ1_19	41.1999	1.88%	0.0510	3.71%	0.452	154.6	2.9	241.4	87.8
0491AZ1_20	40.5718	1.01%	0.0497	2.39%	0.755	157.0	1.6	182.0	56.8
0491AZ1_21	40.4774	1.27%	0.0501	4.11%	0.700	157.3	2.0	200.0	98.3
0491AZ1_22	41.0307	1.22%	0.0491	2.79%	0.620	155.2	1.9	151.5	66.7
0491AZ1_23	40.4617	1.21%	0.0501	2.64%	0.460	157.4	1.9	200.3	62.4
0491AZ1_24	39.5002	3.82%	0.0543	4.21%	0.781	161.2	6.1	382.3	97.4
0491AZ1_25	38.4811	3.84%	0.0019	3.73%	1.372	165.4	6.3	205.8	89.0
0491AZ1_26	39.9841	5.68%	0.0033	6.26%	0.671	159.2	8.9	313.1	149.1
0491AZ1_27	38.8984	8.40%	0.0042	8.18%	0.757	163.6	13.6	249.7	200.0
0491AZ1_29	39.1687	2.99%	0.0017	3.39%	0.623	162.5	4.8	207.9	80.5
0491AZ1_30	39.7894	3.17%	0.0020	4.02%	0.496	160.0	5.0	204.1	96.1

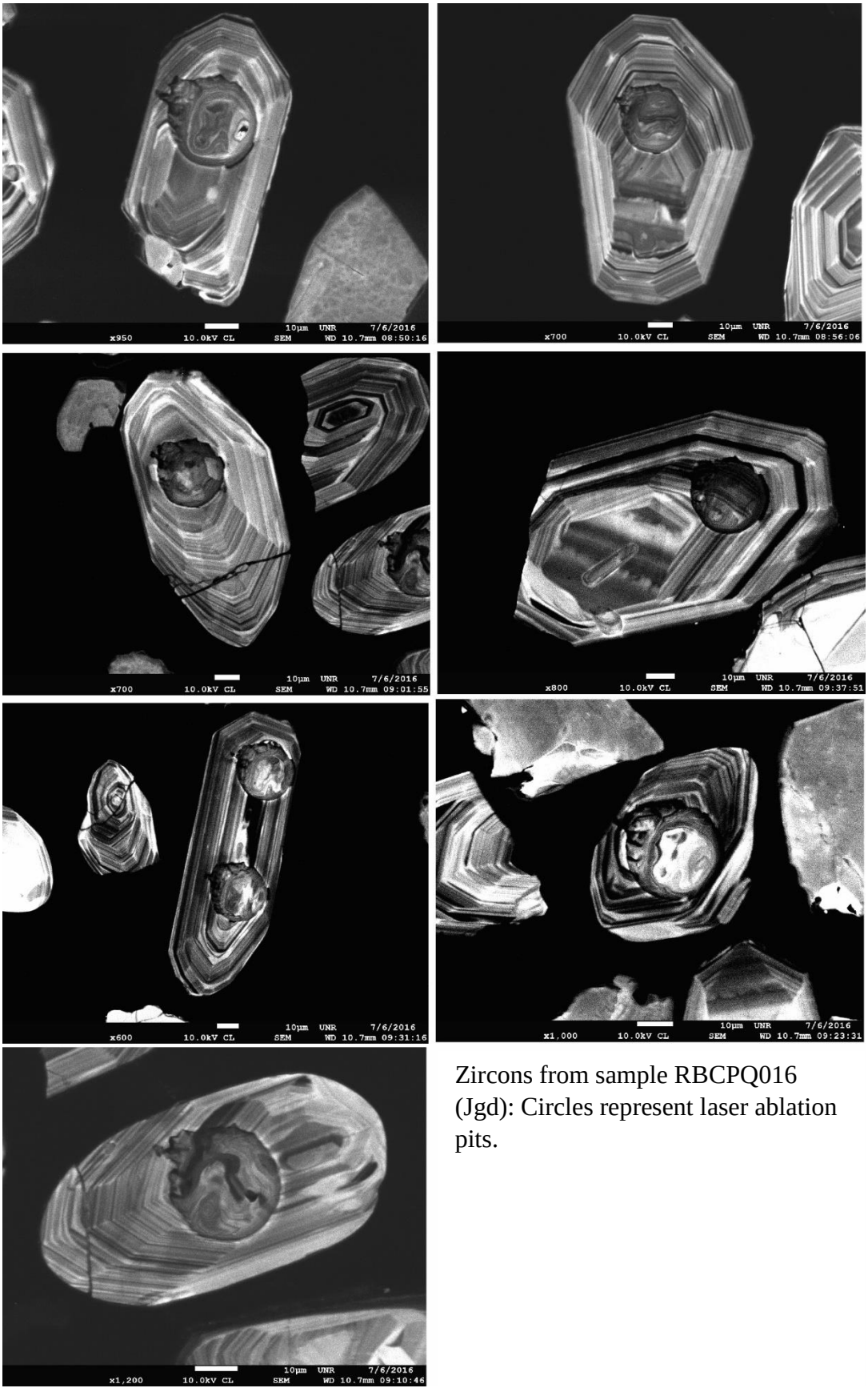

Zircons from sample RBCPQ016 (Jgd): Circles represent laser ablation pits.

BCD-101-170	238U	1 sigma	207Pb	1 sigma	Th	206/238	1 sigma	207/206	1 sigma
Kmd	206Pb	% error	206Pb	% error	U	age	abs err	age	abs err
45 z4-C	93.3721	1.39%	0.0479	2.86%	0.677	68.7	1.0	95.0	66.4
44 z1-B	24.4580	1.18%	0.0511	2.06%	0.788	258.3	3.0	245.5	46.8
43 z1-M	24.6621	1.19%	0.0527	2.16%	0.737	256.2	3.0	314.5	48.4
42 z1-T	24.0563	1.15%	0.0500	2.10%	0.736	262.6	3.0	194.7	48.1
58 z9-C	80.4836	0.96%	0.0468	1.65%	1.121	79.6	0.8	38.9	38.9
57 z7-C	80.5064	0.80%	0.0472	1.37%	1.172	79.6	0.6	57.3	32.5
56 z7-M	80.2311	0.83%	0.0478	1.49%	0.079	79.9	0.7	86.9	35.0
55 z7-R	76.1084	0.75%	0.0477	1.26%	0.336	84.1	0.6	82.5	29.6
54 z6-T	266.3007	1.59%	0.0597	3.63%	0.356	24.2	0.4	592.9	76.7
53 z6-B	274.8546	2.29%	0.0533	5.00%	0.426	23.4	0.5	341.5	109.3
52 z4-LR	88.0998	0.83%	0.0479	1.33%	0.495	72.8	0.6	95.0	31.2
51 z4-R	85.0786	0.82%	0.0476	1.32%	0.371	75.3	0.6	81.5	31.0
29 z3-M	89.3563	1.41%	0.0479	1.56%	0.547	71.7	1.0	92.7	36.6
28 z6-R	79.8642	1.66%	0.0476	1.65%	0.486	80.2	1.3	77.1	38.8
27 z6-C	65.8579	1.61%	0.0467	3.04%	0.470	97.1	1.6	33.9	71.1
25 z4	23.6573	1.54%	0.0503	2.83%	0.682	266.9	4.0	208.4	64.4
24 z3-T	88.2677	1.42%	0.0477	1.43%	0.941	72.6	1.0	82.7	33.5
23 z3-B	81.5277	1.37%	0.0473	1.36%	0.579	78.6	1.1	62.5	32.0
26 z5	40.6883	1.60%	0.0547	2.26%	0.508	156.5	2.5	398.5	49.9

Zircons from sample BCD-101-170 (Kmd): Circles represent laser spots, which are 30µm in diameter.

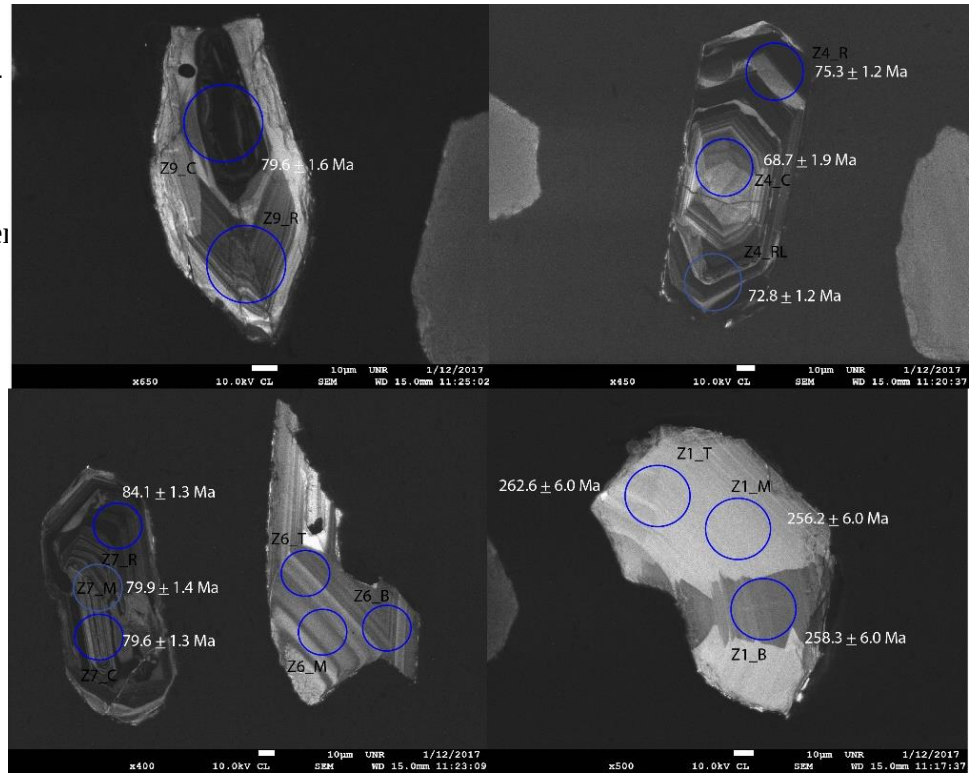

Zircons from sample BCD-101-170 (Kmd): Circles represent laser spots, which are 30µm in diameter.

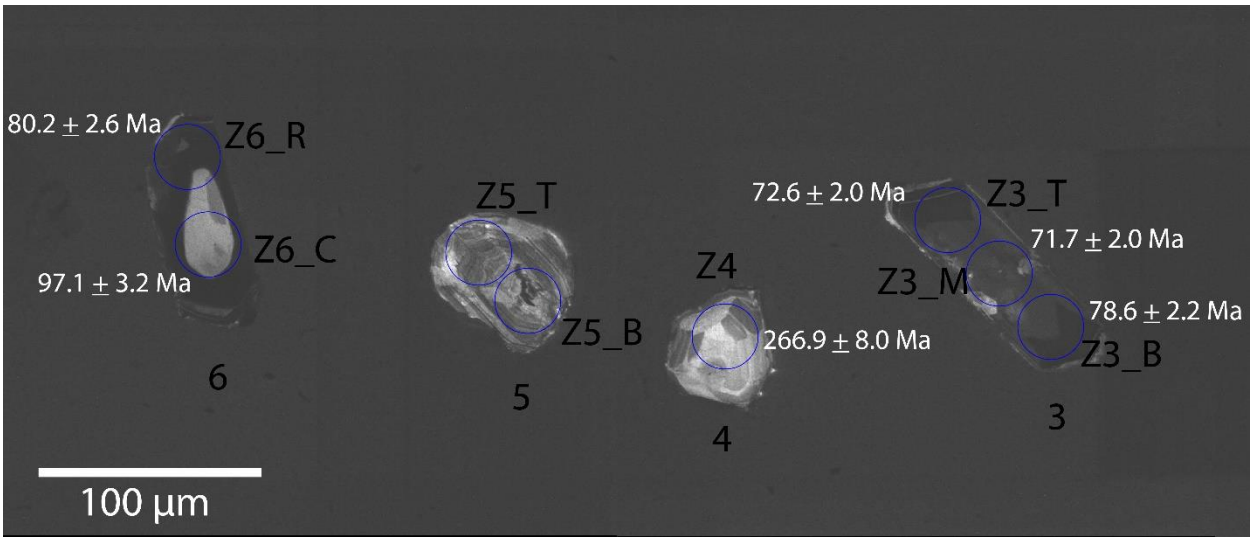

RBCPQ021A	238U	1 sigma	207Pb	1 sigma	Th	206/238	1 sigma	207/206	1 sigma
Klg	206Pb	% error	206Pb	% error	U	age	abs err	age	abs err
0492AZ1_1	40.7792	1.07%	0.0499	3.12%	0.406	156.2	1.7	188.2	74.3
0492AZ1_2	84.1371	2.40%	0.0542	9.49%	0.380	76.2	1.8	379.8	228.9
0492AZ1_3	78.7019	1.11%	0.0495	3.23%	0.350	81.4	0.9	169.5	77.3
0492AZ1_4	80.6703	1.20%	0.0493	3.89%	0.374	79.4	0.9	159.8	93.5
0492AZ1_5	74.3108	1.13%	0.0494	4.03%	0.632	86.2	1.0	168.1	97.1
0492AZ1_7	78.4553	1.04%	0.0481	3.06%	0.431	81.6	0.8	105.4	74.0
0492AZ1_8	81.0206	1.21%	0.0484	3.26%	0.565	79.1	0.9	119.6	78.7
0492AZ1_9	76.3879	1.33%	0.0484	2.86%	0.625	83.8	1.1	118.2	69.0
0492AZ1_10	79.5518	1.27%	0.0472	4.01%	0.423	80.5	1.0	57.0	57.0
0492AZ1_12	68.3885	1.48%	0.0495	2.88%	0.284	93.6	1.4	171.5	68.7
0492AZ1_13	81.9755	1.07%	0.0482	2.39%	0.418	78.2	0.8	107.4	57.6
0492AZ1_14	78.9634	1.00%	0.0479	2.80%	0.277	81.1	0.8	94.8	67.8
0492AZ1_15	62.6287	4.87%	0.0717	27.01%	0.730	102.1	4.9	977.0	677.5
0492AZ1_17	79.6376	1.12%	0.0494	2.41%	0.020	80.4	0.9	165.1	57.4
0492AZ1_18	79.3490	1.17%	0.0488	2.27%	0.227	80.7	0.9	136.9	54.2
0492AZ1_23	80.6221	1.27%	0.0491	2.60%	0.564	79.5	1.0	151.6	62.0
0492AZ1_24	78.1023	1.26%	0.0492	2.30%	0.525	82.0	1.0	159.7	54.7
0492AZ1_25	78.5465	1.20%	0.0490	4.46%	0.210	81.6	1.0	145.5	108.0
0492AZ1_26	79.0571	1.16%	0.0484	2.58%	0.506	81.0	0.9	120.9	61.9
0492AZ1_27	4.6485	8.25%	0.0916	13.21%	0.259	1256.1	94.9	1459.3	274.6
0492AZ1_28	78.5580	1.38%	0.0487	2.59%	0.390	81.5	1.1	131.1	62.1
0492AZ1_29	80.6058	0.99%	0.0487	3.37%	0.269	79.5	0.8	132.2	81.2
0492AZ1_30	61.8913	1.12%	0.0010	2.16%	0.192	103.3	1.1	125.2	51.6

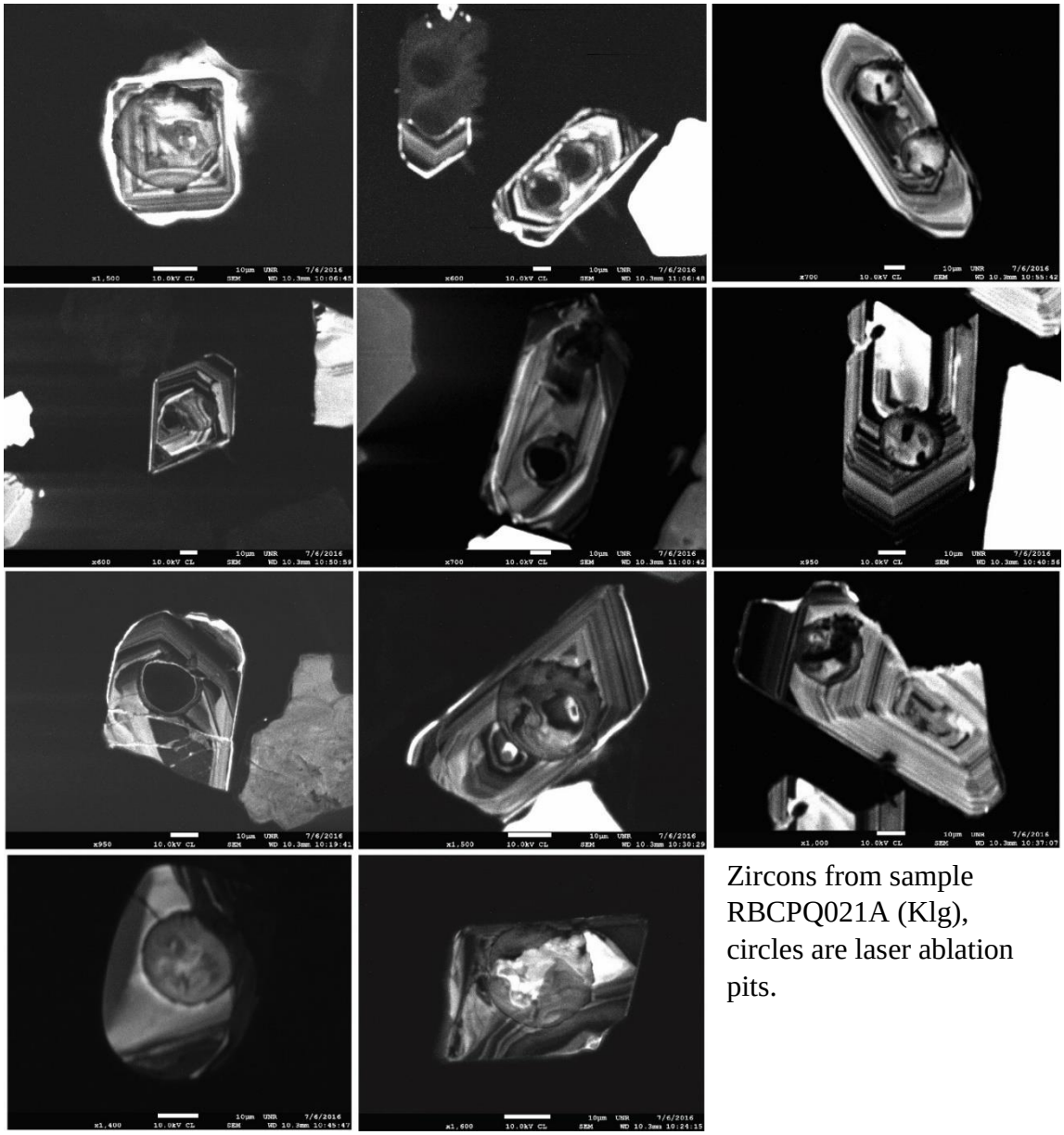

Zircons from sample RBCPQ021A (Klg), circles are laser ablation pits.

BCD-101-150	238U	1 sigma	207Pb	1 sigma	Th	206/238	1 sigma	207/206	1 sigma
Klg	206Pb	% error	206Pb	% error	U	age	abs err	age	abs err
35 z18-R	78.9503	1.12%	0.0490	1.27%	0.550	81.1	0.9	146.0	29.6
34 z18-C	73.5012	1.21%	0.0476	1.54%	0.630	87.1	1.0	78.5	36.2
33 z17-R	70.7718	1.11%	0.0478	1.47%	0.414	90.4	1.0	87.4	34.6
32 z12	65.8761	1.18%	0.0476	1.64%	0.424	97.1	1.1	80.6	38.6
30 z9-C	75.7857	1.58%	0.0467	3.17%	0.762	84.5	1.3	34.6	74.1
29 z8-R	81.3772	1.03%	0.0516	1.22%	0.471	78.7	0.8	265.5	27.7
28 z8-C	71.8310	1.07%	0.0473	1.36%	0.622	89.1	0.9	63.9	32.1
27 z5	79.1645	1.54%	0.0482	2.10%	0.665	80.9	1.2	109.7	49.0
26 z3	76.9439	1.19%	0.0486	1.41%	0.431	83.2	1.0	128.4	32.9
51 z32-C	48.0961	0.79%	0.0496	1.59%	0.374	132.7	1.0	177.1	36.7
50 z29-C	75.5644	1.23%	0.0501	3.54%	0.427	84.8	1.0	200.0	80.2
49 z29-R	76.2811	0.55%	0.0483	1.30%	0.354	84.0	0.5	111.8	30.5
47 z28-R	76.6385	0.56%	0.0478	1.34%	0.266	83.6	0.5	89.8	31.5
46 z26-R	50.7225	0.67%	0.0480	1.38%	0.533	125.9	0.8	98.6	32.3
44 z23	38.0950	0.73%	0.0485	1.47%	0.257	167.0	1.2	124.7	34.2
43 z22	74.1091	0.61%	0.0484	1.34%	0.483	86.4	0.5	116.9	31.4
42 z21	66.8825	0.63%	0.0483	1.22%	0.029	95.7	0.6	115.5	28.6
62 z39	77.3520	0.58%	0.0490	1.36%	0.685	82.8	0.5	147.8	31.6
61 z38	83.1023	0.78%	0.0487	1.45%	0.250	77.1	0.6	132.3	33.9
60 z35-C	72.2150	0.62%	0.0481	1.47%	0.424	88.7	0.5	104.5	34.4
59 z35-R	79.2519	0.53%	0.0474	1.30%	0.637	80.8	0.4	71.5	30.6
58 z32-R	74.0672	1.03%	0.0470	1.60%	0.280	86.5	0.9	49.4	37.8
75 z2-R	73.1815	0.99%	0.0005	1.10%	0.203	87.5	0.9	99.3	25.9
74 z2-C	75.8515	0.99%	0.0005	1.07%	0.124	84.4	0.8	158.5	24.9
73 z1-TR	78.9188	0.99%	0.0005	1.10%	0.192	81.2	0.8	126.0	25.7
72 z1-R	80.1709	1.01%	0.0006	1.28%	0.254	79.9	0.8	28.2	30.5
71 z1-M	80.8059	1.09%	0.0008	1.70%	0.154	79.3	0.9	65.9	40.1
70 z1-L	79.3362	1.08%	0.0007	1.49%	0.192	80.7	0.9	17.5	35.5
91 z12-R	86.9552	1.02%	0.0005	0.97%	0.826	73.7	0.7	106.1	22.7
90 z12-M	44.5340	1.11%	0.0006	1.22%	0.319	143.2	1.6	193.2	28.2
89 z12-C	25.1173	1.01%	0.0006	1.25%	0.767	251.7	2.5	203.8	28.7
88 z10-C	40.6873	1.21%	0.0009	1.80%	0.422	156.5	1.9	197.3	41.2
87 z10-R	79.3090	0.98%	0.0004	0.91%	0.395	80.8	0.8	136.9	21.3
86 z8-R	78.3867	0.95%	0.0004	0.93%	0.286	81.7	0.8	115.1	21.7
85 z8-C	42.9413	1.29%	0.0011	2.22%	0.581	148.4	1.9	166.5	51.1
84 z6-R	59.5104	1.02%	0.0005	0.96%	0.191	107.4	1.1	129.2	22.5
83 z6-M	39.2376	1.01%	0.0005	0.91%	0.155	162.2	1.6	181.4	21.1
82 z6-C	39.3144	0.97%	0.0005	1.00%	0.615	161.9	1.6	173.5	23.1

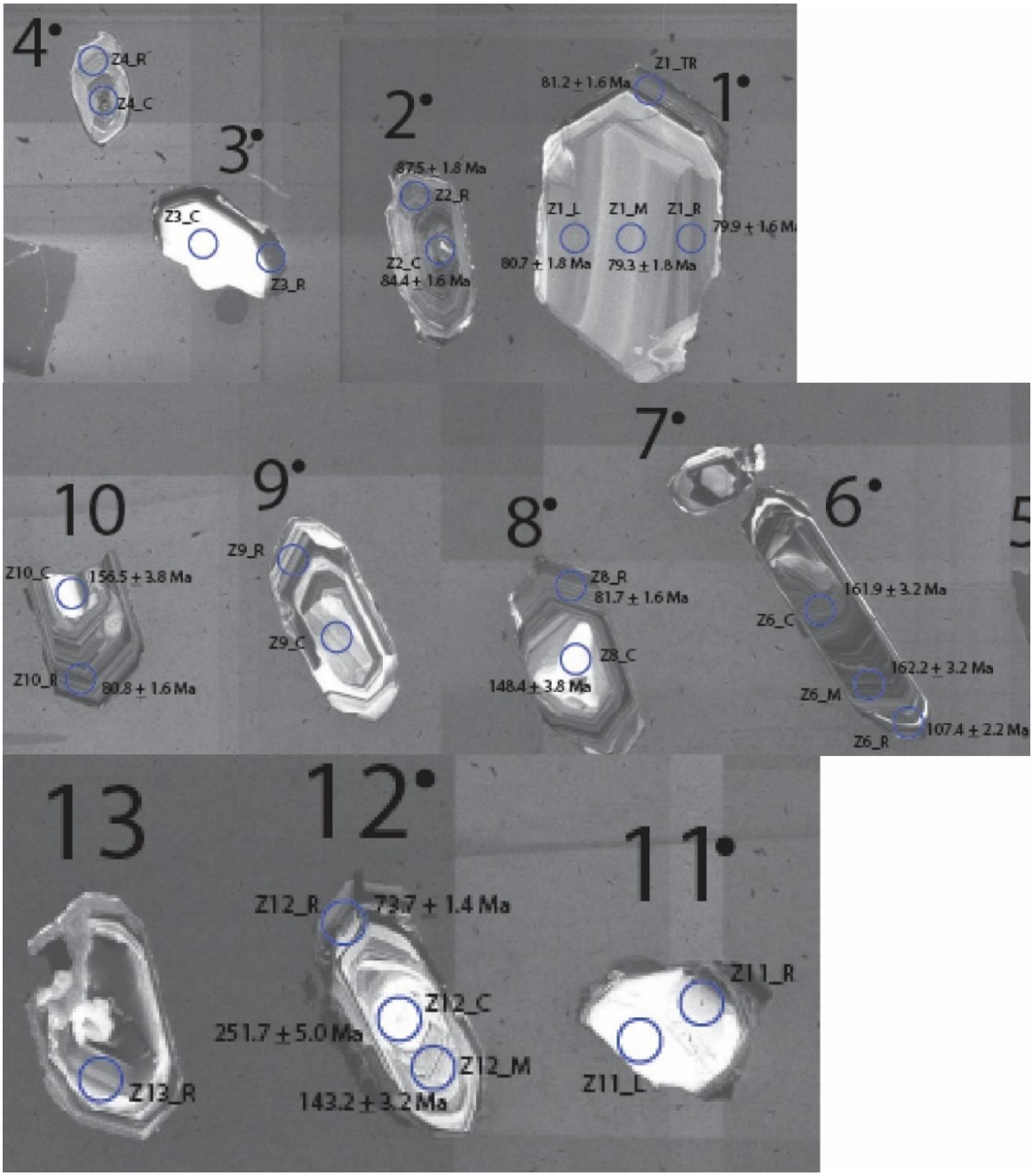

Zircons from sample BCD-101-150 (Klg): Circles represent laser spots, which are 30µm in diameter. Ages for each spot are labled. Circles without an age were not analyzed. Note the more significant inheritance than in other samples.

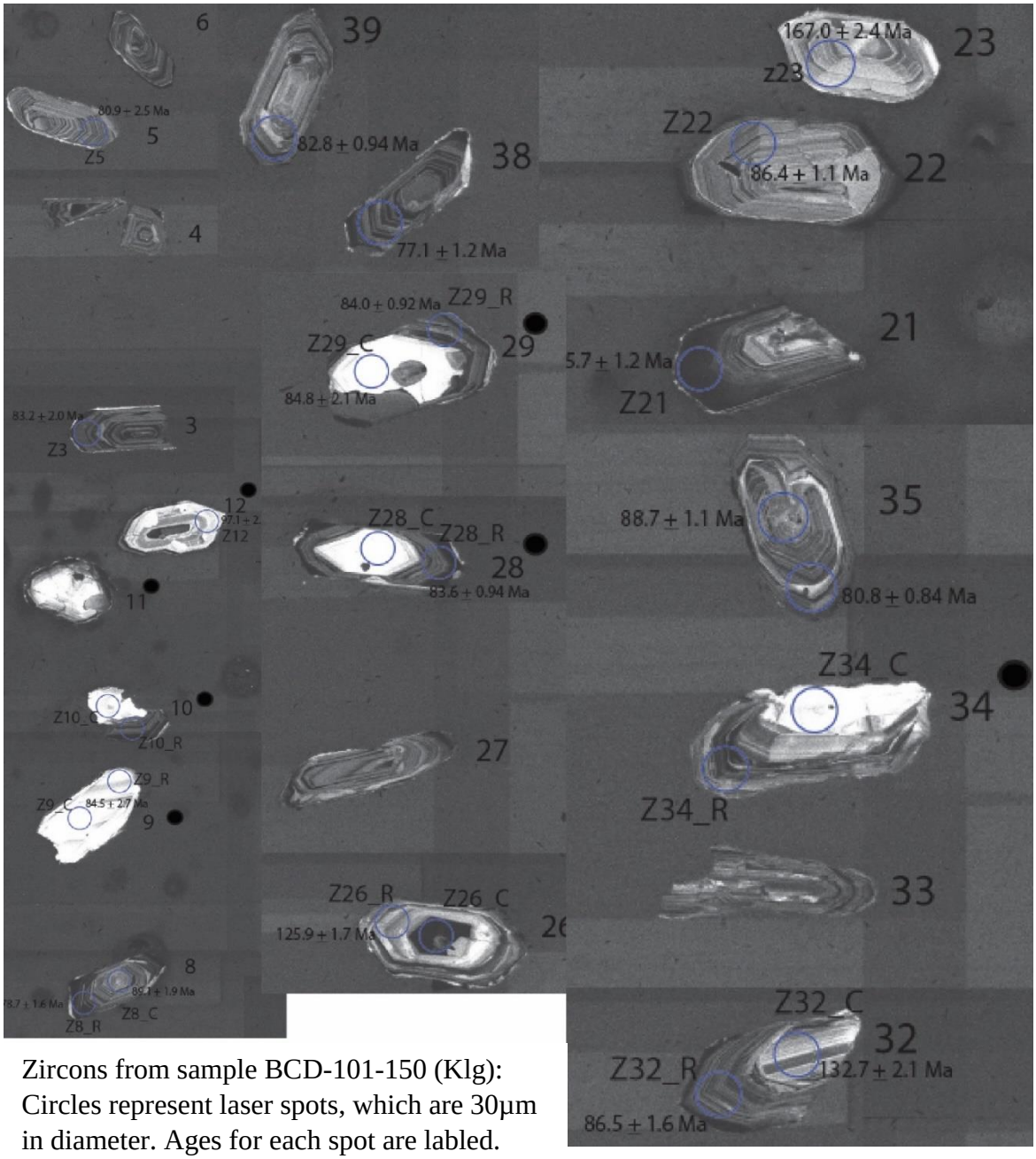

Zircons from sample BCD-101-150 (Klg): Circles represent laser spots, which are 30µm in diameter. Ages for each spot are labled. Circles without an age were not analyzed. Note the more significant inheritance than in

BCD-101-66	238U	1 sigma	207Pb	1 sigma	Th	206/238	1 sigma	207/206	1 sigma
Tmd	206Pb	% error	206Pb	% error	U	age	abs err	age	abs err
0493AZ1_4	248.7386	5.32%	0.0523	9.97%	1.07	25.9	1.4	297.7	245.1
0493AZ1_5	217.8102	8.60%	0.0604	11.16%	0.82	29.5	2.5	618.0	261.2
0493AZ1_8	222.2289	7.78%	0.0792	50.72%	0.45	28.9	2.2	1178.1	1178.1
0493AZ1_10	240.9839	8.68%	0.0837	44.30%	0.82	26.7	2.3	1285.2	1255.8
0493AZ1_11	239.5445	7.61%	0.0728	36.94%	0.81	26.9	2.0	1009.1	1009.1
0493AZ1_12	228.5615	1.78%	0.0530	7.58%	1.35	28.1	0.5	330.6	181.7
0493AZ1_13	245.3433	1.81%	0.0551	9.18%	1.14	26.2	0.5	416.8	219.4
0493AZ1_15	239.0955	3.30%	0.0613	15.89%	0.82	26.9	0.9	648.8	383.9
0493AZ1_16	258.0546	2.58%	0.0514	9.51%	1.00	24.9	0.6	258.9	234.6
0493AZ1_17	204.3462	12.99%	0.0634	69.46%	1.03	31.5	4.1	721.6	721.6
0493AZ1_18	266.5652	1.65%	0.0495	6.69%	1.26	24.1	0.4	173.0	164.1
0493AZ1_19	238.2835	4.70%	0.0646	24.70%	0.58	27.0	1.3	762.0	630.6
0493AZ1_20	262.7445	1.15%	0.0486	2.46%	1.09	24.5	0.3	128.5	59.0
0493AZ1_21	238.2263	3.73%	0.0582	19.08%	0.76	27.0	1.0	536.4	483.3
0493AZ1_22	238.3940	1.48%	0.0508	7.27%	1.21	27.0	0.4	231.8	177.2
0493AZ1_23	233.6846	5.14%	0.0550	23.36%	0.94	27.5	1.4	413.5	413.5
0493AZ1_24	253.2268	2.39%	0.0539	10.23%	1.11	25.4	0.6	366.3	248.7
0493AZ1_25	256.3085	2.65%	0.0533	11.31%	0.80	25.1	0.7	341.1	278.7
0493AZ1_26	259.1505	1.78%	0.0502	5.88%	1.43	24.8	0.4	206.0	142.4
0493AZ1_27	262.1690	2.64%	0.0540	10.14%	0.79	24.5	0.6	369.8	246.3
0493AZ1_28	252.8761	3.23%	0.0583	18.93%	0.75	25.4	0.8	542.9	478.2
0493AZ1_29	249.5242	3.50%	0.0095	16.84%	0.76	25.8	0.9	476.0	423.2
0493AZ1_30	232.0960	4.56%	0.0154	25.24%	0.63	27.7	1.3	641.7	641.7

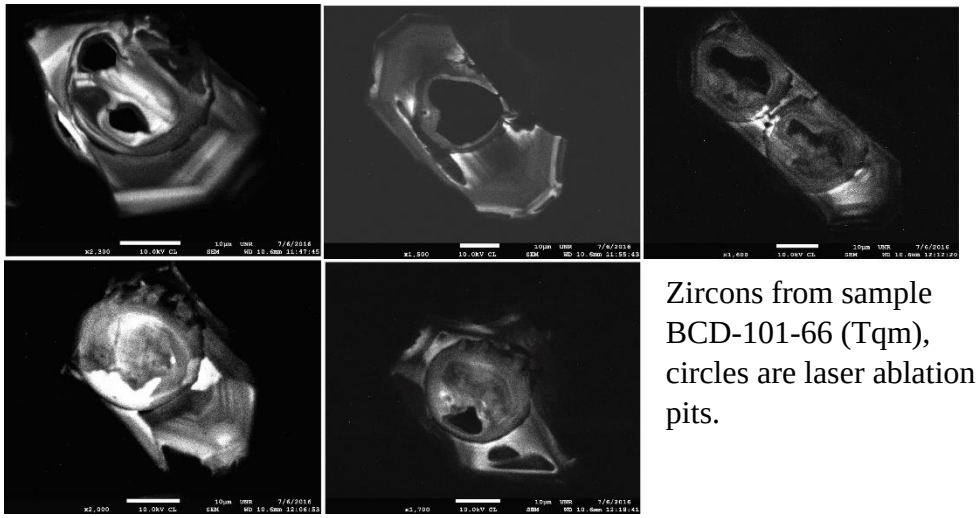

Zircons from sample BCD-101-66 (Tqm), circles are laser ablation pits.

RBCPQ020	238U	1 sigma	207Pb	1 sigma	Th	206/238	1 sigma	207/206	1 sigma
Tg	206Pb	% error	206Pb	% error	U	age	abs err	age	abs err
13 z2-C	78.0341	1.22%	0.0461	2.17%	0.713	82.1	1.0	5.1	51.4
12 z2-R	79.7324	1.31%	0.0480	2.25%	0.694	80.3	1.0	100.5	52.5
11 z1-R	84.9019	1.06%	0.0478	1.31%	0.229	75.5	0.8	88.0	30.8
10 z1-M	78.6185	1.19%	0.0468	2.05%	0.692	81.5	1.0	38.9	48.3
9 z1-L	79.6290	1.20%	0.0463	2.10%	0.983	80.5	1.0	11.1	49.7
28 z1-MR	69.5357	1.15%	0.0488	1.63%	0.414	92.0	1.0	137.3	37.8
27 z6-L	72.3183	1.14%	0.0588	1.57%	0.387	88.5	1.0	561.3	33.8
25 z5-R	261.3293	1.35%	0.0477	2.61%	0.844	24.6	0.3	84.5	60.7
23 z5-ML	259.8908	1.77%	0.0503	3.94%	0.670	24.8	0.4	210.5	88.9
22 z5-L	249.2604	1.83%	0.0487	3.68%	0.582	25.8	0.5	132.0	84.3
21 z4-L	261.0622	1.68%	0.0516	3.61%	0.843	24.6	0.4	269.5	80.7
20 z3-R	260.3724	2.48%	0.0602	6.68%	0.515	24.7	0.6	610.8	138.2
32 z4-T	79.6290	1.54%	0.0479	2.04%	0.243	80.5	1.2	92.7	47.7
31 z4-C	77.2541	1.44%	0.0479	1.80%	0.524	82.9	1.2	92.9	42.1
30 z4-B	81.0213	1.49%	0.0492	1.67%	0.388	79.1	1.2	155.7	38.6
46 z10	84.3826	1.69%	0.0516	2.98%	0.789	75.9	1.3	265.7	66.9
45 z8-L	260.4523	3.56%	0.0864	5.16%	0.849	24.7	0.9	1348.2	96.5
44 z8-R	271.6312	6.05%	0.0982	8.83%	0.880	23.7	1.4	1589.5	156.5
43 z7-R	257.2610	2.76%	0.0608	5.19%	0.865	25.0	0.7	631.1	108.0

Zircons from sample RBCPQ020 (Tg): Circles represent laser spots, which are 30µm in diameter. Ages for each spot are labled. Circles without an age were not analyzed.

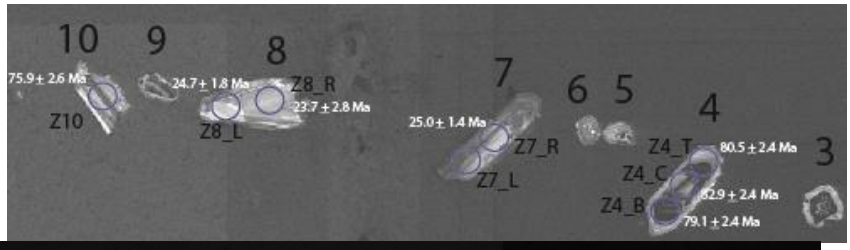

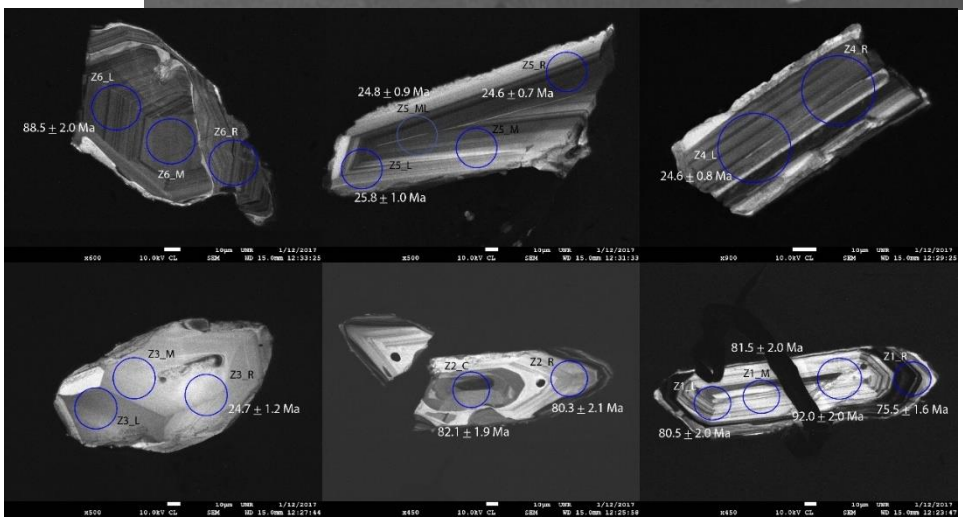

RBCPQ113	238U	1 sigma	207Pb	1 sigma	Th	206/238	1 sigma	207/206	1 sigma
Tqmd	206Pb	% error	206Pb	% error	U	age	abs err	age	abs err
41 z6	77.1117	0.97%	0.0473	1.29%	0.606	83.1	0.8	65.7	30.3
40 z4-L	256.5000	1.10%	0.0462	1.95%	0.928	25.1	0.3	7.6	46.3
39 z4-R	259.0265	1.03%	0.0475	1.64%	0.997	24.8	0.3	73.9	38.5
38 z3-ML	24.9291	1.03%	0.0518	1.59%	0.525	253.5	2.6	276.3	36.0
37 z3-TR	24.7997	1.00%	0.0532	1.55%	0.871	254.8	2.5	337.4	34.8
36 z3-MR	24.7760	0.99%	0.0504	1.59%	0.510	255.1	2.5	212.3	36.4
42 z26	268.3214	2.69%	0.0607	6.22%	0.963	24.0	0.6	627.5	128.7
41 z15	77.1905	1.50%	0.0465	1.79%	0.353	83.0	1.2	22.4	42.3
40 z38	262.0582	1.83%	0.0487	4.46%	1.578	24.6	0.4	131.3	101.6
39 z50	253.9872	2.23%	0.0579	5.51%	1.055	25.3	0.6	526.1	116.4
38 z57	258.4223	4.34%	0.1001	5.64%	0.915	24.9	1.1	1626.7	101.4

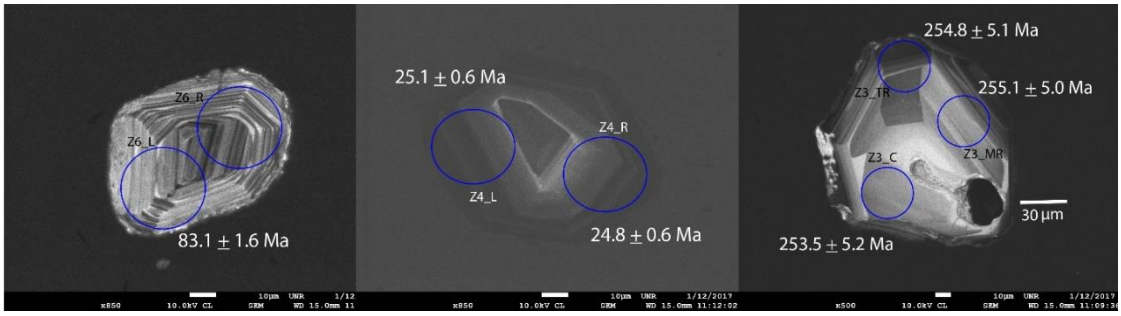

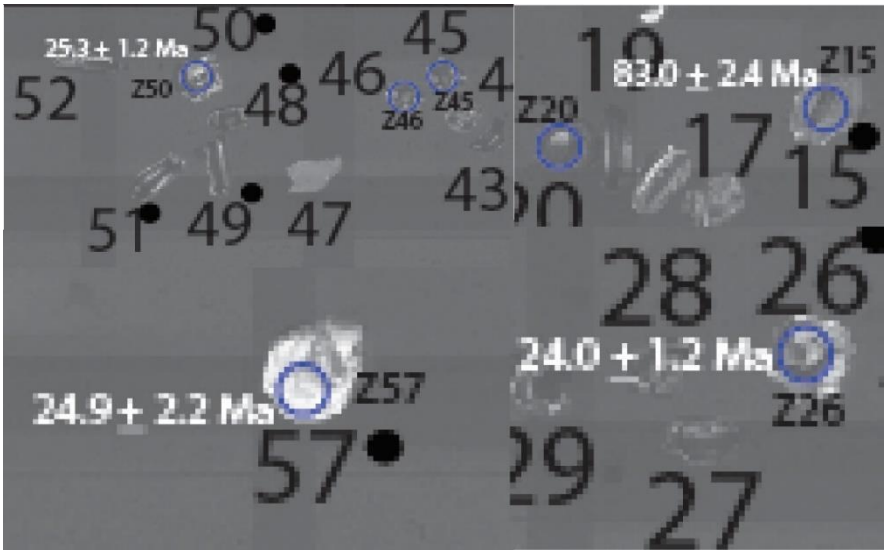

Zircons from sample RBCPQ113 (Tqmd): Circles represent laser spots, which are 30µm in diameter in the top photo and 20 µm in the lower. Ages for each spot are labeled. Circles without an age were not analyzed.

RBCPQ114A	238U	1 sigma	207Pb	1 sigma	Th	206/238	1 sigma	207/206	1 sigma
Td	206Pb	% error	206Pb	% error	U	age	abs err	age	abs err
115 z1_22	78.5874	1.18%	0.0484	1.48%	0.920	81.5	1.0	120.4	34.4
114 z1_21-L	254.1077	1.24%	0.0501	2.73%	0.284	25.3	0.3	198.3	62.2
111 z1_19 r	77.8414	1.00%	0.0489	1.30%	0.358	82.3	0.8	144.9	30.2
110 z1_19-c	85.7971	1.17%	0.0564	1.40%	0.634	74.7	0.9	469.5	30.8
109 z1_7	81.0892	0.98%	0.0480	1.23%	0.813	79.0	0.8	100.5	28.9
108 z1_1-L	266.2671	2.35%	0.0721	5.24%	0.922	24.2	0.6	987.7	103.1
8 z2_2	259.0347	2.17%	0.0476	5.26%	0.385	24.8	0.5	79.1	120.4
4 z2_13	78.0220	1.14%	0.0473	1.86%	0.526	82.1	0.9	61.9	43.7
61 z7	264.6470	2.50%	0.0467	7.15%	0.494	24.3	0.6	33.7	161.4
60 z4-T	77.8225	1.10%	0.0456	1.88%	0.433	82.3	0.9	0.0	21.2
59 z4-L	79.7716	1.07%	0.0487	1.64%	0.346	80.3	0.9	131.8	38.0
58 z3-B	261.7212	2.49%	0.0511	5.84%	0.555	24.6	0.6	244.4	129.2
57 z3-T	275.3868	2.20%	0.0599	5.47%	0.554	23.4	0.5	601.3	114.3
56 z2	247.2855	1.84%	0.0700	3.81%	1.023	26.0	0.5	928.5	76.2
55 z1-B	280.7824	4.41%	0.1050	8.01%	0.359	22.9	1.0	1714.6	140.5
54 z1-ML	217.5116	2.15%	0.1565	3.90%	0.329	29.6	0.6	2418.5	64.7
53 z1-MR	275.2217	2.14%	0.0639	5.05%	0.331	23.4	0.5	737.8	103.4
69 z10-RB	80.0059	1.02%	0.0489	1.47%	0.846	80.1	0.8	142.1	34.2
68 z10-RT	82.5907	1.02%	0.0475	1.27%	0.573	77.6	0.8	72.5	30.0
67 z10-C	78.9309	1.13%	0.0479	2.17%	0.392	81.2	0.9	94.5	50.7

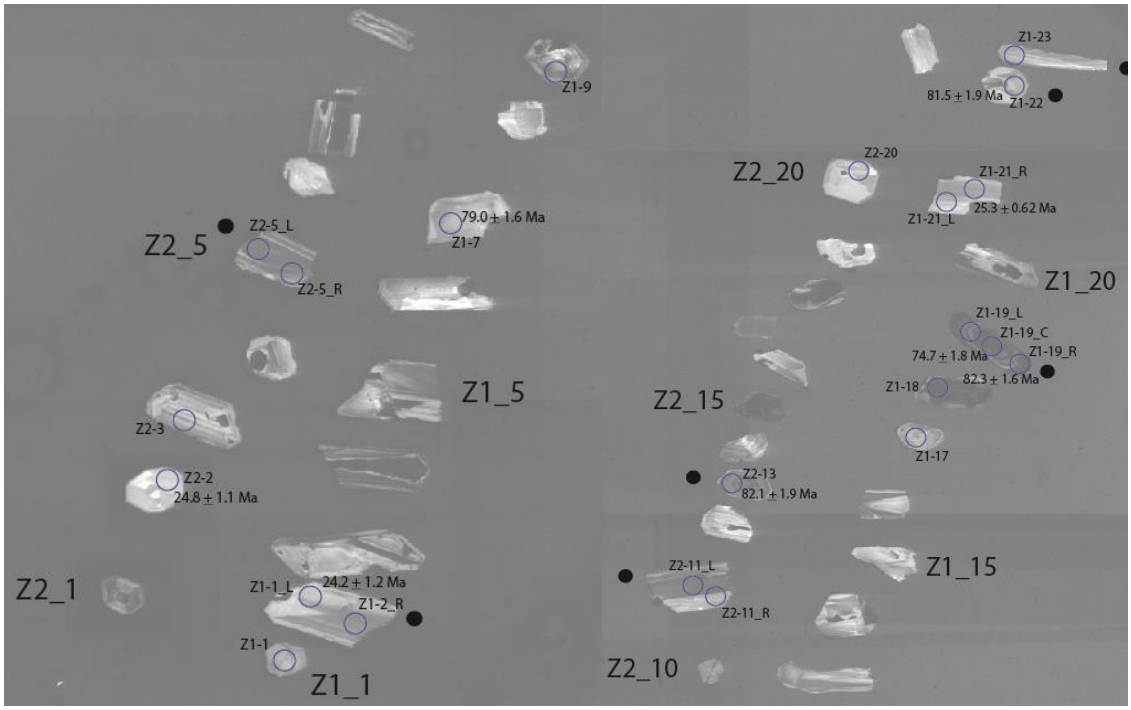

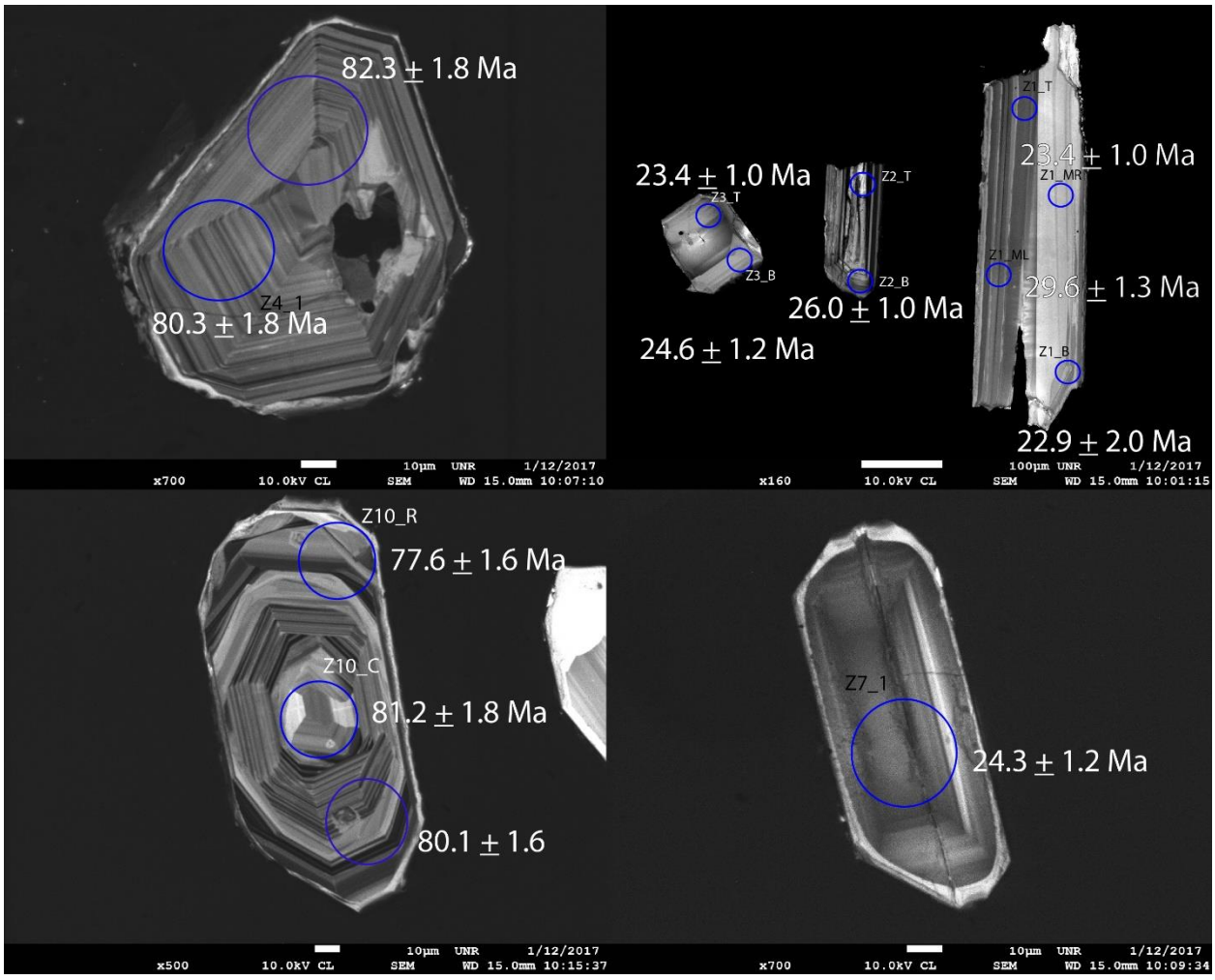

Zircons from sample RBCPQ114A (Td): Circles represent laser spots, which are 30µm in diameter. Ages for each spot are labeled. Circles without an age were not analyzed.

RBCPQ114B	238U	1 sigma	207Pb	1 sigma	Th	206/238	1 sigma	207/206	1 sigma
Tlg	206Pb	% error	206Pb	% error	U	age	abs err	age	abs err
75	112.2759	1.61%	0.1940	2.61%	0.430	57.2	0.9	2776.7	42.2
74	193.0991	1.07%	0.0899	0.89%	0.609	33.3	0.4	1423.3	16.9
73	65.0989	1.00%	0.1184	3.59%	0.336	98.3	1.0	1932.1	62.9
72	79.0857	2.19%	0.3113	0.96%	0.350	81.0	1.8	3527.5	14.7
71	68.2316	1.97%	0.1901	2.28%	0.440	93.8	1.8	2743.4	37.0
93	58.5233	1.22%	0.0512	2.11%	0.497	109.2	1.3	249.8	47.9
92	141.9859	1.28%	0.0652	0.92%	0.354	45.2	0.6	779.6	19.3
91	79.9011	0.85%	0.0904	2.59%	0.170	80.2	0.7	1434.3	48.6
90	190.2172	0.89%	0.0513	0.89%	0.460	33.8	0.3	253.7	20.4
89	76.4556	0.90%	0.1019	1.91%	0.237	83.8	0.8	1659.0	34.9
88	153.3044	1.38%	0.0518	0.87%	0.235	41.9	0.6	278.7	19.7
87P	99.5961	0.98%	0.0866	1.50%	0.585	64.4	0.6	1352.0	28.7
86P	160.3339	1.57%	0.0519	0.83%	0.734	40.1	0.6	281.1	18.8
85P	120.0373	2.49%	0.1612	1.72%	0.422	53.5	1.3	2468.6	28.7

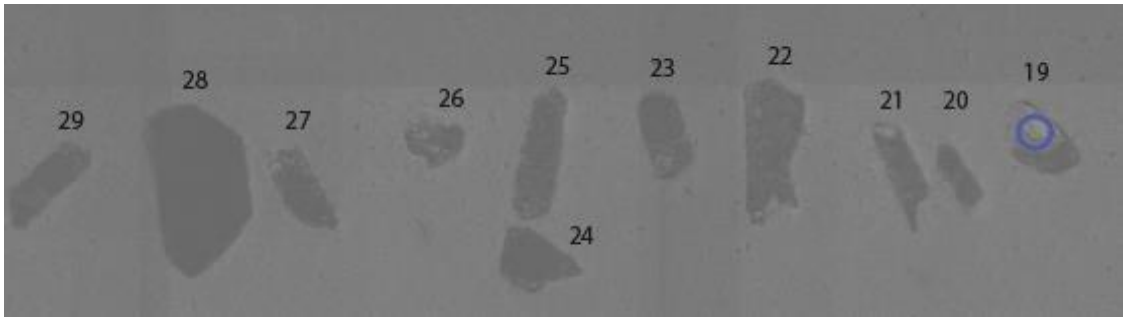

Zircons from 114B (Tlg) are strongly metamict and no concordat age could be determined.